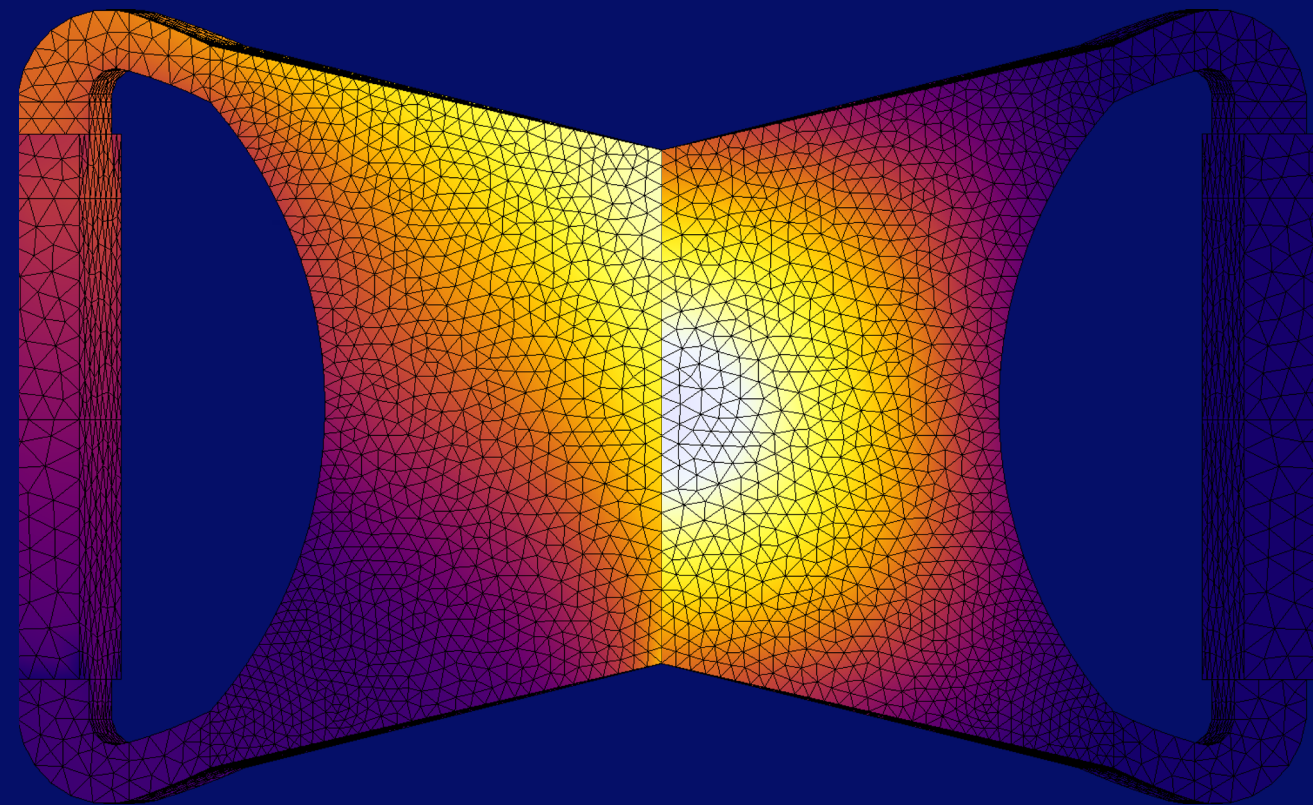


Development of a high-fidelity multi-physics simulation tool for liquid-fuel fast nuclear reactors

Marco Tiberga



M. Tiberga Development of a high-fidelity multi-physics simulation tool for liquid-fuel fast nuclear reactors

You are warmly invited to attend the defence of my thesis with title

Development of a high-fidelity multi-physics simulation tool for liquid-fuel fast nuclear reactors

24th August 2020

at 10:00 in the Senatzaal of TU Delft, Mekelweg 5, Delft

I will give a presentation before the defence at 9:30

Marco Tiberga

Propositions

Belonging to the Ph.D. thesis of Marco Tiberga

DEVELOPMENT OF A HIGH-FIDELITY MULTI-PHYSICS SIMULATION TOOL FOR LIQUID-FUEL FAST NUCLEAR REACTORS

1. A molten salt fast reactor is the most challenging Generation IV nuclear system to model and simulate. (This thesis)
2. The benefits of using accurate numerical methods and models for the simulation of the Molten Salt Fast Reactor are limited by its current design status. (This thesis, Chapter 5)
3. The adjective “innovative” associated with Generation IV nuclear reactor designs¹ is misleading: “revived” would be more correct.
4. The problem of fake-news persistence in social media can be solved only via forms of censorship.²
5. Open-space offices hinder collaboration instead of fostering it.³
6. The CoViD19 pandemic and the societal response to it provide useful lessons to fight climate change.⁴
7. The hardest challenges related to the disposal of long-lived radioactive waste are social and cultural rather than technical.
8. A paradigm shift in house-planning is necessary for healthy remote-working regimes.⁵
9. The clarity of simulation software in development is inversely proportional to the programmer’s productivity.
10. E-readers have detrimental consequences on the professionalism of videoconference backgrounds.⁶

These propositions are regarded as opposable and defensible, and have been approved as such by promoters Prof. dr. ir. J.L. Kloosterman and Dr. ir. D. Lathouwers.

¹Generation IV International Forum. *A Technology Roadmap for Generation IV Nuclear Energy Systems*. Technical Report GIF-002-00, 2002.

²E. Zollo, A. Bessi, M. Del Vicario, A. Scala, G. Caldarelli, L. Shekhtman, S. Havlin, and W. Quattrociocchi, De-bunking in a world of tribes, *PLoS ONE*, **12** (7), e0181821, 2017.

³E. S. Bernstein and S. Turban, The impact of the ‘open’ workspace on human collaboration, *Philosophical Transactions of the Royal Society B: Biological Sciences*, **373** (1753), 20170239, 2017.

⁴D. Pinner, M. Rogers, and H. Samandari, Addressing climate change in a post-pandemic world, *McKinsey Quarterly*, April 2020.

⁵S. Deganello. Smart working, attenzione alla qualità dell’aria nelle stanze . *Il Sole 24 Ore*, March 15, 2020.

⁶A. Hess. The “Credibility Bookcase” Is the Quarantine’s Hottest Accessory. *The New York Times*, May 1, 2020.

Stellingen

Behorende bij het proefschrift van Marco Tibergera

DEVELOPMENT OF A HIGH-FIDELITY MULTI-PHYSICS SIMULATION TOOL FOR LIQUID-FUEL FAST NUCLEAR REACTORS

1. De gesmolten zout reactor is de meest uitdagende Generatie IV reactor om te modelleren en simuleren. (Dit proefschrift)
2. De voordelen van het gebruik van nauwkeurige numerieke methoden en modellen voor de simulatie van de gesmolten zout reactor worden beperkt door de huidige ontwerpstatus. (Dit proefschrift, Hoofdstuk 5)
3. Het bijvoeglijk naamwoord “innovatief” dat wordt geassocieerd met Generatie IV reactoren¹ is misleidend: “hernieuwd” zou juist zijn.
4. Het probleem van de persistentie van nepnieuws in sociale media kan alleen via vormen van censuur worden opgelost.²
5. Kantoortuinen belemmeren samenwerking in plaats van dit te bevorderen.³
6. De CoViD19 pandemie en de maatschappelijke reactie daarop bieden nuttige lessen om klimaatverandering te bestrijden.⁴
7. De grootste uitdagingen met betrekking tot de opslag van langlevend radioactief afval zijn sociaal en cultureel in plaats van technisch.
8. Voor gezond werken op afstand is een paradigmaverschuiving in ontwerp van huis en inrichting nodig.⁵
9. De duidelijkheid van simulatiesoftware in ontwikkeling is omgekeerd evenredig met de productiviteit van de programmeur.
10. E-readers hebben negatieve gevolgen voor de professionaliteit van de bij videoconferenties gebruikte achtergronden.⁶

Deze stellingen worden opponeerbaar en verdedigbaar geacht en zijn als zodanig goedgekeurd door de promotoren Prof. dr. ir. J.L. Kloosterman en Dr. ir. D. Lathouwers.

¹Generation IV International Forum. *A Technology Roadmap for Generation IV Nuclear Energy Systems*. Technical Report GIF-002-00, 2002.

²E. Zollo, A. Bessi, M. Del Vicario, A. Scala, G. Caldarelli, L. Shekhtman, S. Havlin, and W. Quattrociochi, De-bunking in a world of tribes, *PLoS ONE*, **12** (7), e0181821, 2017.

³E. S. Bernstein and S. Turban, The impact of the ‘open’ workspace on human collaboration, *Philosophical Transactions of the Royal Society B: Biological Sciences*, **373** (1753), 20170239, 2017.

⁴D. Pinner, M. Rogers, and H. Samandari, Addressing climate change in a post-pandemic world, *McKinsey Quarterly*, April 2020.

⁵S. Deganello. Smart working, attenzione alla qualità dell’aria nelle stanze. *Il Sole 24 Ore*, March 15, 2020.

⁶A. Hess. The “Credibility Bookcase” Is the Quarantine’s Hottest Accessory. *The New York Times*, May 1, 2020.

**Development of a high-fidelity
multi-physics simulation tool
for liquid-fuel fast nuclear reactors**

Development of a high-fidelity multi-physics simulation tool for liquid-fuel fast nuclear reactors

Proefschrift

ter verkrijging van de graad van doctor
aan de Technische Universiteit Delft,
op gezag van de Rector Magnificus Prof. dr. ir. T.H.J.J. van der Hagen,
voorzitter van het College voor Promoties,
in het openbaar te verdedigen op 24 augustus 2020 om 10:00 uur

door

Marco TIBERGA

Master of Science in Energy and Nuclear Engineering

Politecnico di Torino, Italië

geboren te Asti, Italië

Dit proefschrift is goedgekeurd door de promotoren:

Prof. dr. ir. J.L. Kloosterman

Dr. ir. D. Lathouwers

Samenstelling promotiecommissie:

Rector Magnificus,

voorzitter

Prof. dr. ir. J.L. Kloosterman,

Technische Universiteit Delft, promotor

Dr. ir. D. Lathouwers,

Technische Universiteit Delft, promotor

Onafhankelijke leden:

Prof. dr. A. Pautz,

École Polytechnique Fédérale de Lausanne

Prof. dr. M.R. de Baar,

Technische Universiteit Eindhoven

Prof. dr. M.E. Ricotti,

Politecnico di Milano

Dr. ing. S. Kenjereš,

Technische Universiteit Delft

Prof. dr. ir. B.J. Boersma,

Technische Universiteit Delft

Copyright © 2020 by Marco Tiberga

All rights reserved. No part of this book may be reproduced, stored in a retrieval system, or transmitted, in any form or by any means, without prior permission from the copyright owner.

ISBN 978-94-028-2142-0

Keywords: Molten salt reactor, Fast-spectrum, Nuclear reactor, Thermal-hydraulics, Neutronics, Multi-physics, Coupling, Finite Element Method, Discontinuous Galerkin, S_N neutron transport



This research was performed in the Reactor Physics and Nuclear Materials (RPNM) section of the Department of Radiation Science and Technology (RST) of Delft University of Technology (The Netherlands).

Financial support

This project has received funding from the Euratom research and training programme 2014-2018 under the grant agreement No. 661891.

Printed by: Ipskamp Printing (www.ipskampprinting.nl).

An electronic version of this dissertation is available at

<http://repository.tudelft.nl/>.

Contents

Summary	xi
Samenvatting	xv
1 Introduction	1
1.1 Background	1
1.2 Molten Salt Reactors: brief history and overview of the research current status	2
1.3 The Molten Salt Fast Reactor	3
1.4 Physics phenomena in liquid-fuel nuclear reactors	7
1.4.1 Neutronics	7
1.4.2 Thermal-hydraulics	9
1.5 Research objectives and thesis outline	10
2 DG-FEM solver for the incompressible RANS and $k-\epsilon$ equations	13
2.1 Introduction	14
2.2 Governing equations	16
2.2.1 Boundary and initial conditions	17
2.3 Spatial discretization	19
2.3.1 RANS discretization	20
2.3.2 Discretization of turbulence equations	23
2.4 Temporal discretization	24
2.4.1 Algebraic splitting scheme	25
2.5 Solution of linear systems	27
2.6 Choice of the solution polynomial order	27
2.7 Test cases	30
2.7.1 Manufactured solution	30
2.7.2 Flow over a backward-facing step	34
2.7.3 Vortex-shedding in the wake of a square cylinder	37
2.8 Conclusions	42
3 Neutronics and thermal-hydraulics coupled solver	43

3.1	Introduction	44
3.2	Description of the multi-physics tool	47
3.2.1	Fluid dynamics: DGFloWS code	47
3.2.2	Neutronics: PHANTOM-S _N code	50
3.2.3	Coupling Strategy and Cross Sections Treatment	53
3.2.4	Mesh generation and manipulation	54
3.2.5	Verification and validation	56
3.3	The MSFR: design and modeling approach	57
3.3.1	Design description	57
3.3.2	Modeling approach	58
3.4	Results of preliminary MSFR simulations	63
3.4.1	Steady-state solution	63
3.4.2	Transient: unprotected Total Loss of Power accident	68
3.5	Conclusions	71
4	Benchmark of the multi-physics tool for fast-spectrum MSRs	73
4.1	Introduction	74
4.2	Description of the benchmark	76
4.2.1	General description	76
4.2.2	Geometry and boundary conditions	76
4.2.3	Input data	77
4.3	Phases and steps of the benchmark	79
4.3.1	Phase 0: Single physics benchmark	79
4.3.2	Phase 1: Steady-state coupling	80
4.3.3	Phase 2: Time dependent coupling	82
4.4	Code packages	84
4.5	Results	85
4.5.1	Phase 0: Single physics benchmark	86
4.5.2	Phase 1: Steady-state coupling	89
4.5.3	Phase 2: Time dependent coupling	96
4.6	Conclusions	97
5	Analysis of the MSFR steady-state and transient behavior	99
5.1	Introduction	99
5.2	Modeling choices	101
5.3	Assessment of the MSFR steady-state	102
5.3.1	Thermal-hydraulics analysis	103
5.3.2	Neutronics analysis	105
5.4	Analysis of MSFR transient behavior	110
5.4.1	Unprotected Loss of Heat Sink (ULOHS)	111
5.4.2	Unprotected Loss of Fuel Flow (ULOFF)	115
5.4.3	Total Loss of Power (TLOP)	120
5.4.4	Unprotected Pump Over-speed (UPOS)	124

5.4.5 Salt Over-cooling (OVC)	127
5.5 Conclusions	127
6 Conclusions and recommendations	131
6.1 Conclusions	131
6.2 Recommendations and perspectives	134
6.2.1 Improvements and optimizations	134
6.2.2 Extension of the current models	134
Bibliography	137
A Multi-physics numerical benchmark: Observables fields	153
A.1 Velocity	153
A.2 Temperature	153
A.3 Delayed neutron precursors	153
Acknowledgments	159
List of publications	161
About the author	163

Summary

The Molten Salt Reactor (MSR) is one of the six Generation-IV nuclear reactor designs. It presents very promising characteristics in terms of safety, sustainability, reliability, and proliferation resistance. Numerous research projects are currently carried out worldwide to bring this future reactor technology to a higher maturity. In Europe, efforts are focused on developing a fast-spectrum design, named Molten Salt Fast Reactor (MSFR).

Numerical simulations are essential to develop MSR designs, given the scarce operational experience gained with this technology and the current unavailability of experimental reactors. However, modeling a molten salt reactor is a challenging task, due to the unique physics phenomena induced by the adoption of a liquid fuel that is also the coolant: transport of delayed neutron precursors, strong negative temperature feedback coefficient, distributed generation of heat directly in the coolant. Moreover, the geometry of the core cavity of fast-spectrum designs often induces complex three-dimensional flow effects. For these reasons, legacy codes traditionally used in the nuclear community often prove unsuitable to accurately model MSRs, in particular fast-spectrum designs, and must be replaced by dedicated tools.

This thesis presents the development of one of these multi-physics codes, which aims at accurately modeling the three-dimensional neutron transport, fluid flow, and heat transfer physics phenomena characterizing a fast-spectrum liquid-fuel nuclear reactor. As the research was carried out in the context of the Euratom SAMOFAR project, the MSFR is taken as reference case study, analyzing its behavior at steady-state and during several transient scenarios to assess the safety of the current design.

We first describe the newly developed CFD code. It consists of a discontinuous-Galerkin Finite Element (DG-FEM) solver for the incompressible Reynolds-Averaged Navier-Stokes equations (RANS) coupled to the classic $k - \epsilon$ high-Reynolds turbulence model. We solve for the logarithm of the turbulence quantities to guarantee their positivity. The chosen DG-FEM space discretization combines the local conservation property of Finite Volume schemes with the high-order discretization

and geometric flexibility typical of FEM, necessary to handle the complex geometry of the MSFR core. All governing equations are discretized in time with implicit backward differentiation formulae (BDF). This, combined to a pressure-correction scheme, guarantees global second-order time accuracy. We verify the correctness of the space-time discretization with the method of manufactured solutions. Results of the simulation of a backward-facing step and of a Von Kármán vortex street in the wake of a square cylinder show good agreement with those reported in literature and validate our approach.

Then, we describe the neutronics code and the coupling between the two tools. An existing DG-FEM discrete ordinates transport solver is extended to model the movement of delayed neutron precursors, as well as the decay-heat distribution. Time-dependent problems are handled with the adoption of a second-order accurate BDF scheme for all equations. Attention is paid to increase the efficiency of the preconditioner for the coupled flux-precursors equations in this class of problems. The coupling between the codes is realized by exchanging data and iterating when necessary. To optimize the computational cost, neutronics and thermal-hydraulics meshes can be different, with the latter typically more refined in regions of low neutron importance but large flow gradients (e.g. close to the wall boundaries of the reactor). The hierarchy of the mesh refinement makes the exchange of data easy through Galerkin projection. For steady-state calculations, codes are iterated until convergence, while in transient calculations a loose-coupling strategy is adopted. Proper time-extrapolation of the fields exchanged ensures global second-order time convergence. Preliminary simulations of the MSFR show the capabilities of our multi-physics solver.

Next, we benchmark the multi-physics tool with a test case specifically designed to properly assess the correctness of the coupling scheme and its capability to model the complex physics phenomena characterizing fast-spectrum MSRs. We present the results of a collaboration between TU Delft and several partners of the SAMOFAR project. The characteristics of the nuclear system under investigation make it a simple representation of the MSFR. The benchmark is structured into several steps in which steady-state or transient problems are solved, gradually coupling the various physics phenomena to easily identify sources of error. By comparing our results with those obtained by the other partners, we prove our code is able to correctly model the physics phenomena characterizing a liquid-fueled fast reactor.

In the final part of the thesis, we employ our novel multi-physics tool to extensively analyze the MSFR behavior at steady-state and during several accidental transient scenarios: loss of heat sink, loss of fuel flow, total loss of power, pump over-speed, and salt over-cooling. Steady-state calculations show that previous interventions on the MSFR core geometry were effective in removing unwanted hot spots at the entrance of the core cavity. However, a large recirculation region is still present and

should be eliminated in the future, as it induces localized pressure drops. Moreover, the concentration of fissile material in the fuel salt should be reduced, as the reactor turns out to be supercritical at the intended salt average operating temperature. No threats for the reactor safety could be detected during the simulated transients. The salt temperature always keeps a considerable margin both from the freezing point and the critical temperature causing damages to structural materials, thanks to the large salt heat capacity and the strong negative reactivity feedback coefficient. However, natural circulation is very limited so further optimization of the design should focus on reducing pressure losses in the fuel circuit.

In conclusion, the solver described in this thesis, which is the first multi-physics code dedicated to liquid-fuel fast reactors based on a full-transport neutronics model and on high-order DG-FEM space discretization, proved capable of accurately modeling the complex physics phenomena characterizing this reactor technology. It was employed to derive useful information on the current status of the MSFR design. This research constitutes a solid base for possible follow-up studies, which we discuss.

Samenvatting

De gesmolten zout reactor (MSR) is een van de zes generatie-IV kernreactorontwerpen. Het vertoont veelbelovende kenmerken op het gebied van veiligheid, duurzaamheid, betrouwbaarheid en non-proliferatie. Momenteel lopen wereldwijd diverse onderzoeksprojecten om deze toekomstige reactortechnologie op een hoger niveau te brengen. In Europa zijn de inspanningen gericht op het ontwikkelen van een snel-spectrum ontwerp, genaamd de “Molten Salt Fast Reactor” (MSFR).

Numerieke simulaties zijn essentieel om MSR-ontwerpen te ontwikkelen, gezien de schaarse operationele ervaring met deze technologie en de afwezigheid van experimentele reactoren. Het modelleren van een gesmolten-zout reactor is een uitdaging vanwege de unieke fysische verschijnselen veroorzaakt door het gebruik van een vloeibare brandstof dat tegelijkertijd als koelmiddel dient: transport van precursorkernen, een sterk negatieve temperatuur-terugkoppelcoëfficiënt, en een ruimtelijk verdeelde warmteontwikkeling direct in het koelmiddel. Bovendien induceert de geometrie van het reactorvat van ontwerpen met een snel spectrum vaak complexe driedimensionale stromingseffecten. Om deze redenen blijken traditionele codes gebruikt in de nucleaire gemeenschap vaak te onnauwkeurig om MSR's te modelleren en moeten deze worden vervangen door gespecialiseerde codes.

Dit proefschrift presenteert de ontwikkeling van $\tilde{\text{MSFR}}$ van deze multi-fysica-codes, die is gericht op het nauwkeurig modelleren van de karakteristieke aspecten van een dergelijke reactor, te weten, driedimensionaal neutronentransport, vloeistofstroming, en warmteoverdracht. Aangezien het onderzoek is uitgevoerd in het kader van het Euratom SAMOFAR-project, wordt de MSFR als referentie genomen en wordt het gedrag in stationaire toestand en tijdens verschillende tijdafhankelijke scenario's gesimuleerd om de veiligheid van het huidige ontwerp te beoordelen.

We beschrijven eerst de nieuw ontwikkelde CFD-code. Deze is gebaseerd op een discontinue- Galerkin eindige elementen (DG-FEM) oplosmethode voor de niet-samendrukbare Reynolds-gemiddelde Navier-Stokes-vergelijkingen (RANS) gekoppeld aan het klassieke $k - \epsilon$ hoge Reynolds turbulentie model. We lossen de vergelijkingen op voor de logaritme van de turbulentie-grootheden om hun positiviteit te garanderen. De gekozen ruimte-discretisatie van DG-FEM combin-

eert de lokale behoudseigenschap van de eindige volume methode met hoge orde nauwkeurigheid en geometrische flexibiliteit die typisch is voor de eindige elementen methode, nodig om de complexe geometrie aan te kunnen van de MSFR-kern. De transportvergelijkingen worden impliciet in de tijd gediscretiseerd met achterwaartse differentiatieformules (BDF). Gecombineerd met een drukcorrectie schema, levert dit een gegarandeerde globale nauwkeurigheid van de tweede-orde in de tijd. We controleren de juistheid van de ruimte-tijd discretisatie met de methode van vervaardigde oplossingen. Resultaten van de simulatie van een “backstep” en van een Von Kármán-vortexstraat achter een vierkante cilinder vertonen een goede overeenkomst met de literatuur en valideren onze aanpak.

Vervolgens beschrijven we de neutronica-code en de koppeling tussen de twee tools. Een bestaande DG-FEM discrete-ordinaten transportcode is uitgebreid met het transport van de vertraagde neutronenprecursoren, alsook met de vervalwarmteverdeling. Tijdsafhankelijke problemen worden aangepakt met een tweede orde nauwkeurig BDF-schema voor alle vergelijkingen. Er is aandacht besteed aan het verhogen van de efficiëntie van de preconditioner voor de gekoppelde flux-precursor vergelijkingen in deze klasse van problemen. De koppeling tussen de codes wordt gerealiseerd door gegevens uit te wisselen en te itereren wanneer noodzakelijk. Om de simulatietijd te optimaliseren, kunnen de rekenroosters voor neutronica en thermo-hydraulica verschillen, waarbij de laatste typisch verfijnder zijn in regio's met lage neutronendichtheid maar grote stromingsgradiënten (bijv. dicht bij de wanden van de reactor). De hiërarchische rooster-verfijning maakt de uitwisseling van gegevens eenvoudig via Galerkin-projectie. Voor steady-state berekeningen worden de codes geïtereerd tot convergentie, terwijl in transiënte berekeningen een strategie van losse koppeling wordt gebruikt. Extrapolatie van de uitgewisselde velden zorgt voor een globale tweede-orde tijd convergentie. Voorbereidende simulaties van de MSFR laten de mogelijkheden zien van ons multi-fysica simulatie-pakket.

Vervolgens benchmarken we de multi-fysica simulatietool met een speciaal ontworpen testcase om de juistheid van het koppelingsschema te testen en het vermogen van het simulatieprogramma te beoordelen op het correct simuleren van complexe fysische verschijnselen van snel-spectrum MSRs. We presenteren de resultaten van een samenwerking tussen de TU Delft en verschillende partners van het SAMOFAR-project. Het benchmark systeem is een eenvoudiger weergave van de complete MSFR. De benchmark is gestructureerd in verschillende stappen waarin scenario's geleidelijk complexer worden door introductie van de verschillende fysische verschijnselen om gemakkelijker foutbronnen te identificeren. Door onze resultaten te vergelijken met die van de andere partners, bewijzen we dat onze code in staat is om de fysische verschijnselen die een snelle reactor met vloeibare brandstof kenmerken accuraat te modelleren.

In het laatste deel van het proefschrift gebruiken we onze nieuwe multi-fysica tool

voor een uitgebreide analyse van het MSFR-gedrag in stationaire toestand en tijdens verschillende transiëntscenario's: verlies van koeling, verlies van brandstofstroming, totaal vermogensverlies, pomp over-toeren, en zout over-koeling. Berekeningen van de stationaire toestand laten zien dat eerdere aanpassingen op de geometrie van de MSFR-kern effectief zijn in het verwijderen van ongewenste hotspots bij de ingang van het reactorvat. Er is echter nog steeds een groot recirculatiegebied aanwezig dat in de toekomst dient te worden geëlimineerd omdat het plaatselijke drukvariaties veroorzaakt. Ook de concentratie van splijtbaar materiaal in het brandstofzout moet worden verlaagd, omdat de reactor superkritisch blijkt te zijn bij de beoogde gemiddelde bedrijfstemperatuur van het zout. Tijdens de gesimuleerde transiënten konden geen bedreigingen voor de reactorveiligheid worden gedetecteerd. Vanwege de grote warmtecapaciteit van het zout en de sterke terugkoppeling, houdt de zouttemperatuur altijd een aanzienlijke marge ten opzichte van het vriespunt en de kritische temperatuur die schade aan structurele materialen veroorzaakt. De natuurlijke circulatie is echter zeer beperkt, dus verdere optimalisatie van het ontwerp moet gericht zijn op het verminderen van drukverliezen in het brandstofcircuit.

De oplosmethode ontwikkeld in dit proefschrift beschrijft de eerste multi-fysica code voor snelle reactoren met vloeibare brandstof, gebaseerd op een compleet transport model voor neutronica en op de hoge orde van DG-FEM discretisatie in ruimte. Het model bleek een nauwkeurige beschrijving te geven van de complexe fysische verschijnselen die deze reactortechnologie kenmerken. Het model is gebruikt om nuttige informatie af te leiden over de huidige status van het MSFR-ontwerp. Dit onderzoek vormt een solide basis voor mogelijke vervolgstudies.

(Dutch translation provided by Danny Lathouwers with corrections by Jan Leen Kloosterman.)

CHAPTER 1

INTRODUCTION

1.1 Background

In 2019, the International Energy Agency estimated an increase of the world energy demand between 24% and 34% within 2040 (International Energy Agency, 2019b). In particular, electricity generation will rise by nearly 60% following the economic expansion of the developing countries, the population growth (estimated to reach approximately 11 billion individuals by the end of the century (United Nations, 2019)), and the increasing share of electrical vehicles in the transportation sector.

At the same time, public opinion is urging world leaders to take serious actions against climate change (Laville and Watts, 2019) and to pursue with greater efforts the goals set with the Paris Agreement in 2015 (UNFCCC, 2015). In fact, without consistently reducing the emission of green-house gases in the atmosphere, the average global surface temperature will likely rise above 2°C relative to the period 1850–1900, with well-known catastrophic consequences for the environment and life in general (IPCC, 2013).

Low-carbon energy sources clearly play a fundamental role in accommodating the two aforementioned (partially contrasting) needs, as the power sector contributes to nearly 40% of the total energy-related CO₂ emissions (International Energy Agency, 2019b). In particular, nuclear energy can provide clean, reliable, high-density electricity and high-temperature thermal energy at competing costs (Brook et al., 2014; International Energy Agency, 2019a). However, despite having one of the lowest mortality rates (deaths per produced TWh) among all electricity sources (Markandya and Wilkinson, 2007; Brook et al., 2014; Sovacool et al., 2016), public and political debate on nuclear energy is dominated by concerns on waste management, safety, and use for non-civil purposes of the power plants under

operation.

With the aim of addressing these issues, the Generation IV International Forum (GIF) was formed in 2001, and its activities resulted in the selection of six innovative nuclear reactor designs that are safer, more sustainable, and more proliferation resistant (Generation IV International Forum, 2002).

This thesis focuses on one of them: the Molten Salt Reactor (MSR). The relatively low technology readiness level (TRL) of this reactor design demands a huge research effort for its advancement, both from the experimental and the numerical point of view. In this context, the work described here deals with the development of an advanced multi-physics simulation tool for liquid-fuel reactors and its application to the analysis of the European fast-spectrum MSR (Allibert et al., 2016).

The remainder of this introductory chapter is aimed at providing the unfamiliar reader with some notions on the MSR technology in terms of history and research status (Section 1.2), on the specific MSR design under investigation with its main characteristics, advantages, and challenges (Section 1.3), and on the physical phenomena characterizing this peculiar nuclear reactor (Section 1.4). We conclude focusing on the research objectives of this work and outlining the content of the following chapters (Section 1.5).

1.2 Molten Salt Reactors: brief history and overview of the research current status

Circulating fuel reactors were first proposed in the post World War II as potential compact engines that could propel supersonic aircraft for very long time without refueling needs. To study the feasibility of the technology, the Aircraft Reactor Experiment (ARE) was designed and constructed at Oak Ridge National Lab (ORNL) and operated for a few days in November 1954 (Bettis et al., 1957a,b).

Soon after the interest for military applications vanished, ORNL director Alvin Weinberg started to investigate the potential of the technology for civilian purposes (MacPherson, 1985). The project, carried out in the late fifties and sixties, led to the development and the construction of the Molten Salt Reactor Experiment (MSRE) (Robertson, 1965). This $\sim 8 \text{ MW}_{th}$ graphite-moderated reactor, fueled with a mixture of lithium, beryllium, zirconium, and uranium fluorides, was successfully operated for four years until 1969 proving the soundness, the reliability, and the safety of the technology (Haubenreich and Engel, 1970).

Encouraged by the success of the MSRE operations and the results of the experiments linked to it, ORNL scientists proposed the design of the Molten Salt Breeder Reactor (MSBR), a 1000 MW_e single-fluid thermal reactor fueled with ^{232}Th and ^{233}U having positive breeding gain (Robertson, 1971). However, the entire program was shut down in favor of the competing liquid-metal breeder reactor technology, and research essentially stagnated for the following 30 years.

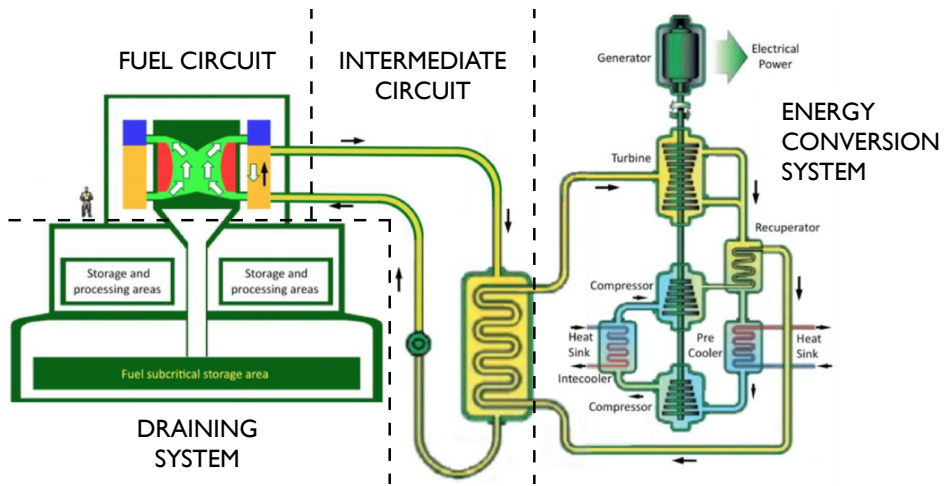
Interest in MSRs regained momentum after the decision of the GIF to include this technology in the list of the new-generation reactors (LeBlanc, 2010), and currently a huge international research effort is carried out to bring the technology to a higher TRL, to be able to construct new experimental and demonstrator reactors. A great diversity of designs is currently investigated all around the world (Serp et al., 2014; Dolan, 2017), including both thermal (e.g., Yoshioka, 2013; LeBlanc and Rodenburg, 2017; Zhang et al., 2018) and fast spectrum reactors (e.g., Ignatiev et al., 2014), but also solid-fuel designs that only exploit the large heat capacity of the molten salt for efficient cooling (e.g., Holcomb et al., 2014; Zhang et al., 2018).

In Europe, research has been focusing on the Thorium Molten Salt Reactor concept, which stems from a re-evaluation of the MSBR design (Vergnes and Lecarpentier, 2002; Nuttin et al., 2005). However, it was soon decided to shift from a thermal to a non-moderated configuration (Mathieu et al., 2006, 2009), which has safer neutronics characteristics (large negative feedback coefficients), eliminates by design the problem of the limited life-time of the graphite moderator, and lowers the reprocessing requirements to obtain high breeding efficiencies. Consequently, this design concept is now referred to as Molten Salt Fast Reactor (MSFR). Together with the MOlten Salt Actinide Recycler and Transmuter (MOSART) concept under development in the Russian Federation (Ignatiev et al., 2012, 2014), they represent the two fast-spectrum MSRs currently studied within the GIF framework (Generation IV International Forum, 2018).

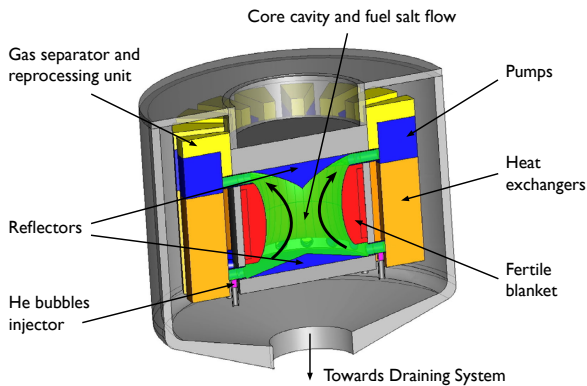
The work described in this thesis was performed in the context of the Euratom Horizon 2020 project Safety Assessment of the MOlten salt FAst Reactor (SAMOFAR, <http://samofar.eu/>). For this reason, we focus on the MSFR design in the remainder, describing its characteristics, main advantages, and the current open challenges. Most of the considerations are however valid for all liquid-fuel reactors in general.

1.3 The Molten Salt Fast Reactor

Figure 1.1 presents a schematic view of the MSFR Balance of Plant (BoP) and a focus on the fuel circuit. The current reference configuration (Allibert et al., 2016; Gérardin et al., 2017; Gérardin, 2018) is a 3000 MW_{th} reactor in which 18 m³ of fluoride salt are circulated through sixteen identical sectors, consisting of a pump, a heat exchanger, and a system for the extraction and the treatment of gas bubbles dispersed in the salt. The core shape is toroidal, with minimum and maximum radii equal to 1.05 m and 1.41 m, and a height varying from 1.6 m at the center to 2.25 m at the boundaries (Rouch et al., 2014). The liquid salt enters from the bottom and rises through the core cavity heating up by approximately 100 °C, resulting in an average temperature of nearly 700 °C. The core is surrounded by a radial blanket filled with fertile LiF-ThF₄ (77.5-22.5 % mol) for breeding purposes



(a) Scheme of the MSFR Balance of Plant.



(b) Scheme of the MSFR fuel circuit.

Fig. 1.1. Schematic representation of the MSFR Balance of Plant and focus on its fuel circuit.

and by upper and lower reflectors which improve neutron economy.

The fuel consists of a mixture of lithium and thorium fluorides with the addition of other fissile actinides; in particular, two compositions have been investigated in the framework of SAMOFAR (Heuer et al., 2014):

- ^{233}U -based: $\text{LiF-ThF}_4\text{-}^{233}\text{UF}_4$ (77.5-20-2.5 % mol); and
- TRU- ^{235}U -based: $\text{LiF-ThF}_4\text{-}^{\text{enr}}\text{UF}_4\text{-(TRU)F}_3$ (77.5-6.6-12.3-3.6 % mol), where U is enriched at 13 % in ^{235}U and the transuranic elements (TRU) are mainly plutonium and other minor actinides.

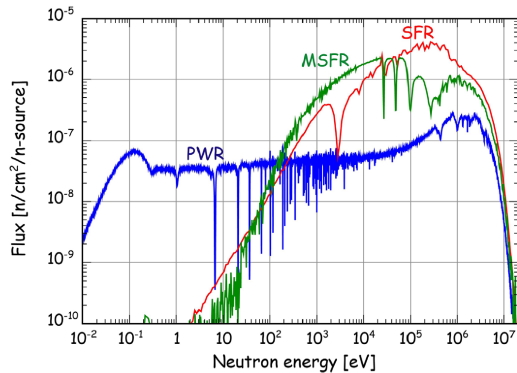


Fig. 1.2. MSFR spectrum compared to the one of a Sodium-cooled Fast Reactor (SFR) and a thermal Pressurized Water Reactor (PWR). From Brovchenko et al. (2019).

The resulting reactor spectrum is fast, as shown in Figure 1.2; however, the presence of light elements (F and Li) in the salt leads to a softer spectrum when compared to other fast reactors (Merle et al., 2012).

The MSFR BoP is completed by an intermediate circuit in which four loops filled with inert sodium fluoroborate (NaF-NaBF_4) (Tripodo et al., 2019) transfer the thermal energy to the Energy Conversion System, constituted by a conventional Joule-Brayton cycle (based on helium or supercritical CO_2). Their design is still under development, but the goal is to reach a conversion efficiency around 45 %.

The use of a liquid salt acting both as fuel and thermal carrier in the primary circuit clearly constitutes the unique feature of this reactor. This, the fast spectrum, and the adoption of the thorium fuel cycle grant the MSFR peculiar characteristics and advantages that fulfill the goals set by the GIF. These features have been extensively treated in the literature (e.g., LeBlanc, 2010; Hargraves and Moir, 2010; Serp et al., 2014; Dolan, 2017), and we summarize here the most relevant ones:

- The fuel presents strong negative Doppler and density feedback coefficients, which enhance the stability of the reactor;
- Reactivity is then controlled by the temperature changes and by dissolving helium bubbles in the salt (Delpech et al., 2009). Control rods are therefore superfluous, and this removes by design some possible accident initiators;
- The fuel has high boiling point (~ 2000 K) and a low vapor pressure, which allow for operations at very low pressures compared to traditional Light Water Reactor designs. This reduces the risk of pipe breaks and lowers the construction costs;

- Meltdown accidents are solved by design. Moreover, in case of necessity the liquid salt can be drained into geometrically sub-critical tanks placed underneath the core (Figure 1.1a), where it is passively cooled down (Wang et al., 2019; Massone et al., 2020). Salt draining is driven by gravitation and can be triggered by the melting of freeze-valves (Tiberga et al., 2019b), so it is completely passive;
- The helium bubbling is used also to remove the gaseous and metallic insoluble fission products. Moreover, batches of salt of a few liters per day are reprocessed in an integrated chemical plant. This controls the reactivity level (concentration of fissile isotopes and of neutron poisons like Xe), reduces the decay heat to be removed after reactor shutdown, and allows for adjustment of the fuel composition;
- The continuous salt recirculation leads to homogeneous irradiation, high burnup, and therefore better fuel utilization. Moreover, the reactor has a breeding ratio higher than one (Heuer et al., 2014);
- The thorium fuel cycle leads to less production of transuranic elements, which can be recirculated until they fission or decay. Actinides burning is also enhanced by the fast spectrum. Therefore, the long-term radiotoxicity of the nuclear waste produced is considerably lower compared to more traditional reactor designs and reaches the level of uranium ore in a few hundred years;
- Thorium is three to four times more abundant than uranium in the Earth's crust and it is already available as a by-product of the rare-earth mining. Moreover, in addition to electricity, the reactor can supply high-temperature heat for hydrogen production or water desalination processes. These aspects increase the sustainability and the economic competitiveness of the technology.

However, a number of challenges have to be addressed and solved to bring the reactor design to a higher TRL. Research is ongoing to

- find suitable structural materials able to last in a high corrosive, high temperature, and high irradiation-level environment (e.g., Surenkov et al., 2018; Ignatiev and Surenkov, 2019);
- define suitable safety procedures and requirements for licensing (e.g., Gérardin et al., 2019; Beils et al., 2019);
- define steps and procedures to reprocess the salt (e.g., Rodrigues et al., 2015);
- characterize the salt from the chemical and thermo-dynamical point of view (e.g., Durán-Klie et al., 2016; Martel et al., 2018), in order to determine its physico-chemical properties (e.g., Tosolin et al., 2019a,b) and the behavior of the fission products in it (e.g., Capelli et al., 2018).

On top of this, accurate numerical simulations have to be constantly performed to assess the safety of the reactor design and to provide indications for further improvements. In fact, data and information derived from the MSRE operation are limited and to a large extent not applicable for fast-spectrum reactors as the MSFR.

1.4 Physics phenomena in liquid-fuel nuclear reactors

MSRs present unique features compared to more traditional solid-fuel reactors which tighten and extend the coupling between the various physics phenomena characterizing a nuclear reactor. Numerical simulations are therefore particularly challenging for MSRs. Legacy codes traditionally used in the nuclear community cannot be used “as they are” and they must be extended or more often replaced by dedicated and more accurate novel multi-physics tools. This thesis is about the development of one of them.

Physics phenomena characterizing nuclear reactors and MSRs are explained in detail in the dedicated literature (e.g., Duderstadt and Hamilton, 1976; Waltar et al., 2012; Luzzi et al., 2012; Dolan, 2017; Demaziere, 2019). However, here we try to concisely describe the phenomena that are taken into account in this work, for a better understanding of the following chapters.

1.4.1 Neutronics

In the MSFR, as in any other nuclear reactor, thermal energy is produced when a fissile isotope absorbs a neutron and fissions. Each event releases approximately 200 MeV and around 2.5 neutrons on average, which can then continue the chain reaction. Whether this process is self-sustained depends on the amount of neutron absorption and leakage (that depends on the reactor geometry, i.e., surface-to-volume ratio). In this work, we adopt the Boltzmann linear transport equation to describe the neutron balance in the system (Bell and Glasstone, 1970): it is an exact model.

The effective multiplication factor (k_{eff}) of a reactor is the ratio of neutron production over removal rates and so concisely quantifies how sustained the chain reaction is: if unitary, the system is called critical and the neutron population and so the reactor power are stable, otherwise the system is sub-critical ($k_{eff} < 1$, the power decreases) or super-critical ($k_{eff} > 1$, the power increases). The reactivity, $\rho = 1 - k_{eff}^{-1}$, is used to indicate how far from criticality a nuclear system is in relative terms.

Important parameters describing the stability of a reactor design are the temperature feedback coefficients, which quantify the reactivity variations with temperature. In the MSFR, two feedback mechanisms are present:

- Doppler: some isotopes have sharp peaks in the absorption microscopic cross section at intermediate neutron energies. These cross sections depend on temperature as they are influenced by the relative velocity between neutron and target nucleus. When temperature rises, the increased thermal motion of the nuclei leads to a broadening of the resonance peaks, resulting in more neutron absorption (parasitic, in particular in the fertile nuclei);
- Density: the density of the material and so its macroscopic cross sections are inversely proportional to the temperature. Therefore, when the latter rises, the neutron mean free path increases resulting in more leakage from the system.

Hence, both coefficients are negative in the MSFR and, as described in the previous section, they are particularly strong and act almost instantaneously due to the heat deposition directly in the fuel salt. This strongly enhances the stability of the reactor and thus its safety, because power variations are quickly opposed by the resulting temperature changes. The physics of neutrons is therefore tightly coupled to the flow physics, which influences the temperature distribution in the system, which in turn depends on the fission power density distribution. However, there is a further reason specific of circulating-fuel reactors.

Of the 2.5 neutrons released on average by a fission event, only a fraction is emitted promptly (i.e., instantaneously). The remaining part (indicated with β) comes from the radioactive decay of some fission products called precursors, which happens on time scales several orders of magnitude longer depending on the half-life of each precursor¹. Despite β being very small (it depends on the fissile isotope, but it is of the order of 0.5%), these delayed neutrons are essential to slow down the response time of a nuclear reactor sufficiently to make its control feasible.

In MSRs, contrary to any solid-fuel reactor, precursors get transported by the salt flow, so delayed neutrons are not emitted where their precursors were generated. However, the probability that a neutron induces fission is space-dependent: it is the highest at the center of the reactor but low at its boundaries where leakages are more likely². Hence, the precursors redistribution has an impact on the reactor dynamics, and it is as if there were less delayed neutrons in the system (i.e., the effective β is reduced). This is of course influenced by the flow characteristics: recirculation time, turbulence level, local flow patterns, etc.

It is therefore clear that a simulation tool for the MSFR must be able to accurately model the neutron physics and the effects that temperature and flow field have on it.

Finally, together with the precursors, also the other fission products get transported by the salt flow. A fraction releases energy upon radioactive decay, resulting

¹For example, the average precursors half-life is around 13s for ²³⁵U.

²This describes the concept of neutron importance, mathematically represented by the adjoint neutron flux.

in the so-called decay heat, which continues to be generated even for long times after reactor shutdown. If not properly removed, decay heat can lead to excessive temperatures in the system with possible catastrophic consequences, as the Chernobyl or the Fukushima-Daiichi accidents showed. An accurate modeling of the decay-heat distribution in the system and its time evolution is therefore mandatory when assessing the safety of a reactor design during long transients.

1.4.2 Thermal-hydraulics

The molten salt fluid dynamics can be described by standard conservation laws for mass, momentum, and energy (Patankar, 1980; Kundu and Cohen, 2007). However, some aspects are worth attention:

- At nominal conditions, the salt recirculation time in the MSFR primary loop is 4 s and the resulting flow is highly turbulent (Reynolds number of the order of 10^5);
- The geometry of the MSFR core cavity, where repeated channel structures as in thermal-MSRs or solid-fuel reactors are absent, induces complex three-dimensional flow effects and might lead to recirculation areas, with consequent impact on the temperature distribution;
- Contrary to other reactors, thermal power deriving from fission and from decay heat is generated directly in the coolant and presents a non-uniform distribution in the entire system. This clearly affects the salt temperature distribution and consequently the dynamics of natural circulation, which is driven by the salt density variations in the primary loop (Pini et al., 2016a,b).

Rigorous Computational Fluid Dynamics (CFD) models are then mandatory to accurately reproduce these phenomena, and consequently the effects that the flow and temperature fields have on neutronics, as described in the previous section.

In this work, we model the turbulent flow physics with Reynolds Averaged Navier-Stokes equations coupled to high-Reynolds turbulence models. The salt is treated as an incompressible medium and the Boussinesq approximation is used to describe buoyancy. This is a well established approach, valid in most of the reactor operational conditions, even off-nominal. In fact, the salt Mach number is of the order of 10^{-3} and the density variations due to the salt temperature differences in the cavity are limited to a few percent. Only conduction and advection transport mechanisms are taken into account in the energy equation. Radiative heat transfer is not considered due to the lack of data on the optical properties of the salt. Viscous heating is ignored as well, because it is negligible compared to the fission power density.

1.5 Research objectives and thesis outline

The goals of this work are

- to develop an advanced multi-physics simulation tool able to accurately model the three-dimensional neutron transport, fluid flow, and heat transfer physics phenomena characterizing a liquid-fuel nuclear reactor;
- to validate and benchmark this tool, not only in its single-physics components, but also assessing the capability to correctly model the coupling between the physics;
- to extensively analyze the MSFR behavior at steady-state and during transient scenarios, taking into account the most recent design advancements made during the SAMOFAR project, with the aim to assess its safety and highlight potential critical issues to be addressed in the future.

We address these objectives in the next four chapters, whose outline is as follows.

Chapter 2 focuses on the fluid-dynamics code, presenting all the details of the incompressible RANS solver. Only isothermal flows are considered. The solver is based on a discontinuous Galerkin Finite Element method (DG-FEM) for space discretization and a backward differentiation formula time-scheme. A literature review of the work previously carried out in the field of CFD DG-FEM solvers is provided. The correctness of the space-time numerical scheme is verified with the method of manufactured solutions, then the code is benchmarked with well-known numerical test cases: the backward-facing step and vortex shedding behind a square cylinder.

Chapter 3 is devoted to the description of the complete multi-physics tool, with an extensive literature review of previous efforts on multi-physics modeling of liquid-fuel reactors. To avoid repetitions, the CFD solver is presented only briefly, highlighting the choices adopted for the resolution of the energy equation and heat-transfer phenomena. The focus is on the neutronics code: an existing neutron transport solver based on a DG-FEM spatial discretization and a discrete ordinates angular approach is extended to simulate time-dependent phenomena, the neutron precursors drift, and decay heat. Then, the coupling between the two codes is described in details. As an example of the capabilities of our simulation tool, which constitutes the first multi-physics code dedicated to liquid-fuel fast reactors based on a full-transport neutronics model and on high-order DG-FEM space discretization, we present preliminary steady-state and transient calculations on the MSFR.

Chapter 4 is about the benchmarking of the multi-physics tool. It presents the results of a collaboration between TU Delft and other SAMOFAR partners who developed multi-physics codes dedicated to the MSFR: Centre national de la recherche scientifique - Grenoble, Politecnico di Milano, and Paul Scherrer Institute.

We first describe in details the problem under investigation, which consists of a two-dimensional molten salt reactor system whose characteristics make it a simple representation of the MSFR. Then, we compare the results obtained by the partners in several steps of the benchmark (each one representing a particular steady-state or transient problem), to prove our numerical tool is able to correctly model the specific physics phenomena characterizing a liquid-fuel fast reactor.

Completing the preliminary assessment carried out in Chapter 3, **Chapter 5** presents an extensive analysis of the MSFR behavior at steady-state and during several transient scenarios, as loss of flow, loss of heat sink, and over-cooling accidents. As mentioned previously, the study aims at finding potential risks for the safe operations of the reactor, thus providing indications for further optimization of the design. A second goal is to investigate potential numerical challenges in the simulation of these complex scenarios.

Finally, **Chapter 6** summarizes the main findings and conclusions of this work and presents recommendations for follow-up studies.

CHAPTER 2

DG-FEM SOLVER FOR THE INCOMPRESSIBLE RANS AND $k - \epsilon$ EQUATIONS

Accurate methods to solve the Reynolds-Averaged Navier-Stokes (RANS) equations coupled to turbulence models are still of great interest, as this is often the only computationally feasible approach to simulate complex turbulent flows in large engineering applications. In this work, we present a novel discontinuous Galerkin (DG) solver for the RANS equations coupled to the $k - \epsilon$ model (in logarithmic form, to ensure positivity of the turbulence quantities). We investigate the possibility of modeling walls with a wall function approach in combination with DG. The solver features an algebraic pressure correction scheme to solve the coupled RANS system, implicit backward differentiation formulae for time discretization, and adopts the Symmetric Interior Penalty method and the Lax-Friedrichs flux to discretize diffusive and convective terms respectively. We pay special attention to the choice of polynomial order for any transported scalar quantity and show it has to be the same as the pressure order to avoid numerical instability. A manufactured solution is used to verify that the solution converges with the expected order of accuracy in space and time. We then simulate a stationary flow over a backward-facing step and a Von Kármán vortex street in the wake of a square cylinder to validate our approach.

This chapter is based on M. Tiberge, A. Hennink, J.L. Kloosterman, and D. Lathouwers. A high-order discontinuous Galerkin solver for the incompressible RANS equations coupled to the $k - \epsilon$ turbulence model. Submitted for publication.

2.1 Introduction

Engineering applications often require the simulation of complex turbulent flows via accurate Computational Fluid Dynamics (CFD) methods. Direct Numerical Simulation (DNS) and Large Eddy Simulation (LES) constitute superior approaches in this regard, as they are able to resolve the stochastic fluctuations (though only the large-scale ones in case of LES) of any turbulent flow quantity (Geurts, 2004). However, nowadays they are still very computationally expensive and often unaffordable for large engineering applications. For this reason, the Reynolds-Averaged Navier-Stokes (RANS) equations coupled to turbulence closure models often remain the preferred approach, even if it only allows for the modeling of the time-averaged flow quantities (Pope, 2000). Accurate and efficient numerical methods to solve the RANS equations are therefore still of great relevance.

In this perspective, discontinuous Galerkin Finite Element methods (DG-FEM) are particularly attractive, due to their flexibility, high accuracy, and robustness. The characteristic feature of DG is that unknown quantities are approximated with polynomial basis functions discontinuous across the mesh elements. This requires the use of numerical fluxes to deal with the discretization of face integrals, as in Finite Volume methods. However, thanks to the lack of continuity constraints, conservation laws are satisfied locally on each element, and the resulting algorithm stencil is compact, making the method suitable for efficient parallelization. As in continuous Galerkin FEM, the accuracy of the solution can be improved by increasing the order of the polynomial discretization. Moreover, DG methods can easily handle complex geometries, structured or unstructured meshes, and non-conformal local mesh and/or order refinement.

This class of Finite Element methods was originally developed in the early '70s to solve radiation transport problems (Reed and Hill, 1973). However, it has become increasingly popular for CFD applications only in the past three decades, after the development of effective DG schemes for hyperbolic and elliptic problems. We refer to the reviews by Cockburn and Shu (2001) and Arnold et al. (2002) for a complete overview of these methods.

Nowadays, substantial experience has been gained in the DG-FEM discretization of the incompressible Navier-Stokes equations, and a variety of approaches can be found in literature. An early research effort in the field is the work of Cockburn et al. (2003), who proposed a locally conservative Local DG (LDG) method for the incompressible Oseen equations. The authors later extended the approach to the full Navier-Stokes system (Cockburn et al., 2004), employing a post-processing operator to obtain an exactly divergence-free convective velocity field. Van der Vegt and Sudirham (2008) presented an original DG scheme for the solution of the Oseen equations, where discontinuous basis functions are also used to discretize the time domain. The method, called space-time DG, is particularly suitable for simulations involving deforming or moving meshes. More recently, Rhebergen et al. (2013) extended the approach to the full Navier-Stokes system. In Bassi et al. (2006), the

incompressibility constraint is relaxed by introducing an artificial compressibility term in the continuity equation. Thus, the numerical flux for the inviscid part of the Navier-Stokes equations can be computed by solving a Riemann problem just like for compressible flows. The coupled system of equations is solved by means of a Newton method with an implicit Euler time scheme. Higher-order Runge-Kutta schemes were instead employed by Bassi et al. (2007). Splitting methods based on pressure or velocity correction approaches have also been proposed in the context of DG solvers (e.g., Girault et al., 2005; Ferrer and Willden, 2011; Krank et al., 2017b; Piatkowski et al., 2018). In particular, the solver presented in this chapter is based on the work of Shahbazi et al. (2007), where a second-order accurate pressure-correction scheme is applied at algebraic level. The Symmetric Interior Penalty (SIP) method is used to discretize the diffusive operator, and the Lax-Friedrichs flux is chosen for the hyperbolic term. Similar solvers, but based on a SIMPLE algorithm, were proposed by Klein et al. (2013) and Klein et al. (2015b).

Regarding turbulent flow simulations, DG solvers have been developed mostly for the compressible RANS equations coupled to either the Spalart-Allmaras (e.g., Nguyen et al., 2007; Landmann et al., 2008; Drosson et al., 2013) or the $k - \omega$ models (e.g., Bassi et al., 2005; Crivellini and Bassi, 2011; Hartmann et al., 2011; Ghidoni et al., 2013). For the latter model, it is customary to solve for the logarithm of ω and to impose a realizability condition on it, to ensure the positivity of the solution and enhance the robustness of the solver. The shear-stress transport model was instead considered in Schoenawa and Hartmann (2014), where particular attention was given to the development of a stabilized continuous FE discretization of the eikonal equation for the computation of the distance to the nearest wall. Far fewer applications of DG schemes to incompressible turbulent flows can be found in literature. The work of Crivellini et al. (2013a) was the first. They extended the artificial compressibility flux method of Bassi et al. (2006) to deal with the set of incompressible RANS equations coupled to the SA model. Particular attention was paid to the treatment of negative values of the turbulent viscosity, thus increasing the robustness of the method. The approach was later tested on complex three-dimensional flows (Crivellini et al., 2013b) and extended to the $k - \omega$ model (Bassi et al., 2014) and to high-order Runge-Kutta time schemes (Massa et al., 2016; Noventa et al., 2016). More recently, Krank et al. (2017a) presented a DG solver for the incompressible RANS equations coupled to the SA model based on a semi-explicit velocity-correction splitting scheme augmented with an explicit step for the turbulence equation.

In this work, we extend a solver for laminar flows presented in Hennink et al. (2020) to handle turbulence through the set of incompressible RANS equations coupled to the $k - \epsilon$ model. We employ a pressure correction scheme to solve the RANS equations. Thus, contrary to most of previous literature, we do not rely on a free artificial compressibility parameter whose optimal value is problem-based. Moreover, our time scheme is fully implicit (as it relies on backward differentiation formulae) also for the turbulence equations. It constitutes the first step towards the

development of a coupled CFD-neutronics solver for large multi-physics problems, such as transient scenarios in molten salt nuclear reactors. In these systems, the flow Reynolds number is of the order of 10^5 or higher, and resolving the steep gradients that characterize the velocity profile close to wall boundaries requires massive computational resources.

To the best of our knowledge, all previous literature on RANS DG solvers deals with wall-resolved turbulent flow simulations. An approach for efficient wall modeling in the DG context was proposed by Krank et al. (2017a), who solved the RANS equations on coarse grids by enriching the polynomial function space for the velocity in the first layer of boundary elements. In this way, they could impose no-slip conditions at the walls and resolve the sharp solution gradients. However, the $k - \epsilon$ model is well-known to perform poorly in the vicinity of a wall. For this reason, in this work we investigate the possibility of using a more standard wall function approach (Launder and Spalding, 1974) to bridge the gap between the viscous layer and the log layer.

The remainder of the chapter is organized as follows. In Section 2.2, we present the governing equations and the boundary conditions that close them. We then describe our spatial and temporal discretization scheme in Sections 2.3 and 2.4, and we provide details on the solver in Section 2.5. In Section 2.6, we focus on the choice of polynomial order for scalar quantities, which differs slightly from what previously proposed in literature for similar DG solvers. In Section 2.7, we verify our numerical scheme with a manufactured solution and we assess the soundness of our approach simulating the steady turbulent flow over a backward-facing step and a Von Kármán vortex street in the wake of a square cylinder, finally drawing some conclusions in Section 2.8.

2.2 Governing equations

The RANS model equations for incompressible flows read (we omit dependencies for clarity) (Pope, 2000)

$$\frac{\partial \mathbf{u}}{\partial t} + \nabla \cdot (\mathbf{u} \otimes \mathbf{u}) + \nabla p - \nabla \cdot \tau = \mathbf{f}, \quad (2.1a)$$

$$\nabla \cdot \mathbf{u} = 0. \quad (2.1b)$$

Here, \mathbf{u} is the velocity and \mathbf{f} represents a known momentum source. The total stress tensor is

$$\tau = (\nu + \nu_t) [\nabla \mathbf{u} + (\nabla \mathbf{u})^T], \quad (2.2)$$

where ν and ν_t are the molecular and the turbulent (or eddy) kinematic viscosities respectively. Finally, $p = \frac{\tilde{p}}{\rho} + \frac{2}{3}k$ is a pseudo kinematic pressure, where \tilde{p} is the fluid pressure, ρ the density, and k the turbulent kinetic energy.

The system is closed by adopting the $k - \epsilon$ turbulence model (Launder and Spalding, 1974), where ϵ indicates the dissipation rate of k . To ensure positivity of

Table 2.1. Values of the closure parameters of the $k - \epsilon$ turbulence model.

Parameter	C_μ	σ_k	σ_ϵ	$C_{1\epsilon}$	$C_{2\epsilon}$
Value	0.09	1.0	1.3	1.44	1.92

the turbulence quantities (which might not be preserved by the numerical scheme), the model equations are cast into a logarithmic form (Ilinca et al., 1998), which is completely equivalent to the original model. Therefore, we solve for

$$\mathcal{K} = \ln(k), \quad \mathcal{E} = \ln(\epsilon), \quad (2.3)$$

and the model equations read (omitting dependencies)

$$\begin{aligned} \frac{\partial \mathcal{K}}{\partial t} + \nabla \cdot (\mathbf{u}\mathcal{K}) - \nabla \cdot \left[\left(\nu + \frac{\nu_t}{\sigma_k} \right) \nabla \mathcal{K} \right] &= \left(\nu + \frac{\nu_t}{\sigma_k} \right) \nabla \mathcal{K} \cdot \nabla \mathcal{K} \\ &+ \nu_t e^{-\mathcal{K}} P_k(\mathbf{u}) - C_\mu \frac{e^{\mathcal{K}}}{\nu_t} + q_{\mathcal{K}}, \end{aligned} \quad (2.4a)$$

$$\begin{aligned} \frac{\partial \mathcal{E}}{\partial t} + \nabla \cdot (\mathbf{u}\mathcal{E}) - \nabla \cdot \left[\left(\nu + \frac{\nu_t}{\sigma_\epsilon} \right) \nabla \mathcal{E} \right] &= \left(\nu + \frac{\nu_t}{\sigma_\epsilon} \right) \nabla \mathcal{E} \cdot \nabla \mathcal{E} \\ &+ C_{1\epsilon} \nu_t e^{-\mathcal{K}} P_k(\mathbf{u}) - C_{2\epsilon} e^{\mathcal{E} - \mathcal{K}} + q_{\mathcal{E}}, \end{aligned} \quad (2.4b)$$

where $P_k(\mathbf{u}) = \nabla \mathbf{u} : [\nabla \mathbf{u} + (\nabla \mathbf{u})^T]$ models the shear production of turbulent kinetic energy. We used the standard values of the model constants proposed by Launder and Spalding (1974) and reported in Table 2.1. The eddy viscosity can be then computed as

$$\nu_t = C_\mu \frac{k^2}{\epsilon} = C_\mu e^{2\mathcal{K} - \mathcal{E}}. \quad (2.5)$$

Clearly, the latter expression ensures ν_t is always positive. Moreover, potentially troublesome divisions by small values of ϵ (or by k in some terms of the turbulence equations) are avoided.

Finally, $q_{\mathcal{K}}$ and $q_{\mathcal{E}}$ are extra source terms that, together with \mathbf{f} , are used in the framework of the method of manufactured solutions to verify the numerical scheme (see Section 2.7.1). Normally, they are set to zero.

2.2.1 Boundary and initial conditions

The coupled system of the RANS (2.1) and turbulence (2.4) equations can be solved only after imposition of proper boundary and initial conditions. The latter consist in imposing suitable values for the initial velocity, pressure, and turbulence fields, which we describe in detail for each test case reported in Section 2.7. For the former, four types of boundary are considered in this work, and we describe them in the following.

2.2.1.1 Inflow boundary

On inflow boundaries, Dirichlet conditions are prescribed for the fluid velocity and the turbulence quantities:

$$\mathbf{u} = \mathbf{u}^D, \quad \mathcal{K} = \mathcal{K}^D = \ln(k^D), \quad \mathcal{E} = \mathcal{E}^D = \ln(\epsilon^D). \quad (2.6)$$

2.2.1.2 Outflow boundary

On outflow boundaries we prescribe a zero-traction condition for the momentum equation and homogeneous Neumann conditions for the turbulence equations:

$$[-pI + \tau] \cdot \mathbf{n} = \mathbf{0}, \quad \mathbf{n} \cdot \nabla \mathcal{K} = 0, \quad \mathbf{n} \cdot \nabla \mathcal{E} = 0. \quad (2.7)$$

Here, \mathbf{n} is the outward unit normal vector at the boundary, and I represents the identity tensor.

2.2.1.3 Wall boundary

The standard $k - \epsilon$ model cannot be used to resolve turbulent flows up to wall boundaries, in the vicinity of which viscous effects are dominant and turbulence is damped. For this reason, we use the well-established wall function approach to describe the solution in these areas (Launder and Spalding, 1974; Durbin, 2009).

The computational boundary is shifted by a distance δ_w from the actual physical wall, so that the first degrees of freedom of the solution are placed in the region of fully turbulent flow (Kuzmin et al., 2007). The gap is bridged by analytical functions that are supposed to be universal for all wall-bounded flows. This leads to a great gain in computational efficiency, in particular for high-Reynolds flows, because mesh elements are not accumulated in the viscous layer to resolve the steep gradients of the solution.

In this work, we adopt the two-velocity scale wall function described by Ignat et al. (1998). Let u_t be the velocity component tangential to the boundary and y the normal distance to the wall. They are made non-dimensional as follows:

$$u^+ = \frac{u_t}{u_\tau}, \quad y^+ = \frac{\delta_w u_k}{\nu}, \quad (2.8)$$

where $u_\tau = \sqrt{\tau_w/\rho}$ is the friction velocity (τ_w is the shear stress at the wall), whereas u_k is a second velocity scale computed from k :

$$u_k = C_\mu^{0.25} \sqrt{k_w} = C_\mu^{0.25} e^{\mathcal{K}_w/2}, \quad (2.9)$$

where k_w is the value of the turbulent kinetic energy at the boundary. The wall function is an analytical relation between u^+ and y^+ :

$$u^+ = \frac{1}{\kappa} \ln(Ey^+) \quad \text{for } y^+ > 11.06, \quad (2.10)$$

where $\kappa = 0.41$ is the Von Kármán constant. Only smooth walls are considered in this work, so the roughness parameter is $E = 9.0$.

Equations (2.9) and (2.10) are used to prescribe a homogeneous Robin-like boundary condition for the momentum equation in the tangential direction. In fact, a linear relation exists between the shear stress and the tangential velocity component:

$$\boldsymbol{\tau} \cdot \mathbf{n} - \mathbf{n}(\mathbf{n} \cdot \boldsymbol{\tau} \cdot \mathbf{n}) = -u_k u_\tau \mathbf{t} = -\frac{u_k}{u^+} [\mathbf{u} - (\mathbf{u} \cdot \mathbf{n})\mathbf{n}] , \quad (2.11)$$

where \mathbf{t} is a unit vector that is tangential to the boundary and $\mathbf{u} - (\mathbf{u} \cdot \mathbf{n})\mathbf{n} = u_t \mathbf{t}$. The boundary condition (2.11) is supplemented by a no-penetration condition in the normal direction:

$$\mathbf{n} \cdot \mathbf{u} = 0 . \quad (2.12)$$

Regarding the turbulent quantities, homogeneous Neumann and Dirichlet boundary conditions are prescribed for k and ϵ respectively:

$$\mathbf{n} \cdot \nabla \mathcal{K} = 0 ; \quad \mathcal{E} = \ln \left(\frac{u_k^3}{\kappa \delta_w} \right) . \quad (2.13)$$

The value of δ_w must be sufficiently large for the wall function (2.10) to be valid, that is, the first degrees of freedom of the FEM solution must be in the logarithmic layer. This parameter can be either estimated as the distance from the wall of the centroid of the first boundary element or fixed to a predetermined value (Kalitzin et al., 2005). This work features standard and predictable flow configurations, so we adopted the second approach.

2.2.1.4 Symmetry boundary

On symmetry boundaries, we prescribe a homogeneous Neumann condition for both turbulence quantities:

$$\mathbf{n} \cdot \nabla \mathcal{K} = 0 ; \quad \mathbf{n} \cdot \nabla \mathcal{E} = 0 . \quad (2.14)$$

For the momentum equation, we prescribe vanishing normal velocity and tangential stress:

$$\mathbf{n} \cdot \mathbf{u} = 0 , \quad \boldsymbol{\tau} \cdot \mathbf{n} - \mathbf{n}(\mathbf{n} \cdot \boldsymbol{\tau} \cdot \mathbf{n}) = \mathbf{0} . \quad (2.15)$$

2.3 Spatial discretization

In this section, we describe in detail the spatial discretization of the governing equations with the discontinuous Galerkin Finite Element method. Some notation and definitions must be introduced first.

Let Ω be the computational domain and Γ its boundary. We indicate with Γ^D , Γ^N , Γ^W , and Γ^S the non-overlapping portions of boundary where Dirichlet (i.e.,

inflow), Neumann (i.e., outflow), wall, and symmetry conditions are imposed, such that $\Gamma = \Gamma^D \cup \Gamma^N \cup \Gamma^W \cup \Gamma^S$.

The domain is meshed into a set of non-overlapping elements \mathcal{T}_h . The set of their interior faces is indicated with \mathcal{F}^i , whereas \mathcal{F}^D , \mathcal{F}^N , \mathcal{F}^W , and \mathcal{F}^S indicate the sets of Dirichlet, Neumann, wall, and symmetry boundary faces, which discretize the respective portions of boundary. Given an element $T \in \mathcal{T}_h$, the set of its faces is denoted with \mathcal{F}^T . The neighbors of face F are grouped into \mathcal{T}_h^F . Any interior face $F \in \mathcal{F}^i$ is equipped with a unit normal vector \mathbf{n}^F with an arbitrary but fixed direction, while for boundary faces \mathbf{n}^F coincides with \mathbf{n} , which is the unit normal vector outward to Ω .

Any scalar unknown is approximated on \mathcal{T}_h with a set of basis functions that are continuous within each element, but discontinuous at the element interfaces. We use a hierarchical set of orthogonal modal basis functions: the solution space within an element is the span of all polynomials up to an order \mathcal{P} , with $\mathcal{P} \geq 1$. For a generic unknown ϕ , we denote its FEM approximation by ϕ_h and its polynomial order by \mathcal{P}_ϕ , so that the solution space can be written as

$$\mathcal{V}_{h,\phi} := \{v \in L^2(\Omega) \mid v|_T \in \mathbb{P}_{\mathcal{P}_\phi}, \forall T \in \mathcal{T}_h\} \quad (2.16)$$

where $\mathbb{P}_{\mathcal{P}_\phi}$ is the set of polynomials up to order \mathcal{P}_ϕ . The velocity FEM approximation lies in the corresponding vector space $\mathcal{V}_{h,u}^d$, where d is the problem dimensionality. Despite not being a requirement of the numerical method, \mathcal{P}_ϕ is the same on each element and the meshes are conforming for all the test cases analyzed in this work.

The trace of ϕ_h on a face $F \in \mathcal{F}^i$ is not unique. For this reason, it is necessary to introduce the average $\{\phi_h\} := \frac{1}{2}(\phi_h^+ + \phi_h^-)$ and the jump $[[\phi_h]] := \phi_h^+ - \phi_h^-$ operators. Here, ϕ_h^+ and ϕ_h^- are the function traces defined as

$$\phi_h^\pm(\mathbf{r} \in F) = \lim_{\varsigma \downarrow 0} \phi_h(\mathbf{r} \mp \varsigma \mathbf{n}^F), \quad (2.17)$$

for a point \mathbf{r} on an interior face $F \in \mathcal{F}^i$. At the boundary, the jump and average operators coincide with the unique trace of ϕ_h .

2.3.1 RANS discretization

The semi-discrete weak formulation of System (2.1) subjected to the boundary conditions described in Section 2.2.1 is obtained by substituting (\mathbf{u}, p) with their DG-FEM approximations (\mathbf{u}_h, p_h) , by multiplying Equation (2.1a) with the test function $\mathbf{v}_h \in \mathcal{V}_{h,u}^d$, by multiplying Equation (2.1b) with $q_h \in \mathcal{V}_{h,p}$, and by subsequently integrating over the entire domain:

Find $\mathbf{u}_h \in \mathcal{V}_{h,u}^d$ and $p_h \in \mathcal{V}_{h,p}$ such that, $\forall \mathbf{v}_h \in \mathcal{V}_{h,u}^d$ and $\forall q_h \in \mathcal{V}_{h,p}$,

$$a^{\text{time}}(\mathbf{u}_h, \mathbf{v}_h) + a^{\text{conv}}(\mathbf{u}_h, \mathbf{u}_h, \mathbf{v}_h) + a^{\text{diff}}(\mathbf{u}_h, \mathbf{v}_h) + a^{\text{div}}(\mathbf{v}_h, p_h) = l(\mathbf{u}_h, \mathbf{v}_h), \quad (2.18a)$$

$$a^{\text{div}}(\mathbf{u}_h, q_h) = l^{\text{div}}(q_h) \quad , \quad (2.18b)$$

where

$$a^{\text{time}}(\mathbf{u}_h, \mathbf{v}_h) = \sum_{T \in \mathcal{T}_h} \int_T \mathbf{v}_h \cdot \frac{\partial \mathbf{u}_h}{\partial t} \, , \quad (2.19)$$

and, letting \mathbf{f}_h be the Galerkin projection of \mathbf{f} onto $\mathcal{V}_{h,u}^d$,

$$l(\mathbf{u}_h, \mathbf{v}_h) = l^{\text{conv}}(\mathbf{u}_h, \mathbf{v}_h) + l^{\text{diff}}(\mathbf{v}_h) + \sum_{T \in \mathcal{T}_h} \int_T \mathbf{v}_h \cdot \mathbf{f}_h \, . \quad (2.20)$$

All other terms are described more in detail in the following.

2.3.1.1 Convective term

The convective term of the momentum equation is discretized as

$$\begin{aligned} a^{\text{conv}}(\boldsymbol{\beta}, \mathbf{w}, \mathbf{v}) = & - \sum_{T \in \mathcal{T}_h} \int_T \mathbf{w} \cdot (\boldsymbol{\beta} \cdot \nabla) \mathbf{v} + \sum_{F \in \mathcal{F}^i} \int_F \llbracket \mathbf{v} \rrbracket \mathcal{H}^F(\boldsymbol{\beta}, \mathbf{w}) \\ & + \sum_{F \in \mathcal{F}^N} \int_F (\mathbf{n}^F \cdot \boldsymbol{\beta}) \mathbf{w} \cdot \mathbf{v} + \sum_{F \in \mathcal{F}^D} \int_F \max(0, \mathbf{n}^F \cdot \boldsymbol{\beta}^D) \mathbf{w} \cdot \mathbf{v} \, , \end{aligned} \quad (2.21)$$

$$l^{\text{conv}}(\boldsymbol{\beta}, \mathbf{v}) = - \sum_{F \in \mathcal{F}^D} \int_F \min(0, \mathbf{n}^F \cdot \boldsymbol{\beta}^D) \mathbf{u}^D \cdot \mathbf{v} \, , \quad (2.22)$$

where $\boldsymbol{\beta}$ is the convective field (i.e., the velocity), and \mathcal{H}^F is a numerical flux function defined on the internal face F . In this work, the Lax-Friedrichs flux is used (Cliffe et al., 2010):

$$\mathcal{H}^F(\boldsymbol{\beta}, \mathbf{w}) = \frac{\alpha^F(\boldsymbol{\beta})}{2} \llbracket \mathbf{w} \rrbracket + \mathbf{n}^F \cdot \{\boldsymbol{\beta} \otimes \mathbf{w}\} \, , \quad (2.23)$$

where α^F is evaluated point-wise along face F according to

$$\alpha^F(\boldsymbol{\beta}) = \Lambda \max(|\mathbf{n}^F \cdot \boldsymbol{\beta}^+|, |\mathbf{n}^F \cdot \boldsymbol{\beta}^-|) \, , \quad (2.24)$$

with $\Lambda = 2$ for the momentum equation.

Note that usually $(\mathbf{n}^F \cdot \boldsymbol{\beta}^D) < 0$ on any $F \in \mathcal{F}^D$, and therefore the corresponding term in Equation (2.21) drops out. However, we included this term because it is relevant for the Taylor-vortex-like manufactured solution in Section 2.7.1, where we impose Dirichlet conditions on the entire boundary, as it is usually done for this class of problems (e.g., Ethier and Steinman, 1994; Shahbazi et al., 2007).

2.3.1.2 Diffusive term discretization

To discretize the diffusive term, we use a generalization of the Symmetric Interior Penalty (SIP) method (Di Pietro and Ern, 2012, , p. 122). Among the several methods available for elliptic problems (Arnold et al., 2002), we opted for the SIP because it is consistent and adjoint consistent, which guarantees optimal convergence rates for any order of the polynomial discretization. Moreover, it is characterized by compact stencil size, as the degrees of freedom on each element are coupled only with those on the first neighbors, with positive impact on memory requirements, computational cost, and parallelization efficiency.

The following bilinear operator and right-hand side term can be defined:

$$\begin{aligned}
 a^{\text{diff}}(\mathbf{w}, \mathbf{v}) &= \sum_{T \in \mathcal{T}_h} \int_T \mathcal{L}^{\text{diff}}(\mathbf{w}) : \nabla \mathbf{v} + \sum_{F \in \mathcal{F}^i \cup \mathcal{F}^D} \int_F \eta^F \llbracket \mathbf{w} \rrbracket \cdot \llbracket \mathbf{v} \rrbracket \\
 &- \sum_{F \in \mathcal{F}^i \cup \mathcal{F}^D} \int_F \mathbf{n}^F \cdot (\llbracket \mathbf{v} \rrbracket \cdot \{\mathcal{L}^{\text{diff}}(\mathbf{w})\} + \{\mathcal{L}^{\text{diff}}(\mathbf{v})\} \cdot \llbracket \mathbf{w} \rrbracket) + a_{\mathcal{F}^W \cup \mathcal{F}^S}^{\text{diff}}(\mathbf{w}, \mathbf{v})
 \end{aligned} \tag{2.25}$$

and

$$l^{\text{diff}}(\mathbf{v}) = \sum_{F \in \mathcal{F}^D} \int_F (\eta^F \mathbf{u}^D \cdot \mathbf{v} - \mathbf{u}^D \cdot \mathcal{L}^{\text{diff}}(\mathbf{v}) \cdot \mathbf{n}^F) , \tag{2.26}$$

where $\mathcal{L}^{\text{diff}}(\mathbf{w})$ is a linear operator that coincides with the stress tensor τ (Equation (2.2)) for the momentum equation, that is, $\mathcal{L}^{\text{diff}}(\mathbf{u}) = \tau$. Note that the effective viscosity (i.e., $\nu + \nu_t$) is variable in space and so $\nabla \cdot \tau \neq (\nu + \nu_t) \nabla^2 \mathbf{u}$, which is why the regular SIP cannot be used here.

The penalty parameter, η^F , must be sufficiently large to ensure stability without impacting too negatively the condition number of the system. We follow the optimal value prescriptions provided by Hillewaert (2013) and Drosson and Hillewaert (2013) in case of anisotropic meshes and highly variable viscosity (as when turbulent flows are resolved):

$$\eta^F = \mathfrak{D} \max_{T \in \mathcal{T}_h^F} \left(\text{card}(\mathcal{F}^T) \frac{\mathfrak{C}_{\mathcal{P},T}}{\mathfrak{L}_T} \right) , \tag{2.27}$$

where $\text{card}(\mathcal{F}^T)$ indicates the number of faces of element T ; $\mathfrak{C}_{\mathcal{P},T}$ is a factor depending on the polynomial order of the solution and the mesh element type,

$$\mathfrak{C}_{\mathcal{P},T} = \begin{cases} (\mathcal{P} + 1)^2 & , \text{ for quadrilaterals and hexahedra} \\ \frac{(\mathcal{P} + 1)(\mathcal{P} + d)}{d} & , \text{ for simplices} \end{cases} . \tag{2.28}$$

\mathfrak{L}_T is a length scale defined as

$$\mathfrak{L}_T = \mathfrak{f} \frac{\|T\|_{\text{leb}}}{\|F\|_{\text{leb}}} , \tag{2.29}$$

where $\|\cdot\|_{\text{leb}}$ represents the Lebesgue measure of a geometrical entity (i.e., length, area, or volume depending on the dimensionality), and $\mathfrak{f} = 2$ for $F \in \mathcal{F}^i$ and $\mathfrak{f} = 1$ for boundary faces; finally, \mathfrak{D} is a scale depending on the diffusion parameter D (i.e., the effective viscosity for the momentum equation), which we evaluate pointwise along the face as

$$\mathfrak{D} = \max(D^+, D^-) . \quad (2.30)$$

The contribution of wall and symmetry faces must still be specified to complete the definition of the SIP bilinear form (2.25). We extend what was proposed by Cliffe et al. (2010) to arbitrarily oriented symmetry boundaries and to walls, where a non-zero shear stress is specified in the tangential direction, leading to a Robin-like boundary condition term (see, for example, Di Pietro and Ern, 2012, p. 127):

$$\begin{aligned} a_{\mathcal{F}^W \cup \mathcal{F}^S}^{\text{diff}}(\mathbf{w}, \mathbf{v}) &= \sum_{F \in \mathcal{F}^W} \int_F \frac{u_k}{u^+} (\mathbf{w} - (\mathbf{w} \cdot \mathbf{n}^F) \mathbf{n}^F) \cdot (\mathbf{v} - (\mathbf{v} \cdot \mathbf{n}^F) \mathbf{n}^F) \\ &- \sum_{F \in \mathcal{F}^W \cup \mathcal{F}^S} \int_F \mathbf{n}^F \cdot (\llbracket \mathbf{v} \cdot \mathbf{n}^F \rrbracket \{ \mathcal{L}^{\text{diff}}(\mathbf{w}) \cdot \mathbf{n}^F \} + \{ \mathcal{L}^{\text{diff}}(\mathbf{v}) \cdot \mathbf{n}^F \} \llbracket \mathbf{w} \cdot \mathbf{n}^F \rrbracket) \\ &+ \sum_{F \in \mathcal{F}^W \cup \mathcal{F}^S} \int_F \eta^F \llbracket \mathbf{w} \cdot \mathbf{n}^F \rrbracket \llbracket \mathbf{v} \cdot \mathbf{n}^F \rrbracket , \quad (2.31) \end{aligned}$$

where u_k/u^+ is the proportionality constant between tangential stress and velocity component (Equation (2.11)).

2.3.1.3 Continuity terms

The discretized continuity equation is constituted by the following discrete divergence operator and right-hand side term (Cockburn et al., 2004; Shahbazi et al., 2007):

$$a^{\text{div}}(\mathbf{v}, q) = - \sum_{T \in \mathcal{T}_h} \int_T q \nabla \cdot \mathbf{v} + \sum_{F \in \mathcal{F}^i \cup \mathcal{F}^D \cup \mathcal{F}^W \cup \mathcal{F}^S} \int_F \{q\} \llbracket \mathbf{v} \rrbracket \cdot \mathbf{n}^F , \quad (2.32)$$

$$l^{\text{div}}(q) = \sum_{F \in \mathcal{F}^D} \int_F q (\mathbf{u}^D \cdot \mathbf{n}^F) . \quad (2.33)$$

2.3.2 Discretization of turbulence equations

The spatial discretization of the turbulence equations (2.4), subjected to the boundary conditions described in Section 2.2.1, proceeds along the same line of what done for the momentum equation. The semi-discrete weak formulations are

Find $\mathcal{K}_h \in \mathcal{V}_{h,\mathcal{K}}$ and $\mathcal{E}_h \in \mathcal{V}_{h,\mathcal{E}}$ such that

$$a^{\text{time}}(\mathcal{K}_h, v_h) + a^{\text{conv}}(\mathbf{u}_h, \mathcal{K}_h, v_h) + a^{\text{diff}}(\mathcal{K}_h, v_h) = l(\mathcal{K}_h, v_h) \quad \forall v_h \in \mathcal{V}_{h,\mathcal{K}}, \quad (2.34a)$$

$$a^{\text{time}}(\mathcal{E}_h, v_h) + a^{\text{conv}}(\mathbf{u}_h, \mathcal{E}_h, v_h) + a^{\text{diff}}(\mathcal{E}_h, v_h) = l(\mathcal{E}_h, v_h) \quad \forall v_h \in \mathcal{V}_{h,\mathcal{E}}. \quad (2.34b)$$

The temporal and right-hand side terms are straightforward extension to the case of scalar unknowns of those described for the momentum equation (Equations (2.19) and (2.20)). All terms on the right-hand side of Equations (2.4a) and (2.4b) are treated explicitly in time and therefore added to the source integrals in $l(\mathcal{K}_h, v_h)$ and $l(\mathcal{E}_h, v_h)$.

The convective terms are discretized as for the momentum equation, though the α^F parameter in the Lax-Friedrichs flux (Equation (2.24)) is evaluated with $\Lambda = 1$. Diffusive terms are treated with the SIP method as in Equations (2.25) and (2.26), where the linear operator $\mathcal{L}^{\text{diff}}(v)$ reduces to $\mathcal{L}^{\text{diff}}(v) = D\nabla v$, with

$$D = \begin{cases} \left(\nu + \frac{\nu_t}{\sigma_k} \right), & \text{for the } \mathcal{K} \text{ equation} \\ \left(\nu + \frac{\nu_t}{\sigma_\epsilon} \right), & \text{for the } \mathcal{E} \text{ equation} \end{cases}. \quad (2.35)$$

These are also the diffusion coefficients used to evaluate the penalty parameter according to Equation (2.27). Finally, wall faces contribute to the SIP bilinear form of the \mathcal{E} equation as other Dirichlet boundaries, whereas for the \mathcal{K} equation their contribution is null, because homogeneous Neumann conditions are imposed on these boundaries. Likewise, for both equations symmetry faces have a null contribution to the SIP bilinear form.

2.4 Temporal discretization

Time derivatives in weak forms (2.18) and (2.34) are discretized implicitly using backward differentiation formulae (BDF) of order M (Shahbazi et al., 2007; Klein et al., 2015b; Krank et al., 2017b). For the generic unknown quantity ϕ and for a constant time step size Δt , it is

$$\frac{\partial \phi}{\partial t} \approx \frac{\gamma_0}{\Delta t} \phi^{n+1} + \sum_{j=1}^M \frac{\gamma_j}{\Delta t} \phi^{n+1-j}, \quad (2.36)$$

where $n + 1$ indicates the new time step and the BDF coefficients γ are reported in Table 2.2. We use up to second-order schemes.

The discretized equations are solved in a segregated way, so that the discrete solution vectors at the new time step, $(\mathbf{u}, \underline{p}, \underline{\mathcal{K}}, \underline{\mathcal{E}})^{n+1}$, are found with the following algorithm:

Table 2.2. Coefficients of the BDF and the extrapolation schemes.

Scheme	Order, M	γ_0	γ_1	γ_2
BDF	1	1	-1	
	2	3/2	-2	1/2
EX	1	1		
	2	2	-1	

1. Obtain predictors for all unknowns at the new time step with an M^{th} -order extrapolation from the previous time steps:

$$\underline{\phi}^{n+1} \approx \underline{\phi}^* = \sum_{j=0}^{M-1} \gamma_j \underline{\phi}^{n-j}, \quad (2.37)$$

where the weights are reported in Table 2.2. A predictor for the eddy viscosity, ν_t^* , can be calculated from $\underline{\mathcal{K}}^*$ and $\underline{\mathcal{E}}^*$ according to Equation (2.5);

2. Solve the RANS system (2.1) in a segregated way with a second-order accurate algebraic splitting scheme described in detail in Section 2.4.1. Use the predictors for the velocity, the turbulent kinetic energy¹, and the eddy viscosity to linearize all terms;
3. Solve the \mathcal{K} equation (2.4a), using \mathbf{u}_h^{n+1} as convective field and ν_t^* ;
4. Solve the \mathcal{E} equation (2.4b), using \mathbf{u}_h^{n+1} as convective field and ν_t^* ;
5. If necessary, update all predictors with the new solutions and iterate steps 2 to 4.

When the BDF2 scheme is used, the time extrapolation of all quantities performed at the beginning of the time step guarantees second-order time convergence even when non-linearities are unresolved (as proven in Section 2.7.1.1). Iterations between RANS and turbulence equations (typically 2 or 3) are performed to resolve non-linearities during particularly violent portions of transient (as it might happen at the start-up of a pseudo-transient towards steady-state conditions), to avoid too severe restrictions on the time step size.

2.4.1 Algebraic splitting scheme

The coupled momentum and continuity equations are solved in a segregated way with a second-order accurate pressure correction method (Van Kan, 1986).

¹Necessary to compute the u_k wall function velocity scale.

Following Shahbazi et al. (2007), we perform the splitting at algebraic level, which does not require the imposition of artificial pressure boundary conditions (Guermond et al., 2006). The fully discretized weak form of the RANS system (2.18) can be cast into the following linear form:

$$\begin{bmatrix} \frac{\gamma_0}{\Delta t} \mathbb{M} + \mathbb{N} & \mathbb{D}^T \\ \mathbb{D} & 0 \end{bmatrix} \begin{bmatrix} \underline{\mathbf{u}} \\ \underline{p} \end{bmatrix}^{n+1} = \begin{bmatrix} \underline{\mathbf{b}}_u \\ \underline{b}_p \end{bmatrix}^{n+1}, \quad (2.38)$$

where \mathbb{M} is the mass matrix, \mathbb{N} contains the implicit parts deriving from the discretization of the convective (2.21) and diffusive (2.25) terms, and \mathbb{D} is the discrete divergence operator (2.32). The right-hand side vector $\underline{\mathbf{b}}_u$ collects all the known terms in the momentum equation (i.e., boundary conditions, external forces, explicit terms from the discretization of the time derivative), while \underline{b}_p represents the fully-discrete right-hand side of the continuity equation (2.33). As explained previously, predictors for the velocity field and the eddy viscosity at the new time step are used to linearize the convective and diffusive terms in \mathbb{N} .

The coupled System (2.38) is solved in a segregated way by replacing (and approximating) the left-hand-side matrix with its incomplete block LU factorization (Guermond et al., 2006),

$$\begin{bmatrix} \frac{\gamma_0}{\Delta t} \mathbb{M} + \mathbb{N} & \mathbb{D}^T \\ \mathbb{D} & 0 \end{bmatrix} \approx \begin{bmatrix} \frac{\gamma_0}{\Delta t} \mathbb{M} + \mathbb{N} & 0 \\ \mathbb{D} & -\frac{\Delta t}{\gamma_0} \mathbb{D} \mathbb{M}^{-1} \mathbb{D}^T \end{bmatrix} \begin{bmatrix} \mathbb{I} & -\frac{\Delta t}{\gamma_0} \mathbb{M}^{-1} \mathbb{D}^T \\ 0 & \mathbb{I} \end{bmatrix}, \quad (2.39)$$

where \mathbb{I} is the identity matrix, and by introducing $\underline{\delta p}^{n+1} = \underline{p}^{n+1} - \underline{p}^n$, such that

$$\begin{bmatrix} \frac{\gamma_0}{\Delta t} \mathbb{M} + \mathbb{N} & 0 \\ \mathbb{D} & -\frac{\Delta t}{\gamma_0} \mathbb{D} \mathbb{M}^{-1} \mathbb{D}^T \end{bmatrix} \begin{bmatrix} \mathbb{I} - \frac{\Delta t}{\gamma_0} \mathbb{M}^{-1} \mathbb{D}^T \\ 0 & \mathbb{I} \end{bmatrix} \begin{bmatrix} \underline{\mathbf{u}} \\ \underline{\delta p} \end{bmatrix}^{n+1} = \begin{bmatrix} \underline{\mathbf{b}}_u \\ \underline{b}_p \end{bmatrix}^{n+1} + \begin{bmatrix} -\mathbb{D}^T \underline{p} \\ 0 \end{bmatrix}^n. \quad (2.40)$$

The discrete velocity and pressure fields at the new time step can therefore be calculated with the following predictor-corrector algorithm:

1. Find an approximate velocity field $\underline{\tilde{\mathbf{u}}}^{n+1}$ by solving

$$\left(\frac{\gamma_0}{\Delta t} \mathbb{M} + \mathbb{N} \right) \underline{\tilde{\mathbf{u}}}^{n+1} = \underline{\mathbf{b}}_u^{n+1} - \mathbb{D}^T \underline{p}^n; \quad (2.41)$$

2. Solve a Poisson equation to get the pressure at the new time step:

$$\left(\frac{\Delta t}{\gamma_0} \mathbb{D} \mathbb{M}^{-1} \mathbb{D}^T \right) \underline{\delta p}^{n+1} = \mathbb{D} \underline{\tilde{\mathbf{u}}}^{n+1} - \underline{b}_p, \quad (2.42)$$

$$\underline{p}^{n+1} = \underline{\delta p}^{n+1} + \underline{p}^n; \quad (2.43)$$

3. Correct the velocity field, so that it satisfies the discrete continuity equation

$$\underline{\mathbf{u}}^{n+1} = \tilde{\underline{\mathbf{u}}}^{n+1} - \frac{\Delta t}{\gamma_0} \mathbb{M}^{-1} \mathbb{D}^T \underline{\delta p}^{n+1} . \quad (2.44)$$

2.5 Solution of linear systems

The numerical scheme described in Sections 2.3 and 2.4 has been implemented in the in-house parallel solver `DGFloWS`.

We employ `METIS` to partition the mesh (Karypis and Kumar, 1998) and the MPI-based software library `PETSc` (Balay et al., 2018) to assemble and solve all linear systems with iterative Krylov methods. The implicit convection treatment leads to non-symmetric matrices for the momentum and turbulence equations. For this reason, those linear systems are solved with the `GMRES` method combined with a block Jacobi preconditioner, with one block per process and an incomplete LU factorization on each block. On the other hand, the pressure-Poisson system is symmetric and positive definite. Hence, we solve it with the conjugate gradient method and an additive Schwarz preconditioner, with one block per process and an incomplete Cholesky decomposition on each block.

Solving the pressure Poisson equation is the most computationally expensive step of our algorithm. This is partially due to the fact that the pressure matrix in Equation (2.42) corresponds to a Laplacian operator discretized with the local DG method, as explained by Shahbazi et al. (2007), and so it is characterized by larger stencil size than the SIP diffusive operator. However, note that the matrix is the same at each time step. Therefore, it is possible to assemble it and compute its preconditioner only once, thus partially alleviating the computational burden. On top of this, we initialize all Krylov solvers with the solution predictors described in Section 2.4 to speed convergence up.

2.6 Choice of the solution polynomial order

In this work, we used a mixed-order discretization for velocity and pressure (i.e., $\mathcal{P}_p = \mathcal{P}_u - 1$), which satisfies the inf-sup condition and guarantees optimal error convergence rates and stability in the low- Δt limit (Fehn et al., 2017; Hennink et al., 2020).

The polynomial order of the turbulence quantities equals that of the pressure, which we believe is essential for a pressure-based DG solver. More precisely, the solution space of an arbitrary transported scalar quantity should be a subset of the solution space of the pressure. We have already mentioned this in (Hennink et al., 2020), but here we corroborate it with more rigorous theoretical and numerical arguments. This choice of polynomial order is in contrast with previous literature on mixed-order DG schemes. For example, Klein et al. (2015a) chose the same solution space for the temperature as for the components of the velocity field. We

suspect that they found good results because their tests were done at a low Prandtl number of 0.7, whereas the problem with the solution spaces manifests itself when the convective term dominates, as shown in the following.

Our choice of polynomial order for any scalar solution stems from the fact that the continuity equation is weighed by the pressure basis functions, so that the numerical velocity satisfies the incompressibility constraint only in a weak sense up to order \mathcal{P}_p (i.e., $\mathbb{D}\mathbf{u}_h = 0$). This means that the convective discretization can only be consistent up to an order \mathcal{P}_p .

To show this, consider the convection of a generic passive scalar quantity ϕ with the numerical velocity \mathbf{u}_h . For simplicity, assume that the domain is closed (i.e., $\mathbf{n} \cdot \mathbf{u} = 0$ on Γ), so that substituting $\beta \leftarrow \mathbf{u}_h$ and the continuous solution (i.e., $w \leftarrow \phi$) into Equations (2.21), (2.22), and (2.23) gives the convective discretization

$$a^{\text{conv}}(\mathbf{u}_h, \phi, v) = - \sum_{T \in \mathcal{T}_h} \int_T \phi \mathbf{u}_h \cdot \nabla v + \sum_{F \in \mathcal{F}^i} \int_F \phi \llbracket v \rrbracket \{\mathbf{u}_h\} \cdot \mathbf{n}^F, \quad (2.45a)$$

$$l^{\text{conv}}(v) = 0, \quad (2.45b)$$

for a test function $v \in \mathcal{V}_{h,\phi}$. Here, we have used the fact that ϕ is continuous, so that $\llbracket \phi \rrbracket = 0$ and $\{\phi\} = \phi$, and so $\mathcal{H}^F(\mathbf{u}_h, \phi) = \phi \{\mathbf{u}_h\} \cdot \mathbf{n}^F$.

Compare this to the discrete continuity equation (Equations (2.32) and (2.33)), which, upon substituting $\mathbf{v} \leftarrow \mathbf{u}_h$, integrating by parts, and using the fact that $\llbracket q\mathbf{u}_h \rrbracket = \llbracket q \rrbracket \{\mathbf{u}_h\} + \{q\} \llbracket \mathbf{u}_h \rrbracket$ on an interior face, can be rewritten as

$$a^{\text{div}}(\mathbf{u}_h, q) = \sum_{T \in \mathcal{T}_h} \int_T \mathbf{u}_h \cdot \nabla q - \sum_{F \in \mathcal{F}^i} \int_F \llbracket q \rrbracket \{\mathbf{u}_h\} \cdot \mathbf{n}^F = 0, \quad (2.46)$$

for a test function q that lies in the pressure solution space $\mathcal{V}_{h,p}$ (Cockburn et al., 2008). It is clear that Equation (2.45a) can be consistent only for a test function v that is part of the test space of the continuity equation. In fact, consider the special case of a constant solution ϕ . The convective term should vanish for all v , but $a^{\text{conv}}(\mathbf{u}_h, \phi, v) = \phi a^{\text{div}}(\mathbf{u}_h, v)$, which only vanishes if $\mathcal{V}_{h,\phi}$ is a subset of $\mathcal{V}_{h,p}$, that is, if the polynomial order of the pressure is at least as high as that of the scalar. If $\mathcal{P}_\phi > \mathcal{P}_p$, the constant solution cannot be preserved in general due to numerical error introduced by the discontinuity across the elements of the velocity field.

We corroborate this with a simple numerical example based on a standard lid-driven cavity problem. The domain is depicted in Figure 2.1. The Reynolds number is 40, based on the lid-velocity U and the characteristic length L , so the flow is laminar. We first found the steady-state velocity (\mathbf{u}_h) and pressure fields by solving the laminar Navier-Stokes equations. Then, we solved a transport equation for a passive scalar ϕ with the numerical velocity \mathbf{u}_h and a diffusion coefficient D :

$$\frac{\partial \phi}{\partial t} + \nabla \cdot (\mathbf{u}_h \phi) = \nabla \cdot (D \nabla \phi), \quad (2.47)$$

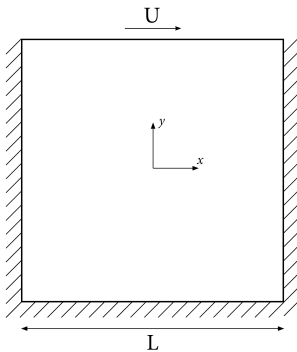


Fig. 2.1. Domain of the lid-driven cavity test case.

with homogeneous Neumann boundary conditions for ϕ . We set a constant initial condition $\phi_0 = \phi(t = 0) = 1$, and took a single time step with the BDF1 scheme and $U\Delta t/L = 1$, choosing a relative tolerance of 10^{-12} for the GMRES and CG Krylov solvers, to minimize any numerical error in the solution of the linear systems. Clearly, the discrete solution ϕ_h should remain unchanged after the time step. We therefore calculated the L^2 -norm error of ϕ_h with respect to the expected exact solution ϕ_0 . To highlight the impact of the velocity divergence and continuity errors, we repeated the test for various spatial refinements. Following Fehn et al. (2018), we used

$$E_D = L \frac{\sum_{T \in \mathcal{T}} \int_T |\nabla \cdot \mathbf{u}|}{\sum_{T \in \mathcal{T}} \int_T \|\mathbf{u}\|} \quad \text{and} \quad E_C = \frac{\sum_{F \in \mathcal{F}^i} \int_F |[\![\mathbf{u}]\!] \cdot \mathbf{n}^F|}{\sum_{F \in \mathcal{F}^i} \int_F \{\mathbf{u}\} \cdot \mathbf{n}^F} \quad (2.48)$$

to estimate the mass conservation error in a strong sense.

Table 2.3 collects the results for two structured meshes made of quadrilateral elements: (i) 50 by 50 uniform (indicated with $M1$); and (ii) 90 by 90 progressively finer towards the boundaries ($M2$). On $M2$, we studied the effect of varying the velocity polynomial order.

Results support our theoretical argument. When $\mathcal{P}_\phi > \mathcal{P}_p$, the constant solution is not preserved, due to the numerical error introduced by discontinuity of the velocity field across the elements. In fact, as expected, the error decreases with spatial refinement, that is, with lower divergence and continuity errors. The problem is more pronounced in convection-dominated problems, as in case of turbulent flows. In fact, the biggest errors correspond to low values of the diffusion coefficient. Increasing D , as expected the error decreases, because the residual becomes progressively more dominated by the elliptic term. Asymptotically, the error is inversely proportional to D . On the other hand, the constant solution is always preserved (up to numerical precision) when $\mathcal{P}_\phi = \mathcal{P}_p$.

Table 2.3. Lid-driven cavity test: L^2 -norm error in the scalar quantity ϕ with respect to the exact solution $\phi_0 = 1$, as a function of the diffusion coefficient (D) and for various meshes and polynomial orders, which affect the divergence (E_D) and continuity (E_C) errors of the velocity field. Note that $\phi_0 = 1$ always lies in the solution space. The scalar quantity is only conserved when $\mathcal{P}_\phi = \mathcal{P}_p$.

	$M1$ ($\mathcal{P}_u = 2, \mathcal{P}_p = 1$)		$M2$ ($\mathcal{P}_u = 2, \mathcal{P}_p = 1$)		$M2$ ($\mathcal{P}_u = 3, \mathcal{P}_p = 2$)	
	$E_D = 5.1\text{e-}2, E_C = 1.2\text{e-}3$		$E_D = 1.1\text{e-}2, E_C = 1.9\text{e-}4$		$E_D = 9.0\text{e-}3, E_C = 7.5\text{e-}5$	
	$\mathcal{P}_\phi = \mathcal{P}_p$	$\mathcal{P}_\phi = \mathcal{P}_u$	$\mathcal{P}_\phi = \mathcal{P}_p$	$\mathcal{P}_\phi = \mathcal{P}_u$	$\mathcal{P}_\phi = \mathcal{P}_p$	$\mathcal{P}_\phi = \mathcal{P}_u$
$D = 1.0\text{e-}07$	1.55E-14	2.53E-01	6.94E-14	8.74E-02	1.61E-13	2.74E-02
$D = 1.0\text{e-}04$	1.04E-14	1.98E-01	1.39E-14	3.01E-03	2.32E-14	1.07E-03
$D = 1.0\text{e-}01$	2.11E-13	8.36E-05	2.79E-13	2.86E-06	1.69E-13	1.06E-06
$D = 1.0\text{e+}01$	2.03E-11	8.37E-07	1.00E-12	2.86E-08	4.63E-12	1.06E-08
$D = 1.0\text{e+}03$	2.26E-13	8.37E-09	8.76E-13	2.86E-10	2.37E-12	1.07E-10

2.7 Test cases

In this section, we verify and benchmark our numerical scheme with three test cases. First, we employ a manufactured solution for the RANS and $\mathcal{K} - \mathcal{E}$ equations to verify the spatial and temporal convergence rates of the solver. Then, we simulate the stationary turbulent flow over a backward-facing step and finally a Von Kármán vortex street in the wake of a square cylinder. In both cases, we compare our results with those obtained from experiments and other numerical simulations reported in literature.

The meshes were generated with the open-source tool **Gmsh** (Geuzaine and Remacle, 2009), which is also used to post-process the solution fields.

2.7.1 Manufactured solution

As first test-case, we employ the method of manufactured solutions to verify the correctness of the implementation of our space-time numerical scheme. Starting from the well-know Taylor-Green vortex solution of the laminar Navier-Stokes equations (see, for example, Shahbazi et al., 2007), we generalized it to the RANS equations and included an expression for the turbulence quantities. The analytical solution is

$$\begin{aligned}
 u^{\text{ex}} &= \exp(-2\tilde{t}) \begin{bmatrix} -\cos(\tilde{x}) \sin(\tilde{y}) \\ +\sin(\tilde{x}) \cos(\tilde{y}) \end{bmatrix}, \\
 p^{\text{ex}} &= -\frac{1}{4} \exp(-4\tilde{t}) (\cos(2\tilde{x}) + \cos(2\tilde{y})), \\
 \mathcal{K}^{\text{ex}} &= \exp(-2\tilde{t}) \cos(\tilde{x}) \cos(\tilde{y}) - 4.5, \\
 \mathcal{E}^{\text{ex}} &= \log(C_\mu) + \mathcal{K}^{\text{ex}}, \\
 \nu_t^{\text{ex}} &= \exp(\mathcal{K}^{\text{ex}}),
 \end{aligned} \tag{2.49}$$

where

$$\tilde{t} := \frac{50 \nu t}{(L/\pi)^2}, \quad \tilde{x} := \frac{x}{L/\pi}, \quad \tilde{y} := \frac{y}{L/\pi}. \quad (2.50)$$

This solution is defined on the domain $(x, y) \in [-L, L]^2$ and $t \geq 0$. It does not satisfy the coupled RANS and $\mathcal{K} - \mathcal{E}$ equations exactly, so the extra source terms \mathbf{f} , $q_{\mathcal{K}}$ and $q_{\mathcal{E}}$ are non-zero. We computed them by substituting (2.49) into Equations (2.1) and (2.4) symbolically with a Python script. We imposed Dirichlet conditions at all boundaries of the domain. Together with the initial conditions, they were evaluated from the analytical solution.

All relative errors reported in the following were evaluated for $L = 1$, $\nu = 2.5 \times 10^{-4}$, and at $t = 4$, which corresponds to almost a threefold decay of the initial condition. We set a relative tolerance of 10^{-12} for the GMRES and CG Krylov solvers. Moreover, all integrals were evaluated with a polynomial accuracy of 20, considerably higher than the usual $3\mathcal{P}_u - 1$. We did this to minimize the quadrature error in the integration of the extra source terms, which are complex non-polynomial functions.

2.7.1.1 Temporal convergence

To verify the temporal convergence of our numerical scheme, we solved Equations (2.1) and (2.4) on a structured mesh consisting of 100 by 100 quadrilateral elements adopting a polynomial order $\mathcal{P}_u = 5$, in order to ensure that the time error was dominant. We carried out the study for both the first-order and second-order BDF schemes, progressively halving the time step size from 2^{-6} to 2^{-11} .

Figure 2.2 shows the relative errors in the L^2 -norm of the velocity, pressure, and turbulence quantities with respect to the analytical solution (2.49) as a function of the time step size. The dashed lines help verifying that the error convergence rate is the expected one for both BDF orders. A slight deviation from the second-order convergence trend can be noticed in the pressure and velocity plots at small Δt , due to the onset of the space-error saturation.

Given the availability of an exact expression for the turbulent viscosity, we could compute an L^2 error also for this quantity. As shown in Figure 2.3, this error also exhibits the correct convergence rates.

2.7.1.2 Spatial convergence

The spatial convergence was verified by solving Equations (2.1) and (2.4) on increasingly refined structured quadrilateral meshes, progressively halving the element size from 2^{-1} to 2^{-5} . The study was repeated for various polynomial orders ($\mathcal{P}_u \in \{2, 3, 4\}$). To ensure the spatial error was dominant, we chose the BDF2 scheme and a time step size $\Delta t = 2.5 \times 10^{-5}$.

Figure 2.4 shows the L^2 -norm errors of the unknown quantities with respect to the analytical solution (2.49) as a function of the element size and the polynomial

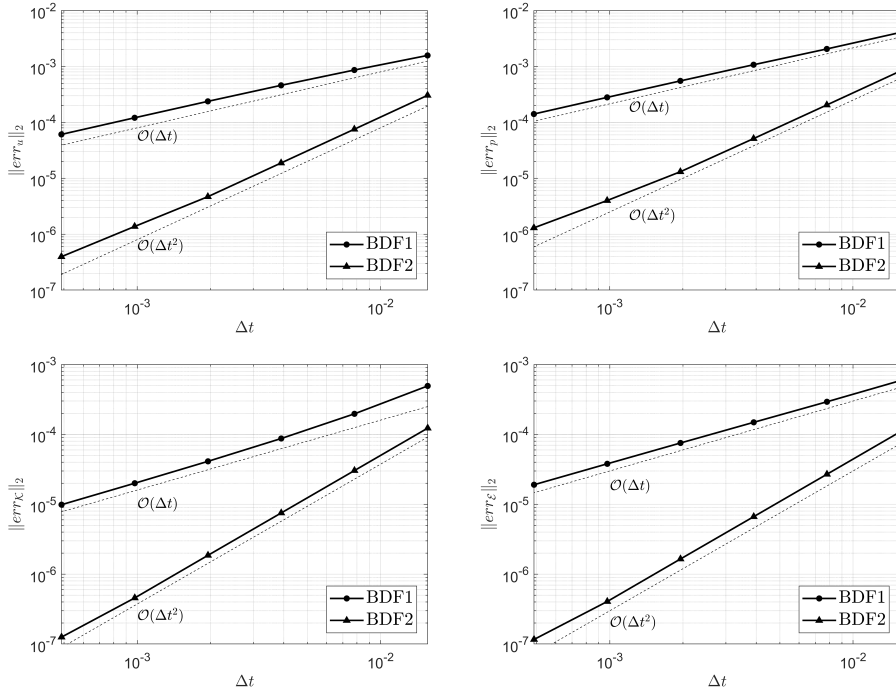


Fig. 2.2. L^2 -norm errors of the velocity, pressure, and turbulence quantities with respect to the exact solution (2.49) as a function of the time step size and for both first and second order BDF schemes. The correct convergence order are reached.

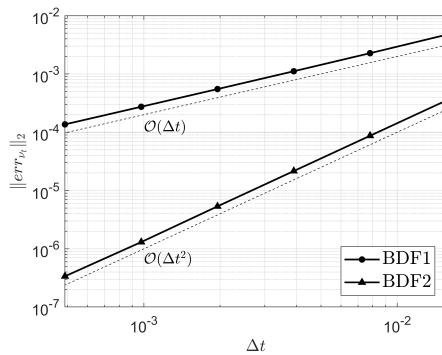


Fig. 2.3. L^2 -norm error of the eddy viscosity with respect to the exact solution (2.49) as a function of the time step size and for both first and second order BDF schemes. The error exhibits the expected convergence rate.

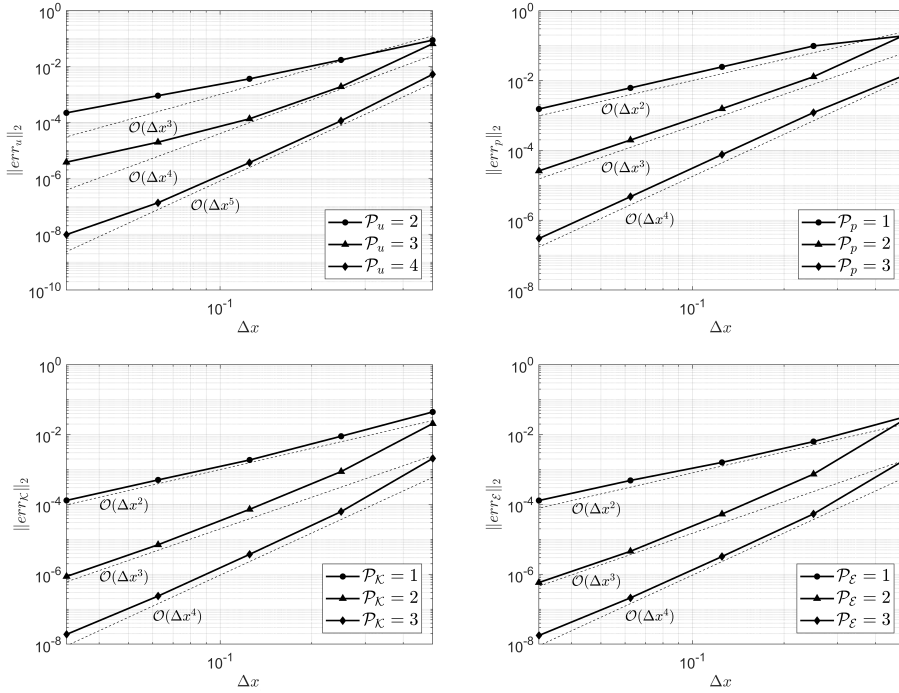


Fig. 2.4. L^2 -norm errors of the velocity, pressure, and turbulence quantities with respect to the exact solution (2.49) as a function of the element size and for several orders of the polynomial discretization. Scalar quantities exhibit the theoretical convergence rate, whereas that of the velocity is sub-optimal.

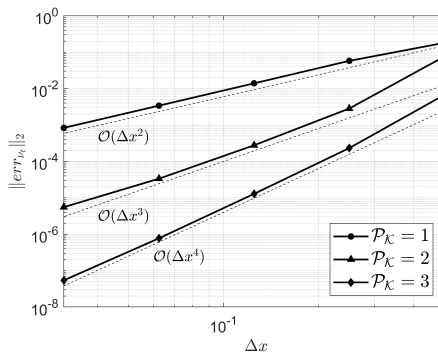


Fig. 2.5. L^2 -norm error of the eddy viscosity with respect to the exact solution (2.49) as a function of the element size and for several orders of the polynomial discretization of \mathcal{K} . The error exhibits the expected convergence order.

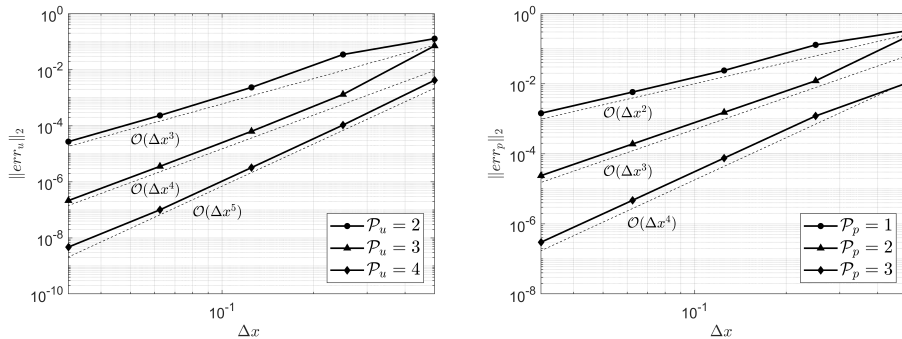


Fig. 2.6. L^2 -norm errors of the velocity and pressure when Equation (2.1) is solved imposing the analytical expression for the eddy viscosity from Equation (2.49). The optimal convergence rate of the velocity is recovered in this case.

order. The errors of the pressure and the two turbulence quantities converge with the expected theoretical order (highlighted by the dashed lines). On the other hand, the velocity error exhibits a sub-optimal convergence rate, in particular for the second-order and third-order discretizations. This is due to the fact that the residual of the momentum equation is dominated by the error in the turbulent viscosity, which converges at the theoretical rate for the scalar quantities, as shown in Figure 2.5.

To corroborate this conclusion, we repeated the test, this time imposing the exact expression of the eddy viscosity (from Equation (2.49)) in the momentum equation, thus decoupling the RANS set from the turbulence equations. Results reported in Figure 2.6 demonstrate that the theoretical convergence rate of the velocity error can be recovered in this case.

2.7.2 Flow over a backward-facing step

As second test case, we study the turbulent flow over a backward-facing step. The problem is a well-known benchmark for turbulence solvers and many variants have been investigated. Here, we consider the same configuration as in the experimental study by Kim et al. (1980)², depicted in Figure 2.7. The ratio of the inlet channel height (H_i) to step height (H) is 2 and $Re = 44737$, based on the reference free-stream velocity U_0 , the step height and the kinematic viscosity ν .

We imposed Dirichlet boundary conditions at the inlet, placed at a distance $L_i = 4H$ upstream of the step. We used an analytical profile for the stream-wise

²Experimental measurements by Kim et al. (1980) have been retrieved from the turbulent flow database described in Bradshaw et al. (1996) and available at <https://turbmodels.larc.nasa.gov/bradshaw.html>.

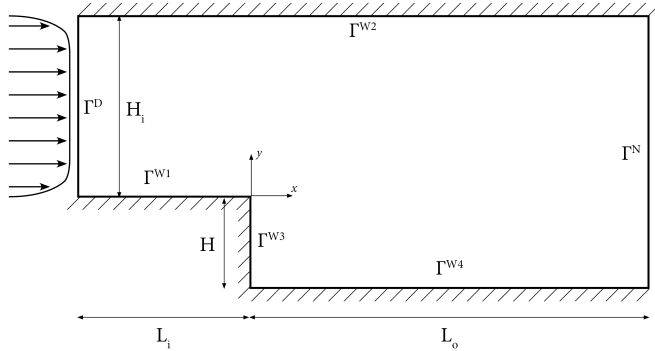


Fig. 2.7. Backward-facing step domain (not in scale).

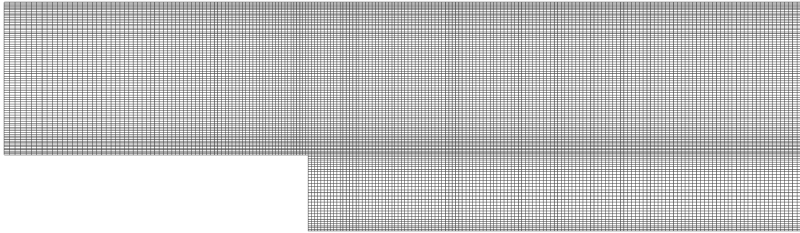


Fig. 2.8. $M3$ structured mesh used for the turbulent backward-facing step test case. It consists of 55500 elements.

velocity (u_x) that matches the experimental data provided by Kim et al. (1980) (reasonably) well,

$$u_x^D = U_0 f(y), \text{ with } f(y) = \begin{cases} 1 - e^{-18(y+0.0495)} & , 0 \leq y \leq 1 \\ 1 - e^{-18(2+0.0495-y)} & , 1 < y \leq 2 \end{cases}, \quad (2.51)$$

and we set a turbulence intensity of 7.5% and a ratio $\nu_t/\nu = 35$, with which we computed uniform profiles for \mathcal{K}^D and \mathcal{E}^D . Outflow boundary conditions were imposed at a distance $L_o = 30H$ downstream of the step. Finally, we imposed wall functions on the top and bottom walls, with a distance from the physical wall of the computational boundary set to $\delta_w = 0.04$ for Γ^{W3} and to $\delta_w = 0.02$ for the others.

We computed the steady-state solution on three structured meshes, finer towards the wall boundaries, consisting of 12420 (mesh indicated with $M1$ in the following), 29700 ($M2$), and 55500 ($M3$) quadrangles. A portion of the latter mesh is shown in Figure 2.8. To study the influence of the polynomial order, we performed calculations with both $\mathcal{P}_u = 3$ and $\mathcal{P}_u = 4$.

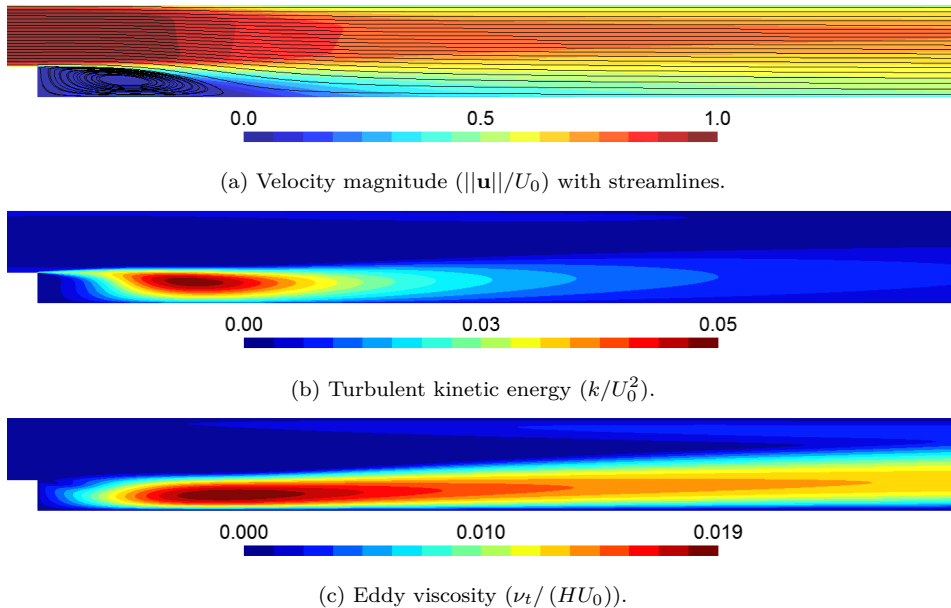


Fig. 2.9. Turbulent flow over a backward-facing step: steady state (a) velocity and streamlines, (b) turbulent kinetic energy, and (c) eddy viscosity fields obtained on the $M3$ mesh for $\mathcal{P}_u = 4$.

Figure 2.9 shows the steady-state velocity, turbulent kinetic energy, and eddy viscosity fields obtained on the finest mesh for $\mathcal{P}_u = 4$. They are in good qualitative agreement with those, for example, reported by Kuzmin et al. (2007). For a more quantitative assessment of our results, Table 2.4 compares the dimensionless recirculation length (L_R) we obtained with the experimental measurement by Kim et al. (1980) and other numerical predictions. Our results differ only a few percent at most from the most accurate predictions reported in literature, and always towards a better agreement with the experimental results. In all cases, the recirculation length is underestimated by around 6%, which is expected with the $k - \epsilon$ model. Differences in L_R on $M2$ and $M3$ are limited to 0.5% at most, and the impact of a richer polynomial representation is limited to less than 1%, thus showing the mesh convergence of our calculations.

Finally, Figure 2.10 shows the vertical profiles of the stream-wise velocity component at different locations downstream of the step, obtained with $\mathcal{P}_u = 4$ and for different meshes. Profiles on $M2$ and $M3$ are barely distinguishable. Results compare reasonably well with the experimental measurements of Kim et al. (1980) up to $x/H = 8.0$, then the discrepancies due to the limitations of the $k - \epsilon$ model become apparent, as already documented in Ilinca et al. (1998), for example.

Table 2.4. Comparison of the dimensionless recirculation length (L_R) obtained in the present work (for different meshes and polynomial orders) with experimental and numerical results (obtained with the $k - \epsilon$ model) reported in literature. The relative error is computed with respect to the experimental measurements by Kim et al. (1980).

Reference	L_R/H	Relative error	
Kim et al. (1980), experiment	7.0 ± 0.5		
Zijlema (1996)	5.90	-15.7 %	
Thangam and Speziale (1992)	6.25	-10.7 %	
Muller et al. (2018)	6.33	-9.6 %	
Kuzmin et al. (2007)	5.40	-22.9 %	
Shih et al. (1995)	6.35	-9.3 %	
Ilinca et al. (1998)	6.20	-11.4 %	
Present, $\mathcal{P}_u = 3$,	$M1$	6.42	-8.3 %
	$M2$	6.54	-6.6 %
	$M3$	6.56	-6.4 %
$\mathcal{P}_u = 4$,	$M1$	6.47	-7.6 %
	$M2$	6.56	-6.2 %
	$M3$	6.60	-5.7 %

2.7.3 Vortex-shedding in the wake of a square cylinder

The last simulation is of turbulent flow past a cylinder with square cross section, characterized by the appearance of a Von Kármán vortex street in the wake of the obstacle. Even if the flow features stochastic three-dimensional fluctuations, which can be resolved only with LES or DNS approaches (see, e.g., Rodi, 1997; Trias et al., 2015), the problem is used as a two-dimensional test case for RANS solvers. The flow is in fact characterized by a mean periodicity that can be captured with unsteady RANS equations.

Figure 2.11 shows the problem domain. The Reynolds number is $Re = 22000$, based on the square cylinder side (D), the far-field velocity (U_∞), and the kinematic viscosity ν . Experimental measurements on this problem were carried out by Lyn et al. (1995).

Symmetry conditions were imposed on the top and bottom boundaries (distant $H = 30D$), whereas an outlet was placed at $L_o = 40D$ downstream of the obstacle to avoid any influence on the flow in the cylinder region. For the same reason, the inlet boundary was placed at $L_i = D$ upstream of the cylinder. The following uniform Dirichlet condition for the velocity was imposed:

$$\mathbf{u}^D(t) = (U_\infty f(t), 0)^T, \text{ with } f(t) = \begin{cases} \frac{t^2}{4}(3-t) & , 0 \leq t \leq 2 \\ 1 & , t > 2 \end{cases}. \quad (2.52)$$

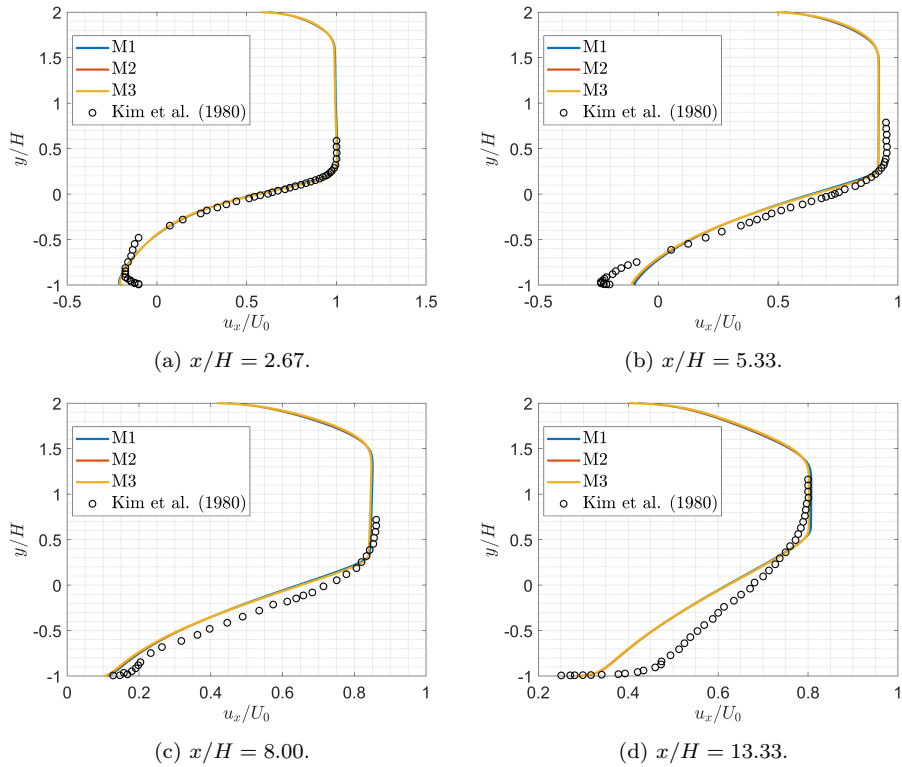


Fig. 2.10. Turbulent flow over a backward-facing step: Comparison with the experimental measurements of Kim et al. (1980) of the stream-wise velocity profiles obtained at different locations for $\mathcal{P}_u = 4$ and the three meshes employed. Results on the two most refined meshes are barely distinguishable.

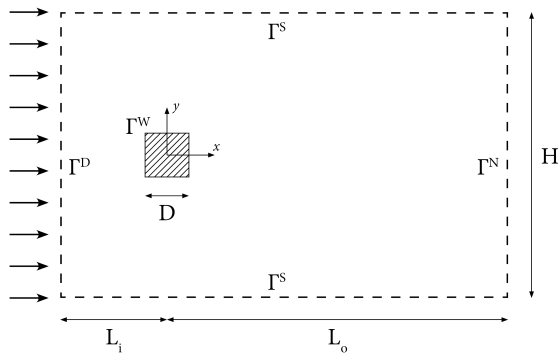
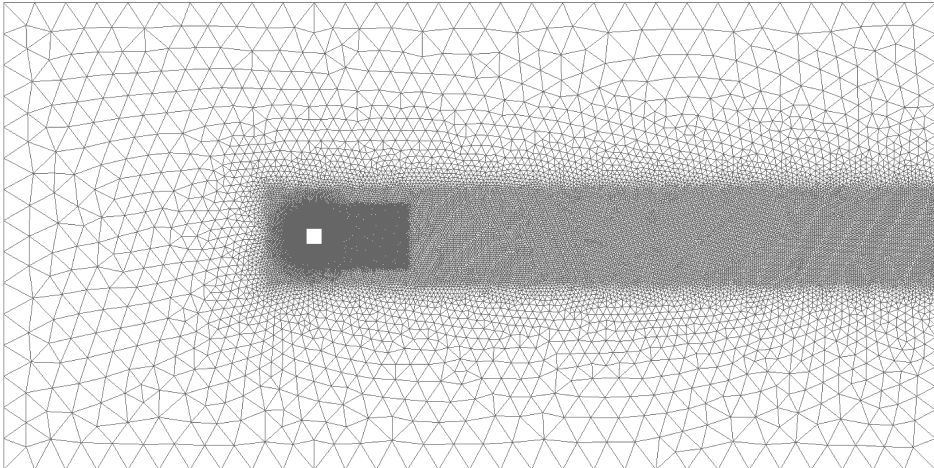
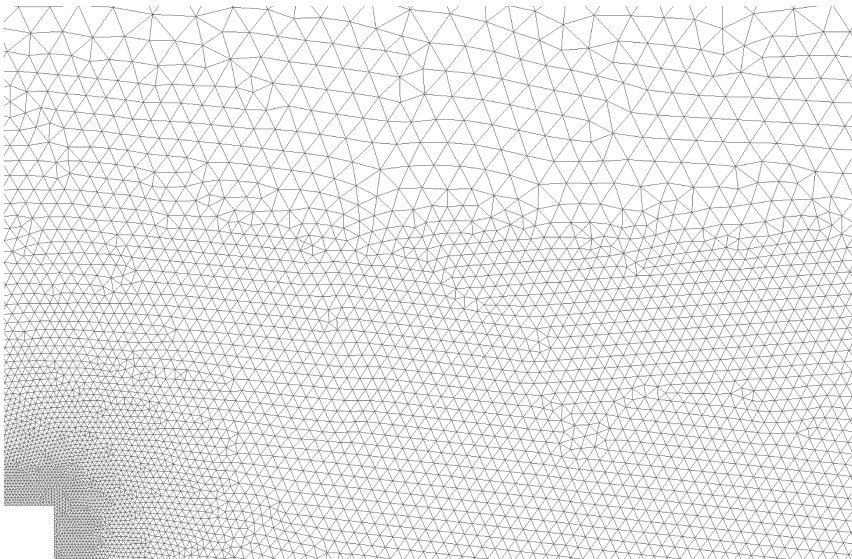


Fig. 2.11. Geometry of the flow past a square cylinder test case (not in scale).



(a) Complete overview.



(b) Detail near the square cylinder.

Fig. 2.12. $M3$ unstructured mesh used for the turbulent flow past a square cylinder test case: complete overview (left) and detail around the obstacle (right). It consists of 64963 triangles, most of which are concentrated in the proximity and the wake of the cylinder.

Moreover, following Bosch and Rodi (1998), we calculated the inlet values of \mathcal{K} and \mathcal{E} to match a turbulence intensity level of 2% and a viscosity ratio $\nu_t/\nu = 10$, which correspond to the experiments of Lyn et al. (1995). Finally, wall functions were imposed on the edges of the cylinder, setting the distance of the computational domain from the physical wall to $\delta_w = 0.015$.

We sampled the time variations in the drag and lift coefficients, defined as

$$C_d = \frac{2F_x}{DU_\infty^2} \quad \text{and} \quad C_l = \frac{2F_y}{DU_\infty^2}, \quad (2.53)$$

where F_x and F_y indicate the stream-wise and vertical components of the force acting on the cylinder. The mean periodicity of the flow can be quantified in terms of the Strouhal number $St = fD/U_\infty$, where f is the oscillation frequency, which we determined from the time trend of C_l .

We performed our calculations with the BDF2 time scheme and $\Delta t = 1.25 \times 10^{-3}$. To study the influence of space errors on the results, we used three unstructured meshes consisting of 40281 (indicated with $M1$), 51913 ($M2$), and 64963 ($M3$, shown in Figure 2.12) triangles, progressively more refined towards the obstacle. On the finest mesh then, we varied the time step size to $\Delta t = 2.5 \times 10^{-3}$ and $\Delta t = 5.0 \times 10^{-3}$.

Figure 2.13 shows an example of the instantaneous velocity magnitude and eddy viscosity fields obtained for $\Delta t = 1.25 \times 10^{-3}$ and $\mathcal{P}_u = 3$ on $M3$. The vortex shedding is clearly visible. Table 2.5 reports the results we obtained in terms of Strouhal number, average C_d , and root mean square values of the fluctuations of C_d and C_l , comparing them with experimental measurements, DNS and other RANS results. We ended our simulations at $t_{end} = 152$, corresponding to almost 2.5 flow-through periods which is sufficient to reach flow periodicity, and evaluated the quantities of interest over the final 8 oscillation periods.

Results on $M3$ and for $\Delta t = 1.25e - 3$ are fully converged in time (they do not change even quadrupling the Δt) and nearly mesh independent. The Strouhal number agrees with the experimental measurements and the DNS predictions, and it differs only 1.5% from the value reported by Bosch and Rodi (1998) for a standard $k - \epsilon$ model. The discrepancy is much more relevant when comparing the other quantities of interest though. This might be due to the great sensitivity of the force fluctuations to the numerical details of the problem (e.g., position of inlet boundary, Dirichlet conditions imposed, blockage ratio) as documented, for example, by Bosch and Rodi (1998) and Han et al. (2012). In any case, our values are inside the range of RANS results reported by Rodi et al. (1997) and Voke (1997). The discrepancy with experimental and DNS results in terms of force coefficients is expected, due to the limitations of the $k - \epsilon$ model in predicting the strength of the shedding motion.

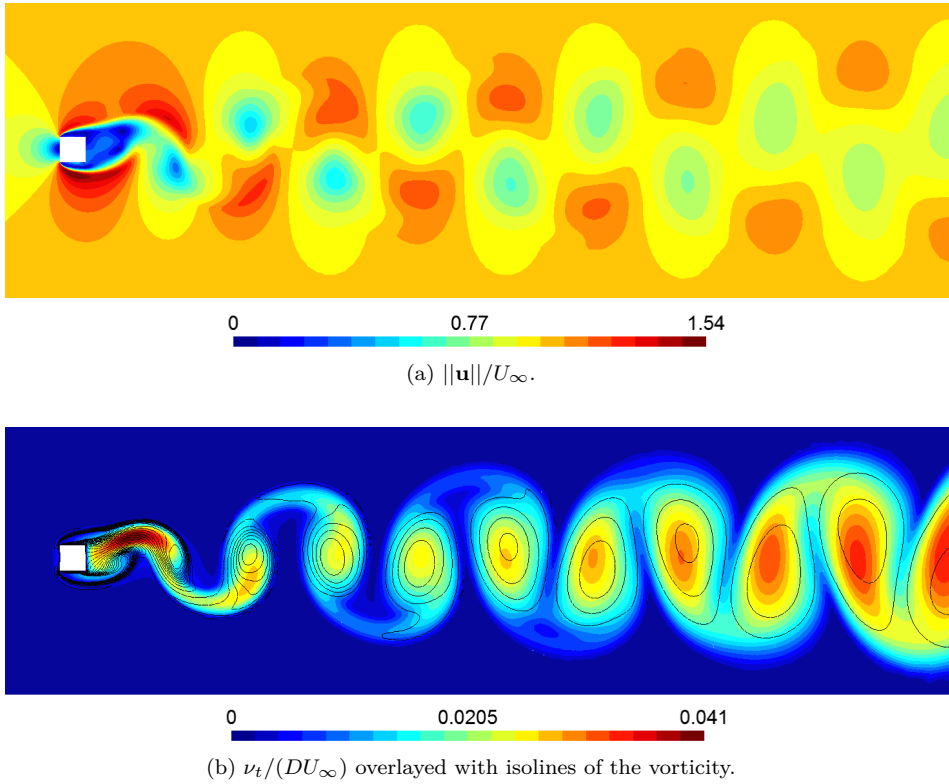


Fig. 2.13. Flow past a square cylinder: Instantaneous velocity (top) and eddy viscosity (bottom) fields obtained on $M3$ for $\mathcal{P}_u = 3$.

Table 2.5. Comparison of the force coefficients (in terms of average value, root mean square of the fluctuations, and frequency) obtained in the present work for three meshes and time step sizes with experimental and numerical results reported in literature.

Reference	\bar{C}_d	$C_{d,rms}$	$C_{l,rms}$	St	
Lyn et al. (1995), experiment	2.100	–	–	0.132	
Trias et al. (2015), DNS	2.180	0.205	1.710	0.132	
Bosch and Rodi (1998), $k-\epsilon$	1.637	0.002	0.305	0.134	
Rodi et al. (1997); Voke (1997), RANS models	1.64–2.43	$\approx 0-0.27$	0.31–1.49	0.134–0.159	
Present, $M1$	$\Delta t = 1.25e-3$	1.687	0.008	0.460	0.129
$M2$	$\Delta t = 1.25e-3$	1.775	0.014	0.632	0.131
$M3$	$\Delta t = 1.25e-3$	1.788	0.015	0.657	0.132
$M3$	$\Delta t = 2.5e-3$	1.788	0.015	0.657	0.132
$M3$	$\Delta t = 5.0e-3$	1.788	0.015	0.657	0.132

2.8 Conclusions

In this work, we have presented a novel high-order discontinuous Galerkin Finite Element (DG-FEM) solver for the incompressible Reynolds-Averaged Navier-Stokes (RANS) equations coupled with the $k - \epsilon$ closure model. Positivity of the turbulence quantities is ensured by solving for their logarithm. Integration of the equations up to the wall boundary leads to poor results in case of the $k - \epsilon$ model, and in any case this approach can still be too computationally expensive in complex engineering applications. For these reasons, we have investigated the possibility of employing a two-velocity scale wall function approach, in combination with DG, to bridge the gap between the viscous and the logarithmic layer.

Contrary to most of previous literature, our solver features a second-order accurate algebraic pressure correction scheme to solve the coupled RANS system. The approach does not rely then on an artificial compressibility parameter whose value must be tuned for each problem. Implicit backward differentiation formulae are adopted for time discretization of all the equations. Proper time extrapolation of the solution ensures global second-order accuracy even if no iterations are performed between the highly coupled RANS and $k - \epsilon$ equations. For space discretization, we have chosen the Symmetric Interior Penalty method to deal with elliptic terms and the Lax-Friedrichs flux for convection.

We have paid particular attention to the choice of polynomial order for the turbulence quantities. We have theoretically and numerically proven that, to avoid any numerical instability, the polynomial order for the pressure and any transported scalar quantity must be the same when the velocity field is not point-wise divergence free. This contrasts with the choices made in previous literature.

We have verified the correct implementation of our space-time numerical scheme with a manufactured solution. However, it has shown that the convergence rate of the velocity error could be degraded by the slower convergence of the eddy-viscosity error (due to the lower polynomial order discretization of the turbulence quantities), in case the residual is dominated by the diffusive term. To prevent this, one could move to an equal-order discretization or, to avoid any instability problem, try to reduce the divergence and continuity errors of the velocity field with extra element-wise penalty terms in the momentum equation as proposed by Krank et al. (2017b). Another possibility would be to apply a post-projection operator on the convective field to ensure that the incompressibility constraint is satisfied exactly (Cockburn et al., 2008; Rhebergen et al., 2013).

Simulations of turbulent flows over a backward-facing step and past a square cylinder, inducing vortex shedding, have shown the soundness of our approach. Though we are bound by the well-known limitations of the $k - \epsilon$ model, our results are in general good agreement with those reported in literature. Compared to previous works that used the $k - \epsilon$ model, our discrepancies are always towards a better agreement with the experimental or DNS/LES results.

CHAPTER 3

NEUTRONICS AND THERMAL-HYDRAULICS COUPLED SOLVER

Performing accurate numerical simulations of molten salt reactors is challenging, especially in case of fast-spectrum designs, due to the unique physics phenomena characterizing these systems. The limitations of codes traditionally used in the nuclear community often require the development of novel high-fidelity multi-physics tools to advance the design of these innovative reactors. In this work, we present the most recent code developed at Delft University of Technology for multi-physics simulations of liquid-fueled fast reactors. The coupling is realized between an incompressible RANS model and an S_N neutron transport solver. The models are implemented in two in-house codes, based on the discontinuous Galerkin Finite Element discretization, which guarantees high-quality of the solution. We report and discuss the results of preliminary simulations of the Molten Salt Fast Reactor at steady-state and during a Total Loss of Power transient. Results prove our code has capabilities for steady-state and transient analysis of non-moderated liquid-fueled reactors.

This chapter is based on M. Tiberga, D. Lathouwers, and J.L. Kloosterman. A multi-physics solver for liquid-fueled fast systems based on the discontinuous Galerkin FEM discretization, *Progress in Nuclear Energy*, **127**, 103427, 2020. <https://doi.org/10.1016/j.pnucene.2020.103427>

3.1 Introduction

Interest in molten salt reactors (MSR) has increased over the past two decades (LeBlanc, 2010), after the inclusion of this technology among the six Generation IV nuclear reactors in 2002 (Generation IV International Forum, 2002). Many MSR concepts are currently being investigated worldwide by companies and research institutes (Dolan, 2017), encouraged by the success of the Molten Salt Reactor Experiment (MSRE), which operated at Oak Ridge National Lab in the late sixties demonstrating the safety and the feasibility of the technology (Haubenreich and Engel, 1970; MacPherson, 1985).

Numerical simulations play an essential role in developing these innovative reactor designs, given the lack of substantial operational experience and know-how compared to the field of light-water reactors. However, simulating an MSR is a challenging task, as the use of a liquid salt both as fuel and coolant leads to unique physics phenomena which strongly (and non-linearly) couple neutronics and thermal-hydraulics (Rubiolo et al., 2017): distributed, internal heat generation in the coolant; transport of delayed neutron precursors; feedback induced by fuel density variations. Moreover, in non-moderated designs, as the Molten Salt Advanced Reactor Transmuter (MOSART) (Ignatiev et al., 2014) or the Molten Salt Fast Reactor (MSFR) (Allibert et al., 2016), the traditional core shape with repeated structures (e.g., fuel pins) is lost.

Some efforts have been made to equip classical codes used in the nuclear community to model traditional solid-fueled reactors with the features necessary to address MSR simulations (e.g., Zanetti et al., 2015). However, legacy codes were usually developed decades ago, when strong computational capabilities were unavailable, and are often characterized by modeling assumptions (e.g., 1D flow model, point kinetics) that limit their range of usability. For these reasons, accurate simulations of molten salt reactor systems (especially fast-spectrum designs) need the development of new dedicated tools. We give hereafter a (non-exhaustive) overview of the previous work in the field before introducing our contribution.

The first decade of the century saw a succession of preliminary studies and modeling approaches based on simplifying assumptions (see Cammi et al., 2011, for a complete overview). First investigations on the coupling between neutron dynamics and fuel motion were performed by Lapenta et al. (2001) and Dulla et al. (2004), using simple neutronics models and considering only a 1D imposed velocity field with no temperature feedback. A prescribed salt velocity was considered also in the multi-group diffusion code `Cinsf1D` (Lecarpentier and Carpentier, 2003), used for the analysis of the AMSTER system (Vergnes and Lecarpentier, 2002). The temperature feedback on cross sections was taken into account by solving the energy equation in the fluid and graphite structures coupled through empirical heat transfer correlations.

Křepel et al. (2005) developed the `DYN1D-MSR` code, devoted to the transient analysis of the MSRE. Here, a 1D two-group diffusion model is coupled with 1D

models for the fuel flow and the temperature distribution in the graphite moderator. The neutronics model was later extended into a 3D version (Křepel et al., 2007). A similar multi-physics tool was developed at Delft University of Technology (TU Delft) by Kópházi et al. (2009), by coupling the in-house codes THERM and DALTON. Under the reasonable approximation of uni-directional flow inside the graphite channels of the MSRE, the former code implements a 1D model for the fuel flow, coupled to a 3D multi-group diffusion model implemented in the latter. Three-dimensional calculations were performed to evaluate heat transfer within graphite, coupled to the core channels via Nusselt number correlations.

Preliminary steady-state and transient studies on the MOSART design were performed by Wang et al. (2006) and Nicolino et al. (2008). The first extended the thermal-hydraulics and neutronics models and the fuel properties libraries of the SIMMER-III code. Nicolino et al. (2008) adopted a fully-coupled approach in which the incompressible Navier-Stokes equations are solved together with the multi-group diffusion and the delayed precursors equations using a Jacobian-Free Newton Krylov algorithm. Both previous models are 2D, axisymmetric (exploiting the cylindrical geometry of the MOSART core), but consider the flow to be laminar, a strongly simplifying assumption in case of non-moderated reactors, given the high Reynolds numbers characterizing the salt flow in the core cavity.

On the other hand, over the past 10 years, given the availability of more powerful computational resources and the maturity level reached in the field, simplifying assumptions and models have been abandoned for full multi-physics approaches. Cammi et al. (2011) were the first to propose a coupled neutronics (multi-group diffusion) and thermal-hydraulics (RANS/ $k - \epsilon$ and temperature equation in the graphite moderator) model implemented in the same simulation environment (COMSOL Multiphysics®). It was used to get a deeper insight into the steady-state and transient characteristic of the Molten Salt Breeder Reactor (Robertson, 1971). At TU Delft, Van der Linden (2012) coupled the multi-group diffusion code DALTON with a full RANS/ $k - \epsilon$ thermal hydraulic model. In the framework of the Euratom FP7 EVOL project (EVOL, 2010–2013), the two aforementioned multi-physics codes were used to conduct an extensive investigation of the behavior of the MSFR, both at steady-state and during accidental transient scenarios (Fiorina et al., 2014). A 2D axisymmetric geometry was adopted, given the cylindrical shape of the MSFR core at that time.

Aufiero et al. (2014b) developed the first OpenFOAM® multi-physics tool for MSRs, coupling a diffusion model with the RANS/ $k - \epsilon$ equations. Being capable of dealing with full-core 3D analysis, the tool was employed to investigate for the first time an asymmetric loss of flow accident inside the MSFR. A single-group diffusion model was adopted to relieve the computational burden though. A similar tool is the OpenMC/TANSY code system developed by Hu et al. (2017) for the analysis of the MOSART. More innovative from the neutronics point of view is the MSFR multi-physics tool of Laureau et al. (2017). The Transient Fission Matrix method was in fact chosen to reproduce transient Monte Carlo-like calculations

with a reduced computational cost.

Fiorina et al. (2015) presented GeN-Foam, a multi-physics code coupling a RANS/ $k - \epsilon$ model, extended to coarse-mesh applications thanks to the adoption of a porous-medium approach, and a multi-group diffusion neutronics solver. The code is also equipped with a displacement-based thermal-mechanics solver and a finite-difference model for the temperature field in the fuel, since it targets homogeneous liquid-fueled reactors as well as light-water or liquid-metal reactors. This tool was recently used by Altahhan et al. (2019) to perform preliminary design investigations of the primary loop of a chloride-based molten salt fast reactor.

All previously mentioned multi-physics models consider the fuel salt to be an incompressible fluid. However, Aufiero et al. (2017) pointed out that taking into account the fuel compressibility is essential to correctly model the fuel-expansion feedback during fast, super-prompt critical transients. This was confirmed by their simulations, performed on a simplified MSFR geometry, using a novel multi-physics tool coupling a compressible flow model, available in OpenFOAM[®], with the Monte Carlo code Serpent (Leppänen et al., 2015). Further investigations have been recently performed by Cervi et al. (2019a), using a multi-physics tool consisting of a multi-group diffusion model coupled to a two-phase compressible RANS solver (both implemented in OpenFOAM[®]), able therefore to model the effects of non-uniform distributions of gas bubbles (helium) in the fluid mixture. The neutronics model was later improved adopting a Simplified P_3 approximation of the neutron transport equation (Cervi et al., 2019b).

In this work, our goal is to present the most recent advances in the field of multi-physics simulations of (non-moderated) MSR made at TU Delft. In the framework of the H2020 SAMOFAR project (<http://samofar.eu/>), we developed a novel multi-physics tool realized by coupling an incompressible RANS model with an S_N neutron transport solver, implemented in two in-house codes. In both of them, the discontinuous Galerkin Finite Element method (DG-FEM) is adopted to discretize in space the model equations. The method was chosen as it combines the advantages of local conservation, as in finite volumes, with the high-order discretization and high geometric flexibility (thus easily handling complex shapes as the MSFR core) of finite elements, guaranteeing high accuracy of simulations.

The MSFR can be considered a highly homogeneous system when compared to solid-fueled reactors, so diffusion models provide very good results in standard scenarios (as those considered in this work). Nevertheless, the simulation of reactor conditions characterized by significant material discontinuities will have to be carried out at a later development stage. For example, it will be necessary to consider draining scenarios of the reactor or the blanket, or malfunctions of the helium bubbling system (Delpech et al., 2009) leading to large and non-uniform concentration of bubbles in the fuel salt. In this situations, a full-transport model is necessary to describe more accurately the neutronics behavior of the reactor (Duderstadt and Hamilton, 1976). In this perspective, the combination of S_N with the DG-FEM discretization leads to a state-of-the-art deterministic method to

solve the Boltzmann equation (Reed and Hill, 1973; Wareing et al., 2001) which guarantees high-quality of the solution even in presence of large discontinuities in material properties. Our tool constitutes therefore a useful contribution to the set of available multi-physics codes dedicated to the analysis of molten salt fast reactors.

The chapter is outlined as follows. In Section 3.2, we describe in detail the thermal-hydraulics and the neutronics models and the coupling between them. Then, as an example of the capabilities of the coupled code, which has been benchmarked against other similar numerical tools in a recent work of some of the authors (Tiberga et al., 2020a), we perform preliminary simulations of the MSFR behavior at steady-state and during the first 30s of an unprotected Total Loss of Power (TLOP) accident. For this reason, we first describe the MSFR design and the modeling choices adopted in Section 3.3. Then, we report and analyze the results of our simulations in Section 3.4, drawing some conclusions in Section 3.5.

3.2 Description of the multi-physics tool

In this section, we describe in details the models constituting our multi-physics code. The coupling is realized between two in-house Fortran codes: `DGFlows` for CFD, and `PHANTOM-SN` for neutron transport.

3.2.1 Fluid dynamics: `DGFlows` code

`DGFlows` is designed to solve the set of Navier-Stokes equations in the low-Mach number limit (Hennink et al., 2020). Turbulent flows are handled through Reynolds Averaged Navier-Stokes (RANS) models. The RANS model equations read (omitting dependencies for clarity) (Patankar, 1980)

$$\frac{\partial \rho h}{\partial t} + \nabla \cdot (\mathbf{u} \rho h) = \nabla \cdot [(\kappa + \kappa_t) \nabla T] + S_h, \quad (3.1a)$$

$$\frac{\partial \mathbf{m}}{\partial t} + \nabla \cdot (\mathbf{u} \otimes \mathbf{m}) = -\nabla p + \nabla \cdot \boldsymbol{\tau} + \mathbf{F}_{buoy} + \mathbf{F}_m, \quad (3.1b)$$

$$\frac{\partial \rho}{\partial t} + \nabla \cdot \mathbf{m} = 0. \quad (3.1c)$$

Here, ρ is the fluid density, \mathbf{m} the mass flux and $\mathbf{u} = \mathbf{m}/\rho$ the velocity, p a pseudo-pressure, and h the specific enthalpy. The shear stress tensor, $\boldsymbol{\tau}$, is defined as

$$\boldsymbol{\tau} = (\mu + \mu_t) \left[\nabla \mathbf{u} + (\nabla \mathbf{u})^T - \frac{2}{3} (\nabla \cdot \mathbf{u}) I \right], \quad (3.2)$$

where I is the identity tensor, while μ and μ_t are the molecular and turbulent (or *eddy*) dynamic viscosities. κ in Equation (3.1a) is the molecular thermal conductivity, while κ_t is the turbulent one. The latter is computed as $\kappa_t = \mu_t c_p / Pr_t$,

where c_p is the salt specific heat capacity and Pr_t is the turbulent Prandtl number. Finally, S_h is the energy source term (e.g., fission heat), \mathbf{F}_{buoy} is the buoyancy force, and \mathbf{F}_m includes all other possible momentum sources.

In this work, as we did not address any super-prompt critical transient, we safely considered the salt density to be constant, thus reducing System (3.1) to the set of incompressible RANS, and we adopted the Boussinesq approximation to model buoyancy:

$$\mathbf{F}_{buoy} = \rho \mathbf{g} = -\rho_{ref} \mathbf{g} \beta_{buoy} (T - T_{ref}), \quad (3.3)$$

where T_{ref} is the Boussinesq reference temperature, \mathbf{g} is the gravity acceleration, β_{buoy} is the fluid thermal expansion coefficient, and ρ_{ref} is the salt density computed at the reference temperature.

System (3.1) has to be closed with a turbulence model and proper initial and boundary conditions. In this work we adopted the standard $k - \epsilon$ model (Launder and Spalding, 1974), as customary in the context of MSR's multi-physics simulations (e.g., Cammi et al., 2011; Fiorina et al., 2014; Aufero et al., 2014b; Laureau et al., 2017). The model was modified to take into account the turbulence production by buoyancy (Van der Linden, 2012; Van Maele and Merci, 2006) and cast into a logarithmic form to ensure the positivity of turbulence quantities (Ilinca et al., 1998):

$$\begin{aligned} \frac{\partial \rho \mathcal{K}}{\partial t} + \nabla \cdot (\mathbf{u} \rho \mathcal{K}) = \nabla \cdot \left[\left(\mu + \frac{\mu_t}{\sigma_k} \right) \nabla \mathcal{K} \right] + \left(\mu + \frac{\mu_t}{\sigma_k} \right) \nabla \mathcal{K} \cdot \nabla \mathcal{K} \\ + e^{-\mathcal{K}} (P_k + P_b) - \rho^2 C_\mu \frac{e^{\mathcal{K}}}{\mu_t}, \end{aligned} \quad (3.4a)$$

$$\begin{aligned} \frac{\partial \rho \mathcal{E}}{\partial t} + \nabla \cdot (\mathbf{u} \rho \mathcal{E}) = \nabla \cdot \left[\left(\mu + \frac{\mu_t}{\sigma_\epsilon} \right) \nabla \mathcal{E} \right] + \left(\mu + \frac{\mu_t}{\sigma_\epsilon} \right) \nabla \mathcal{E} \cdot \nabla \mathcal{E} \\ + C_{1\epsilon} e^{-\mathcal{K}} [P_k + C_{3\epsilon} \max(P_b, 0)] - \rho C_{2\epsilon} e^{\mathcal{E} - \mathcal{K}}. \end{aligned} \quad (3.4b)$$

Here, $\mathcal{K} = \ln(k)$ and $\mathcal{E} = \ln(\epsilon)$, $\mu_t = \rho C_\mu e^{2\mathcal{K} - \mathcal{E}}$. Turbulence is produced by both shear stress and buoyancy:

$$P_k = \mu_t \nabla \mathbf{u} : [\nabla \mathbf{u} + (\nabla \mathbf{u})^T], \quad (3.5a)$$

$$P_b = \frac{\mu_t}{Pr_t} \beta_{buoy} \mathbf{g} \cdot \nabla T. \quad (3.5b)$$

The latter term can actually be negative in case of thermal stratification. All remaining closure coefficients are reported in Table 3.1.

All boundary and initial conditions chosen for the simulations reported in this study are described in Section 3.3.2.6.

Table 3.1. Values of the closure parameters of the $k - \epsilon$ turbulence model (Launder and Spalding, 1974; Van Maele and Merci, 2006).

Parameter	C_μ	σ_k	σ_ϵ	$C_{1\epsilon}$	$C_{2\epsilon}$	$C_{3\epsilon}$
Value	0.09	1.0	1.3	1.44	1.92	1.0

3.2.1.1 Spatial and temporal discretization and solution of the linear systems

The discontinuous Galerkin FEM is chosen to discretize in space the model equations. We briefly describe here only the key ingredients of the discretization, and refer to Hennink et al. (2020) (and the references cited therein) for more details.

Instead of primitive quantities, as usual, we solve for the set of conservative variables, to fully exploit the local conservation of DG. All unknowns are represented in the Galerkin space using a hierarchical set of modal basis functions up to order \mathcal{P} (for vector quantities) and $\mathcal{P} - 1$ (for all other scalars). Diffusive terms are discretized with the Symmetric Interior Penalty (SIP) method, which is consistent and stable and leads to optimal spatial convergence rates and compact stencil size (Shahbazi et al., 2007). The Lax-Friedrichs numerical flux is chosen for the convective terms (Cliffe et al., 2010).

The general transport equation for quantity ζ is discretized implicitly in time with the backward differentiation formula (BDF) of order 2 (with constant time step Δt):

$$\frac{\gamma_0}{\Delta t} \zeta^{n+1} + A(\mathbf{u}^*) \zeta^{n+1} = - \sum_{m=1}^2 \frac{\gamma_m}{\Delta t} \zeta^{n+1-m} + S_\zeta^{n+1}, \quad (3.6)$$

where $\gamma_0 = 3/2$, $\gamma_1 = -2$, and $\gamma_2 = 1/2$, and the superscript $n + 1$ indicates the new time step. Matrix A collects all contributions deriving from the discretization of diffusive and convective terms.

The discretized RANS/ $k - \epsilon$ system is solved starting from the energy equation. Then, the coupled momentum-continuity equations are solved in a segregated way using a second-order time accurate pressure correction scheme (Van Kan, 1986); the splitting is done at algebraic level, as explained by Shahbazi et al. (2007), to avoid the imposition of pressure boundary conditions. Finally, the equations for the turbulence quantities are solved in sequence. All non-linearities (e.g., in the convective terms, or in the $k - \epsilon$ equations) are solved by initializing the interested quantity, ζ^* , with a second-order extrapolation from the previous time steps, that is, $\zeta^* = 2\zeta^n - \zeta^{n-1}$, or by simply choosing $\zeta^* = \zeta^{n+1}$, when the latter is known. Moreover, if necessary, inner iterations between the momentum and the pressure-Poisson equation and outer iterations between the momentum-continuity block and the $k - \epsilon$ block can be performed.

DGFlows has capabilities for parallel computation. We use METIS to partition

the mesh (Karypis and Kumar, 1998) and the MPI-based software library PETSc (Balay et al., 2018) to assemble and solve all linear systems. The pressure-Poisson equation is solved with the conjugate gradient method and an additive Schwarz preconditioner, with one block per process and an incomplete Cholesky factorization on each block; all other linear systems are solved with the GMRES method and a block Jacobi preconditioner, with one block per process and an incomplete LU factorization on each block. All linear solvers are initialized with a second-order time extrapolated solution from the previous time steps, in order to accelerate convergence.

3.2.2 Neutronics: PHANTOM-S_N code

PHANTOM-S_N is a solver for the multi-group Boltzmann neutron transport equation. This in-house code, already capable of calculating criticality and time eigenvalues (Kópházi and Lathouwers, 2012), of performing both regular and generalized perturbation analysis (Perkó, 2015, Ch. 3) and goal-oriented mesh refinement (Lathouwers, 2011a,b), was extended to solve time-dependent problems and, in particular, to handle the transport of delayed neutron precursors.

The time-dependent multi-group model equations read (omitting dependencies for clarity) (Lewis and Miller, 1993)

$$\frac{1}{v_g} \frac{\partial \varphi_g}{\partial t} + \mathbf{\Omega} \cdot \nabla \varphi_g + \Sigma_{t,g} \varphi_g = \sum_{g'} \int_{4\pi} \Sigma_{s,g' \rightarrow g}(\mathbf{\Omega}' \cdot \mathbf{\Omega}) \varphi_{g'} d\mathbf{\Omega}' + \frac{(1-\beta)\chi_g^p}{4\pi} \sum_{g'} \bar{\nu}_{g'} \Sigma_{f,g'} \Phi_{g'} + \frac{\chi_g^d}{4\pi} \sum_i \lambda_i C_i, \quad (3.7a)$$

$$\frac{\partial C_i}{\partial t} + \nabla \cdot (\mathbf{u} C_i) + \lambda_i C_i = \nabla \cdot \left[\left(\frac{\nu}{Sc} + \frac{\nu_t}{Sc_t} \right) \nabla C_i \right] + \beta_i \sum_g \bar{\nu}_g \Sigma_{f,g} \Phi_g. \quad (3.7b)$$

Here, φ and Φ are the angular and scalar fluxes, Σ_t and Σ_f are the total and fission macroscopic cross sections, while $\Sigma_s(\mathbf{\Omega}' \cdot \mathbf{\Omega})$ is the scattering differential cross section. $\bar{\nu}$ indicates the average number of neutrons emitted per fission event, χ is the fission spectrum (superscript p and d indicate the prompt and delayed spectra), $\mathbf{\Omega}$ is the neutron travel direction, while v is the neutron speed. Subscripts g and g' span all energy groups. C_i , β_i , and λ_i are the concentration, fraction, and decay constant of the i^{th} -family of delayed neutron precursors, and $\beta = \sum_i \beta_i$. In

Equation (3.7b), ν and ν_t are the molecular and turbulent kinematic viscosities, while Sc and Sc_t are the molecular and turbulent Schmidt numbers. Standard vacuum (i.e., zero incoming flux) or reflective boundary conditions typically close Equation (3.7a).

In case of steady-state calculations, System (3.7) is cast into a criticality eigenvalue problem, by removing the time derivative terms and dividing $\bar{\nu}$ by the

multiplication factor k_{eff} . The resulting flux is then normalized to the desired reactor power level.

When simulating long-term transient scenarios in nuclear reactors, it is paramount to take decay heat into account. In PHANTOM-S_N, we implemented transport equations to model the evolution of the fission products responsible for the decay heat. Following Aufiero et al. (2014b), the approach is very similar to what is done for the delayed neutron precursors. The decay heat fission products are divided into “families”, each one characterized by a decay constant λ_j^{dh} , and a fraction β_j^{dh} . The transport equation for family j reads

$$\frac{\partial d_j}{\partial t} + \nabla \cdot (\mathbf{u}d_j) + \lambda_j^{dh} d_j = \nabla \cdot \left[\left(\frac{\nu}{S_C} + \frac{\nu_t}{S_{C_t}} \right) \nabla d_j \right] + \beta_j^{dh} \sum_g E_{f,g} \Sigma_{f,g} \Phi_g, \quad (3.8)$$

where E_f is the average energy released by each fission event. This equation models the balance of d_j , the concentration of decay heat precursors in family j multiplied by the average energy released by that decay family. As the delayed neutron precursors, also the decay heat fission products are drifted by the flow in liquid-fueled systems, hence the presence of the convective and diffusive terms in (3.8).

When decay heat is modeled, the power density term to be passed to Equation (3.1a) becomes

$$P_{dens} = \left(1 - \sum_j \beta_j^{dh} \right) \sum_g E_{f,g} \Sigma_{f,g} \Phi_g + \sum_j \lambda_j^{dh} d_j. \quad (3.9)$$

3.2.2.1 Spatial and temporal discretizations and solution of the linear systems

After the expansion of the scattering term in a series of spherical harmonics, Equation (3.7a) is discretized in angle by the method of discrete ordinates, selecting directions and weights based on the level-symmetric quadrature set (Lewis and Miller, 1993). The DG-FEM is adopted for spatial discretization, upwinding the flux values in all face integrals of the weak formulation. This is a well established approach in the transport community (e.g., Reed and Hill, 1973; Wareing et al., 2001). Moreover, all the details of it have been reported by Kópházi and Lathouwers (2012), so they are not repeated here. Equations (3.7b) and (3.8) are discretized in space with the DG-FEM, adopting the same choices as in DGF_{lows} (see Section 3.2.1.1). Finally, in transient calculations, all time derivatives are discretized using the implicit BDF2 scheme (Equation (3.6)).

The coupled discrete System (3.7) can be cast into the following linear form:

$$\begin{bmatrix} A_{\varphi\varphi}^t - A_{\varphi\varphi}^f - A_{\varphi\varphi}^s & -A_{\varphi C} \\ -A_{C\varphi}^f & A_{CC}(\mathbf{u}^*) \end{bmatrix} \begin{bmatrix} \varphi \\ C \end{bmatrix}^{n+1} = \begin{bmatrix} b_\varphi \\ b_C \end{bmatrix}, \quad (3.10)$$

where $A_{\varphi\varphi}^t$, $A_{\varphi\varphi}^f$, and $A_{\varphi\varphi}^s$ represent respectively the discretization of the transport, fission, and scattering operators in Equation (3.7a); $A_{\varphi C}$ represents the delayed neutron precursors decay in Equation (3.7a), $A_{CC}(\mathbf{u}^*)$ the precursors time-derivative, convection, diffusion, and decay, and $A_{C\varphi}^f$ is the fission source term in Equation (3.7b). The right hand side vector collects the known terms deriving from the discretization of the time derivatives.

In steady-state calculations, System (3.10) is cast into the following eigenvalue problem:

$$\begin{bmatrix} A_{\varphi\varphi}^t - A_{\varphi\varphi}^s & -A_{\varphi C} \\ 0 & A_{CC}(\mathbf{u}^*) \end{bmatrix} \begin{bmatrix} \varphi \\ C \end{bmatrix} = \frac{1}{k_{eff}} \begin{bmatrix} A_{\varphi\varphi}^f & 0 \\ A_{C\varphi}^f & 0 \end{bmatrix} \begin{bmatrix} \varphi \\ C \end{bmatrix}, \quad (3.11)$$

which is solved with a standard power method approach (Golub and Van Loan, 2013).

Linear Systems (3.10) and (3.11) are solved by a flexible Krylov method (e.g., GCR), with a physics-based preconditioning approach, which depends on the type of problem. Let \mathbf{r} be the residual and \mathbf{z} the preconditioned residual vectors at iteration l of the outer Krylov method. For steady-state calculations, System (3.11) is preconditioned by a standard block Jacobi method:

$$\begin{bmatrix} A_{\varphi\varphi}^t - A_{\varphi\varphi}^s & 0 \\ 0 & A_{CC}(\mathbf{u}^*) \end{bmatrix} \begin{bmatrix} z_{\varphi} \\ z_C \end{bmatrix}^{l+1} = \begin{bmatrix} r_{\varphi} \\ r_C \end{bmatrix}^l. \quad (3.12)$$

This is a good enough preconditioner, taking into account that the contribution of the delayed precursors to the neutron transport equation is small, at steady-state. Moreover, System (3.11) is typically solved with large tolerances, in order to quickly move to the next iteration of the power method.

In transient calculations, on the other hand, System (3.10) must be solved with sufficient accuracy, but a standard block Gauss-Seidel method does not perform well, as the contribution of the precursors to Equation (3.7a) is essential. For this reason, we adopted an “improved” version of a block Gauss-Seidel preconditioner. As explained by Pautz and Birkhofer (2003), if the fuel were solid, one could easily diagonalize the time-discretized System (3.7) by inverting the left hand side of the precursors equation (thanks to the absence of convective and diffusive terms) and plugging C_i^{m+1} into Equation (3.7a). This would lead to an equation for φ_g only with a modified fission spectrum,

$$\tilde{\chi}_g = \chi_g^p(1 - \beta) + \chi_g^d \sum_i \lambda_i \omega_i \beta_i, \quad (3.13)$$

where $\omega_i = \left(\frac{\gamma_0}{\Delta t} + \lambda_i \right)^{-1}$, and an additional term to the right hand side:

$$- \chi_g^d \sum_{m=1}^2 \sum_i \lambda_i \omega_i \frac{\gamma_m}{\Delta t} C^{m+1-m}. \quad (3.14)$$

At preconditioner step, we modify the neutron transport equation in a similar fashion, as if the fuel were solid. In fact, we take a modified equation for the precursors' preconditioned residual:

$$\tilde{A}_{CC} z_C^{l+1} - A_{C\varphi}^f z_\varphi^{l+1} = r_C^l, \quad (3.15)$$

in which \tilde{A}_{CC} is an approximation of $A_{CC}(\mathbf{u}^*)$, without convection and diffusion terms. Hence, we easily invert it and plug z_C^{l+1} into the equation for z_φ^{l+1} . Therefore, the full preconditioner is

$$\begin{bmatrix} A_{\varphi\varphi}^t - A_{\varphi\varphi}^f - A_{\varphi\varphi}^s - A_{\varphi C} \tilde{A}_{CC}^{-1} A_{C\varphi}^f & 0 \\ -A_{C\varphi}^f & A_{CC}(\mathbf{u}^*) \end{bmatrix} \begin{bmatrix} z_\varphi \\ z_C \end{bmatrix}^{l+1} = \begin{bmatrix} r_\varphi + A_{\varphi C} \tilde{A}_{CC}^{-1} r_C \\ r_C \end{bmatrix}^l. \quad (3.16)$$

This is an improved Gauss-Seidel method, as it takes into account the contribution of the precursors in the flux equation (even if just approximately), thus leading to faster convergence of the outer Krylov method. This preconditioner is the more effective the smaller Δt , as $\lim_{\Delta t \rightarrow 0} A_{CC}(\mathbf{u}^*) = \tilde{A}_{CC}$ (and, of course, the lower is the salt flow rate). To conclude, it is worth to underline that the flexibility of the outer Krylov method is fundamental for convergence, given the variability of the described preconditioners at each iteration.

Independently from the chosen preconditioner, the multi-group flux subsystem is solved with Gauss-Seidel iterations. Each group fixed-source problem is in turn solved as proposed by Warsa et al. (2004), that is, by applying a Krylov method preconditioned with a directional sweep procedure that inverts the group transport operator. Then, as the molten salt is a highly scattering medium, we apply a Diffusion Synthetic Acceleration preconditioner as well. Our DSA scheme is partially consistent and based on an SIP-DG discretization of the diffusion-like equation (Wang and Ragusa, 2010). A more detailed description of the solution technique for the multi-group problem can be found in Kópházi and Lathouwers (2012). Precursors subsystems (as well as the decay heat precursors systems) are solved with GMRES and ILU preconditioner implemented in PETSc. Finally, as in DGFloWS, all solvers are initialized with a second-order time extrapolated solution in transient calculations, to speed-up convergence.

3.2.3 Coupling Strategy and Cross Sections Treatment

Figure 3.1 displays the structure of the multi-physics tool and the data exchanged between the codes. The fission power density is transferred to DGFloWS as it appears on the right hand side of the energy equation. Velocity and turbulent viscosity fields influence the precursors distribution, so they follow the inverse route. Moreover, DGFloWS computes an average temperature on each element (\bar{T}_E) and exports it to the routines in PHANTOM-S_N devoted to the computation of cross sections. Based on these temperatures, cross sections are interpolated starting from a set of

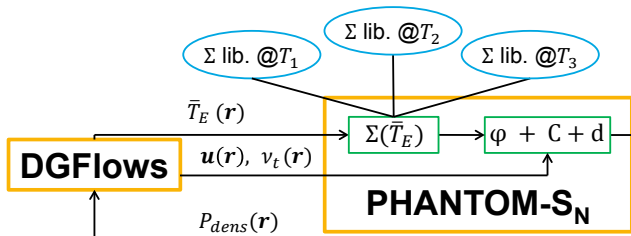


Fig. 3.1. Computational scheme of the multi-physics tool. `DGFlows`, the CFD solver, and `PHANTOM-SN`, the neutron transport code, exchange data at each iteration to resolve the coupling between the various physical phenomena characterizing a molten salt fast reactor.

libraries at prescribed temperatures, generated by Monte Carlo or deterministic codes. In case only a single library is prescribed (as for the calculations reported in this work), cross sections are corrected by assuming a linear dependence on the fuel density and a logarithmic dependence on the temperature to model Doppler feedback (Waltar et al., 2012; Aufiero et al., 2014b):

$$\Sigma_r(T) = \left[\Sigma_r(T_0) + \alpha_r \ln \left(\frac{T}{T_0} \right) \right] \frac{\rho(T)}{\rho_{ref}}, \quad (3.17)$$

where T_0 is the library reference temperature, ρ_{ref} is the reference density at which macroscopic cross sections are evaluated¹, and α_r is a coefficient.

In transient simulations, a loose-coupling strategy is adopted, where `DGFlows` is run first and, after completion of a time-step, `PHANTOM-SN` is called to handle the neutronics physics. In order to have a nonlinear-consistent coupling scheme (Ragusa and Mahadevan, 2009), thus preserving a global second order time accuracy, the power density passed to `DGFlows` at the beginning of a new time step is extrapolated using a second order scheme from the values at the previous time steps. In steady-state simulations, the codes are iterated until convergence.

3.2.4 Mesh generation and manipulation

Both codes can handle structured and unstructured meshes with tetrahedral or hexahedral elements (triangles or quadrangles in 2D), generated with the open source tool `Gmsh` (Geuzaine and Remacle, 2009). Starting from the same “master” mesh, each code independently can perform a local, hierarchical refinement. However, in practice the neutronics mesh corresponds to the master mesh, while `DGFlows` refines it (even more than once) in regions where the flow gradients have

¹For convenience, it corresponds to the reference density chosen for the Boussinesq approximation.

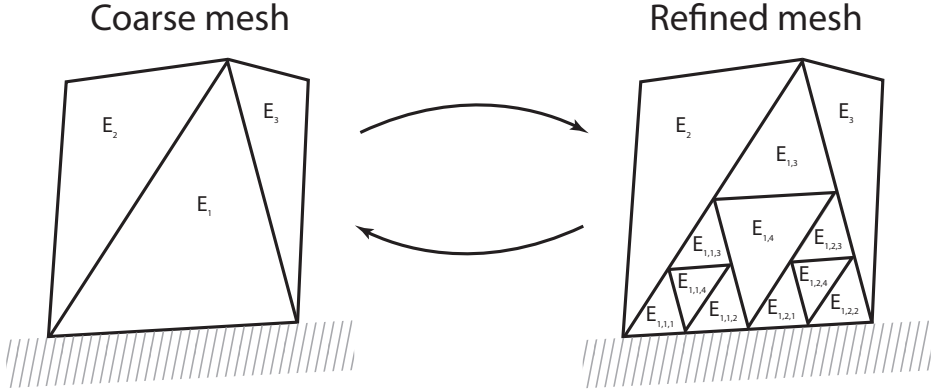


Fig. 3.2. Illustration of the hierarchic refinement of a triangular master mesh. Element E_1 is refined twice. Galerkin projection procedures are used to map quantities between the two meshes.

to be resolved but the neutron importance is low (e.g., close to walls, or in portions of the fuel circuit far from the core cavity). Figure 3.2 illustrates the hierarchic refinement on a simple triangular mesh².

The hierarchy of the refinement makes the exchange of data between the two meshes easy, exploiting Galerkin projection routines. Let E_R be an element on the refined mesh and E_C the corresponding mother on the coarse mesh; let also ζ^C and ζ^R be the vectors of coefficients of the DG-FEM expansion for quantity ζ on E_C and E_R , respectively. The coarse-to-refined mapping is performed as follows:

For each element of the refined mesh,

1. if E_R is equal to E_C (i.e., there is no actual refinement), then $\zeta^R = \zeta^C$; otherwise:
2. compute the quadrature points (ξ^R) and weights (w^R) on E_R and map them onto E_C ;
3. compute the FEM mass matrix on E_R (M_R), and solve the following linear system:

$$M^R \zeta^R = b^R(\zeta^C), \quad (3.18)$$

where the right hand side vector is evaluated by

$$b_i^R(\zeta^C) = \sum_q \sum_k \zeta_k^C \theta_k^C(\xi_q^{R \rightarrow C}) \theta_i^R(\xi_q^R) w_q^R. \quad (3.19)$$

²The hierarchic refinement leads to 4 children in case of 2D elements (both triangles and quadrangles), whereas it leads to 8 children in case of tetrahedra or hexaedra.

Here, θ^R and θ^C indicate the basis functions on E_R and E_C , while $\xi^{R \rightarrow C}$ the mapped quadrature point; index q spans all the quadrature points, and indices i and k span the degrees of freedom on E_R and E_C respectively.

This mapping is exact. The refined-to-coarse mapping is performed as follows:

For each element of the coarse mesh, do

1. if E_C is equal to E_R , then $\zeta^C = \zeta^R$; otherwise:
2. compute the FEM mass matrix on E_C (M_C)
3. initialize $\zeta^C = 0$. Then, for each child element on the refined mesh,
 - a) compute the quadrature points and weights on E_R and map them onto E_C ;
 - b) solve the linear system

$$M^C \zeta^C = b^C(\zeta^R), \quad (3.20)$$

with the right hand side vector evaluated by

$$b_i^C(\zeta^R) = \sum_q \sum_k \zeta_k^R \theta_k^R(\xi_q^R) \theta_i^C(\xi_q^{R \rightarrow C}) w_q^R. \quad (3.21)$$

Here, indices i and k span the degrees of freedom on E_C and E_R respectively, while q spans all quadrature points on E_R ;

- c) $\zeta^C = \zeta^C + \zeta^C$.

This mapping inevitably leads to loss of information. This has no significant impact when transferring the eddy viscosity field to the neutronics mesh. However, the loss of accuracy on the velocity field is detrimental for the precursors solution, because the velocity field no longer satisfies the divergence-free constraint in a discrete sense on the neutronics mesh. For this reason, in PHANTOM- S_N the velocity field is not mapped to the neutronics mesh when discretizing the convection integrals in the weak form of Equations (3.7b) and (3.8). Instead, each integral on an element of the neutronics mesh is computed as the sum of the integrals on the corresponding children elements of the CFD mesh. The velocity is computed at quadrature points on the latter, so that no loss of accuracy is introduced. The same technique is also used to compute the average temperature on each element of the neutronics mesh, without loss of information.

3.2.5 Verification and validation

Activities to validate and verify the single-physics codes were carried out in previous works (Kópházi and Lathouwers, 2012; Hennink et al., 2020).

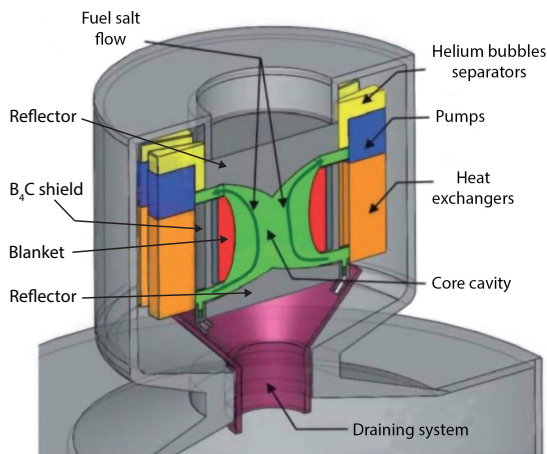


Fig. 3.3. Schematic view of the MSFR fuel circuit.

Recently, the coupled-code took part in a benchmarking campaign for multi-physics simulation tools dedicated to liquid-fuel fast reactors, whose results were published in Tiberghien et al. (2020a)³. The system under investigation consisted of a molten salt reactor whose characteristics make it a simple representation of the MSFR. Several steady-state or transient problems were simulated, in which physics phenomena were progressively coupled to easily identify potential sources of error. We compared our results with those obtained by other partners of the SAMOFAR project. The very good agreement proved our code can correctly reproduce and model the unique physics phenomena characterizing fast-spectrum MSRs both at steady-state and during transients.

3.3 The MSFR: design and modeling approach

In this section, we describe the MSFR design under investigation and the modeling choices for the simulations reported in Section 3.4.

3.3.1 Design description

The current MSFR concept (Allibert et al., 2016; Gérardin et al., 2017) is a non-moderated reactor operating in the thorium fuel cycle. The molten salt mixture acts both as fuel and thermal carrier, and it is characterized by a strong negative temperature feedback coefficient (Brovchenko et al., 2013; Heuer et al., 2014) that increases the reactor safety and makes the presence of control rods in the core cavity unnecessary.

³It is the subject of Chapter 4.

Table 3.2. Main MSFR design parameters considered in the present study (Allibert et al., 2016; Gérardin et al., 2017).

Parameter	Symbol	Unit	Value
Total thermal power	P	MW	3000
Total salt volume (in-core percentage)	V	m ³	18 (50%)
Fuel circulation time	t_{circ}	s	4
Average fuel salt temperature	T_{avg}	K	973.15
Minimum fuel salt temperature	T_{min}	K	923.15
Average intermediate salt temperature	T_{int}	K	908.15
Pressure drop across heat exchanger	Δp	bar	4.5
Fuel salt composition	–	% mol	LiF(77.5)-ThF ₄ (6.6)- ^{enr} UF ₄ (12.3)-(Pu-MA)F ₃ (3.6)
Blanket salt composition	–	% mol	LiF(77.5)-ThF ₄ (22.5)

Figure 3.3 schematically displays a cross section of the fuel circuit design. The molten salt enters the core cavity at the bottom, rises, and then flows out towards sixteen identical loops called *sectors*. Each sector is equipped with a pump and a heat exchanger, where the fuel salt releases heat to an intermediate circuit. Both pump and heat exchanger designs are not fully specified at the moment, though a preliminary analysis of a Printed Circuit Heat exchanger (PCHE) was carried out during the SAMOFAR project (Di Ronco et al., 2019). Dispersion of helium bubbles in the salt mixture is foreseen to remove gaseous and metallic fission products and as potential reactivity control mechanism (Delpech et al., 2009).

The toroidal core shape is the result of optimization studies carried out during the EVOL project and aimed at homogenizing the fuel temperature in the core cavity thus eliminating large hot spot regions (Rouch et al., 2014). The central torus is surrounded by a blanket, containing a fertile mixture of lithium and thorium fluorides, which improves the reactor’s breeding capabilities. Nickel-based alloy reflectors are present at the top and bottom of the core to improve neutron economy. The gap between the blanket and the external sectors is filled with a boron-carbide shield (Heuer et al., 2014). Table 3.2 reports the MSFR design parameters relevant for this study.

3.3.2 Modeling approach

3.3.2.1 Geometry and mesh

Figure 3.4 shows the MSFR geometry used in this work. Given the symmetry of the problem, only a single recirculation loop was simulated, in order to reduce the computational burden. Moreover, heat transfer in reflectors and blanket was not modeled. However, these regions are included in our neutron transport calculations.

Two sets of meshes were generated, to study the variation of the main results upon refinement:

- Set “M1” The same master mesh is used for both neutronics and CFD calculations. It has 68001 tetrahedra, of which 60468 within the boundaries of the

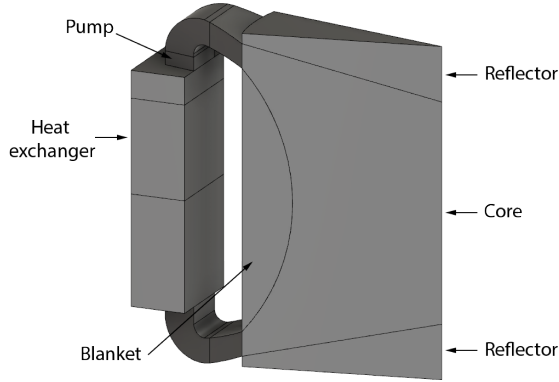


Fig. 3.4. MSFR geometry used for simulations: only $1/16^{th}$ of the core was modeled, with the associated sector.

fuel salt domain. The two meshes are shown in Figure 3.5;

Set “M2” A master mesh having 28574 tetrahedra (23032 in the fuel salt domain) is used for neutronics. This mesh is finer than *M1* in the core, but much coarser in the external sector, where neutron importance is low, thus optimizing neutronics calculations from a computational point of view. For this reason, the master mesh is refined for CFD calculations: once, uniformly in the outer-core region (i.e., legs, pump, and heat exchanger), and then once more close to the wall boundaries, to better resolve the boundary layers, resulting into 189464 elements. The two meshes are shown in Figure 3.6;

3.3.2.2 Pump modeling

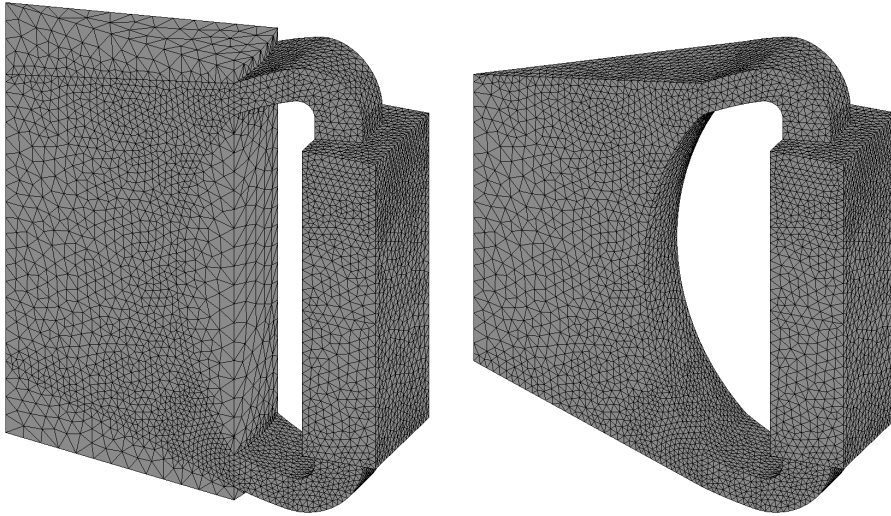
The MSFR pump design has not been defined yet. For this reason, it was modeled as a simple momentum source:

$$\mathbf{F}_{pump} = -(\Delta p_{pump}/H_{pump}) \hat{\mathbf{e}}_z, \quad (3.22)$$

where $H_{pump} = 0.1$ m is the height of the portion of the outlet leg identified with the pump (see Figure 3.4), Δp_{pump} is a parameter suitably tuned to obtain the desired volumetric flow rate of $4.5 \text{ m}^3 \text{ s}^{-1}$, and $\hat{\mathbf{e}}_z$ is the unit vector indicating the direction of the z -axis.

3.3.2.3 Heat exchanger modeling

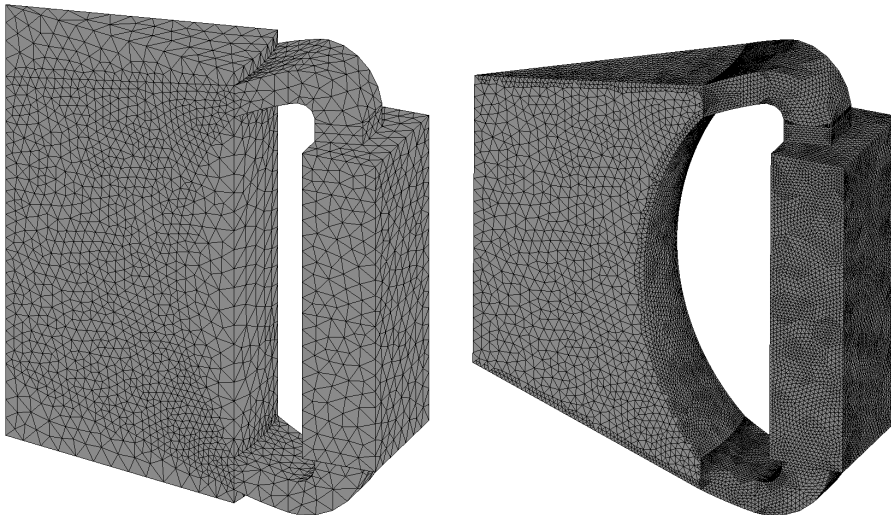
The heat exchanger was modeled through a porous medium approach. In fact, a detailed CFD simulation of the component would be unfeasible, from a computational



(a) *M1* mesh: neutronics

(b) *M1* mesh: CFD

Fig. 3.5. *M1* mesh set. The neutronics mesh (left) has 68001 tetrahedra, while the CFD mesh (right) has 60468 elements. The CFD mesh presents no local refinement with respect to the neutronics one.



(a) *M2* mesh: neutronics

(b) *M2* mesh: CFD

Fig. 3.6. *M2* mesh set. The neutronics mesh (left) has 28574 tetrahedra, while the CFD mesh (right) has 189464 elements. The latter is derived from the former by refining it once uniformly in the outer-core region, then again close to all wall boundaries.

point of view; moreover, its design has not been finalized yet. However, based on preliminary studies during SAMOFAR (Di Ronco et al., 2019), we considered only a portion of the sector “box” to be active (Figure 3.4), 0.69 m long. Resistance to flow was reproduced by the following force:

$$\mathbf{F}_{hx} = -\frac{1}{2}K_{loss} |\mathbf{u}| \mathbf{m}, \quad (3.23)$$

where K_{loss} is a loss coefficient suitably tuned to obtain the desired pressure drop of 4.5 bar.

Salt cooling was modeled via a volumetric heat sink term:

$$S_{hx} = \gamma (T_{int} - T(\mathbf{r})), \quad (3.24)$$

where γ is a volumetric heat transfer coefficient suitably tuned in order to achieve the target minimum salt temperature in the system of 650 °C. This coefficient does not depend on the salt velocity, because the small size of the channels of the PCHE limits the salt flow to laminar conditions, thus leading to a constant Nusselt number (Di Ronco et al., 2019).

3.3.2.4 Salt physical properties

Two fuel salt compositions are currently being investigated for the MSFR (Allibert et al., 2016; Gérardin et al., 2017). In this work, as reported in Table 3.2, we opted for the TRU-based composition, due to the availability of values and equations of state for the physical properties. These are reported in Table 3.3. Moreover, we considered a turbulent Prandtl number of 0.85, and, in absence of detailed data on the diffusion of species in the salt mixture, we assumed a turbulent Schmidt number of 0.85 (Aufiero et al., 2014b).

Table 3.3. Fuel salt properties (TRU-based composition) (Beneš et al., 2013).

Property	Symbol	Unit	Value/Equation of state
Density	ρ	kg m ⁻³	4306.7 (*)
Thermal expansion coefficient	β_{buoy}	K ⁻¹	1.9119 × 10 ⁻⁴ (*)
Dynamic viscosity	μ	Pa s	6.187 × 10 ⁻⁴ exp(772.2/(T(K) - 765.2))
Specific heat capacity	c_p	J kg ⁻¹ K ⁻¹	1594
Thermal conductivity	κ	W m ⁻¹ K ⁻¹	1.7
Melting point	T_{melt}	K	854.15

(*) Values evaluated at the Boussinesq reference temperature $T_{ref} = 973.15$ K from the equation of state $\rho(T) = 5108 - 0.8234 T$.

Table 3.4. Energy group structure used for the MSFR neutronics calculations.

Group, g	Upper energy bound (MeV)
1	2.000×10^1
2	2.231×10^0
3	4.979×10^{-1}
4	2.479×10^{-2}
5	5.531×10^{-3}
6	7.485×10^{-4}

Table 3.5. Fraction and decay constant for each family of delayed neutron precursors.

Family, i	β_i (-)	λ_i (s^{-1})
1	2.33102×10^{-4}	1.24667×10^{-2}
2	1.03262×10^{-3}	2.82917×10^{-2}
3	6.81878×10^{-4}	4.25244×10^{-2}
4	1.37726×10^{-3}	1.33042×10^{-1}
5	2.14493×10^{-3}	2.92467×10^{-1}
6	6.40917×10^{-4}	6.66488×10^{-1}
7	6.05805×10^{-4}	1.63478×10^0
8	1.66016×10^{-4}	3.55460×10^0

3.3.2.5 Neutronics data

A set of six-groups condensed neutronics data was used, evaluated at temperature $T_0 = 900$ K with Serpent (Leppänen et al., 2015), selecting the JEFF-3.1.1 nuclear data library (Santamarina et al., 2009). The energy group structure is reported in Table 3.4. Despite the few groups, this structure proved to be sufficient to reproduce the overall MSFR spectrum and the relevant neutronics parameters when compared to Monte Carlo calculations (Fiorina et al., 2012). The coefficients α_r in Equation (3.17) were evaluated by logarithmic interpolation of Serpent cross sections between 900 K and 1200 K.

Eight families of delayed neutron precursors were modeled. Their fractions and decay constants, taken from the JEFF-3.1.1 library, are reported in Table 3.5. Decay heat was modeled through Equation (3.8), taking into account three families of precursors. As shown by Aufiero et al. (2014b), the superposition of three exponentially decaying terms is an acceptable approximation for transients limited to a few minutes, as the one described in Section 3.4.2. The considered decay heat precursors fractions and time constants are reported in Table 3.6.

3.3.2.6 Boundary conditions

Boundary conditions for CFD calculations included symmetry conditions at the wedge sides and standard logarithmic wall-functions plus adiabatic conditions at all walls. Neglecting the heat transfer with reflectors, blanket, and external environment is an acceptable approximation and is conservative (Rouch et al., 2014).

For neutronics, reflective boundary conditions were imposed at the wedge sides and vacuum conditions everywhere else. Surfaces delimiting the gap between blanket and heat exchanger can be reasonably assumed to be facing void, given the presence of the boron-carbide layer (a strong neutron absorber). The convective and diffusive terms in Equations (3.7b) and (3.8) were included only in the mesh portion corresponding to the fuel salt domain. Hence, homogeneous Neumann and no-inflow conditions were imposed at all walls.

3.4 Results of preliminary MSFR simulations

In this section, as an example of the capabilities of our code-system, we report and discuss the results of preliminary simulations aimed at investigating the steady-state and transient behavior of the MSFR.

All simulations were run adopting a polynomial approximation of order $\mathcal{P} = 2$ for the mass flux and $\mathcal{P} = 1$ for all other quantities. Order $N = 4$ was chosen for the discrete-ordinates discretization, and the scattering anisotropy was taken into account up to first order. To investigate the effect of mesh refinement, we report the results obtained on both meshes described in Section 3.3.2.1. Transient calculations were run choosing a coupling time step size $\Delta t = 0.025$ s on the *M1* mesh and of $\Delta t = 0.01$ s on the finer one; to keep the CFL number in CFD calculations sufficiently small and avoid numerical instabilities, sub-steps were performed in *DGFlows*: 10 on the *M1* mesh, and 20 on the *M2* mesh.

3.4.1 Steady-state solution

As explained in Section 3.2.3, the steady-state solution was sought by iterating *PHANTOM-S_N* and *DGFlows* until convergence, and adjusting the pump head, the friction factor and the heat transfer coefficient in the heat exchanger to obtain the desired design specifications reported in Table 3.2. The final values of these parameters are reported in Table 3.7.

Table 3.6. Fraction and decay constant for each family of decay heat precursors.

Family, j	β_j^{dh} (-)	λ_j^{dh} (s ⁻¹)
1	1.170×10^{-2}	1.973×10^{-1}
2	1.290×10^{-2}	1.680×10^{-2}
3	1.860×10^{-2}	3.580×10^{-4}

3. Neutronics and thermal-hydraulics coupled solver

Table 3.7. Value of the parameters describing pump and heat exchanger used to obtain the steady-state solution on the two meshes.

Parameter (unit)	Value on <i>M1</i>	Value on <i>M2</i>
Δp_{pump} (Pa)	5.513×10^5	5.518×10^5
K_{loss} (-)	2.811×10^2	2.811×10^2
γ ($\text{W m}^{-3} \text{K}^{-1}$)	1.995×10^7	1.995×10^7

Table 3.8. Interesting design parameters evaluated from the steady-state solution. Results obtained on both meshes are reported for comparison. The largest error is 0.3% and characterizes the maximum temperature.

Quantity	Symbol	Unit	Results <i>M1</i>	Results <i>M2</i>
Temperature difference across heat exchanger	ΔT_{hx}	K	89.2	89.3
Average temperature	T_{avg}	K	965.9	966.1
Maximum temperature	T_{max}	K	1084.4	1087.3
Effective multiplication factor	k_{eff}	-	1.00998	1.00994

Table 3.9. History per coupling iteration of the design parameters of interest evaluated on mesh *M2*. Four iterations were sufficient to reach convergence.

Iteration	ΔT_{hx} (K)	T_{avg} (K)	T_{max} (K)	k_{eff} (-)
1	89.9	965.8	1093.2	1.01293
2	89.2	966.1	1087.2	1.00995
3	89.3	966.1	1087.3	1.00994
4	89.3	966.1	1087.3	1.00994

Table 3.8 reports some design parameters of interest derived from the steady-state solution (comparing them on meshes *M1* and *M2*). Table 3.9 reports the history per coupling iteration of the same parameters evaluated on *M2*. As the initial step is a k_{eff} calculation with static and isothermal fuel conditions, the non-linearities related to thermal feedback and precursors motion are resolved mostly in the second iteration. Four iterations in total were sufficient to reach convergence.

Figure 3.7 shows the power density and temperature fields obtained on meshes *M1* and *M2*. The power density (Figure 3.7a) has the expected shape: almost a cosine in the axial direction and a Bessel J_0 function in the radial one, deformed by the non-uniform temperature field and the presence of reflectors and blanket. This is confirmed by the axial and radial power profiles shown in Figure 3.8. As expected, the power quickly drops in the legs and heat exchanger but it does not reach zero, due to the distribution of the fission products which decay and release heat throughout the domain. Contrary to solid-fueled reactors, these large

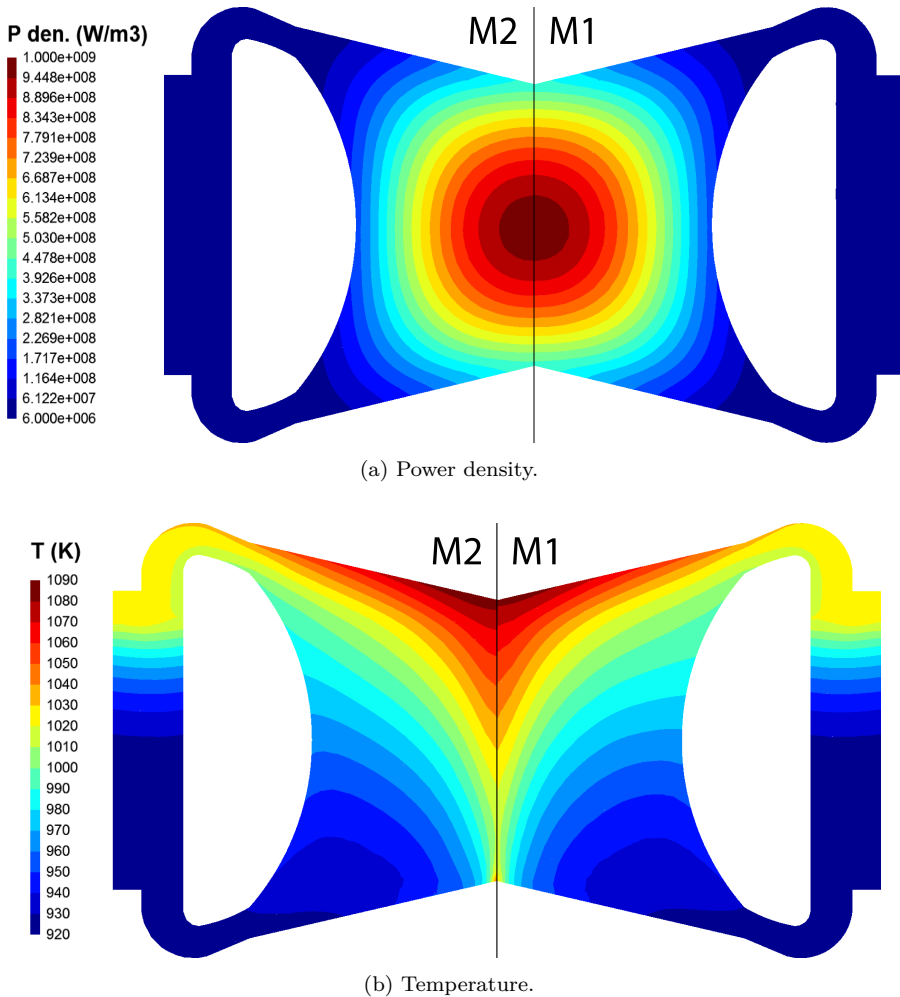


Fig. 3.7. Power density (left) and temperature fields (right) obtained at steady-state with the two meshes (mid-plane cuts). Only small differences in the fields can be noticed between the two meshes, confirming the good convergence of the results.

power gradients are not a concern in the MSFR, thanks to a homogeneous fuel irradiation ensured by recirculation and the absence of safety criteria limiting the power shape to preserve the integrity of the solid fuel pins. Actually, these gradients are beneficial, as they lead to lower radiation-induced damage on the core vessel. From Figure 3.7a, no relevant differences can be observed between the two meshes. The k_{eff} reported in Table 3.8 indicates the reactor is quite far from criticality, so the concentration of fissile material should be adjusted. However,

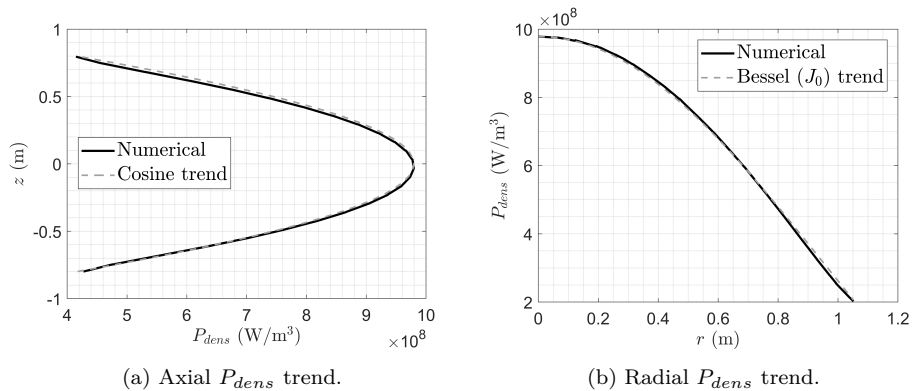


Fig. 3.8. Power density trends (on the $M2$ mesh): along the core axis (left) and radial at the reactor mid-plane (right), compared with the expected analytical trends. Coordinate zero corresponds to the reactor center.

a criticality search was not in the scope of the present study. The difference in reactivity between the two meshes is less than 4 pcm.

The salt temperature increases in the core cavity, but not uniformly. From Figure 3.7b, one can see that the salt is the hottest at the center of the core cavity, at the boundary with the upper reflector, where the fluid is almost stagnant. The upper reflector is in general subject to high temperatures and strong thermal gradients. On the contrary, there is no hot spot at the interface with the blanket, at core inlet, confirming the effectiveness of previous core-shape optimization studies (Rouch et al., 2014). The maximum salt temperature is around 70 K higher than the average temperature of the salt in the outlet leg. In the heat exchanger, as reported in Table 3.8, the temperature drops less than the reference 100 K (Allibert et al., 2016), due to a peak in the turbulent diffusivity, as explained in the following. The average salt temperature is around 700 °C, as expected.

From Figure 3.7b and Table 3.8, only minor discrepancies can be noticed in the results on the two meshes. Considering the solution on $M2$ as reference, the error on ΔT_{hx} and T_{avg} calculated on $M1$ is below 0.1%. The better boundary layer resolution on $M2$ leads to a T_{max} 3 K higher than on $M1$, but the difference is only 0.3% in relative terms.

Having proved the mesh-convergence of the results, we continue the analysis considering only the simulations on $M2$, which led to a better flow resolution. Figure 3.9 shows the velocity field in the domain. The salt Reynolds number is around 4.6×10^5 in the middle of the core cavity and 1.75×10^5 in the pump region. However, the salt velocity increases considerably (almost threefold) towards the outer leg, due to the significant reduction of cross section. The contribution of natural circulation to the total mass flow rate is negligible at nominal conditions,

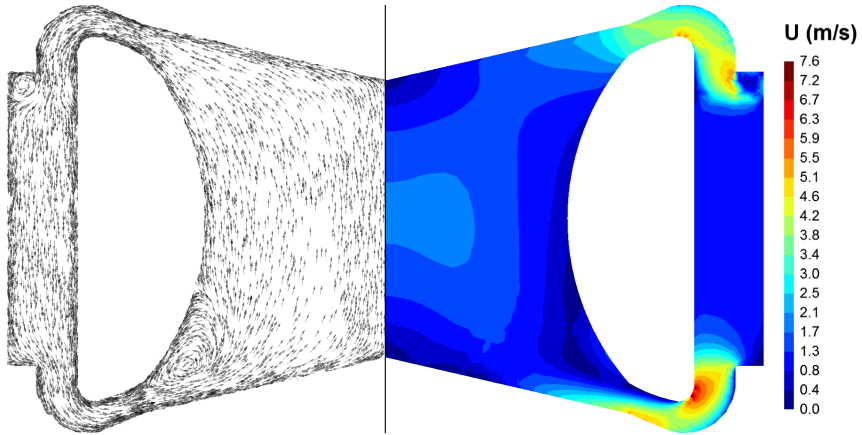


Fig. 3.9. Velocity obtained at steady-state with the $M2$ mesh (mid-plane cuts). The right portion of the figure reports the velocity magnitude, while arrows on the left represent the flow direction. One can clearly notice the large recirculation area at the entrance of the core.

due to the large pressure drop in the heat exchanger. At the core inlet, boundary layer detachment can be noticed, but this does not lead to local hot spots. Another detachment is present at the entrance of the heat exchanger “box”, due to the sudden expansion. However, the flow in this region is of less interest, given the simple and unrealistic geometry used to represent this portion of fuel circuit.

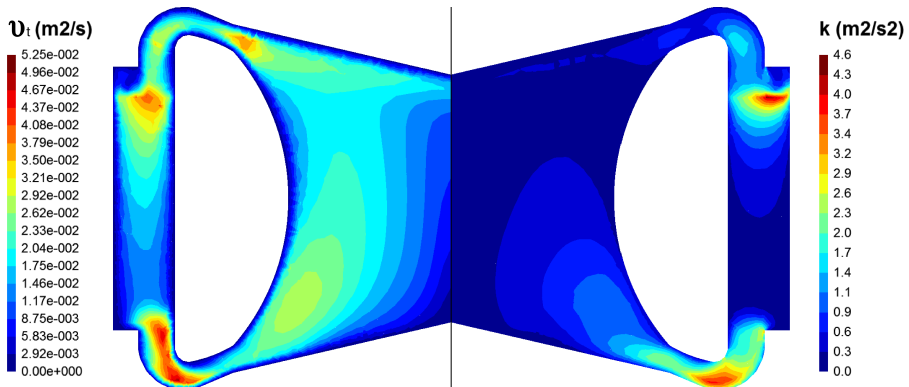


Fig. 3.10. Eddy viscosity (left) and turbulent kinetic energy (right) fields obtained at steady-state on the $M2$ mesh (mid-plane cuts). Turbulence is generated at the entrance of the core, due to the presence of a vortex, and at the core outlet. Salt thermal stratification suppresses turbulence in the core cavity.

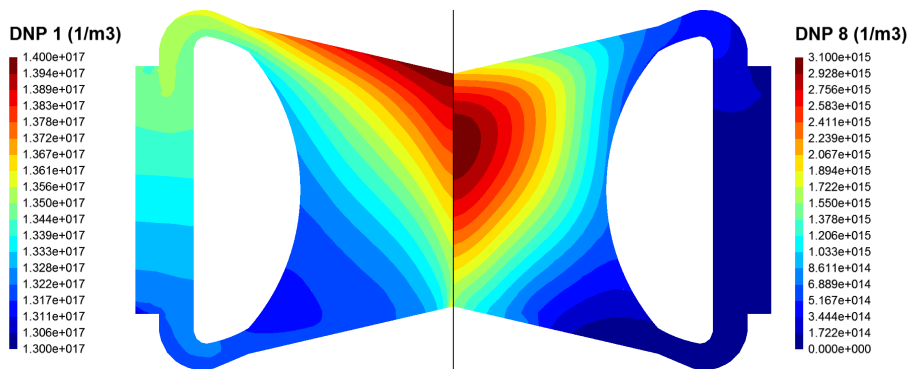


Fig. 3.11. Distribution of the first ($T_{1/2} = 55.6$ s, on the left) and the last ($T_{1/2} = 0.195$ s, on the right) family of delayed neutron precursors, obtained at steady-state with the $M2$ mesh (mid-plane cuts). The short-lived precursors decay mostly within the core cavity, contrary to the long-lived ones.

The large recirculation at the entrance of the core leads to a peak in the turbulent kinetic energy and diffusivity, as shown in Figure 3.10. The temperature distribution suppresses the salt turbulence while the salt rises through the core, but then turbulence increases again when the salt accelerates towards the outlet leg. The highest values of k and ν_t are found in the heat exchanger and inner leg regions, but, once more, these are of less interest. A more realistic design of the heat exchanger “box” would eliminate the large vortex at the entrance and thus the spike in turbulence production. This would also lead to a drop in the salt temperature across the heat exchanger closer to the reference 100 K.

To conclude the steady-state analysis, Figure 3.11 shows the distribution of the first delayed neutron precursors family on the left side and the one of the last family on the right. Both distributions are largely distorted by the flow field. However, the short-lived precursors manage to decay mostly within the core cavity, contrary to the long-lived ones, which can be found in high concentration in the heat exchanger region. This reduces the margin to prompt criticality (Aufiero et al., 2014a).

3.4.2 Transient: unprotected Total Loss of Power accident

As an example of transient scenario, to show the potential of our code package, we chose one of the most (potentially) severe accidents that can happen in the MSFR: the unprotected Total Loss of Power (TLOP). This accident could occur in case of total blackout; the absence of electricity would stop the pumps in the fuel, intermediate, and energy conversion circuits; moreover, the removal of the fission power from the core would become impossible.

In this work, the pump stop was modeled through an exponential decay of \mathbf{F}_{pump}

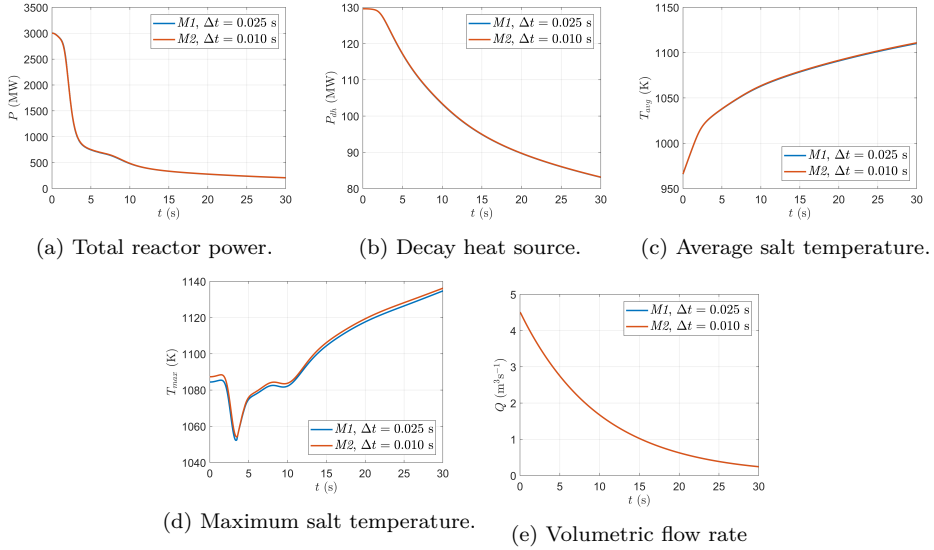


Fig. 3.12. Evolution of various characteristic quantities during the first 30s of a TLOP accident. Results for the two different meshes and associated time step sizes are reported. Differences are minimal.

in Equation (3.22), to take into account the pump inertia. In absence of precise design specifications, a time constant of 5 s was chosen. The intermediate and energy conversion circuits would continue, in reality, to remove some power from the fuel circuit, thanks to their thermal inertia; passive decay heat removal systems are foreseen as well and their design is under study; moreover, a non-negligible fraction of power would be exchanged with the external environment by passive heat transfer mechanisms, as conduction or radiative transfer. However, throughout this accident scenario, we conservatively assumed that no heat is removed from the heat exchanger (achieved by imposing $\gamma = 0$ in Equation (3.24)) and that the adiabatic boundary conditions described in Section 3.3.2.6 continue to hold. Considering one recirculation loop only is reasonable, as this accident affects all 16 loops in the same way. The initial condition is represented by the steady-state solution described in the previous section. Since the reactor is not critical at steady-state with the current salt composition, the fission operator was scaled by a factor $1/k_{eff}$.

Figure 3.12 shows the time trends of various characteristic quantities during the first 30s of the accident. Up to 1 s, the reactor power (Figure 3.12a) does not vary significantly, thanks to the precursors hold-back, but then it quickly drops to less than one-third after 4 s; at 5 s, the descent slows down, and the power reaches almost a plateau around 7 s; from roughly 8 s onward, finally, the power decreases

monotonically. At $t = 30$ s, the total power is reduced to 208.5 MW, 40 % of which is constituted by decay heat (see Figure 3.12b).

The plateau in the power trend around 7 s is due to a peculiar phenomenon of liquid-fueled reactors. In the first seconds of the transient, before the power drops, a certain amount of delayed neutron precursors exits the core. The long lived portion does not decay in the sector but only after it re-enters the core. This injects positive reactivity and slows down the power decay provoked by the increase in T_{avg} . The time scale at which this happens depends on the recirculation time. Here, it is longer than the nominal 4 s (Table 3.2) due to the reduction in the mass flow rate, as can be seen in Figure 3.12e. The flow rate decay is exponential, with a time constant of around 10 s, as expected. In fact, the momentum forces in the loop are roughly proportional to the square of the flow rate (see, e.g., Equation (3.23)).

Figures 3.12c and 3.12d show the evolution of the salt average and maximum temperature, respectively. T_{avg} can only increase in time, due to the absence of any heat exchange with the external environment. A quick rise of 50 K in the first 2.5 s is followed by a milder temperature increase, due to the drop in the total power. The maximum salt temperature has a more interesting trend. A first slight increase, due to the increased power-to-flow ratio, is followed by a drop of 30 K, due to the abrupt power drop and a first partial homogenization of the temperature in the core cavity, determined by the still quite high turbulent diffusivity. Then, T_{max} rises again, due to the plateau in the power around 7 s. The same pattern is repeated in the range 8–10 s, after the power starts to decrease again. After 20 s, both T_{avg} and T_{max} rise at a similar rate (1.68 K s^{-1} for the former and 1.63 K s^{-1} for the latter), almost constant, due to the almost constant residual power in the system. With these heating-up rates, the grace time before the salt reaches the critical temperature of 1200 °C, at which the reactor incurs structural damage, lies between 235 s and 250 s (evaluated considering T_{max} and T_{avg} , respectively). This is half the grace time of 480 s estimated by Brovchenko et al. (2013). Considering the temperature increase rate as constant is too conservative in this case, so longer simulations are necessary to better estimate this important safety parameter. In fact, the grace time strongly influences the design of safety devices such as the freeze-plugs (Tiberga et al., 2019b): passive valves of frozen fuel salt that should melt fast enough to allow for the salt draining in large tanks underneath the core (see Figure 3.3), to avoid structural damage.

No relevant differences can be noticed between the two meshes and the two time-step sizes, proving the space-time convergence of the results. The differences in the T_{max} trend are to be prescribed to the higher boundary layer resolution of $M2$, as explained in the previous section, and are always limited to less than 0.3 %.

Finally, Figure 3.13 shows snapshots of the temperature distribution in the fuel circuit at different times. As time passes, the salt temperature rises and homogenizes, due to the reduction of the power density and the mass flow rate (the difference $T_{max} - T_{avg}$ is reduced to around 25 K after 30 s). At $t = 2.5$ s one

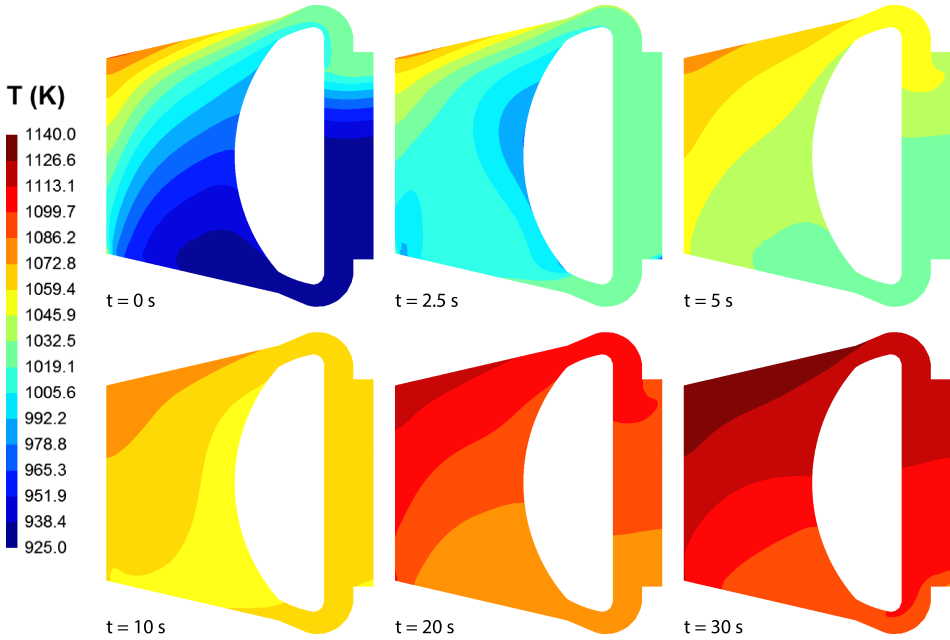


Fig. 3.13. Evolution of salt temperature distribution in the fuel circuit during the TLOP accident (on the $M2$ mesh).

can see that the maximum temperature in the top-left corner of the core cavity is lower than at $t = 0$, and that the temperature field is smoother.

3.5 Conclusions

In this work, we have presented a novel multi-physics tool for molten salt fast reactors developed at Delft University of Technology. The code couples an incompressible RANS/ $k - \epsilon$ model with a solver for the S_N multi-group neutron transport equation and the delayed neutron precursors equations. Decay heat is modeled as well through a set of balance equations that take the drift of the fission products into account. The models are implemented in two in-house codes, based on the discontinuous Galerkin Finite Element method for spatial discretization of the model equations. Second-order implicit schemes are adopted for time discretization. This guarantees high accuracy of simulations. The codes are iterated until convergence in steady-state simulations, while a loose-coupling strategy is adopted during transients. The quantities exchanged between the codes are properly time extrapolated, thus preserving its global second order time accuracy.

To show the capabilities of our multi-physics tool, we have reported the results of preliminary simulations aimed at studying the Molten Salt Fast Reactor (MSFR)

at steady-state and during an unprotected Total Loss of Power (TLOP) accident, taking into account the most recent updates to the design brought in the framework of the H2020 SAMOFAR project.

The reactor steady-state conditions revealed that previous studies on the optimization of the core toroidal shape were effective in eliminating hot spots in the core cavity. However, a large recirculation region is still present at inlet, and this induces localized pressure drops and makes the flow less predictable in the core cavity. To avoid this, further improvements of the core design are necessary. Moreover, particular care has to be taken in designing the upper wall, which separates the core from the upper reflector. In fact, it is subject to high temperatures and large thermal gradients, which enhance corrosion effects and induce large mechanical stresses. Finally, the reference fuel composition should be adjusted, reducing the uranium enrichment, thus eliminating the reactivity excess of almost 1000 pcm found at steady-state.

During a TLOP accident, the reactor power quickly drops to less than one-third due to the strong negative temperature feedback coefficient, but after 30 s it is still at a few hundred MW, due to decay heat. Our code proved able to reproduce the temporarily injection of positive reactivity induced by the re-entrance in core of delayed neutron precursors, which is a peculiar feature of molten salt systems. No conclusions could be retrieved though in terms of grace time before the salt reaches the maximum allowed temperature. Longer simulations are required to analyze this aspect further. This, together with the assessment of the MSFR behavior during a broader spectrum of accidental scenarios is the subject of a future publication, which will also compare our results with those obtained by other partners of the SAMOFAR project.

CHAPTER 4

BENCHMARK OF THE MULTI-PHYSICS TOOL FOR FAST-SPECTRUM MSRs

Verification and validation of multi-physics codes dedicated to fast-spectrum molten salt reactors (MSR) is a very challenging task. Existing benchmarks are meant for single-physics codes, while experimental data for validation are absent. This is concerning, given the importance numerical simulations have in the development of fast MSR designs. A coupled numerical benchmark specifically designed to assess the physics-coupling capabilities of the aforementioned codes is described in this work. The benchmark focuses on the specific characteristics of fast MSRs and features a step-by-step approach, where physical phenomena are gradually coupled to easily identify sources of error. The results obtained during the benchmarking campaign of four multi-physics tools developed within the SAMOFAR project are collected and compared. Results show excellent agreement for all the steps of the benchmark.

This chapter has been adapted from M. Tiberger, R.G.G. de Oliveira, E. Cervi, J.A. Blanco, S. Lorenzi, M. Aufiero, D. Lathouwers, and P. Rubiolo. Results from a multi-physics numerical benchmark for codes dedicated to molten salt fast reactors, *Annals of Nuclear Energy*, **142**, 107428, 2020. <https://doi.org/10.1016/j.anucene.2020.107428>

4.1 Introduction

Interest in liquid-fuel nuclear reactor research has increased in the last decades (LeBlanc, 2010), especially after the Generation IV International Forum included the Molten Salt Reactor (MSR) in the list of the new generation reactors aiming at delivering a breakthrough in nuclear electricity production in terms of safety, sustainability, and proliferation resistance (Generation IV International Forum, 2002). The use of a molten salt both as fuel and coolant leads to unique physics phenomena in MSRs: internal heat generation in the coolant; thermal feedback induced by fuel expansion; transport of delayed neutron precursors; and, thus, stronger coupling between neutronics and thermal-hydraulics. These features are absent in traditional solid-fuel reactors, therefore classical codes used in the nuclear community are unsuitable for simulating MSRs behavior “as they are”. Even when some efforts have been made to provide these codes with the capabilities required by MSR modeling (e.g., Zanetti et al., 2015), the code structure (usually developed in the ’60s/’70s when strong computational capabilities were not available), along with the often strong modeling assumptions taken (e.g. a 1D modeling) make them unappealing for the study of MSR physics. In addition, the verification and validation campaign that makes these legacy codes suitable for the study of conventional reactors cannot be considered applicable to the study of MSRs due to the peculiar reactor characteristics.

As a consequence, several dedicated multi-physics tools (e.g., Kópházi et al., 2009; Aufiero et al., 2014b; Fiorina et al., 2014; Nagy et al., 2014; Qiu et al., 2016; Laureau et al., 2017; Aufiero et al., 2017; Hu et al., 2017; Lindsay et al., 2018; Cervi et al., 2019a; Tibergera et al., 2019a; Blanco et al., 2020) have been developed in the context of research projects related to molten salt reactors all around the world (e.g., Serp et al., 2014; Allibert et al., 2016; Dolan, 2017; Zhang et al., 2018) with the aim of performing high-fidelity numerical simulations to assess and optimize the investigated reactor designs.

A comprehensive verification and validation program is necessary in order to increase the confidence in these research codes and bring them close to the level of industrial ones. However, this is a very challenging task, especially when considering tools targeting non-moderated MSR designs, as the Molten Salt Fast Reactor (MSFR) (Allibert et al., 2016; Brovchenko et al., 2019). Validation is in fact not possible, as experimental data are available only as result of the operation of the Molten Salt Reactor Experiment (Haubenreich and Engel, 1970). This was a thermal reactor with graphite moderator and salt channels, characteristics which make it vastly different from the current fast MSR designs. Verification of single-physics codes can be achieved for many applications (see Ghia et al., 1982; Ethier and Steinman, 1994; Botella and Peyret, 1998; Pautz, 2001, for examples in the field of CFD and neutronics), but verification of multi-physics codes remains a difficult task (De Oliveira and Mikityuk, 2018), especially when the coupled problem is solved by iterating different solvers, each one addressing a specific set

of equations.

To help overcome the last issues, in this work we propose the use of a numerical benchmark for multi-physics tools dedicated to fast-spectrum molten salt reactors. It was originally developed at LPSC/CNRS-Grenoble (Aufiero, 2015; Laureau, 2015; Aufiero and Rubiolo, 2018), and for this it is referred to as “CNRS benchmark” in the following.

The CNRS benchmark is divided into several steps, in which stationary or transient simulations of an MSFR-like system are prescribed. The coupling between the various physics phenomena is gradually introduced, so that it is easy to assess the physics coupling capabilities of the codes, and to highlight possible sources of discrepancy and fix the underlying errors. In this perspective, complex phenomena to model as turbulence or Doppler feedback are also absent. Other results available in literature could be used as benchmark for multi-physics codes dedicated to MSRs. For example, Fiorina et al. (2014) and Brovchenko et al. (2019) reported code-to-code comparisons of MSFR steady and transient calculations performed during the Euratom FP7 EVOL project. However, the complexity of full-reactor calculations hinders the understanding of where possible discrepancies in the results stem from, whether only from specific modeling/data choices (cross section libraries, turbulence models, etc.) or real errors in the code packages. In this perspective, the test case presented here is a more powerful tool for benchmark purposes, especially when the assessed multi-physics code is at early stages of development.

In the CNRS benchmark, the fluid problem assumes the salt to be incompressible, but no prescription is given for the neutronics model, thus making this benchmark suitable to virtually any multi-physics tool developed for fast MSRs. This test case can even be useful to benchmark tools intended for thermal-spectrum MSRs, but no assessment of the capability of such codes to model the peculiar physics phenomena related to the moderator is possible.

The purpose of this work is threefold. First, we present for the first time a complete version of the CNRS benchmark. Then, we collect all results obtained during the benchmarking campaign of four multi-physics tools developed in the framework of the Horizon 2020 Euratom SAMOFAR project (<http://samofar.eu/>), and we compare them in order to assess the capability of the codes to correctly model the peculiar physics phenomena in a molten salt fast reactor. Finally, and most importantly, the results and the benchmark description itself are meant to be a useful tool for any other institution interested in testing its own multi-physics tool or in developing a new one. In this perspective, the coupled tools assessed here include both diffusion and transport codes, and both finite volume and finite element solvers, thus providing the interested reader with a broad spectrum of results to compare with.

The remainder of the chapter is organized as follows. In Section 4.2, a general description of the benchmark is provided and all the data useful to perform calculations are reported. In Section 4.3, the benchmark phases and steps are described in detail, together with the definition of the output quantities of interest.

Section 4.4 is devoted to a brief description of the code packages involved in the benchmark campaign and used to obtain the results collected and analyzed in Section 4.5. Finally, our conclusions are discussed in Section 4.6.

4.2 Description of the benchmark

4.2.1 General description

The multi-physics benchmark described in this work features a molten salt system whose characteristics (neutron spectrum, strong temperature feedback, salt composition, precursors movement) make it a simple representation of the MSFR. In order to assess the coupling capabilities of the multi-physics tools in a systematic way, facilitating the identification of possible sources of inconsistency in the results, the benchmark is structured into three *phases*, sub-divided into *steps*, with Phase 0 as single physics verification, Phase 1 as steady-state coupling, and Phase 2 as time dependent coupling.

The salt flow is considered to be incompressible and laminar, and buoyancy is modeled adopting the Boussinesq approximation. However, no prescription is given regarding the neutronics model. Sources of complexity as turbulence or 3D geometry are explicitly avoided, as these are features other benchmarks deal with. Decay heat is neglected as well. For these reasons, the benchmark is fairly general and suitable to virtually any multi-physics tool dedicated to MSRs, even at early stages of development.

4.2.2 Geometry and boundary conditions

Figure 4.1 shows the domain of the problem. It is a 2 m by 2 m cavity filled with molten salt at the initial temperature of 900 K. Point-wise comparison of the

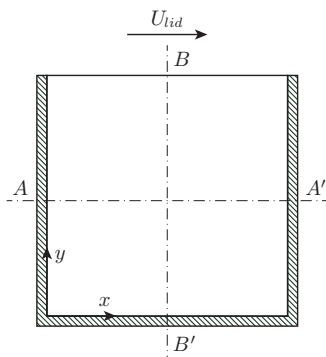


Fig. 4.1. CNRS benchmark: 2 m by 2 m domain. The cavity is insulated, surrounded by vacuum, and filled with molten salt at initial temperature of 900 K. Observables are compared pointwise along the centerlines AA' and BB' at several benchmark steps.

Table 4.1. Fuel salt composition.

Isotope	⁶ Li	⁷ Li	⁹ Be	¹⁹ F	²³⁵ U
Atomic fraction (%)	2.11488	26.0836	14.0992	56.3969	1.30545

observables in the different steps of the benchmark is performed along the cavity centerlines AA' and BB' .

The domain is treated as a homogeneous, bare reactor. Therefore, the standard vacuum conditions are applied for the neutron flux to each boundary, together with a homogeneous Neumann condition for the delayed neutron precursors. A no-slip boundary condition, with zero fluid velocity, is applied to all walls except the top lid, which moves at U_{lid} . All walls are adiabatic, and salt cooling is simulated with a volumetric heat sink¹:

$$q'''(\mathbf{r}) = \gamma(T_{ext} - T(\mathbf{r})), \quad (4.1)$$

where $T(\mathbf{r})$ is the salt temperature at point \mathbf{r} , $T_{ext} = 900$ K, and the volumetric heat transfer coefficient, γ , is uniform throughout the entire domain. All steady-state steps of the benchmark are criticality eigenvalue problems, in which the reactor power is normalized to the reference power, P .

4.2.3 Input data

The fuel salt is a LiF-BeF₂-UF₄, whose molar composition is reported in Table 4.1. Its fluid properties are considered constant with temperature and uniform in space. They are reported in Table 4.2. Composition and properties were optimized to highlight the impact of possible errors in physics coupling strategies. For example, the Schmidt number value is a trade off between two opposite needs: to limit mixing of delayed neutron precursors, thus magnifying the impact of the flow field on their distribution, and to cover the impact of the numerical diffusivity of a specific discretization scheme on the results.

Regarding nuclear data, the JEFF-3.1 library (Koning et al., 2006) at $T_{ref} = 900$ K is prescribed². Multi-group codes can work with neutronics data generated with Serpent (Leppänen et al., 2015) and condensed into six groups, using the spatial-homogenization and group-collapsing models described by Leppänen et al. (2016). The complete set of multi-group neutronics data are reported in Tiberga et al. (2020a) and, for brevity, are not repeated here. As the reactor system considered here has a similar spectrum to the one of the full MSFR, the same

¹Even if the domain is 2D, all quantities are reported with standard 3D units in this work, in order to improve clarity. For the same reason, the heat sink and the heat transfer coefficient are indicated as “volumetric”. For an exact unit match, one should consider the domain to have a depth of 1 m along a pseudo z -axis. However, this is irrelevant from the numerical point of view, since all quantities do not depend on z .

²For convenience, the same reference temperature is chosen for the Boussinesq approximation.

Table 4.2. Salt thermodynamic and transport properties.

Property	Units	Value
Density	kg m^{-3}	2.0×10^3
Kinematic viscosity	$\text{m}^2 \text{s}^{-1}$	2.5×10^{-2}
Volumetric heat capacity	$\text{J m}^{-3} \text{K}^{-1}$	6.15×10^6
Thermal expansion coefficient	K^{-1}	2.0×10^{-4}
Prandtl number	-	3.075×10^5
Schmidt number	-	2.0×10^8

Table 4.3. Definition of energy groups.

Group, g	Upper energy bound (MeV)
1	2.000×10^1
2	2.231×10^0
3	4.979×10^{-1}
4	2.479×10^{-2}
5	5.531×10^{-3}
6	7.485×10^{-4}

six energy groups used in previous works to model the MSFR were chosen. This energy-group structure, reported in Table 4.3, was tested in previous works (Fiorina et al., 2012, 2013) against ERANOS (using up to 1968 energy groups) and Serpent, and it proved capable of reproducing with sufficient accuracy the overall MSFR spectrum and relevant neutronics parameters.

In this benchmark, the Doppler effect on microscopic cross sections is negligible; this avoids biases arising from the differences in treatment of this complex effect by each code. Consequently, cross sections and diffusion coefficients are affected only by the salt-expansion feedback and scale with the temperature according to

$$\Sigma_r(T) = \Sigma_r(T_{ref}) \frac{\rho_{fuel}(T)}{\rho_{fuel}(T_{ref})}, \quad (4.2a)$$

$$D(T) = D(T_{ref}) \frac{\rho_{fuel}(T_{ref})}{\rho_{fuel}(T)}, \quad (4.2b)$$

where ρ_{fuel} is the fuel density. Finally, eight families of delayed neutron precursors are considered. Their decay constants and fractions are reported in Tiberga et al. (2020a) and are not repeated here for brevity.

4.3 Phases and steps of the benchmark

In this section, we describe each phase and step of the benchmark. Each step is schematically described in terms of goal, required input, and the output quantities of interest (the *observables*).

4.3.1 Phase 0: Single physics benchmark

In this phase, as a preliminary benchmark of the codes, steady-state simulations are carried out without any coupling between the different physics.

4.3.1.1 Step 0.1: Velocity field

The solution of steady-state incompressible flow is studied. This step is aimed at testing the capability of the codes to get a correct velocity field, which is mandatory to obtain consistent multi-physics coupling.

Input

- $U_{lid} = 0.5 \text{ m s}^{-1}$.

Observables

- Velocity components along centerlines AA' and BB' .

4.3.1.2 Step 0.2: Neutronics

The neutronics criticality eigenvalue problem is studied with static and isothermal fuel, given the single physics purpose of this phase. The aim is to verify the neutronics solutions of the codes in simple, static-fuel conditions. Before proceeding to further comparisons, agreement between codes must be verified for the fission source distribution and the estimation of the effective multiplication factor. Minor differences in the effective multiplication factor, k_{eff} , might arise from different neutronics models and approximations adopted and are considered acceptable considering the purpose of the benchmark. The reactor power, P , is set to normalize the neutron flux.

Input

- $T = 900 \text{ K}$; and
- $P = 1 \text{ GW}$.

Observables

- Fission rate density, $\int_E \Sigma_f \Phi dE$, along AA' ; and
- Reactivity, ρ .

4.3.1.3 Step 0.3: Temperature

The passive scalar transport capability of the codes is assessed independently from the solution of the fluid flow and the neutronics problems. The aim is to compare the temperature distributions obtained by the different codes, fixing the velocity field and the heat source distribution.

Input

- Fixed flow field from Step 0.1;
- Fixed heat source distribution from Step 0.2; and
- $\gamma = 1 \times 10^6 \text{ W m}^{-3} \text{ K}^{-1}$.

Observables

- Temperature distribution along centerlines AA' and BB' .

4.3.2 Phase 1: Steady-state coupling

In this phase, steady-state solutions are found gradually coupling the several physics phenomena characterizing the molten salt fast system.

4.3.2.1 Step 1.1: Circulating fuel

The criticality eigenvalue problem is solved in the presence of fuel motion, with a fixed velocity field and uniform fuel temperature. This step is aimed at assessing a correct evaluation of the effects of the fluid flow on neutronics. In particular, the consistency of reactivity loss due to fuel motion is verified.

Input

- Fixed flow field from Step 0.1;
- $T = 900 \text{ K}$; and
- $P = 1 \text{ GW}$.

Observables

- Delayed neutron source, $\sum_i \lambda_i C_i$, along AA' and BB' ; and
- Reactivity change from Step 0.2, $\rho - \rho_{s_{0.2}}$.

4.3.2.2 Step 1.2: Power coupling

The coupling between neutronics and thermal-hydraulics is investigated in the simple case of a fixed velocity field. The goal is to analyze the flux shape deformation caused by the non-uniform fuel temperature field and the effects of this deformation, in turn, on the temperature distribution. The capability of reproducing correctly this coupling, via the fuel density feedback, is assessed in this step.

Input

- Fixed flow field from Step 0.1;
- $P = 1$ GW; and
- $\gamma = 1 \times 10^6 \text{ W m}^{-3} \text{ K}^{-1}$.

Observables

- Temperature distribution along AA' and BB' ;
- Reactivity change from Step 1.1, $\rho - \rho_{s_{1.1}}$; and
- Change of fission rate density along AA' and BB' with respect to the solution obtained at Step 0.2, $\int_E \Sigma_f \Phi dE - \int_E \Sigma_{f,s_{0.2}} \Phi_{s_{0.2}} dE$.

4.3.2.3 Step 1.3: Buoyancy

The full multi-physics problem is analyzed in the easiest conditions, without an external source of momentum. The fuel flow is driven by buoyancy effects caused by the temperature gradients. The main objective is to test the codes' capability to predict the correct velocity field induced by the fission heat source and the correct reactivity introduction due to the movement of precursors. Discrepancies in the results of this step can be considered mainly related to buoyancy effects or to its modeling, as most of the multi-physics coupling issues for steady-state eigenvalue problems are studied in Step 1.1 and Step 1.2.

Input

- $P = 1 \text{ GW}$;
- $U_{lid} = 0$; and
- $\gamma = 1 \times 10^6 \text{ W m}^{-3} \text{ K}^{-1}$.

Observables

- Velocity components along AA' and BB' ;
- Temperature distribution along AA' and BB' ;
- Delayed neutron source along AA' and BB' ; and
- Reactivity change from Step 0.2, $\rho - \rho_{s_{0.2}}$.

4.3.2.4 Step 1.4: Full coupling

This step is thought as representative of realistic reactor simulations in terms of physical phenomena, because it involves the full solution of the multi-physics problem. All the phenomena analyzed separately in the previous steps are introduced here simultaneously: (i) external momentum source (i.e., non-null lid velocity); (ii) buoyancy effects; (iii) delayed neutron precursors motion; and (iv) flux deformation due to an asymmetric temperature distribution.

Input

- $\gamma = 1 \times 10^6 \text{ W m}^{-3} \text{ K}^{-1}$.
- P variable in the range $[0, 1] \text{ GW}$ with a step of 0.2 GW ; and
- U_{lid} variable in the range $[0, 0.5] \text{ m s}^{-1}$, with a step of 0.1 m s^{-1} .

Observables

- Reactivity change from Step 0.2, $\rho - \rho_{s_{0.2}}$, as a function of P and U_{lid} .

4.3.3 Phase 2: Time dependent coupling

The transient behavior of the reactor is simulated in this last phase, taking into account the full coupling between the physics phenomena.

4.3.3.1 Step 2.1: Forced convection transient

In order to perform a general assessment, no standard transient is simulated (e.g., reactivity insertion, loss of heat sink), since the comparison would be limited to the specific transient and its characteristic time constant and physical phenomena. The goal is instead to be as general as possible, so we assess the response of the system (in terms of gain and phase shift) to a perturbation in the frequency domain. This approach is limited by the possible influence of the perturbation amplitude, since a linear analysis tool is used on a modeled system characterized by non-linearities. This drawback is overcome using a fixed, small amplitude variation. This type of analysis allows characterizing the outcomes of the multi-physics codes as a function of the excitation frequency, observing in a synthetic, yet quantitative way the different physics at work and their associated dynamics. In this way, in case of discrepancy among the codes, it is quite immediate to understand in which phenomenon the code is failing to reproduce the correct behavior. As a perturbation, we study how an oscillation on the heat transfer coefficient affects the power production.

Input (initial condition)

- Steady-state solution from Step 1.4 with $U_{lid} = 0.5 \text{ m s}^{-1}$ and $P = 1.0 \text{ GW}$; and
- $\gamma = 1 \times 10^6 \text{ W m}^{-3} \text{ K}^{-1}$.

Transient description Starting from the initial condition, the volumetric heat transfer coefficient γ is uniformly perturbed according to a sine wave of amplitude 10 % and frequency $f \in [0.0125, 0.025, 0.05, 0.1, 0.2, 0.4, 0.8]$ Hz. The variation in the cooling of the salt leads to a sinusoidal power trend induced by the negative density feedback coefficient.

Observables

- Power gain and phase-shift as a function of the perturbation frequency.

The power gain is defined as

$$Gain = \frac{(P_{max} - P_{avg})/P_{avg}}{(\gamma_{max} - \gamma_{avg})/\gamma_{avg}},$$

where the denominator corresponds to the amplitude of the heat transfer coefficient sine wave (10%), P_{max} is the maximum power, and P_{avg} is the time-averaged power, corresponding to the initial power of 1 GW.

Table 4.4. PoliMi code - Time steps sizes chosen for transient calculations of Step 2.1.

Frequency (Hz)	0.0125	0.025	0.05	0.1	0.2	0.4	0.8
dt (s) ($\times 10^{-3}$)	8.0	4.0	2.0	1.0	1.0	1.0	0.5

4.4 Code packages

In this section, we briefly describe the multi-physics tools participating to the benchmark campaign, and we report the specific choices adopted for the calculations by each partner (e.g., mesh, time step, time discretization scheme). The code packages were developed during the SAMOFAR project at the *Centre national de la recherche scientifique - Grenoble* (indicated with CNRS from here on), the *Politecnico di Milano* (PoliMi), the *Paul Scherrer Institute* (PSI) and the *Delft University of Technology* (TUD). For all the details of the code packages of CNRS, PoliMi, and PSI, the reader is referred to Tiberge et al. (2020a) and the references cited therein.

CNRS The recently developed multi-physics tool described by Blanco et al. (2020) was employed. It implements various neutronics and thermal hydraulic models using Finite Volume OpenFOAM (OpenFOAM, 2013) libraries. For this analysis, the Simplified P_N models of first (SP_1) and third order (SP_3) were chosen for neutronics. The cavity domain was discretized using a structured, non-uniform mesh

was employed with a Courant number limit of 0.8.

PoliMi A multi-physics solver for fast molten salt systems implemented using the Finite Volume OpenFOAM library was employed (Cervi et al., 2019a,b). Among the several neutronics models available, a multi-group diffusion model was chosen (Cervi et al., 2019a). All simulations were performed with a 400 by 400 uniform structured mesh, ensuring that results were not affected by further refinement of the grid. The time scheme chosen for transient calculation was the first order implicit Euler scheme, using the time step sizes reported in Table 4.4.

PSI The Finite Volume GeN-Foam multi-physics tool was used in this study (Fiorina et al., 2015). A multi-group diffusion model was chosen for neutronics. A structured mesh of 200 by 200 elements, gradually refined towards the walls, was used to discretize the domain³.

³More details about the PSI calculations are available on GitHub at <https://github.com/de0liveira-R/nuclearCavity.git>.

TU Delft The multi-physics tool described in Chapter 3 was used. All simulations were performed on a 50 by 50 uniform structured mesh, adopting a polynomial order $\mathcal{P} = 2$ to approximate the velocity field and $\mathcal{P} = 1$ for all the other quantities. These options proved to ensure mesh independent results. Neutronics simulations were carried out both with order S_2 , qualitatively close to diffusion, thus obtaining results more fairly comparable to those obtained by the other diffusion codes, and S_6 , to get “full-transport” solutions, able to take into account the full anisotropy of scattering up to order three. Transient calculations were performed taking a time step equal to $1/200$ of the perturbation period and using a BDF2 time discretization scheme.

4.5 Results

In this section, we report and compare the results obtained by each partner performing the steps of the benchmark described in Section 4.3. Whenever an observable is required along the centerlines AA' and/or BB' , we report a table with its values at 9 equidistant points along the line. The complete 1D profiles (201 equidistant points along the line of interest) can be downloaded from Tibergera et al. (2020b). One plot with the complete profile of each observable is reported as well per benchmark step, in order to give a better idea to the reader on how the results (qualitatively) compare along the whole centerline. The plots of some observables in the entire domain for some steps of the benchmark are reported in Appendix A for the sake of completeness, but again they allow for a qualitative comparison of the results only. CNRS performed calculations with two angular discretizations, as described in Section 4.4, indicated with “CNRS- SP_1 ” and “CNRS- SP_3 ”. The same was done by TUD, whose results are indicated with “TUD- S_2 ” and “TUD- S_6 ”.

In absence of a reference solution, we report and discuss the *discrepancy* among the values obtained by each partner. At each point \mathbf{r}_i , we collect N_c values (one per code) of a quantity Q . We define the average value as $Q_{avg}(\mathbf{r}_i) = \frac{1}{N_c} \sum_{c=1}^{N_c} Q_c(\mathbf{r}_i)$.

The discrepancy of each quantity Q_c is then calculated as

$$\epsilon_c = \sqrt{\frac{\sum_{i=1}^{N_p} (Q_c(\mathbf{r}_i) - Q_{avg}(\mathbf{r}_i))^2}{\sum_{i=1}^{N_p} Q_{avg}^2(\mathbf{r}_i)}},$$

where $N_p = 201$ is the number of sampling points of the quantity Q . The average discrepancy is then calculated as $\epsilon = \frac{1}{N_c} \sum_{c=1}^{N_c} \epsilon_c$.

4. Benchmark of the multi-physics tool for fast-spectrum MSRs

Table 4.5. Step 0.1 - Velocity components along centerlines AA' and BB' .

Observable	Code	Results along AA' (points coordinates are expressed in m)								
		(0,1)	(0,25,1)	(0,5,1)	(0,75,1)	(1,1)	(1,25,1)	(1,5,1)	(1,75,1)	(2,1)
u_x (m s ⁻¹)	CNRS	0.000E+00	-1.924E-02	-5.372E-02	-8.369E-02	-1.025E-01	-1.043E-01	-7.972E-02	-3.080E-02	0.000E+00
	PoliMi	0.000E+00	-1.922E-02	-5.365E-02	-8.357E-02	-1.023E-01	-1.041E-01	-7.947E-02	-3.066E-02	0.000E+00
	PSI	0.000E+00	-1.929E-02	-5.366E-02	-8.332E-02	-1.018E-01	-1.034E-01	-7.912E-02	-3.072E-02	0.000E+00
	TUD	1.002E-06	-1.922E-02	-5.372E-02	-8.371E-02	-1.025E-01	-1.044E-01	-7.977E-02	-3.081E-02	4.198E-06
u_y (m s ⁻¹)	CNRS	0.000E+00	7.266E-02	8.575E-02	6.084E-02	1.251E-02	-4.789E-02	-9.606E-02	-8.722E-02	0.000E+00
	PoliMi	0.000E+00	7.139E-02	8.433E-02	6.007E-02	1.269E-02	-4.691E-02	-9.472E-02	-8.621E-02	0.000E+00
	PSI	0.000E+00	7.265E-02	8.534E-02	6.021E-02	1.230E-02	-4.734E-02	-9.536E-02	-8.720E-02	0.000E+00
	TUD	5.877E-06	7.269E-02	8.580E-02	6.089E-02	1.252E-02	-4.794E-02	-9.613E-02	-8.726E-02	-1.013E-05
Observable	Code	Results along BB' (points coordinates are expressed in m)								
		(1,0)	(1,0,25)	(1,0,5)	(1,0,75)	(1,1)	(1,1,25)	(1,1,5)	(1,1,75)	(1,2)
u_x (m s ⁻¹)	CNRS	0.000E+00	-3.517E-02	-6.242E-02	-8.720E-02	-1.025E-01	-8.766E-02	-1.147E-02	1.717E-01	5.000E-01
	PoliMi	0.000E+00	-3.423E-02	-6.107E-02	-8.613E-02	-1.023E-01	-8.861E-02	-1.299E-02	1.706E-01	5.000E-01
	PSI	0.000E+00	-3.511E-02	-6.217E-02	-8.667E-02	-1.018E-01	-8.731E-02	-1.191E-02	1.705E-01	5.000E-01
	TUD	1.494E-06	-3.519E-02	-6.244E-02	-8.724E-02	-1.025E-01	-8.770E-02	-1.146E-02	1.718E-01	5.000E-01
u_y (m s ⁻¹)	CNRS	0.000E+00	5.641E-05	6.309E-04	3.862E-03	1.251E-02	2.524E-02	3.048E-02	1.500E-02	0.000E+00
	PoliMi	0.000E+00	9.118E-05	7.484E-04	4.046E-03	1.269E-02	2.534E-02	3.050E-02	1.500E-02	0.000E+00
	PSI	0.000E+00	7.727E-05	6.822E-04	3.875E-03	1.230E-02	2.472E-02	2.994E-02	1.481E-02	0.000E+00
	TUD	1.501E-06	5.260E-05	6.209E-04	3.853E-03	1.252E-02	2.528E-02	3.053E-02	1.502E-02	7.987E-06

4.5.1 Phase 0: Single physics benchmark

4.5.1.1 Step 0.1: Velocity field

Table 4.5 reports the velocity components along the centerlines, showing good agreement between the codes. This is not surprising, as this step reproduces a well-known benchmark in the CFD community (Ghia et al., 1982; Botella and Peyret, 1998). The average relative discrepancy is below 0.35% for velocity profiles along AA' and rises up to 0.8% for the BB' profiles. The profile of u_x along BB' can be seen in Figure 4.2: the agreement is excellent. At the boundaries, the TUD velocity is not exactly null, due to the DG-FEM discretization adopted, which requires a weak imposition of the boundary conditions. It is worth noticing that the second polynomial order chosen by TUD for the velocity field leads to excellent results despite the coarse mesh selected.

4.5.1.2 Step 0.2: Neutronics

The profile of the fission rate density along AA' is reported in Table 4.6 and in Figure 4.3. Results are very similar considering the diffusion codes (PoliMi and PSI) and the CNRS- SP_1 and TUD- S_2 calculations. This is expected, since a diffusion model with P_1 scatter is theoretically equivalent to the SP_1 and S_2 discretizations. Differences increase when considering the higher order transport discretizations. However, the average relative discrepancy is below 0.3%; this is expected in a large homogeneous geometry like the one of this benchmark, where using a more advanced transport model does not lead to great differences in the results. The values obtained by each partner scatter the most at the boundaries, but this is

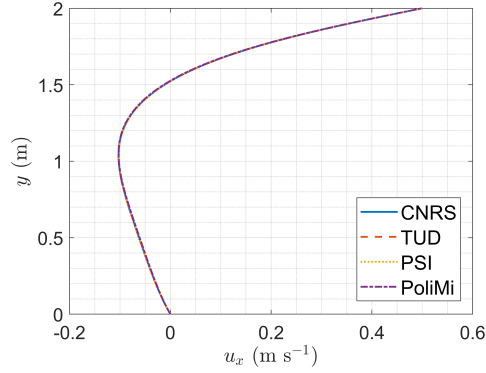


Fig. 4.2. Step 0.1 - Horizontal velocity component along BB' .

Table 4.6. Step 0.2 - Fission rate density along AA' .

Observable	Code	Results along AA' (points coordinates are expressed in m)								
		(0,1)	(0.25,1)	(0.5,1)	(0.75,1)	(1,1)	(1.25,1)	(1.5,1)	(1.75,1)	(2,1)
$\int_E \Sigma_f \Phi dE$ ($\text{m}^{-3} \text{s}^{-1}$)	CNRS- SP_1	6.896E+17	7.436E+18	1.305E+19	1.678E+19	1.809E+19	1.678E+19	1.305E+19	7.436E+18	6.896E+17
	CNRS- SP_3	6.206E+17	7.450E+18	1.303E+19	1.673E+19	1.802E+19	1.673E+19	1.303E+19	7.450E+18	6.206E+17
	PoliMi	7.780E+17	7.470E+18	1.310E+19	1.684E+19	1.815E+19	1.684E+19	1.310E+19	7.470E+18	7.780E+17
	PSI	8.622E+17	7.436E+18	1.305E+19	1.678E+19	1.809E+19	1.678E+19	1.305E+19	7.436E+18	8.622E+17
	TUD- S_2	6.626E+17	7.433E+18	1.307E+19	1.682E+19	1.814E+19	1.682E+19	1.307E+19	7.433E+18	6.626E+17
	TUD- S_6	6.833E+17	7.463E+18	1.300E+19	1.667E+19	1.796E+19	1.667E+19	1.300E+19	7.463E+18	6.833E+17

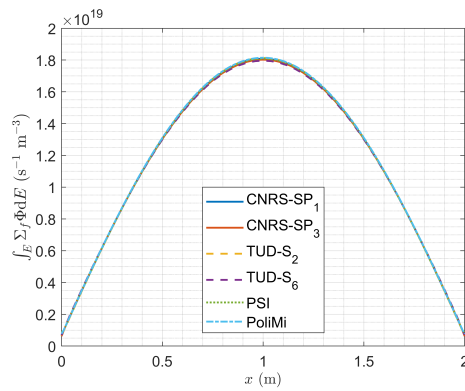


Fig. 4.3. Step 0.2 - Fission rate density along AA' .

Table 4.7. Step 0.2 - Reactivity.

Code	ρ (pcm)
CNRS- SP_1	411.3
CNRS- SP_3	353.7
PoliMi	421.2
PSI	411.7
TUD- S_2	482.6
TUD- S_6	578.1

expected due to the difference in the imposition of the vacuum boundary conditions between diffusion and transport models.

Finally, the system reactivity is shown in Table 4.7. Diffusion and CNRS- SP_1 results differ only by 10 pcm, the S_2 model by TUD is only around 70 pcm off the diffusion ones; not surprisingly, the more advanced transport models lead to different results, but only slightly (around 150 pcm of difference from the diffusion ones).

4.5.1.3 Step 0.3: Temperature

Table 4.8 reports the temperature profiles along AA' and BB' . The agreement among the codes is excellent, with an average discrepancy of around 0.1% for both profiles. This is confirmed by the complete plot along BB' shown in Figure 4.4. Once more, the maximum disagreement between the codes is to be found at the boundaries and can be explained by the different treatment of boundary conditions by the DG-FEM discretization adopted by TUD and the differences in

Table 4.8. Step 0.3 - Temperature distribution along centerlines AA' and BB' .

Observable	Code	Results along AA' (points coordinates are expressed in m)								
		(0,1)	(0.25,1)	(0.5,1)	(0.75,1)	(1,1)	(1.25,1)	(1.5,1)	(1.75,1)	(2,1)
T (K)	CNRS- SP_1	9.253E+02	1.194E+03	1.358E+03	1.363E+03	1.305E+03	1.224E+03	1.131E+03	1.034E+03	9.251E+02
	CNRS- SP_3	9.236E+02	1.194E+03	1.357E+03	1.361E+03	1.304E+03	1.224E+03	1.131E+03	1.034E+03	9.235E+02
	PoliMi	9.253E+02	1.196E+03	1.361E+03	1.364E+03	1.305E+03	1.224E+03	1.132E+03	1.035E+03	9.252E+02
	PSI	9.253E+02	1.196E+03	1.356E+03	1.363E+03	1.306E+03	1.226E+03	1.133E+03	1.037E+03	9.252E+02
	TUD- S_2	9.212E+02	1.194E+03	1.359E+03	1.364E+03	1.305E+03	1.224E+03	1.131E+03	1.032E+03	9.225E+02
	TUD- S_6	9.219E+02	1.194E+03	1.356E+03	1.360E+03	1.303E+03	1.223E+03	1.131E+03	1.034E+03	9.233E+02
Observable	Code	Results along BB' (points coordinates are expressed in m)								
		(1,0)	(1,0.25)	(1,0.5)	(1,0.75)	(1,1)	(1,1.25)	(1,1.5)	(1,1.75)	(1,2)
T (K)	CNRS- SP_1	9.252E+02	1.139E+03	1.273E+03	1.305E+03	1.305E+03	1.314E+03	1.321E+03	1.265E+03	9.322E+02
	CNRS- SP_3	9.236E+02	1.140E+03	1.272E+03	1.304E+03	1.304E+03	1.313E+03	1.320E+03	1.265E+03	9.322E+02
	PoliMi	9.253E+02	1.140E+03	1.275E+03	1.307E+03	1.305E+03	1.313E+03	1.321E+03	1.265E+03	9.303E+02
	PSI	9.252E+02	1.139E+03	1.273E+03	1.307E+03	1.306E+03	1.312E+03	1.319E+03	1.263E+03	9.481E+02
	TUD- S_2	9.215E+02	1.139E+03	1.273E+03	1.305E+03	1.305E+03	1.315E+03	1.322E+03	1.265E+03	9.374E+02
	TUD- S_6	9.222E+02	1.140E+03	1.272E+03	1.303E+03	1.303E+03	1.312E+03	1.319E+03	1.264E+03	9.390E+02

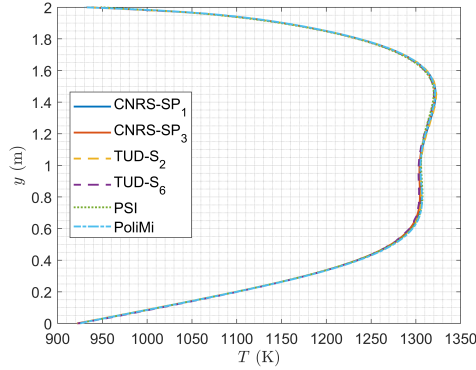


Fig. 4.4. Step 0.3 - Temperature along BB' .

fission density described in Section 4.5.1.2.

4.5.2 Phase 1: Steady-state coupling

4.5.2.1 Step 1.1: Circulating fuel

The profiles of the delayed neutron precursors source along the cavity centerlines are shown in Table 4.9. Very good agreement can be noticed among all codes, with an average discrepancy of 0.35% for the profile along AA' and of 0.3% for the one along BB' (shown in Figure 4.5 as well). Results scatter again at the boundaries, but, taking into account the differences in velocity and fission density analyzed in Sections 4.5.1.1 and 4.5.1.2, this is acceptable.

Finally, Table 4.10 reports the value of reactivity insertion with respect to the

Table 4.9. Step 1.1 - Delayed neutron source along AA' and BB' .

Observable	Code	Results along AA' (points coordinates are expressed in m)								
		(0,1)	(0.25,1)	(0.5,1)	(0.75,1)	(1,1)	(1.25,1)	(1.5,1)	(1.75,1)	(2,1)
$\sum_i \lambda_i C_i$ ($\text{m}^{-3} \text{s}^{-1}$)	CNRS- SP_1	1.335E+16	1.452E+17	2.212E+17	2.411E+17	2.268E+17	1.923E+17	1.461E+17	9.214E+16	1.316E+16
	CNRS- SP_3	1.251E+16	1.454E+17	2.209E+17	2.406E+17	2.264E+17	1.921E+17	1.462E+17	9.245E+16	1.233E+16
	PoliMi	1.321E+16	1.450E+17	2.219E+17	2.414E+17	2.266E+17	1.920E+17	1.459E+17	9.188E+16	1.292E+16
	PSI	1.325E+16	1.453E+17	2.214E+17	2.413E+17	2.270E+17	1.925E+17	1.463E+17	9.218E+16	1.314E+16
	TUD- S_2	1.093E+16	1.438E+17	2.228E+17	2.426E+17	2.278E+17	1.927E+17	1.464E+17	8.968E+16	1.184E+16
	TUD- S_6	1.132E+16	1.437E+17	2.212E+17	2.405E+17	2.261E+17	1.916E+17	1.461E+17	9.029E+16	1.224E+16
Observable	Code	Results along BB' (points coordinates are expressed in m)								
		(1,0)	(1,0.25)	(1,0.5)	(1,0.75)	(1,1)	(1,1.25)	(1,1.5)	(1,1.75)	(1,2)
$\sum_i \lambda_i C_i$ ($\text{m}^{-3} \text{s}^{-1}$)	CNRS- SP_1	1.306E+16	1.190E+17	1.881E+17	2.193E+17	2.268E+17	2.261E+17	2.178E+17	1.754E+17	3.079E+16
	CNRS- SP_3	1.222E+16	1.193E+17	1.879E+17	2.189E+17	2.264E+17	2.257E+17	2.175E+17	1.753E+17	3.072E+16
	PoliMi	1.297E+16	1.186E+17	1.881E+17	2.194E+17	2.266E+17	2.260E+17	2.177E+17	1.756E+17	2.805E+16
	PSI	1.299E+16	1.189E+17	1.881E+17	2.195E+17	2.270E+17	2.261E+17	2.176E+17	1.752E+17	2.730E+16
	TUD- S_2	1.109E+16	1.174E+17	1.882E+17	2.203E+17	2.278E+17	2.281E+17	2.193E+17	1.768E+17	2.655E+16
	TUD- S_6	1.143E+16	1.178E+17	1.872E+17	2.186E+17	2.261E+17	2.264E+17	2.179E+17	1.761E+17	2.728E+16

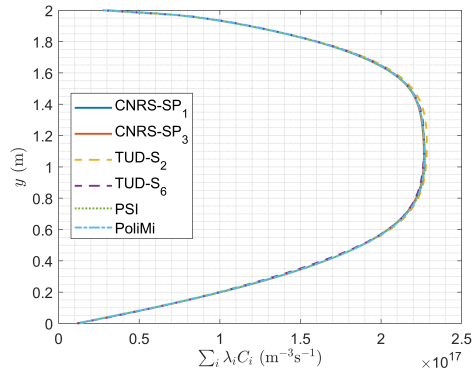


Fig. 4.5. Step 1.1 - Delayed neutron source along BB' .

Table 4.10. Step 1.1 - Reactivity change from Step 0.2.

Code	$\rho - \rho_{s0.2}$ (pcm)
CNRS- SP_1	-62.5
CNRS- SP_3	-62.6
PoliMi	-62.0
PSI	-63.0
TUD- S_2	-62.0
TUD- S_6	-60.7

static case (Step 0.2). The agreement between the codes is excellent, with a minimal difference between the TUD- S_6 and the others, which is expected, given the more advanced transport model. It can be deduced that all the assessed multi-physics tools can correctly reproduce the effect induced on the effective multiplication factor by the transport of delayed neutron precursors inside the cavity.

4.5.2.2 Step 1.2: Power coupling

The profiles of the temperature along AA' and BB' are reported in Table 4.11. Results are very similar to the ones obtained for Step 0.3 (see Section 4.5.1.3), with an excellent agreement among all numerical tools. In fact, the average discrepancy is 0.09% for both profiles. Table 4.11 also reports the values of the change of fission rate density along AA' and BB' with respect to the solution obtained at Step 0.2. Differences are more considerable here, as can be noticed also in the complete plot shown in Figure 4.6. Nevertheless, the average discrepancy is lower than 1.6% for both profiles. PSI and TUD results are those affected by the highest discrepancy (around 2.5% for the former, 2% for the latter). For PSI, this is to be ascribed

Table 4.11. Step 1.2 - Profiles along AA' and BB' of the temperature and the change of fission rate density with respect to the solution obtained at Step 0.2.

Observable	Code	Results along AA' (points coordinates are expressed in m)								
		(0,1)	(0,25,1)	(0,5,1)	(0,75,1)	(1,1)	(1,25,1)	(1,5,1)	(1,75,1)	(2,1)
T (K)	CNRS- SP_3	9.280E+02	1.195E+03	1.341E+03	1.349E+03	1.298E+03	1.225E+03	1.136E+03	1.041E+03	9.278E+02
	CNRS- SP_3	9.262E+02	1.195E+03	1.341E+03	1.348E+03	1.298E+03	1.225E+03	1.137E+03	1.042E+03	9.260E+02
	PoliMi	9.281E+02	1.198E+03	1.343E+03	1.350E+03	1.300E+03	1.226E+03	1.138E+03	1.045E+03	9.280E+02
	PSI	9.282E+02	1.197E+03	1.340E+03	1.349E+03	1.300E+03	1.227E+03	1.139E+03	1.045E+03	9.280E+02
	TUD- S_2	9.235E+02	1.196E+03	1.343E+03	1.350E+03	1.300E+03	1.226E+03	1.137E+03	1.041E+03	9.250E+02
	TUD- S_6	9.243E+02	1.196E+03	1.340E+03	1.347E+03	1.298E+03	1.225E+03	1.137E+03	1.042E+03	9.258E+02
$-\int_E \Sigma_f \Phi dE$ $(m^{-3} s^{-1})$	CNRS- SP_3	7.800E+16	1.169E+17	-5.694E+17	-9.490E+17	-7.979E+17	-2.853E+17	2.626E+17	4.611E+17	7.776E+16
	CNRS- SP_3	7.016E+16	1.156E+17	-5.668E+17	-9.427E+17	-7.941E+17	-2.869E+17	2.575E+17	4.578E+17	6.993E+16
	PoliMi	7.556E+16	1.141E+17	-5.682E+17	-9.440E+17	-7.906E+17	-2.800E+17	2.628E+17	4.563E+17	7.522E+16
	PSI	2.188E+15	1.226E+17	-5.486E+17	-9.275E+17	-7.807E+17	-2.725E+17	2.702E+17	4.632E+17	1.835E+15
	TUD- S_2	7.203E+16	1.069E+17	-5.648E+17	-9.534E+17	-8.186E+17	-2.724E+17	2.628E+17	4.531E+17	7.194E+16
	TUD- S_6	7.304E+16	1.041E+17	-5.572E+17	-9.382E+17	-8.098E+17	-2.791E+17	2.466E+17	4.431E+17	7.274E+16
Observable	Code	Results along BB' (points coordinates are expressed in m)								
		(1,0)	(1,0.25)	(1,0.5)	(1,0.75)	(1,1)	(1,1.25)	(1,1.5)	(1,1.75)	(1,2)
T (K)	CNRS- SP_3	9.281E+02	1.148E+03	1.272E+03	1.301E+03	1.298E+03	1.304E+03	1.307E+03	1.253E+03	9.350E+02
	CNRS- SP_3	9.262E+02	1.149E+03	1.272E+03	1.300E+03	1.298E+03	1.303E+03	1.306E+03	1.253E+03	9.351E+02
	PoliMi	9.281E+02	1.150E+03	1.275E+03	1.304E+03	1.300E+03	1.304E+03	1.307E+03	1.253E+03	9.470E+02
	PSI	9.282E+02	1.148E+03	1.273E+03	1.303E+03	1.300E+03	1.303E+03	1.306E+03	1.252E+03	9.517E+02
	TUD- S_2	9.240E+02	1.148E+03	1.274E+03	1.302E+03	1.300E+03	1.306E+03	1.309E+03	1.254E+03	9.424E+02
	TUD- S_6	9.247E+02	1.149E+03	1.272E+03	1.300E+03	1.298E+03	1.303E+03	1.306E+03	1.253E+03	9.442E+02
$-\int_E \Sigma_f \Phi dE$ $(m^{-3} s^{-1})$	CNRS- SP_3	8.205E+16	2.640E+17	-2.264E+17	-6.431E+17	-7.979E+17	-7.557E+17	-4.923E+17	-3.953E+16	8.353E+16
	CNRS- SP_3	7.377E+16	2.615E+17	-2.273E+17	-6.407E+17	-7.941E+17	-7.525E+17	-4.902E+17	-3.919E+16	7.493E+16
	PoliMi	7.961E+16	2.639E+17	-2.256E+17	-6.389E+17	-7.942E+17	-7.536E+17	-4.922E+17	-4.164E+16	8.050E+16
	PSI	9.174E+16	2.639E+17	-2.287E+17	-6.506E+17	-8.020E+17	-7.479E+17	-4.856E+17	-3.479E+16	9.059E+16
	TUD- S_2	7.595E+16	2.513E+17	-2.336E+17	-6.589E+17	-8.186E+17	-7.703E+17	-4.964E+17	-4.656E+16	6.931E+16
	TUD- S_6	7.677E+16	2.436E+17	-2.373E+17	-6.540E+17	-8.098E+17	-7.612E+17	-4.906E+17	-4.534E+16	6.990E+16

to the more refined mesh towards the boundary used combined with the vacuum conditions imposed by the diffusion model. For TUD, this is due to the different approach adopted for correcting cross sections with temperature (element-wise in TUD calculations, point-wise in the other codes). Anyway, the agreement of TUD with the other partners is good in a discrete sense.

Finally, Table 4.12 reports the value of reactivity insertion with respect to Step 1.1. The agreement between the multi-physics tools is excellent (maximum difference less than 40 pcm) and the same considerations made in Section 4.5.2.1 hold here. We can conclude that all partners can correctly reproduce the simple “two-way” coupling between flux shape and temperature distribution, via the fuel-density feedback.

4.5.2.3 Step 1.3: Buoyancy

Table 4.13 reports the profiles of the observables along the cavity centerlines AA' and BB' . Note that the profile of u_x along BB' is not reported as it is null. In fact, the problem is perfectly symmetric to the vertical centerline. Once more, a very good agreement can be noticed among the codes. Velocity components present an average discrepancy that does not exceed 0.7%. Again, TUD simulations disagree most at the boundaries due to the DG-FEM discretization. Temperature profiles agree excellently, with an average discrepancy lower than 0.08%. This is confirmed

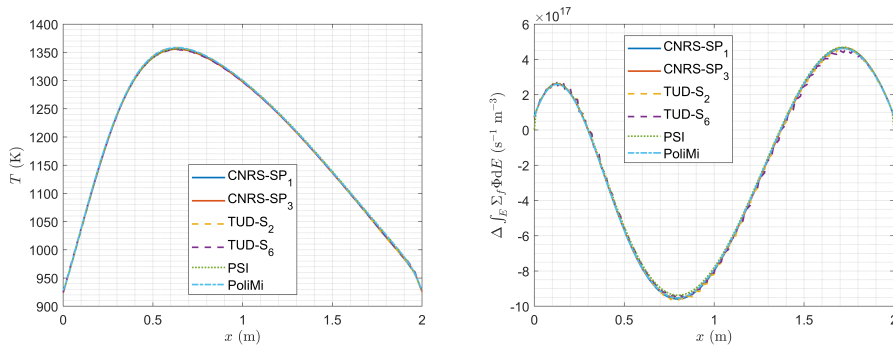


Fig. 4.6. Step 1.2 - Temperature and change of fission rate density along AA' .

Table 4.12. Step 1.2 - Reactivity change from Step 1.1.

Code	$\rho - \rho_{s_{1.1}}$ (pcm)
CNRS- SP_1	-1152.0
CNRS- SP_3	-1152.7
PoliMi	-1161.0
PSI	-1154.8
TUD- S_2	-1145.2
TUD- S_6	-1122.0

by the plots shown in Figure 4.7.

For what concerns the delayed neutron source, its profiles are characterized by a discrepancy of around 0.5% along AA' and 1.2% along BB' . For the latter profile, in particular, we notice a good agreement between PSI and CNRS, and between TUD and PoliMi. We therefore ascribe the small discrepancy in these results to the non-uniform mesh used by both CNRS and PSI, coarser in the middle of the domain. The plot in Figure 4.7 corroborates this: a small discrepancy can be noticed only at the center of the cavity. However, considering the differences pointed out in the previous steps as well, the disagreement is considered acceptable.

This is confirmed by the results on the reactivity difference with respect to Step 0.2 reported in Table 4.14. In fact, all values differ less than 50 pcm and are coherent with the ones analyzed in Section 4.5.2.2. This proves that all multi-physics codes can correctly reproduce the effects induced by salt buoyancy on velocity, temperature, neutron flux, and delayed neutron precursors fields.

Table 4.13. Step 1.3 - Velocity components, temperature distribution, and delayed neutron source along AA' and BB' . Given the symmetry of the problem, u_x is null along BB' and so not reported.

Observable	Code	Results along AA' (points coordinates are expressed in m)								
		(0,1)	(0.25,1)	(0.5,1)	(0.75,1)	(1,1)	(1.25,1)	(1.5,1)	(1.75,1)	(2,1)
u_x (m s ⁻¹)	CNRS- SP_1	0.000E+00	1.641E-02	2.310E-02	1.579E-02	1.250E-09	-1.579E-02	-2.310E-02	-1.641E-02	0.000E+00
	CNRS- SP_3	0.000E+00	1.636E-02	2.302E-02	1.572E-02	1.000E-09	-1.572E-02	-2.302E-02	-1.636E-02	0.000E+00
	PoliMi	0.000E+00	1.637E-02	2.312E-02	1.578E-02	-1.125E-10	-1.578E-02	-2.312E-02	-1.637E-02	0.000E+00
	PSI	0.000E+00	1.630E-02	2.263E-02	1.519E-02	-8.525E-09	-1.519E-02	-2.263E-02	-1.630E-02	0.000E+00
	TUD- S_2	6.054E-06	1.644E-02	2.316E-02	1.584E-02	-2.218E-06	-1.584E-02	-2.316E-02	-1.644E-02	-6.054E-06
	TUD- S_6	5.982E-06	1.631E-02	2.295E-02	1.566E-02	-2.196E-06	-1.566E-02	-2.295E-02	-1.631E-02	-5.982E-06
u_y (m s ⁻¹)	CNRS- SP_1	0.000E+00	-1.777E-01	1.721E-02	1.376E-01	1.649E-01	1.376E-01	1.721E-02	-1.777E-01	0.000E+00
	CNRS- SP_3	0.000E+00	-1.771E-01	1.708E-02	1.372E-01	1.645E-01	1.372E-01	1.708E-02	-1.771E-01	0.000E+00
	PoliMi	0.000E+00	-1.767E-01	1.741E-02	1.368E-01	1.638E-01	1.368E-01	1.741E-02	-1.767E-01	0.000E+00
	PSI	0.000E+00	-1.779E-01	1.662E-02	1.376E-01	1.659E-01	1.376E-01	1.662E-02	-1.779E-01	0.000E+00
	TUD- S_2	-2.886E-05	-1.780E-01	1.735E-02	1.379E-01	1.650E-01	1.379E-01	1.735E-02	-1.780E-01	-2.886E-05
	TUD- S_6	-2.929E-05	-1.766E-01	1.694E-02	1.368E-01	1.639E-01	1.368E-01	1.694E-02	-1.766E-01	-2.929E-05
T (K)	CNRS- SP_1	9.279E+02	1.193E+03	1.278E+03	1.284E+03	1.280E+03	1.284E+03	1.278E+03	1.193E+03	9.279E+02
	CNRS- SP_3	9.260E+02	1.193E+03	1.278E+03	1.284E+03	1.280E+03	1.284E+03	1.278E+03	1.193E+03	9.260E+02
	PoliMi	9.279E+02	1.193E+03	1.279E+03	1.286E+03	1.282E+03	1.286E+03	1.279E+03	1.193E+03	9.279E+02
	PSI	9.279E+02	1.191E+03	1.278E+03	1.284E+03	1.280E+03	1.284E+03	1.278E+03	1.191E+03	9.279E+02
	TUD- S_2	9.248E+02	1.193E+03	1.279E+03	1.285E+03	1.281E+03	1.285E+03	1.279E+03	1.193E+03	9.248E+02
	TUD- S_6	9.257E+02	1.192E+03	1.277E+03	1.283E+03	1.280E+03	1.283E+03	1.277E+03	1.192E+03	9.257E+02
$\sum_i \lambda_i C_i$ (m ⁻³ s ⁻¹)	CNRS- SP_1	1.499E+16	1.468E+17	2.001E+17	2.123E+17	1.988E+17	2.123E+17	2.001E+17	1.468E+17	1.499E+16
	CNRS- SP_3	1.409E+16	1.469E+17	2.000E+17	2.121E+17	1.986E+17	2.121E+17	2.000E+17	1.469E+17	1.409E+16
	PoliMi	1.436E+16	1.464E+17	1.992E+17	2.113E+17	1.944E+17	2.113E+17	1.992E+17	1.464E+17	1.436E+16
	PSI	1.477E+16	1.469E+17	2.005E+17	2.126E+17	1.983E+17	2.126E+17	2.005E+17	1.469E+17	1.477E+16
	TUD- S_2	1.041E+16	1.488E+17	2.017E+17	2.141E+17	1.942E+17	2.141E+17	2.017E+17	1.488E+17	1.041E+16
	TUD- S_6	1.086E+16	1.485E+17	2.006E+17	2.128E+17	1.931E+17	2.128E+17	2.006E+17	1.485E+17	1.086E+16
Observable	Code	Results along BB' (points coordinates are expressed in m)								
		(1,0)	(1,0.25)	(1,0.5)	(1,0.75)	(1,1)	(1,1.25)	(1,1.5)	(1,1.75)	(1,2)
u_x (m s ⁻¹)	CNRS- SP_1	0.000E+00	3.512E-02	8.947E-02	1.359E-01	1.649E-01	1.665E-01	1.307E-01	5.756E-02	0.000E+00
	CNRS- SP_3	0.000E+00	3.510E-02	8.933E-02	1.356E-01	1.645E-01	1.660E-01	1.303E-01	5.740E-02	0.000E+00
	PoliMi	0.000E+00	3.507E-02	8.909E-02	1.351E-01	1.638E-01	1.656E-01	1.302E-01	5.743E-02	0.000E+00
	PSI	0.000E+00	3.537E-02	9.055E-02	1.374E-01	1.659E-01	1.669E-01	1.309E-01	5.780E-02	0.000E+00
	TUD- S_2	-1.234E-05	3.510E-02	8.950E-02	1.360E-01	1.650E-01	1.667E-01	1.308E-01	5.763E-02	-2.808E-05
	TUD- S_6	-1.327E-05	3.506E-02	8.912E-02	1.352E-01	1.639E-01	1.655E-01	1.299E-01	5.719E-02	-2.872E-05
T (K)	CNRS- SP_1	9.280E+02	1.067E+03	1.156E+03	1.226E+03	1.280E+03	1.315E+03	1.326E+03	1.283E+03	9.284E+02
	CNRS- SP_3	9.261E+02	1.067E+03	1.156E+03	1.226E+03	1.280E+03	1.315E+03	1.325E+03	1.282E+03	9.266E+02
	PoliMi	9.280E+02	1.067E+03	1.157E+03	1.228E+03	1.282E+03	1.317E+03	1.327E+03	1.284E+03	9.282E+02
	PSI	9.281E+02	1.068E+03	1.156E+03	1.226E+03	1.280E+03	1.314E+03	1.324E+03	1.281E+03	9.287E+02
	TUD- S_2	9.250E+02	1.066E+03	1.156E+03	1.227E+03	1.281E+03	1.316E+03	1.327E+03	1.283E+03	9.137E+02
	TUD- S_6	9.258E+02	1.069E+03	1.157E+03	1.226E+03	1.280E+03	1.314E+03	1.325E+03	1.282E+03	9.149E+02
$\sum_i \lambda_i C_i$ (m ⁻³ s ⁻¹)	CNRS- SP_1	1.479E+16	8.797E+16	1.377E+17	1.746E+17	1.988E+17	2.087E+17	2.017E+17	1.659E+17	1.721E+16
	CNRS- SP_3	1.383E+16	8.839E+16	1.378E+17	1.746E+17	1.986E+17	2.084E+17	2.015E+17	1.659E+17	1.631E+16
	PoliMi	1.451E+16	8.624E+16	1.344E+17	1.706E+17	1.944E+17	2.045E+17	1.977E+17	1.623E+17	1.583E+16
	PSI	1.477E+16	8.782E+16	1.373E+17	1.741E+17	1.983E+17	2.083E+17	2.014E+17	1.658E+17	1.689E+16
	TUD- S_2	1.337E+16	8.510E+16	1.335E+17	1.700E+17	1.942E+17	2.047E+17	1.980E+17	1.621E+17	1.243E+16
	TUD- S_6	1.378E+16	8.605E+16	1.335E+17	1.693E+17	1.931E+17	2.034E+17	1.969E+17	1.616E+17	1.300E+16

4. Benchmark of the multi-physics tool for fast-spectrum MSRs

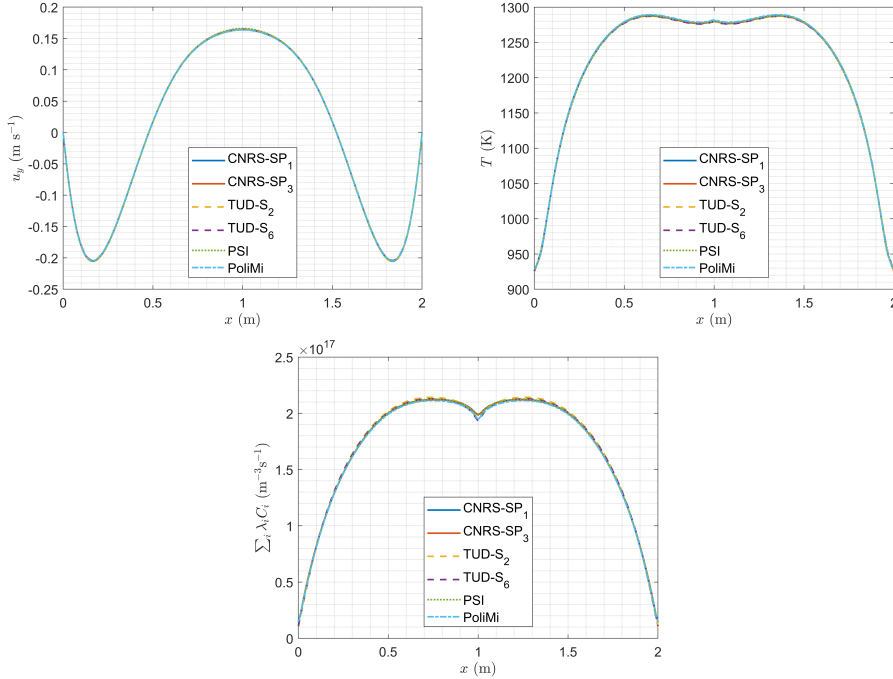


Fig. 4.7. Step 1.3 - Vertical velocity component, temperature, and delayed neutron source along AA' .

Table 4.14. Step 1.3 - Reactivity change from Step 0.2.

Code	$\rho - \rho_{s0.2}$ (pcm)
CNRS-SP ₁	-1220.5
CNRS-SP ₃	-1220.7
PoliMi	-1227.0
PSI	-1219.6
TUD-S ₂	-1208.5
TUD-S ₆	-1184.4

4.5.2.4 Step 1.4: Full coupling

The reactivity change with respect to Step 0.2 is reported in Table 4.15, for each reactor power and lid-velocity considered. As expected, higher power levels correspond to more significant insertions of negative reactivity, due to the increased average temperature in the system. The lid-velocity has a dual effect on reactivity,

Table 4.15. Step 1.4 - Reactivity change from Step 0.2 as a function of P and U_{lid} .

Code	$\rho - \rho_{s_{0.2}}$ (pcm)					
	U_{lid} (m s ⁻¹) \backslash P (GW)	0.2	0.4	0.6	0.8	1.0
CNRS- SP_1	0.0	-264.5	-503.4	-737.8	-974.2	-1220.5
CNRS- SP_3		-265.8	-503.4	-738.5	-976.2	-1220.7
PoliMi		-266.0	-498.0	-734.0	-975.0	-1227.0
PSI		-268.0	-504.8	-739.0	-975.0	-1215.1
TUD- S_2		-263.7	-498.1	-731.1	-967.2	-1208.5
TUD- S_6		-258.0	-487.8	-716.3	-947.9	-1184.4
CNRS- SP_1	0.1	-268.5	-503.6	-738.2	-975.8	-1219.6
CNRS- SP_3		-268.8	-503.8	-738.2	-976.2	-1219.7
PoliMi		-269.0	-500.0	-734.0	-975.0	-1225.0
PSI		-270.2	-505.3	-738.6	-974.4	-1214.1
TUD- S_2		-265.8	-498.4	-730.7	-966.5	-1207.6
TUD- S_6		-260.1	-488.2	-716.0	-947.2	-1183.5
CNRS- SP_1	0.2	-270.5	-503.3	-736.5	-973.9	-1216.3
CNRS- SP_3		-270.8	-503.6	-736.8	-974.1	-1216.5
PoliMi		-275.0	-501.0	-733.0	-971.0	-1222.0
PSI		-272.4	-505.3	-737.3	-972.1	-1211.0
TUD- S_2		-267.9	-498.4	-729.4	-964.2	-1204.4
TUD- S_6		-262.2	-488.3	-714.8	-945.0	-1180.5
CNRS- SP_1	0.3	-269.5	-502.9	-735.2	-970.9	-1212.1
CNRS- SP_3		-269.8	-503.5	-735.3	-971.0	-1212.4
PoliMi		-278.0	-503.0	-734.0	-970.0	-1219.0
PSI		-274.0	-504.8	-735.6	-969.1	-1206.8
TUD- S_2		-269.5	-498.1	-727.7	-961.2	-1200.2
TUD- S_6		-263.8	-488.0	-713.2	-942.2	-1176.4
CNRS- SP_1	0.4	-274.5	-503.3	-733.8	-968.3	-1208.2
CNRS- SP_3		-274.8	-503.4	-734.0	-968.4	-1208.4
PoliMi		-280.0	-504.0	-735.0	-969.0	-1216.0
PSI		-275.9	-504.5	-734.1	-966.4	-1202.9
TUD- S_2		-271.2	-497.8	-726.2	-958.5	-1196.2
TUD- S_6		-265.6	-487.8	-711.8	-939.6	-1172.7
CNRS- SP_1	0.5	-276.5	-503.5	-732.9	-966.3	-1204.8
CNRS- SP_3		-276.8	-503.5	-733.0	-966.5	-1205.2
PoliMi		-284.0	-508.0	-737.0	-972.0	-1214.0
PSI		-278.1	-504.6	-733.1	-964.3	-1199.8
TUD- S_2		-273.1	-497.8	-725.2	-956.4	-1193.0
TUD- S_6		-267.5	-487.8	-710.8	-937.6	-1169.7

depending on the power level. At low power, higher lid-velocities correspond to higher negative reactivity differences, whereas the effect is reversed from $P = 0.6$ GW. In fact, the more intense is forced-convection, the more precursors and energy get redistributed in the cavity, and this influences reactivity via two competing mechanisms. Shifting the peak of the precursors concentration further from the cavity center introduces more negative reactivity, with respect to the case $U_{lid} = 0$, whereas shifting the temperature peak introduces positive reactivity as the temperature gets lower in the region of higher importance. According to the power level, one effect prevails on the other, because at lower power the effect of the temperature redistribution is less significant.

Results are satisfactory. The differences between codes are always limited (the maximum difference varies from 10 to 45 pcm) and can be prescribed to the superposition of the effects already denoted in the previous steps.

4.5.3 Phase 2: Time dependent coupling

4.5.3.1 Step 2.1: Forced convection transient

Figure 4.8 shows the power gain and phase-shift, summarized into Bode diagrams, as a function of the oscillation frequency of the heat transfer coefficient γ . Numerical values can be downloaded from Tiberger et al. (2020b). They were evaluated after the system response reached an asymptotic behavior at all frequencies.

Good agreement is found among the codes. The gain values are characterized by an average discrepancy of around 0.6 %. Phase-shift values are more scattered, with a discrepancy of around 2.2 %. However, this is considered acceptable.

From a physics point of view, the system dynamic response is as expected:

- at low frequencies, the power follows the variation of the extracted one (i.e., gain ≈ 1 and minimal phase shift), as precursors can reach an equilibrium during the slow transient;
- at high frequencies, on the contrary, the contribution of the delayed neutrons to the entire neutron population is filtered, as some precursors families do not “perceive” the temperature reactivity feedback due to their long half-life; so, the system response amplitude decreases (i.e., gain less than one). Moreover, the phase shift approaches -90° ; in fact, when γ reaches a maximum, the temperature time-derivative is at its maximum (at high frequencies, the time derivative term in the energy equation is dominating over the convective and diffusive ones), and so is the reactivity change and the derivative of the neutrons population, which shifts to a cosine wave.

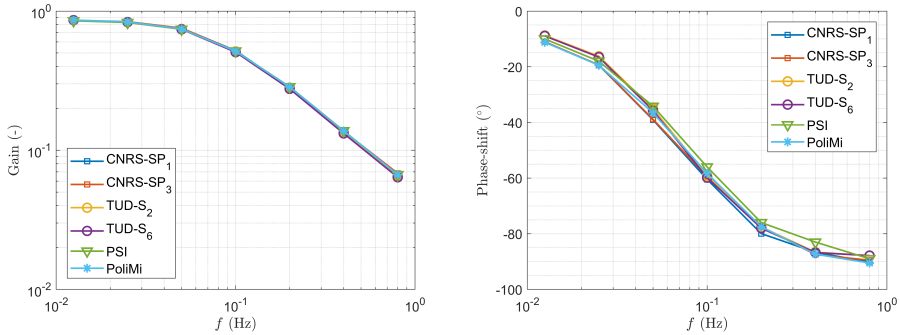


Fig. 4.8. Step 2.1 - Bode diagrams of power gain and phase-shift as a function of the frequency of the γ wave.

4.6 Conclusions

In this chapter, we have presented a coupled neutronics and fluid-dynamics benchmark for multi-physics codes targeting fast-spectrum molten salt reactors. The problem is based on a simple liquid-fuel reactor system which is representative of the main characteristics of the Molten Salt Fast Reactor (MSFR): strong coupling between thermal-hydraulics and neutronics, fast spectrum, and transport of delayed neutron precursors.

The simplicity of the benchmark and its step-by-step approach, in which physics phenomena are coupled two at a time, make it an excellent tool to test multi-physics tools, because possible sources of discrepancy can be easily detected and fixed (as, in fact, it happened in our experience). This is in contrast with other complex benchmarks currently available in literature. Moreover, the generality of the problem makes this benchmark suitable for virtually any code. Multi-physics tools intended for thermal-spectrum MSRs may benefit from it too, even though the absence of a graphite moderator does not allow for a complete assessment.

We have presented the results collected during the benchmarking campaign involving four multi-physics tools developed in the context of the Horizon 2020 Euratom SAMOFAR project. A CFD- SP_N transport tool developed at the Centre national de la recherche scientifique - Grenoble (CNRS), two CFD-diffusion solvers developed at the Politecnico di Milano (PoliMi) and the Paul Scherrer Institute (PSI), and a CFD- S_N transport code developed at the Delft University of Technology (TUD). The comparison has shown very good agreement among the partners. Differences vary between a few tenths of a percent and a few percent maximum, depending on the particular benchmark step and quantity compared. They stem mainly from the use of different meshes between participants. Another reason for discrepancy is the neutronics model used. Diffusion solvers have been found to be often in excellent agreement, together with the CNRS- SP_1 and TUD- S_2 transport

results, whereas TUD- S_6 transport results tend to have the largest differences. Moreover, the discontinuous Galerkin Finite Element discretization adopted by TUD often introduces slight discrepancies in the solution at the walls, where boundary conditions can be imposed only in a weak sense. The largest differences have been found in the fission density distribution of Step 1.2. They are mainly due to the different approach adopted by TUD in correcting cross sections with density feedback, that is, using the average temperature in each element. The differences are, however, considered acceptable.

In conclusion, the results prove that the recently developed multi-physics codes assessed in this work are able to reproduce accurately the physics phenomena characterizing fast-spectrum MSRs, both at steady-state and during transients. More in general, together with the complete benchmark description itself, they constitute a very useful tool for the future testing and development of any other multi-physics code dedicated to MSRs, as the interested reader is provided with a quite large spectrum of results to compare with.

CHAPTER 5

ANALYSIS OF THE MSFR STEADY-STATE AND TRANSIENT BEHAVIOR

In this work, we use the multi-physics Discontinuous-Galerkin FEM tool described in Chapter 3 to carry out an extensive analysis of the Molten Salt Fast Reactor (MSFR) steady-state conditions and behavior during accidental transients. Six scenarios are investigated, ranging from over-cooling to total loss of heat sink, including both pump coast-down and over-speed failures. Despite the reactor design still being at a preliminary stage (in terms of geometry, heat exchanger and pumps specifications, etc.), the goal of this study is to obtain a general characterization of the MSFR and to detect potential risks for its safe operation. A second goal is to investigate possible numerical challenges in the simulation of these complex scenarios. The results prove that in general the reactor exhibits an excellent behavior from the safety point of view during all the analyzed transients. The salt temperature always remains far from both the freezing point and the critical temperature jeopardizing structural integrity. However, the current reactor design is characterized by very limited natural circulation. Therefore, further optimization efforts should focus on a reduction of the pressure losses in the primary circuit.

5.1 Introduction

Numerical simulations play a fundamental role in the progress of nuclear reactor designs belonging to Generation IV. This is true in particular for the Molten Salt

Fast Reactor, due to the current unavailability of experimental molten salt reactors. Moreover, operational experience has been obtained only with the Molten Salt Reactor Experiment, which was successfully operated at Oak Ridge National Lab in the late '60s (MacPherson, 1985). However, that reactor vastly differed from the current MSFR design in terms of neutron spectrum, core shape, presence of a graphite moderator, etc. Numerical analysis is therefore the only tool currently available to assess the safety of the MSFR design and to highlight potential threats or weak points to be addressed in further optimization stages.

During the EVOL project (EVOL, 2010–2013), a first large numerical simulation effort aimed at characterizing the MSFR behavior during transients and at steady-state was performed by Fiorina et al. (2014). Those simulations highlighted the presence of large salt recirculation regions inside the core cavity causing temperature hot spots. For this reason, CFD simulations were exploited by Rouch et al. (2014) to optimize the core shape from a hydro-dynamics point of view, removing the problematic hot spots. Similar analyses were carried out by Li et al. (2015) using the multi-physics COUPLE-SIMMER III code. First full-reactor, 3D simulations on the optimized MSFR geometry were carried out by Aufiero et al. (2014b), who investigated a pump coast-down accident happening in one of the sixteen recirculation loops, highlighting the potential risk of salt freezing during such a scenario. However, only a single-group diffusion neutronics model was used to limit the computational burden. A more advanced Transient Fission Matrix approach was implemented by Laureau et al. (2017) in their multi-physics simulation tool, used to carry out a large parametric study on the MSFR response during load-following, over-cooling, and reactivity insertion accidents.

More recently, Cervi et al. (2019a) developed a multi-physics solver based on a compressible, two-phase flow model that was employed to perform preliminary assessments of the effect of fuel compressibility during super-prompt critical transients and of the presence of helium bubbles dispersed in the salt mixture (Cervi et al., 2019c).

In this work, we use the multi-physics Discontinuous-Galerkin FEM (DG-FEM) tool recently developed at TU Delft described in Chapter 3 to perform new investigations of the MSFR steady-state and transient behavior. The most recent advancements in the characterization of the reactor design made during the SAMOFAR project (<http://samofar.eu/>) are taken into account. From this perspective, the results analyzed here should be considered the last outcome of the numerical simulation campaign aimed at investigating and improving the MSFR design.

However, the design of important components in the fuel circuit such as the pump or the heat exchanger is still undefined or only preliminary (Di Ronco et al., 2019). The transient behavior of the reactor is greatly influenced by these components and the way they are modeled though. The geometry of the outer-core region is still preliminary too. For these reasons, a comprehensive and exhaustive safety analysis of the MSFR is not possible yet. Nevertheless, as done by the previously mentioned authors, we can use our results to derive useful information on the reactor behavior

and to highlight potential critical issues that should be addressed in further design optimization studies. A second goal of this work is to identify and discuss potential numerical challenges in the simulation of these complex multi-physics scenarios, thus deriving useful information for similar studies in the future.

The chapter is organized as follows. In Section 5.2, we describe the choices adopted for the MSFR simulations. Chapter 3 already presented preliminary steady-state and transient calculations on the MSFR design, and the modeling choices adopted here remained unchanged for a large part. For this reason, we avoid repetition and focus only on the main differences. Section 5.3 is devoted to the analysis of the steady-state solution. It extends and completes the preliminary assessment reported in Chapter 3. In Section 5.4, we investigate the MSFR behavior during six transient scenarios. Finally, we draw some conclusions and provide some suggestions for future research efforts in Section 5.5.

5.2 Modeling choices

The simulations analyzed in this work were performed on the same MSFR design and very similar modeling choices adopted for the preliminary calculations described in Chapter 3. We considered also the same salt physical properties and neutronics data described in Sections 3.3.2.4 and 3.3.2.5. For this reason, we refer to the data and the information reported in Section 3.3, and we focus here on the relevant differences only.

We considered the same MSFR design parameters used for the preliminary calculations (reported in Table 3.2), except for the pressure drop across the heat exchanger, for which an updated value of 4 bar became available at the time of this study (Di Ronco et al., 2019).

All calculations were performed considering one recirculation loop only. Taking into account the mesh convergence studies reported in Section 3.4, we selected a mesh that could minimize the computational burden while still guaranteeing the accuracy of the solution. Figure 5.1 illustrates the mesh adopted. The master mesh, used for the neutronics calculations without any refinement, consists of 33924 tetrahedra (27674 in the fuel salt domain). For CFD calculations, the master mesh was refined once uniformly in the outer-core region (i.e., legs, pump, and heat exchanger) and once again close to the walls of the core region, resulting into 94902 elements in the fuel salt domain. Contrary to the mesh *M2* described in Section 3.3.2.1, we did not refine the walls of the outer-core region. In fact, this extra refinement proved to lead to minimal changes in the parameters of interest (see Figure 3.7 and Table 3.8), but it substantially increased the computational cost, which was not affordable for the transient simulations reported in the following. Moreover, a non-detailed resolution of the flow fields in the outer-core region is considered acceptable, given that the design of this region is still preliminary.

In all calculations reported below, we adopted a second-order polynomial ap-

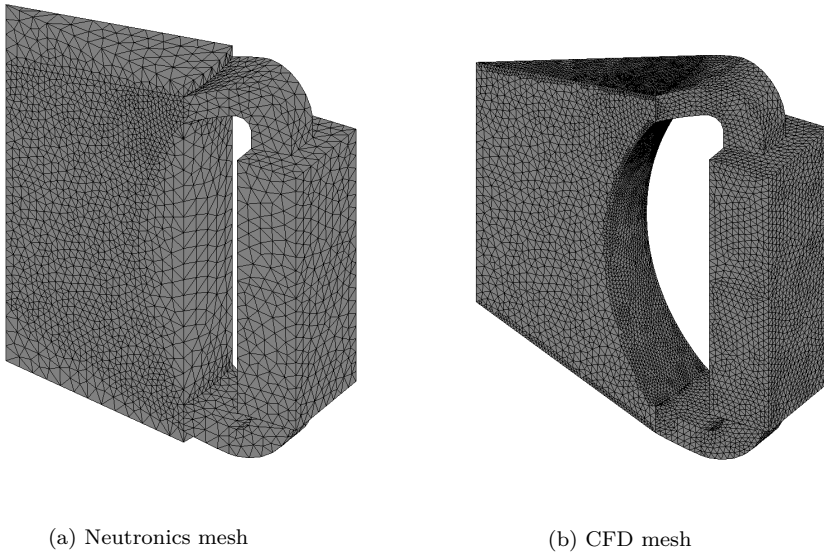


Fig. 5.1. Mesh adopted for the steady-state and transient calculations reported in this chapter. The neutronics mesh (left), corresponding to the master-mesh, consists of 33924 tetrahedra (27674 in the fuel salt domain), while the CFD mesh (right) has 94902 elements. The latter is derived by refining the former once uniformly in the outer-core region and once again close to the core wall boundaries.

proximation for the mass flux and a first-order one for all other quantities. An S_4 angular discretization was chosen for the neutron flux, taking into account the scattering anisotropy up to first order.

5.3 Assessment of the MSFR steady-state

The steady-state solution is the initial condition for any transient simulation, so it is fundamental to analyze it first. Actually, the steady-state solution obtained with the new design parameters and mesh is very close to the one obtained in our preliminary calculations described in Chapter 3. Some of its main aspects have already been analyzed in Section 3.4.1, in particular from the thermal-hydraulics point of view. For this reason, in the following sections we briefly summarize the main characteristics of the MSFR steady-state, avoiding repetitions, and then we highlight the differences (when necessary) or provide complementary information.

Table 5.1. Values of the parameters describing pump and heat exchanger used to obtain a steady-state solution.

Parameter (unit)	Value
Δp_{pump} (Pa)	5.033×10^5
K_{loss} (-)	2.497×10^2
γ ($\text{W m}^{-3} \text{K}^{-1}$)	1.995×10^7

Table 5.2. Relevant thermal-hydraulics design parameters obtained from the steady-state solution. Due to the high thermal diffusivity at the entrance of the heat exchanger active region, the ΔT_{hx} is lower than the desired 100 K (Allibert et al., 2016).

Quantity	Symbol	Unit	Value
Temperature difference across heat exchanger	ΔT_{hx}	K	89.2
Average temperature	T_{avg}	K	965.9
Maximum temperature	T_{max}	K	1083.1

5.3.1 Thermal-hydraulics analysis

Table 5.1 reports the final values of the pump head, the friction factor and the heat transfer coefficient in the heat exchanger selected to obtain a steady-state solution with the prescribed design specifications on the new mesh. The friction factor and consequently the pump head had to be reduced with respect to the values adopted for the preliminary calculations (Table 3.7) due to the lower pressure drop prescribed across the heat exchanger. From the value of the pump head, we notice that the extra pressure losses in the system, outside the heat exchanger region, amount to almost 1 bar. They are mainly due to the abrupt expansions and contractions, and the small-radius pipe bends characterizing the outer-core portion of the primary loop.

Table 5.2 and Figures 5.2–5.4 prove there are no significant changes in the steady-state solution with respect to the preliminary one analyzed in Section 3.4.1. As expected, the 11% lower flow resistance in the heat exchanger promoted a small increase of the natural circulation in the core cavity that enhanced mixing, thus leading to slightly lower temperature gradients. This is confirmed by the value of the maximum temperature reported in Table 5.2, almost 4 K lower than the one found in our preliminary calculations. However, the contribution of the natural circulation to the total flow rate remains negligible.

The main thermal-hydraulics characteristics of the steady-state solution are in general preserved with respect to our preliminary calculations:

- the salt temperature distribution presents axial but also radial gradients in the core (Figure 5.2). The hottest salt is in the upper-central region of the

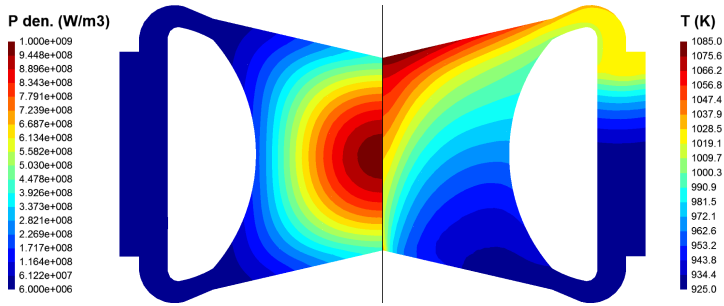


Fig. 5.2. Vertical mid-plane cuts of the power density (left portion) and temperature fields (right portion) obtained at steady-state.

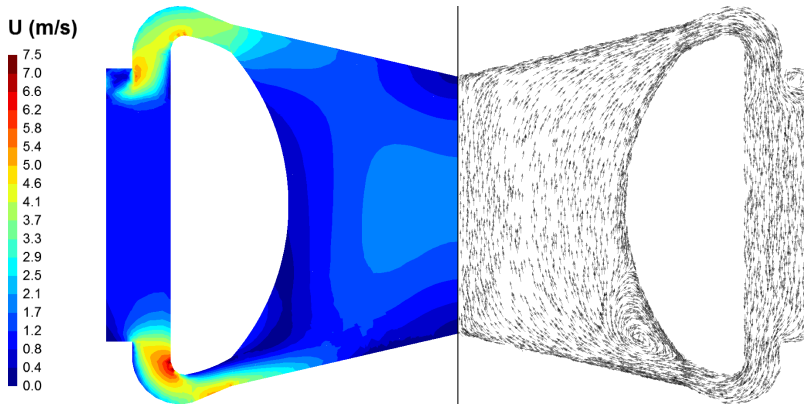


Fig. 5.3. Steady-state velocity field (vertical mid-plane cut): velocity magnitude (left portion), and flow direction (right portion). Boundary-layer detachment can be clearly noticed at the entrance of the core and at the entrance of the heat-exchanger box, due to the abrupt expansion.

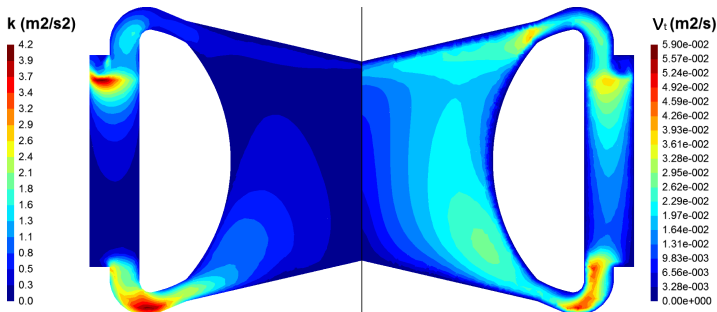


Fig. 5.4. Vertical mid-plane cuts of the turbulent kinetic energy (left portion) and eddy viscosity (right portion) fields obtained at steady-state. Thermal stratification suppresses turbulence in the core cavity.

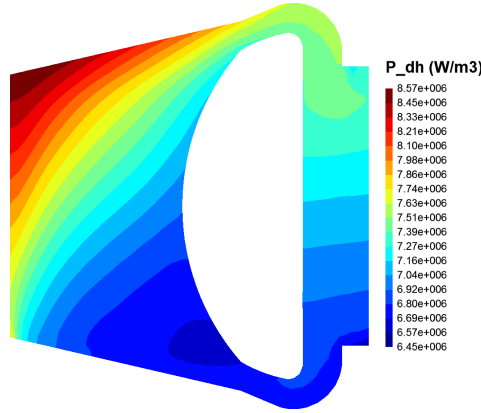


Fig. 5.5. Steady-state distribution of the decay heat power density source (vertical mid-plane cut). The contribution to the total power is around 4.3%.

core, where it is almost stagnant and the power level is high;

- a large recirculation region is detected at the entrance of the core (Figure 5.3), but it does not induce local hot spots, confirming the effectiveness of the core-optimization studies carried out during the EVOL project (Rouch et al., 2014);
- turbulence is suppressed in the core cavity by thermal stratification and peaks in the outer-core region, especially at the entrance of the heat exchanger due to the presence of a large recirculation region (Figure 5.4). Here, the high value of the eddy viscosity (and, consequently, of turbulent thermal conductivity¹) leads to a temperature drop across the heat exchanger of approximately 11 K lower than the desired 100 K (Allibert et al., 2016).

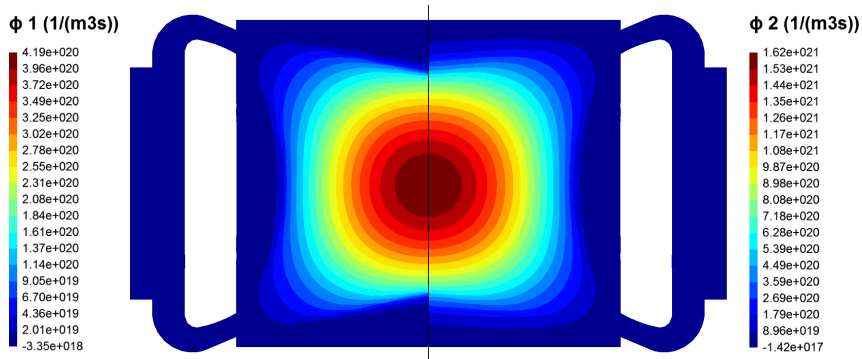
Finally, Figure 5.5 shows the distribution of the decay heat production rate. The long-lived fission products are distributed almost uniformly in the entire domain, which leads to a fairly uniform power distribution. With 129.6 MW, decay heat contributes to the 4.32 % of the total power at steady-state.

5.3.2 Neutronics analysis

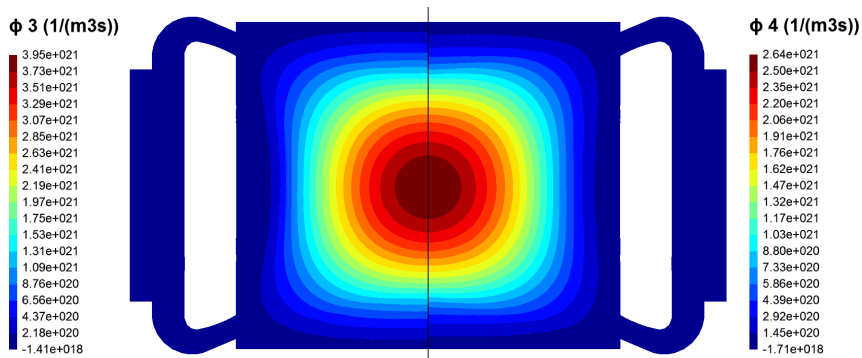
Figure 5.6 shows the 6-groups scalar fluxes in the entire domain. The highest flux values are in the epithermal region, as expected from the reactor spectrum (Fiorina et al., 2013; Heuer et al., 2014; Brovchenko et al., 2019). Fast neutrons have the highest probability to be captured by the fuel, hence their negligible presence in

¹In the core region, the turbulent thermal conductivity is around 20 times larger than the molecular one on average, but it reaches peaks 70 times larger in the external sector.

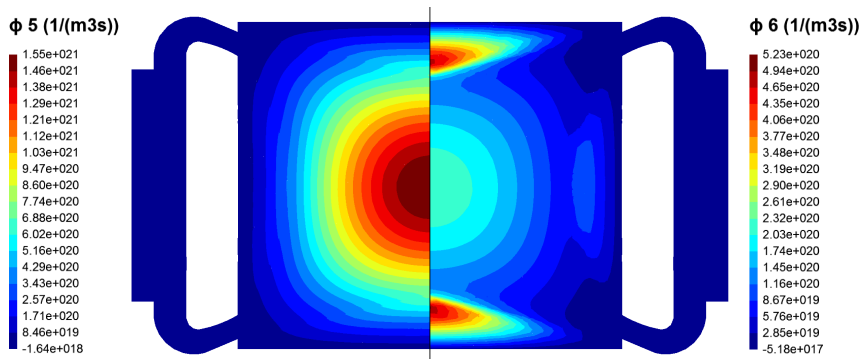
5. Analysis of the MSFR steady-state and transient behavior



(a) Scalar flux groups 1 (left) and 2 (right).



(b) Scalar flux groups 3 (left) and 4 (right).



(c) Scalar flux groups 5 (left) and 6 (right).

Fig. 5.6. Vertical mid-plane cuts of the steady-state scalar flux in each energy group (the scale changes in each plot). As expected, the fast and epithermal fluxes are negligible outside the salt domain, whereas the thermal flux has a peak in the reflectors.

the blanket or reflector regions, where, on the other hand, there is a peak of the lowest-energy flux. This is due to the high scattering cross section characterizing the reflector material.

Flux values in the reflectors and blanket must be taken with a grain of salt though. The temperature field is not resolved in these regions, so a uniform and constant value of $T = 900$ K was considered in all our calculations. This was done to be consistent with the calculations performed by other partners within the SAMOFAR project, whose results will be compared with the ones reported here in a forthcoming publication. They did not consider blanket and reflectors in their neutronics calculations but used albedo boundary conditions with albedo coefficients evaluated with Serpent at the reference temperature of $T = 900$ K. Realistically, the temperature is expected to be higher than 900 K in these regions, especially in the upper reflector (in contact with the hottest salt) and in the blanket, where a heat source estimated around 25 MW is present due to spontaneous fission of ^{233}U and radiative capture of ^{232}Th in the fertile salt (Rouch et al., 2014). Anyway, this approximation is considered to have a negligible impact on the accuracy of our calculations, especially considering the level of uncertainty of the reactor design.

Finally, one can notice negative values in the legends of Figure 5.6. This is of course nonphysical, but possible with a DG-FEM discretization. In this case, negative values are found in the heat-exchanger or in the outermost portion of the reflectors: this is due to the low resolution in those regions (coarse mesh and first-order polynomial discretization) and to the vicinity of vacuum boundaries. However, these are regions of very low importance, so the impact on the overall solution and on reaction rates is negligible.

The multiplication factor is reported in Table 5.3: the reactor is supercritical, so the concentration of fissile material should be adjusted accordingly. However, this was outside the scope of the present analysis. The MSFR strongly relies on the temperature feedback to control reactivity variation, as control rods are absent in the SAMOFAR reactor design. To quantify the total feedback (Doppler plus density) coefficient, we ran multiple criticality eigenvalue calculations assuming an isothermal reactor but with the true steady-state flow field. Results are reported

Table 5.3. Effective multiplication factor as a function of the average salt temperature. The first line represents the values characterizing the steady-state solution.

T_{avg} (K)	k_{eff} (-)	Reactivity (pcm)
965.9	1.00998	988.3
900	1.01343	1325.3
1000	1.00917	908.9
1100	1.00499	496.1
1200	1.00083	82.98

in Table 5.3. The total fuel temperature feedback is around -4.1 pcm K^{-1} for all the intervals considered, which is consistent with data reported by Heuer et al. (2014) for a TRU-started MSFR at Beginning Of Life. By comparing the reactivity value obtained at steady-state and the associated average temperature, we realize the latter is not suitable to quantify feedback effects. In fact, the salt average temperature in the reactor follows from energy conservation and the selected minimum temperature in the system. For reactivity estimations, one should compute an “effective” average temperature, that is, weighted by the adjoint flux. With the aforementioned feedback coefficient, we can estimate the steady-state effective average temperature to be 980.9 K.

Finally, Figure 5.7 shows the distribution of each family of delayed neutron precursors. As expected, the concentration in the entire domain is the more uniform the longer the family half-life. This is confirmed by the percentages of delayed neutrons emitted in the core region by each family reported in Table 5.4. In particular, we notice that the first four families emit delayed neutrons with almost the same probability in the entire domain (the in-core salt volume is 50 % of the total, see Table 3.2), whereas only 7 % of the shortest-lived precursors decay outside the core. In total, 55.76 % of delayed neutrons are lost in the low-importance outer-core regions, thus reducing the β_{eff} (Aufiero et al., 2014a). As our code system is based on a rigorous time-dependent model, it has no need for explicit β_{eff} calculations. However, by comparing the results of a criticality eigenvalue calculation adopting static-fuel conditions (with the steady-state temperature field), we could find that reactivity is reduced by 259 pcm by the precursors drift. This $\Delta\beta_{eff}$ is in good accordance with the data reported by Aufiero et al. (2014a) for the EVOL MSFR geometry and the TRU- ^{235}U fuel composition, taking into account the difference in effective in-core-to-total volume ratio between the EVOL and the SAMOFAR reactor geometries.

Table 5.4. Half-life of each family of precursors and corresponding fraction of delayed neutrons emitted in the core region. The first four families emit neutrons with the same probability both in and outside the core, whereas the short-lived precursors mostly decay inside the core region.

Family, i	$T_{1/2}$ (s)	$\frac{\int_{core} \lambda_i C_i d\mathbf{r}}{\int_{total} \lambda_i C_i d\mathbf{r}}$ (%)
1	55.6	49.66
2	24.5	49.74
3	16.3	49.78
4	5.21	50.31
5	2.37	52.01
6	1.04	58.64
7	0.42	77.23
8	0.20	92.73

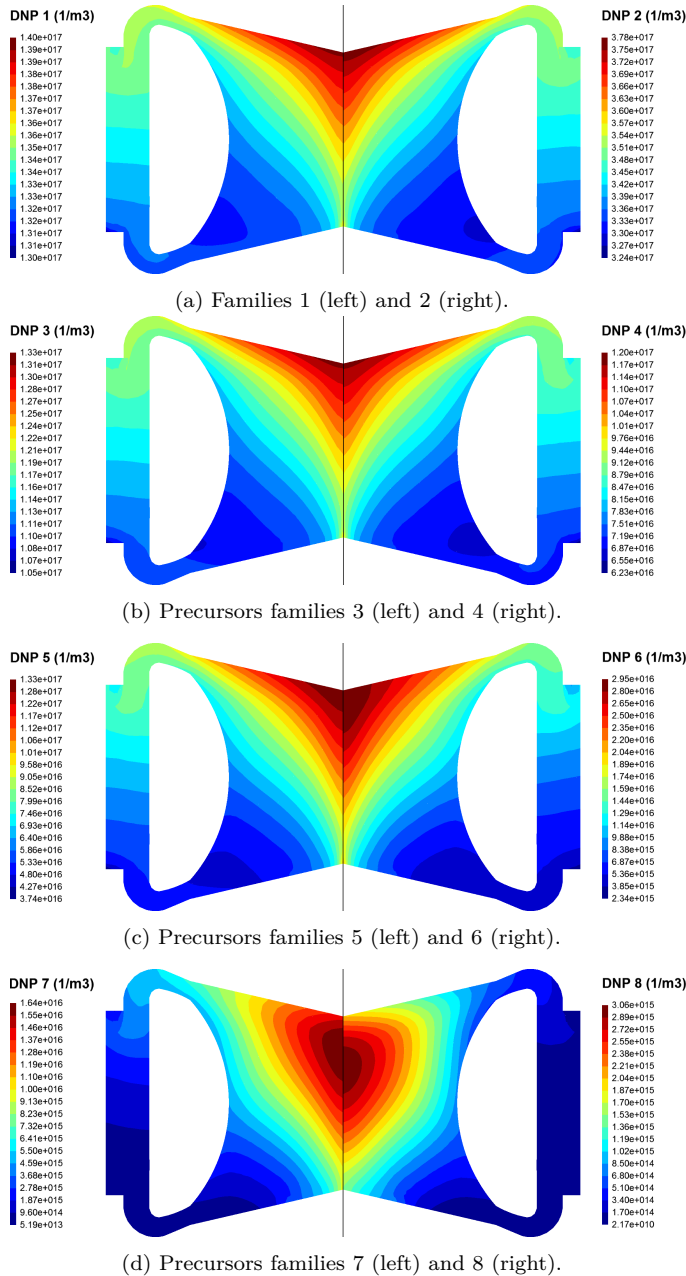


Fig. 5.7. Steady-state distributions of each family of neutron precursors, along the reactor vertical mid-plane (the scale changes in each plot). Families with long half lives have high concentrations in the outer-core region, reducing the margin to prompt-criticality. Short-lived precursors mostly decay in the core.

5.4 Analysis of MSFR transient behavior

In this section, we investigate the MSFR behavior during several beyond-operational transients. All scenarios are supposed to be “unprotected”, that is, no mitigating actions are taken into account throughout the simulation. Only the free-dynamics of the reactor is therefore analyzed. Moreover, all scenarios are supposed to be symmetric, that is, happening in all sixteen circulation loops at the same time. This allowed us to perform calculations with the one-sixteenth mesh shown in Figure 5.1, thus greatly relieving the computational burden of the simulations.

Two main transients initiators were considered:

- a failure of the fuel-circuit pump, experiencing either a coast-down or an over-speed;
- a quick change in the heat removal capabilities in the heat exchanger, leading to a loss of heat-sink or an over-cooling transient; and
- a superposition of both, typically stemming from a loss of electricity in the entire power plant.

As described in the following, both the primary pump over-speed and the over-cooling transients lead to positive reactivity insertions, but other more “classical” over-power accidents (prompt or super-prompt critical) as those described by Fiorina et al. (2014) were not investigated, for two main reasons. First, it is difficult to imagine a realistic transient initiator leading to a uniform reactivity insertion. Control rods are absent in the MSFR, so reactivity can be inserted accidentally in the core only by a malfunction in the helium bubbling system (used in fact also for reactivity control purposes (Delpech et al., 2009)) and/or in the chemical reprocessing plant connected to the reactor. Both initiators involve a local injection of fissile material or helium bubbles, therefore the transport of species or of a gaseous phase in the salt should be simulated to properly investigate this transient. This is not yet possible with our simulation tool. On top of this, recently Aufiero et al. (2017) and Cervi et al. (2019a) proved that taking into account the fuel compressibility is essential to model correctly the fuel-expansion feedback during rapid super-prompt critical transients. Our code system implements an incompressible flow solver at the moment, but the incompressibility hypothesis leads to an overestimation of the density feedback because it acts as prompt, whereas in reality density perturbations propagate at the speed of sound in the salt, which is finite (~ 1200 m/s). This phenomenon acts therefore on time scales of a few milliseconds typically, a thousand times longer than the lifetime of a prompt neutron in a fast reactor (≤ 1 μ s) (Aufiero et al., 2017; Cervi et al., 2019a).

Six transient scenarios were investigated: (two types of) loss of heat sink (ULOHS), loss of fuel flow (ULOFF), pump over-speed (UPOS), over-cooling (OVC), and total loss of power (TLOP). All of them start from the steady-state

solution described in Section 5.3. The reactor was forced to be critical at $t = 0$ by scaling the fission operator by a factor $1/k_{eff}$.

5.4.1 Unprotected Loss of Heat Sink (ULOHS)

The first class of scenarios considered in this work consists of a reduction of the capability to remove heat from the fuel circuit resulting in a rise of the average temperature of the salt.

These transients are initiated by malfunctions in the intermediate circuit or in the Energy Conversion System (ECS). For example, a reduction in the intermediate mass flow rate decreases the heat transfer coefficient with the fuel salt in the primary heat exchangers. A reduction of the mass flow rate in the ECS induces a rise in the average temperature of the intermediate salt, thus decreasing the fuel salt cooling capabilities (see the model of the primary heat exchanger described in Section 3.3.2.3).

In the following two sections we investigate two kinds of ULOHS transients: the first is very conservative, while the second is based on more realistic assumptions.

5.4.1.1 Total ULOHS

This transient is initiated by a step reduction to zero of the volumetric heat transfer coefficient γ of the primary heat exchanger (Equation (3.24)). No power is therefore extracted from the fuel circuit from $t = 0$, and no other heat exchange mechanisms are possible due to the adiabatic boundary conditions imposed (Section 3.3.2.6). The scenario is very unrealistic (a fraction of the total power can always be dissipated to the environment through passive mechanisms as conduction or radiative heat transfer), but it is characterized by the most severe conditions and therefore provides conservative results on the MSFR response to this class of accidents.

Simulations were carried out for the first 80s choosing a coupling time step size $\Delta t = 0.02$ s, with 20 sub-steps performed in DGFlows to limit the CFL number in the CFD calculations and avoid numerical instabilities.

Figure 5.8 shows the MSFR response to the transient initiator in terms of power and salt temperature. The average salt temperature starts to rise as soon as the heat removal is set to zero in order to obey energy conservation. The negative reactivity introduced quickly induces a significant drop in the power, after a time delay of 1s both due to the precursors hold-back and the necessary salt flow time from the heat-exchanger to the high-importance regions in the core. The power trend is exponential, given by the superimposition of the decay-heat curve and the contribution of the delayed neutron precursors. However, during the first 20s, oscillations are clearly visible with a period of almost 4s. This is a peculiar phenomenon of liquid fuel reactors and is due to the precursor drift. When the power is still at 3GW, a certain amount of precursors exit the core

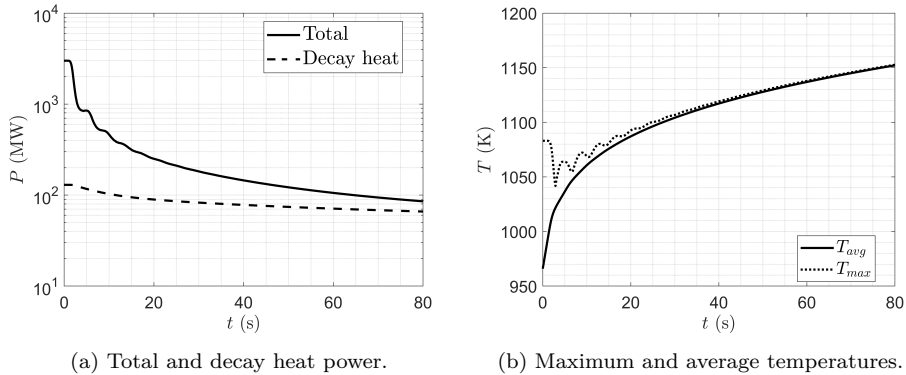


Fig. 5.8. Total ULOHS: time evolution of power (left) and salt average and maximum temperature (right).

region and travel through the external sector. Part of the longest-lived fraction decays after re-entrance in the core, where in the meantime the power dropped due to thermal feedback. This injection of extra neutrons induces therefore a local peak in the power or at least slows down its decay. The phenomenon has a frequency determined by the salt circulation time (here, 4 s), but after 20 s is no longer detectable as most of the long-lived precursors produced at the highest power level have already decayed. After 80 s, the power level is around 85.4 MW, 77% of which is given by decay heat. The remaining 23% is still due to the slow decay of the long-lived fraction of delayed neutron precursors.

The maximum salt temperature (Figure 5.8b) drops by almost 40 K after 1 s due to the fast reduction of the power, then it increases with 4 s-period oscillations that follow those of the power. Temperature gradients are quickly smeared out and, after 30 s, the difference between the maximum and the average salt temperature is reduced to less than 3 K. The quick temperature homogenization is confirmed by the snapshots of the temperature distribution inside the reactor shown in Figure 5.9.

Without any mechanism of heat extraction or dissipation, the salt temperature will increase further and could reach the critical value of 1200 °C at which the reactor incurs structural damages. The MSFR is equipped with passive safety devices, called freeze-plugs, which are valves of frozen fuel salt meant to melt fast enough to allow for the drainage of the salt in large passively-cooled tanks placed underneath the core before any damage occurs (Tiberga et al., 2019b; Massone et al., 2020). Clearly, the design of these components is strongly affected by the grace time before the salt reaches the critical temperature. Despite we simulated only the first 80 s of the ULOHS transient, after which the average temperature is still way below 1200 °C, we try in the following to give an estimation of this

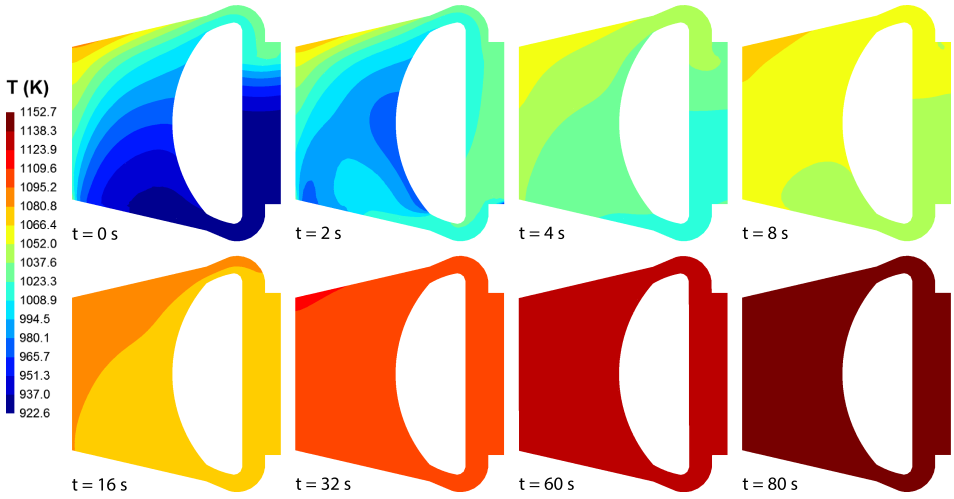


Fig. 5.9. Total ULOHS: evolution of salt temperature distribution (vertical mid-plane cuts).

important safety parameter.

Our calculations showed that the salt temperature distribution after 80 s is very homogeneous in the entire reactor. Hence, the trend of the average temperature can be very well approximated by

$$T_{avg}(t) = T_{avg}(t = 80 \text{ s}) + \frac{1}{V\rho_{salt}c_p} \int_{80}^t P(t)dt, \quad (5.1)$$

where V is the total volume of the reactor, $\rho_{salt}c_p$ is the salt volumetric heat capacity, $t \geq 80$ s, and P is the residual power. We considered two approximations for the two contributions to the residual power (decay heat and residual fission power due to the slow decay of the long-lived precursors):

- constant (very conservative): $P(t) = P_{fiss}(t) + P_{dh}(t) = P_{fiss}(t = 80 \text{ s}) + P_{dh}(t = 80 \text{ s}) = 85.4 \text{ MW}$;
- exponential (realistic): $P(t) = P_{fiss}(t) + P_{dh}(t) = A_{fiss}e^{-t/\tau_{fiss}} + A_{dh}e^{-t/\tau_{dh}}$,

where $A_{fiss} = 181.2 \text{ MW}$, $\tau_{fiss} = 35.8 \text{ s}$, $A_{dh} = 86.17 \text{ MW}$, $\tau_{dh} = 299.5 \text{ s}$. These constants were obtained from an interpolation of the power values during the last 5 s of the transient.

Figure 5.10 shows the extrapolated trends of the average temperature computed up to 1000 s with Equation 5.1 for the two approximations of the residual power. With a realistic exponential approximation of the power, it seems the temperature never reaches the critical value. Even if encouraging, this should be taken with

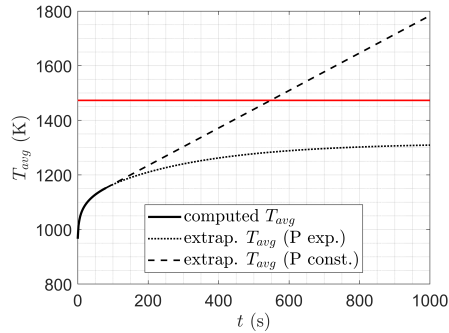


Fig. 5.10. Total ULOHS: extrapolation of average salt temperature to evaluate grace time before reaching the critical temperature of 1200 °C indicated with the red line.

a grain of salt, because the decay heat model we used is a valid approximation of the Serpent burnup results only up to a few minutes (Aufiero et al., 2014b). Nevertheless, it can be seen that the highly conservative linear extrapolation of the temperature reaches the critical value only after 547.5 s. Therefore, we conclude that the grace time is at least 15 % longer than the 480 s estimated by Brovchenko et al. (2013).

5.4.1.2 Partial ULOHS

The second ULOHS transient considered is a more realistic scenario. The insufficient fuel salt cooling is initiated by the failure of both the intermediate and the ECS pumps, resulting in a reduction of the mass flow rates in those circuits to 20 % of the nominal value. This increases the intermediate salt average temperature and decreases the heat transfer coefficient of the primary heat exchanger according to

$$\gamma(t) = \gamma(t_0) - [\gamma(t_0) - \gamma(t_{end})] (1 - e^{-t/5}), \quad (5.2a)$$

$$T_{int}(t) = T_{int}(t_0) + [T_{int}(t_{end}) - T_{int}(t_0)] (1 - e^{-t/5}). \quad (5.2b)$$

The exponential trend with time constant of 5 s was assumed to mimic the pumps coast-down, in absence of more detailed design specifications for these components. The initial values $\gamma(t_0) = 1.995 \times 10^7 \text{ W m}^{-3} \text{ K}^{-1}$ and $T_{int}(t_0) = 650 \text{ °C}$ are the ones used to get the steady-state solution (Section 3.3.2.3), whereas the final values $\gamma(t_{end}) = 6.720 \times 10^6 \text{ W m}^{-3} \text{ K}^{-1}$ and $T_{int}(t_{end}) = 688 \text{ °C}$ correspond to the reduced intermediate and ECS mass flow rates. They were computed by the SAMOFAR partners from Politecnico di Milano using a recently developed power plant simulator for the MSFR (Tripodo et al., 2019).

As for the previous ULOHS transient, we simulated the first 80 s using a coupling time step size $\Delta t = 0.02 \text{ s}$ with 20 sub-steps performed in DGFloWS.

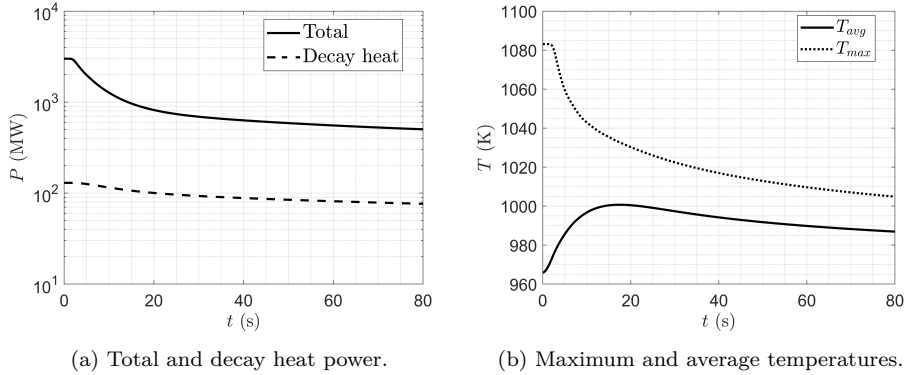


Fig. 5.11. Partial ULOHS: time evolution of power (left) and salt average and maximum temperature (right).

The MSFR response to the perturbations described by Equation 5.2 is depicted in Figure 5.11, in terms of power and temperature trends. The transient is much milder than the total ULOHS described in the previous section. The average temperature increases by almost 35 K in the first 18 s, inducing a quick reduction of the total power. Afterwards, it decreases due to the balance between the extracted and the produced power. After 80 s, the system has almost reached a new steady-state at around 500 MW and 986 K average temperature. A true steady-state can however be reached only after hundreds of seconds, due to the slowly vanishing exponential terms in the power deriving from the decay heat and the long-lived precursors.

Figure 5.12 shows a few snapshots of the temperature distribution in the MSFR during the transient. The temperature does not homogenize as during the total ULOHS, but gradients are quickly smeared out. The average effective temperature in the core has to go back to the nominal value when criticality is restored. In fact, the salt temperature in the core at $t = 80$ s lies between 975 K and 1000 K.

To conclude, Figure 5.11b also shows the trend of the maximum temperature, which follows the power trend: it quickly decreases due to the reduced power-to-flow ratio. Therefore, no threats for the reactor integrity can be detected during this kind of transients.

5.4.2 Unprotected Loss of Fuel Flow (ULOFF)

The second class of transients is initiated by a failure of the primary circuit pump. Lacking any design specification, we modeled the pump coast-down with an exponential law having a time constant of 5 s that realistically takes into account

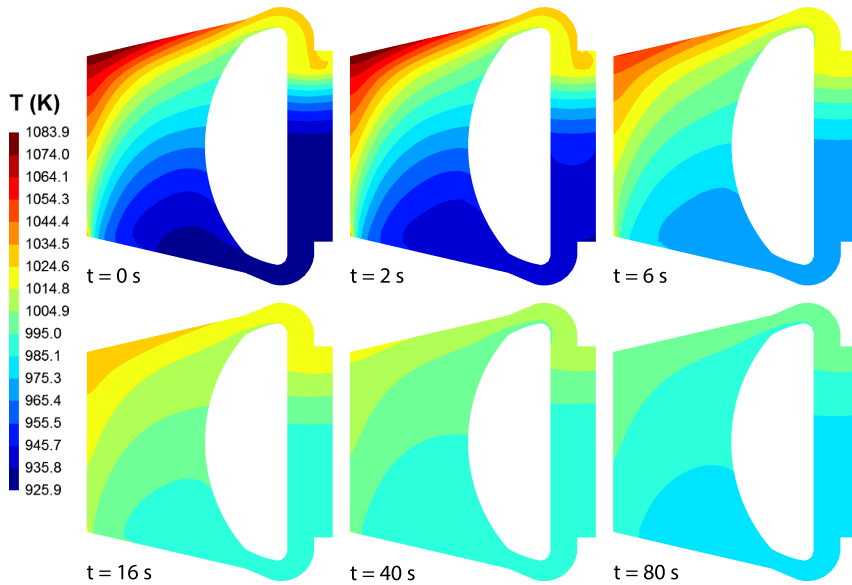


Fig. 5.12. Partial ULOHS: evolution of salt temperature distribution (vertical mid-plane cuts).

the pump's flywheel inertia. The pump force is modeled by

$$\mathbf{F}_{pump}(t) = \mathbf{F}_{pump}(t_0) e^{-t/5}, \quad (5.3)$$

where $\mathbf{F}_{pump}(t_0)$ is the steady-state momentum source computed according to Equation (3.22).

The heat transfer coefficient in the heat exchanger was not modified, because the flow is expected to have laminar conditions in the small channels of the printed circuit design (Di Ronco et al., 2019) independently of the fuel mass flow rate, thus leading to a constant Nusselt number. We simulated the first 30 s of the transient, using a coupling time step size $\Delta t = 0.02$ s with 20 sub-steps performed in DGFloWS.

Figure 5.13 shows the time evolution of the most relevant quantities monitored throughout the simulations. The salt volumetric flow rate closely follows a theoretical exponential decay with time constant equal to 10 s, which comes from the proportionality with the square root of the pressure drops in the system (which, of course, follow the trend of the pump head). The contribution of natural circulation becomes clear only after 20 s. The flow rate departs from the exponential trend and almost reaches a plateau around $0.3 \text{ m}^3 \text{ s}^{-1}$ at 30 s. At the end of the simulated portion of the transient, the salt flow rate is limited to 6.5% of the nominal value only.

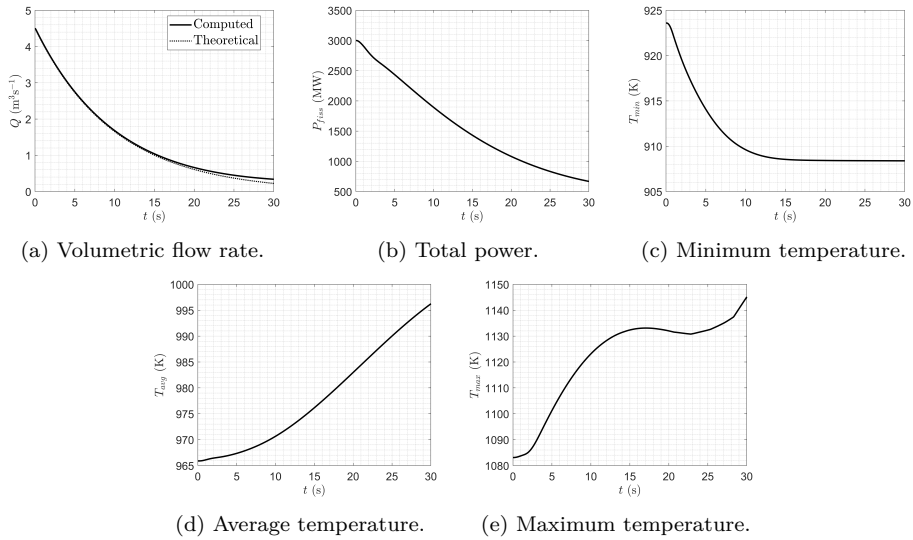


Fig. 5.13. ULOFF: time evolution of the most relevant characteristic quantities.

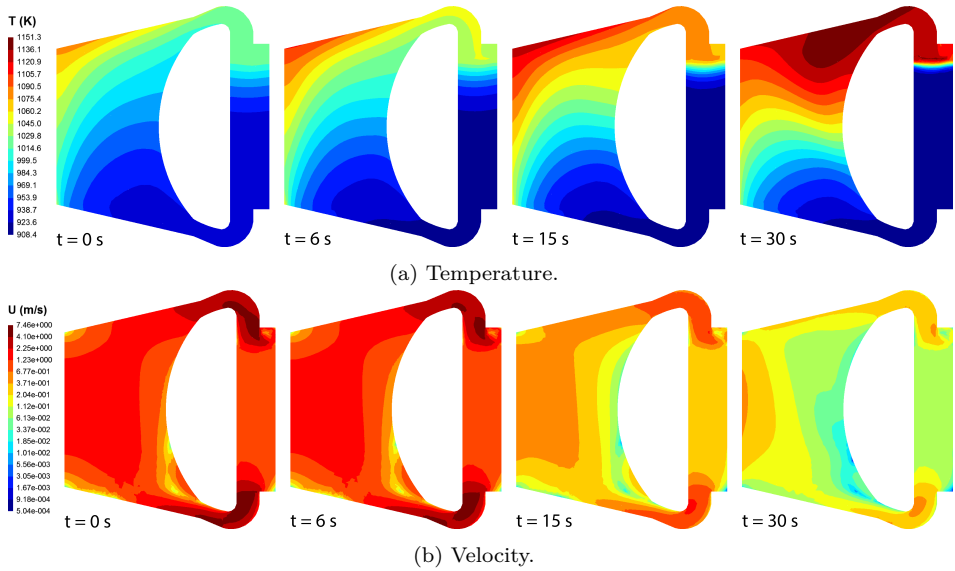


Fig. 5.14. ULOFF: evolution of the distributions of temperature and velocity along the reactor vertical mid-plane. The latter plot uses a logarithmic scale to magnify the low velocity magnitudes at the end of the transient.

The flow rate reduction induces two effects with opposite repercussions on the reactor power. It reduces the fraction of neutron precursors leaving the core region, increasing β_{eff} and introducing positive reactivity. On the other hand, it quickly leads to a rise of the temperature level in the system, due to the increased power-to-flow ratio, thus introducing large amounts of negative reactivity. Clearly, the second effects prevails, and the reactor power starts to decrease soon after the initiating event, after a few instants in which it stays constant due to the precursors hold-back (Figure 5.13b). The reactor power is at 670 MW after 30 s, with a power-to-flow ratio almost three times larger compared to nominal conditions.

Figures 5.13c, 5.13d, and 5.13e show the time evolution of the minimum, average, and maximum salt temperature in the core, respectively. The minimum temperature decreases following the reduction of the salt flow-rate. It reaches a steady-state value of 908 K after almost 15 s. However, this behavior is determined by the fact that this lower limit corresponds to the average temperature of the intermediate salt used to model the heat removal in the heat exchanger (Equation (3.24)).

The average temperature, as already explained, rises due to the increased power-to-flow ratio and to compensate the increase of the β_{eff} , but not without bound. Even if a new steady-state value is not reached within the simulated portion of transient, one can notice a change in the sign of the second derivative of the curve, indicating that this will happen, at a value lower than 1000 K, quite far from the critical temperature of 1200 °C inducing structural damages. When the criticality condition is restored, we expect the average effective temperature in the reactor to rise by around 60 K to compensate for the increase of β_{eff} .

The maximum temperature trend is encouraging as well: it first increases by about 50 K in the first 15 s of the transient, then starts to decrease. However, from 23 s it quickly starts to increase again. This is unfortunately the sign of the onset of numerical instabilities, due to the very low salt velocities and thus turbulent levels in the core cavity.

This is illustrated more clearly by Figures 5.14 and 5.15. The latter compares the eddy viscosity distribution in the reactor at the beginning and end of the simulations. It can be seen that it decreased by almost two orders of magnitude in general, and it gets even lower in the top-right region of the core cavity at the boundary with the blanket, where its value is close to the molecular viscosity. From Figure 5.14b, we see this region is characterized by very low salt speed. Despite the flow pattern in the core did not change throughout the simulation (as confirmed by Figure 5.16), this region is probably experiencing the onset of a secondary vortex, extending throughout the boundary with the blanket and eventually merging with the primary vortex at the inlet to the core cavity. The incipient growth of a secondary vortex seems to be confirmed by the plots of the evolution of the temperature distribution shown in Figure 5.14a. In the upper half of the core cavity, the radial temperature gradient is almost null at 15 s and becomes even positive at 30 s.

The reason for the numerical instability detected in Figure 5.13e is now clear.

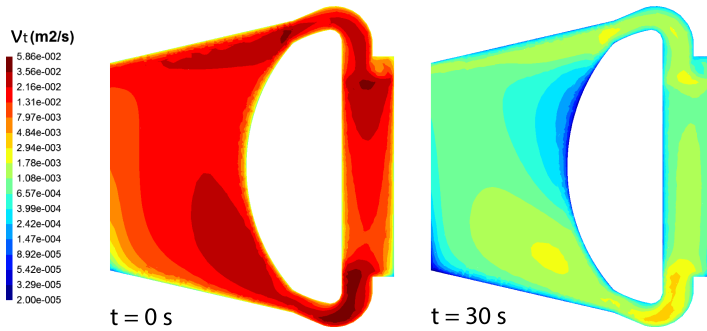


Fig. 5.15. ULOFF: eddy viscosity distribution along the reactor vertical mid-plane at the beginning and the end of the transient. A logarithmic scale is adopted to magnify the low values at $t = 30$ s.

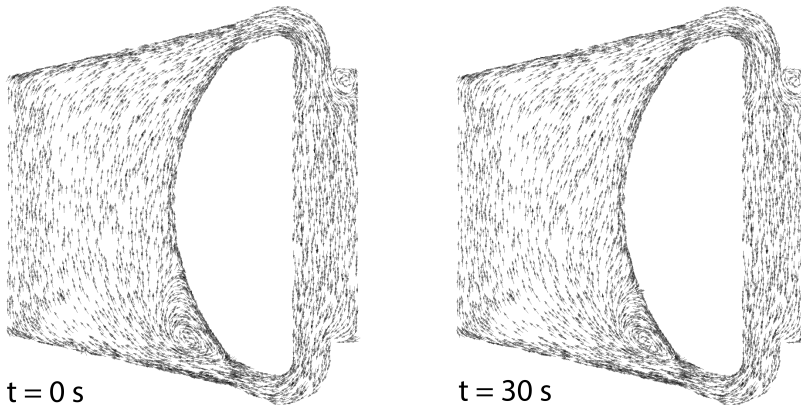


Fig. 5.16. ULOFF: flow pattern at the beginning and the end of the transient (vertical mid-plane cuts). No relevant changes can be detected.

From $t = 15$ s, very low values of turbulent viscosity and therefore thermal conductivity are found not only at the boundaries but also in a region (growing in size) in the upper-central portion of the core cavity, where the spatial resolution (not-fine-enough mesh combined with first order polynomial approximation of the enthalpy) is no longer sufficient to properly resolve the large localized temperature gradients (induced by the low salt conductivity), which therefore grow without bound. This most likely explains also why the hottest salt location moves from the central-upper part of the core more towards the outer leg, close to the region of low thermal conductivity.

Finally, from Figure 5.14a we notice that from 15 s onward a large portion of the heat exchanger is inactive, because the fuel salt temperature reaches the (assumed) average temperature of the intermediate salt. Consequently, huge temperature gradients are found at the entrance of the heat exchanger. A more realistic model

for this component is therefore required to properly simulate this transient. The minimum salt temperature might get much closer to the freezing point than is apparent from our calculations.

5.4.3 Total Loss of Power (TLOP)

A sudden power plant blackout would stop the ECS, intermediate, and primary pumps simultaneously, so the active cooling of the fuel salt would become impossible. This scenario is therefore a combination of the ULOHS and the ULOFF analyzed in the previous sections, and it is considered one of the most severe accidents that could occur in the MSFR. For this reason, we chose to adopt a conservative approach and study the reactor response to the worst case scenario, that is, a reduction to zero of the salt cooling capabilities from $t = 0$, combined with adiabatic boundary conditions that do not allow any heat dissipation. The transient is therefore modeled with

$$\gamma(t) = 0, \quad (5.4a)$$

$$\mathbf{F}_{pump}(t) = \mathbf{F}_{pump}(t_0) e^{-t/5}. \quad (5.4b)$$

Here, we extend the preliminary investigation carried out in Chapter 3 and analyze the first 70 s of the transient. For the simulations, we used a coupling time step size $\Delta t = 0.02$ s with 20 sub-steps performed in `DGFloWS`.

The MSFR response to the transient is described by the time evolution of the quantities reported in Figure 5.17. As for the ULOFF transient, the salt flow rate decreases with an exponential trend with time constant of 10 s. However, natural circulation is hindered here by the suppression of heat removal, therefore the departure from the exponential trend takes place only after 45 s. At 70 s, the flow rate reached a steady-state value of $0.08 \text{ m}^3 \text{ s}^{-1}$, lower than 2% of the nominal value.

The power trend is also very similar to the one analyzed for the total ULOHS transient (Section 5.4.1.1). After a couple of seconds during which the power is maintained at 3 GW by the precursor decay, it quickly drops following an exponential decay due to the rise of the average salt temperature. The “wave” at around 7 s is again due to the re-entrance and decay in the core region of the delayed neutron precursors exited when the power was still at nominal level. Other power oscillations are too small to be detected here, because the quick reduction of the mass flow rate and the resulting increased flow-through period damp the phenomenon. At the end of the simulation, the residual power is 102.2 MW, 67% of which stems from decay heat.

The average temperature, reported in Figure 5.17c, is bound to grow indefinitely due to the complete absence of heat exchange mechanisms with the external environment. Repeating the analysis carried out for the total ULOHS transient (Section 5.4.1.1), we can derive useful information on the grace time before the

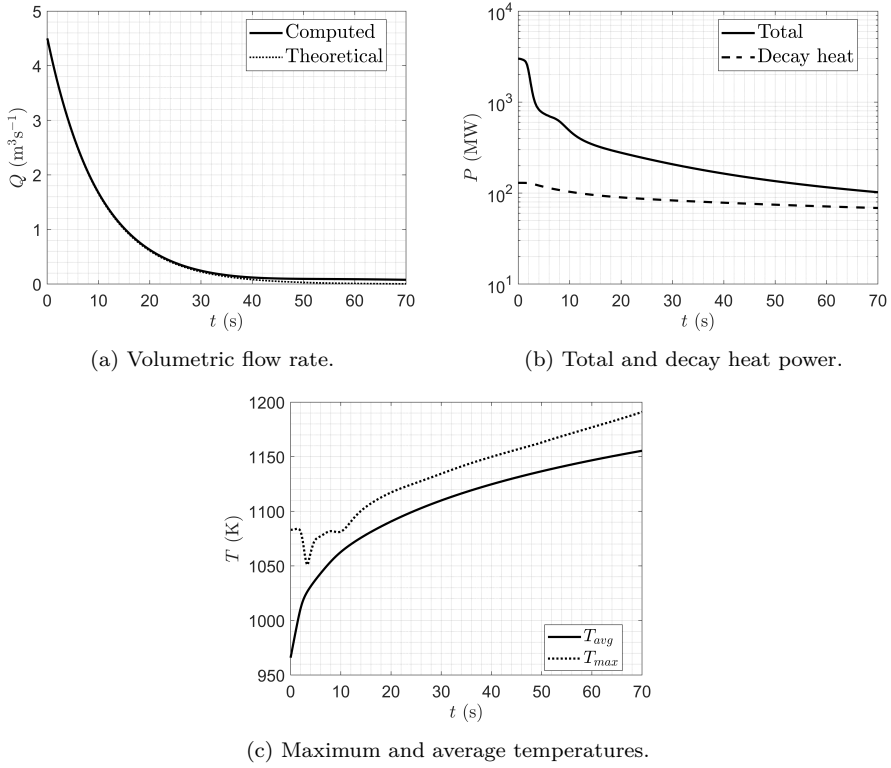


Fig. 5.17. TLOP: time evolution of most relevant characteristic quantities.

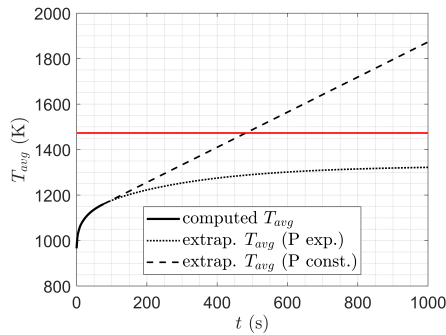


Fig. 5.18. TLOP: extrapolation of average salt temperature to evaluate grace time before reaching the critical temperature of 1200°C indicated with the red line.

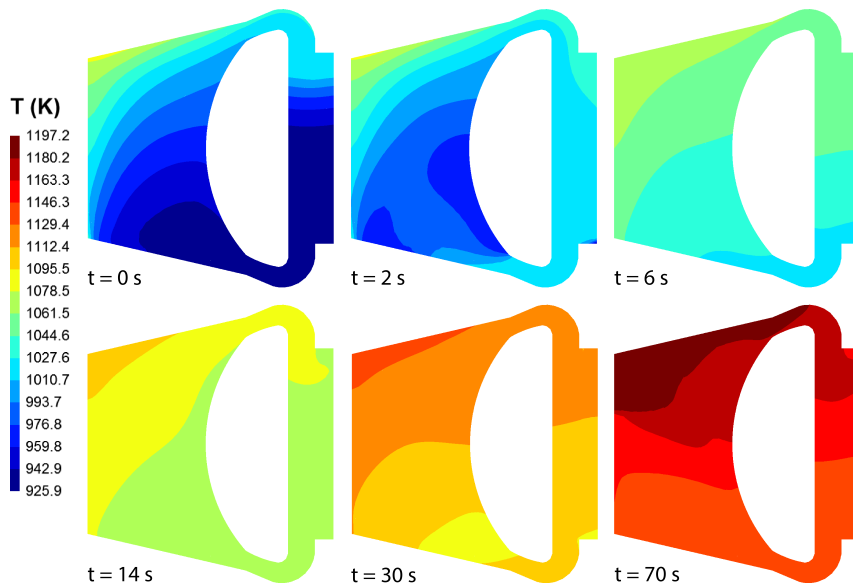


Fig. 5.19. TLOP: evolution of salt temperature distribution (vertical mid-plane cuts).

average temperature reaches the dangerous value of 1200°C . Figure 5.18 shows the extrapolated trends obtained with a very conservative (constant) and a more realistic (exponential) approximation of the residual power trend. The constants of the latter trend were obtained by interpolation of the data in the last 5 s of the transient. The constant A_{fiss} had to be updated to 236.9 MW. Once more, the realistic extrapolation never reaches the critical threshold, whereas the expected grace time for the linear extrapolation is 481 s.

Contrary to the total ULOHS, however, the salt temperature during a total loss of power accident is not uniform inside the reactor. This can be noticed from the snapshots of the temperature field reported in Figure 5.19 and the evolution of the maximum salt temperature displayed in Figure 5.17c. After an initial drop of 30 K and a few oscillations in the first 15 s, which follow from the behavior of the residual power, the maximum temperature starts to rise with the same rate as the average but always keeping a deviation of around 25 K, which increases further from 50 s onward.

As already discussed for the ULOFF (Section 5.4.2), this faster increase of the maximum temperature is also related to the onset of numerical instabilities stemming from the very low turbulent viscosity and thermal conductivity. The absence of heat removal smears out temperature gradients in the core cavity, so the simulation could go on way past the 30 s simulated for the ULOFF transient. However, as can be seen from Figure 5.20, after 70 s the eddy viscosity is in general

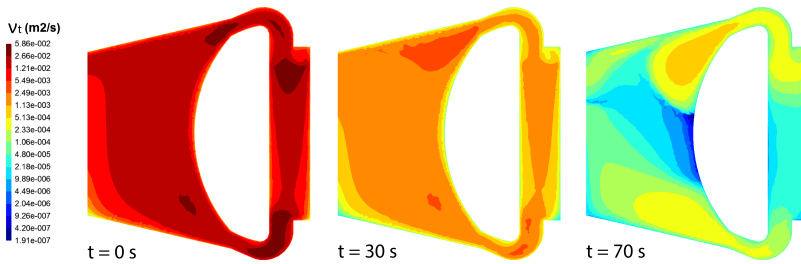


Fig. 5.20. TLOP: evolution of the eddy viscosity distribution along the reactor vertical mid-plane during the transient. A logarithmic scale is adopted to magnify the low values.

at least two orders of magnitude lower than at nominal conditions, with a large central region in which it drops to the level of the molecular viscosity because it is suppressed by thermal stratification in the cavity. Temperature gradients in this region get therefore magnified due to the no longer sufficient spatial resolution, as the last snapshot in Figure 5.19 shows.

Finally, Figures 5.21 and 5.22 show the velocity magnitude distribution and the flow field at various instants of the transient. The hypothesis of the onset of a secondary vortex in the top-right part of the core at $t = 30$ s made during the analysis of the ULOFF transient is confirmed here. Then, at 70 s a regular flow in the cavity is completely lost. The absence of any suction by the pump and the temperature gradients inside the cavity induce multiple secondary vortices.

Despite the reliability of the flow pattern at the end of the simulation is jeopardized by the no longer sufficient resolution of the temperature field, it is reasonable to hypothesize the formation of such secondary natural convection vortices in the core cavity. This constitutes a potential risk for the reactor structural integrity, as hot spots might appear in the upper part of the core, far from the freeze-plugs, which are in contact with a “colder” salt. The grace-time estimation made previously with a uniform-salt temperature hypothesis seems therefore inaccurate and more advanced models should be adopted.

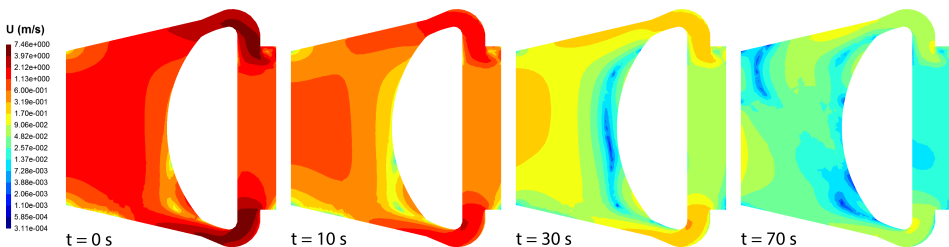


Fig. 5.21. TLOP: variation of the velocity distribution (vertical mid-plane cuts). A logarithmic scale is adopted to magnify the low values.

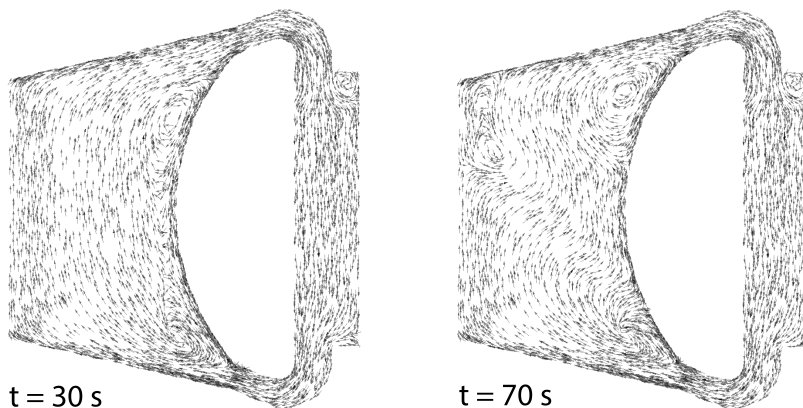


Fig. 5.22. TLOP: flow pattern at 30 s and 70 s (vertical mid-plane cuts). Secondary vortices induced by local temperature gradients can be detected inside the core cavity.

However, the initial hypothesis for these scenarios is very conservative. In reality, the intermediate circuit and the ECS will continue to cool down the salt for a certain amount of time due to their thermal inertia. Moreover, a fraction of power will always be transferred to the external environment via purely passive mechanisms, that is, heat conduction through the reactor metal structures and radiative heat transfer. Finally, the installation of a passive decay heat removal system in the intermediate loop is envisaged, thus guaranteeing a certain amount of salt cooling. This promotes natural circulation, which lowers and homogenizes the salt temperature in the core.

5.4.4 Unprotected Pump Over-speed (UPOS)

Another type of malfunction of the primary pump can lead to an increase of the mass flow rate in the fuel circuit. Once more, in absence of any detail regarding the design of this component, we assumed a linear twofold increase of the momentum source in the first 0.5 s:

$$\mathbf{F}_{pump}(t) = \begin{cases} (1 + 2t) \mathbf{F}_{pump}(t_0), & \text{if } t \leq 0.5 \text{ s,} \\ 2 \mathbf{F}_{pump}(t_0), & \text{otherwise.} \end{cases} \quad (5.5)$$

We simulated the first 15 s of the transient, using a coupling time step size $\Delta t = 0.005$ s with 8 sub-steps performed in `DGFlows`.

The salt volumetric flow rate depicted in Figure 5.23a shows the expected behavior: after a linear increase in the first 0.5 s, it stabilizes on a new steady value that is exactly $\sqrt{2}$ times the nominal one. This follows from the dependence of the pressure drops in the system on the square of the flow rate.

An increased average salt velocity has multiple consequences:

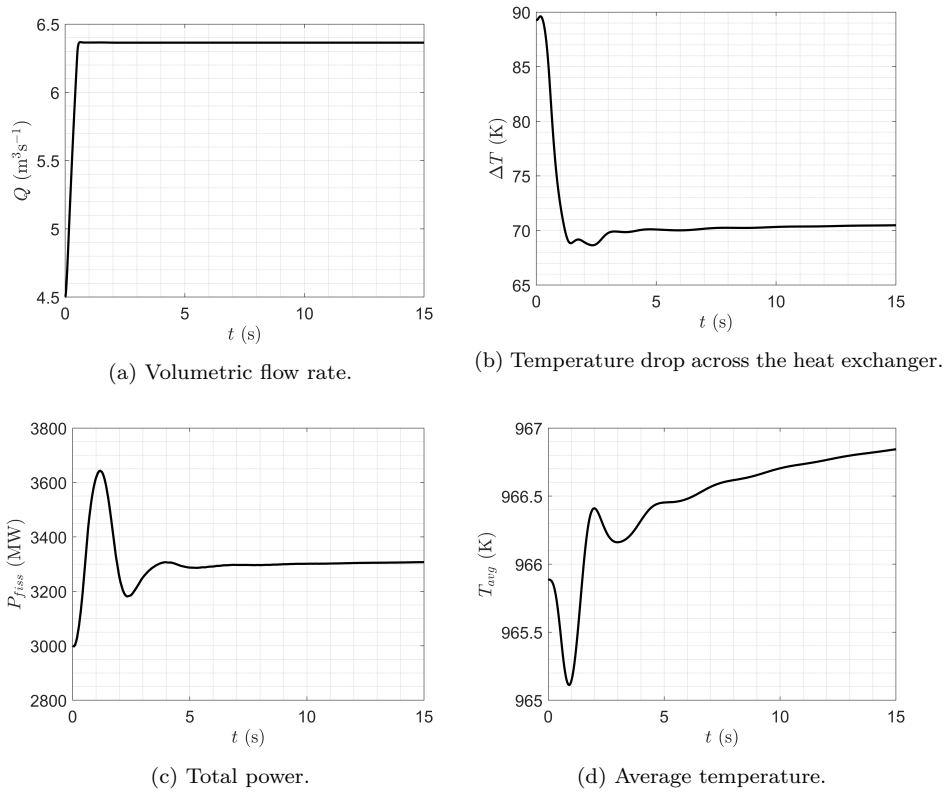


Fig. 5.23. UPOS: time evolution of most relevant characteristic quantities.

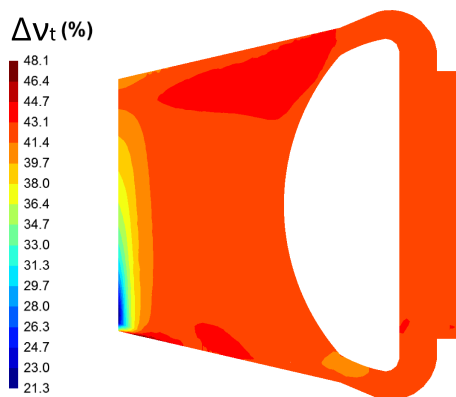


Fig. 5.24. UPOS: vertical mid-plane cut of the asymptotic variation of the eddy viscosity.

5. Analysis of the MSFR steady-state and transient behavior

- the fraction of delayed neutron precursors decaying in the outer core region increases, thus reducing β_{eff} and introducing negative reactivity. By performing a criticality eigenvalue calculation with the flow field at the end of the UPOS transient and with the nominal steady-state temperature distribution, we found $\Delta\beta_{eff} = -9$ pcm. This must therefore be compensated by a reduction of the average effective salt temperature (by almost 2 K);
- at fixed power, the increased flow rate induces a reduction of the temperature drop across the heat exchanger (Figure 5.23b);
- however, turbulence levels in the system are increased. This can be clearly seen from Figure 5.24: the eddy viscosity increases by 40–50 % in the entire domain, and so does the turbulent thermal conductivity. Therefore, temperature gradients in the core cavity are smeared out, so the salt at the inlet of the heat exchanger gets hotter;
- this leads to an increase of the average temperature in the heat exchanger, with consequent rise of the extracted power, despite the heat transfer coefficient was not varied (constant Nusselt number).

The system response in terms of produced power and average salt temperature is therefore the result of these competing effects (Figures 5.23c and 5.23d). The power oscillates in the first 5 s due to the large thermal inertia of the salt, then it stabilizes on a new steady-state level 307 MW higher than the nominal value. The average salt temperature obeys energy conservation and ends up to be almost 1 K higher than the nominal one. However, as can be clearly noticed from Figure 5.25, the salt temperature at the center of the core decreases in general, to reach the correct average value.

In conclusion, despite a 10 % increase in the power, the temperature in the core is more homogeneous thanks to the higher turbulent conductivity and flow rate. Therefore, this kind of scenarios hardly constitutes a threat for the safety of the reactor operations.

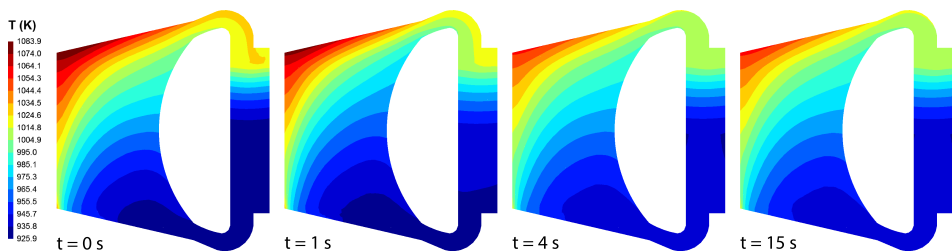


Fig. 5.25. UPOS: evolution of salt temperature distribution (vertical mid-plane cuts).

5.4.5 Salt Over-cooling (OVC)

The strong negative temperature feedback coefficient characterizing the MSFR salt can lead to risky transient scenarios in case of fast increase of the power extracted from the heat exchanger, with resulting reduction of the salt average temperature. As for the ULOHS transient, this scenario is generally initiated by failures of the intermediate loop or in the ECS.

Here, we simulated an over-cooling transient initiated by a fast reduction of the intermediate salt average temperature, which could for example be caused by a fast depressurization of the ECS:

$$T_{int}(t) = T_{int}(t_0) + [T_{int}(t_{end}) - T_{int}(t_0)](1 - e^{-t}). \quad (5.6)$$

The exponential trend with time constant of 1 s takes into account at some extent the inertia of the intermediate circuit, while $T_{int}(t_{end}) = 858.15$ K. This reduction of 50 K can constitute a threat as T_{int} gets very close to the fuel salt melting point (854.15 K). We simulated the first 30 s of the transient, using a coupling time step size $\Delta t = 0.01$ s with 10 sub-steps performed in `DGFloWS`.

As soon as the intermediate salt cools down, the average and minimum salt temperatures decrease, as shown in Figures 5.26b and 5.26c. After 1 s, colder salt enters the core, so the reactor becomes supercritical and the power increases by 50 % in only 3 s (Figure 5.26a). This increases the maximum temperature in the system, thus slowing down and then inverting the average temperature trend.

As a result, the average effective temperature in the core goes back to the nominal value and a criticality condition is slowly restored. In fact, from 5 s onward only minor variations can be detected in the power or the monitored temperatures (see also the snapshots in Figure 5.27). After 30 s, the system power almost reached a constant value of around 5 GW (a true steady-state is reached only after several hundreds of seconds, when the very long-lived delayed neutron and decay heat precursors reach their new equilibrium levels). Due to the increased power-to-flow ratio, the temperature difference across the heat exchanger increases, but the minimum salt temperature maintains a safe 30 K margin above freezing, and the maximum only increases by 70 K. The new average salt temperature is 12 K lower than the nominal one. Once more, we see that this quantity is not suitable to quantify the reactivity introduced in the system due to feedback.

In conclusion, also this event does not raise concerns regarding the reactor safety.

5.5 Conclusions

In this work, we have used the multi-physics simulation tool described in Chapter 3 to carry out an extensive analysis of the MSFR steady-state and its behavior during six accidental transients. The scenarios have been supposed to be initiated by two main events: (i) a malfunction in the fuel salt pump (control), leading to loss of fuel flow or over-speed transients; and (ii) a problem in the intermediate

5. Analysis of the MSFR steady-state and transient behavior

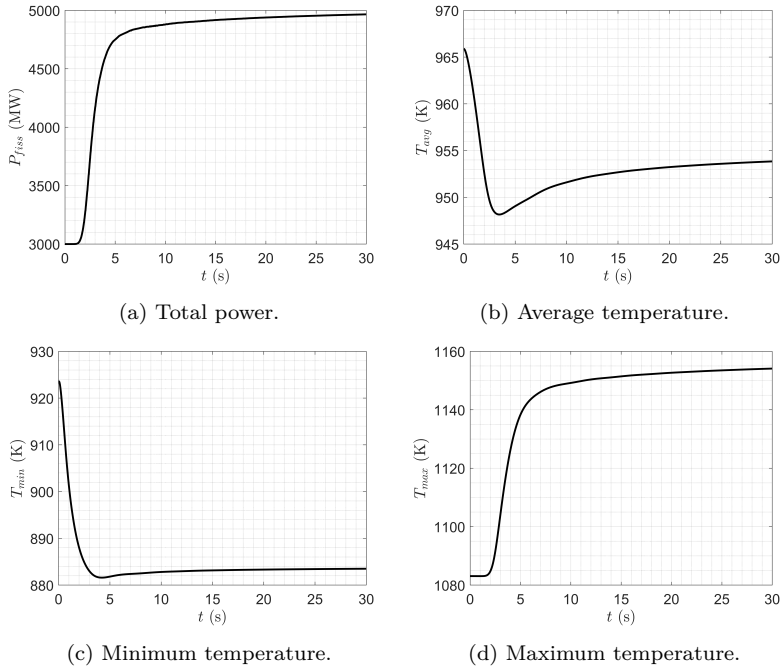


Fig. 5.26. OVC: time evolution of most relevant characteristic quantities.

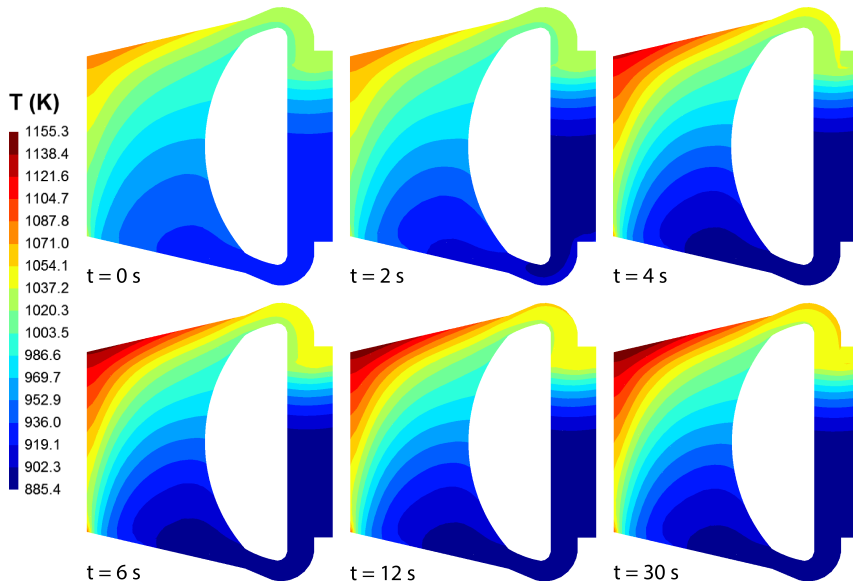


Fig. 5.27. OVC: evolution of salt temperature distribution (vertical mid-plane cuts).

circuit and/or in Energy Conversion System (ECS) that ultimately changes the heat transfer coefficient and the average intermediate salt temperature, which are the two parameters governing the amount of power removed from the system in our model. This power can therefore increase or decrease or be set to zero from the beginning. A superposition of these events, caused by an electricity outage, results in a total loss of power accident.

Despite the large uncertainties on the salt composition and thermal properties, and even if the reactor design is still at a preliminary stage of development (especially for what concerns primary pumps and heat exchangers), we could derive useful indications on the general reactor behavior and on the aspects that pose challenges both from the design safety and from the numerical assessment of these scenarios.

For what concerns the reactor steady-state, previous design optimization studies (Rouch et al., 2014) proved to be effective in eliminating hot spots at the entrance of the core. However, a large recirculation region is still present inducing localized pressure losses. Further optimization of the shape of the blanket and lower-reflector walls is recommended. The temperature high value and large gradient at the top of the core might represent a challenge for the material selection of the boundary wall with the upper reflector, due to the induced thermo-mechanical stresses and enhanced corrosion effects. Finally, the concentration of fissile material in the fuel salt should be reduced, as the reactor is almost 1000 pcm above criticality.

In general, the simulated reactor response to the investigated transient scenarios is excellent. No major weak points could be detected regarding the safety of the MSFR design. The large heat capacity of the salt leads to modest temperature variations both in case of an over-cooling transient and when less heat is removed by the intermediate circuit. Large power variations are quickly damped and controlled by the strong negative feedback coefficient of the salt. In case of a total loss of heat sink, very conservative extrapolations of the average temperature indicated that the grace time before the salt reaches temperatures dangerous for the reactor structural integrity is at least one minute longer than what previously estimated by Brovchenko et al. (2013). During a realistic loss of heat sink scenario on the other hand, the temperature increase is limited to 35 K only.

The major concern lies in the very limited natural circulation in the fuel loop. After 30s of a loss of flow accident, the salt flow rate drops to only 7.5% of the nominal flow rate. It is even lower (2%) at 70s of a total loss of power accident. This first represents a challenge from the numerical point of view. The flow tends to relaminarize in the core cavity and the resulting very low thermal diffusivity emphasizes temperature gradients, which therefore demand (especially with a DG-FEM discretization) higher spatial resolution in the cavity and not only at the wall boundaries to prevent the onset of numerical instabilities. However, higher levels of natural circulation would be beneficial also for the reactor operations. In fact, at steady-state it would lower the power consumed by the primary pumps, and during loss of flow scenarios it would help continuing removing heat from the

primary circuit, limiting the salt temperature gradients, and thus avoiding the risk of formation of secondary vortices in the core cavity with associated temperature hot spots.

For this reason, further studies should focus on optimizing the geometry of the outer-core region from a fluid dynamics point of view. Sudden large variation of cross sections or small-radius pipe bends should be avoided and the pressure drop across the heat exchanger should be reduced.

Finally, the salt temperature maintained a safe margin above the freezing point during all the transients investigated. However, improved models of the intermediate circuit should be adopted to derive more reliable information on this safety issue. In fact, the assumption of a constant intermediate salt temperature limited (considerably) the decrease of the minimum fuel temperature during the loss of flow accident. In general, coupling the detailed multi-physics model with a simple (even 0D) model of the intermediate loop and the ECS could lead to much more detailed and realistic simulations of the transient scenarios.

CONCLUSIONS AND RECOMMENDATIONS

In this thesis, we have developed a high-fidelity multi-physics simulation tool able to model the complex physics phenomena characterizing liquid-fuel fast nuclear reactors. The main motivation of this work was to assess with high-accuracy numerical methods the safety and reliability of the current design of the Molten Salt Fast Reactor (MSFR), one of the most promising Generation IV nuclear reactor systems. A great experimental and numerical research effort is in fact necessary to bring this reactor design to a higher technology readiness level. The work has been conducted in the framework of the Euratom Horizon 2020 SAMOFAR project.

This chapter highlights the key results and conclusions of this research and provides recommendations for possible follow-up studies.

6.1 Conclusions

The most important outcomes can be summarized as follows:

- We have developed a novel high-order discontinuous Galerkin (DG) solver for the incompressible RANS equations coupled to the $k - \epsilon$ turbulence model. With the method of manufactured solutions, we have verified that the theoretical space-time convergence rates of the solution error could be reached. Moreover, by simulating classical steady-state (a backward-facing step) and time-dependent (a Von Kármán vortex street in the wake of a square cylinder) test cases, we have demonstrated the capability of our code to handle correctly turbulent flows. Taking into account the well-known

limitations of the chosen turbulent model, our results are in good agreement with those reported in literature, and discrepancies are always towards a better accordance with experimental or DNS/LES results.

- We have shown that a non exactly divergence-free convective velocity field can lead to significant numerical error in the solution of the transport equation for any scalar quantity, unless the latter is discretized with the same polynomial order than the pressure. This contrasts with the choices adopted in previous DG literature.
- We have demonstrated that our newly developed multi-physics code is able to reproduce correctly the physics phenomena characterizing the steady-state and dynamic behavior of fast-spectrum MSR. To do so, we have employed a test case designed and structured in such a way that it is easy to detect sources of errors in modeling the coupling between the physics phenomena characterizing fast MSR. In all the steady-state and transient problems investigated, our code has produced results in excellent agreement with those obtained by other partners of the SAMOFAR project. Discrepancies are limited to a few percent at most (a few tens of pcm for what concerns reactivity values), and reduce further, as expected, when considering only the S_2 discretization, which is theoretically equivalent to the diffusion models used by most partners. The high-order discretization has allowed us to use a much coarser mesh than the other partners.
- More in general, in Chapter 4 we have collected results obtained with a broad spectrum of multi-physics tools, including diffusion and transport codes, finite volume and finite element solvers. Together with the detailed description of the benchmark problem, the results constitute therefore a very useful tool for the testing of any other multi-physics code dedicated to MSR that are or will be developed by other research institutes.
- In the final part of this thesis, we have extensively analyzed the MSFR behavior taking into account the most recent advancements in the design made during the SAMOFAR project. At steady-state, we have detected a large salt recirculation region at the entrance of the core cavity. Even if it does not lead to hot spots, it causes localized pressure drops and should therefore be eliminated by further reshaping of the blanket and lower-reflector walls. Attention should be paid to the material selection for the upper-reflector wall, as it is exposed to the hottest salt and to large temperature gradients which might lead to excessive thermo-mechanical stresses and corrosion effects. With criticality eigenvalue calculations, we have found the reactor is supercritical at the intended average operating temperature (by almost 1000 pcm). For this reason, the concentration of fissile material in the fuel salt should be reduced.

- We have simulated six transient scenarios: loss of heat sink (total and partial) (ULOHS), loss of fuel flow (ULOFF), total loss of power (TLOP), pump over-speed (UPOS), and salt over-cooling (OVC). Despite being outside the range of operational conditions, the partial ULOHS and the OVC scenarios have demonstrated that the reactor has excellent load-following capabilities. In fact, a new steady-state condition could practically be reached within a few tens of seconds from the initial perturbation. More in general, the reactor has presented outstanding safe behavior. The large salt heat capacity limits temperature variations and at the same time the strong negative feedback coefficient quickly dampens any large perturbation in the power. The salt temperature is always safely above the freezing point, and through all investigated scenarios the increase of the maximum salt temperature is at most 70 K. An exception is of course constituted by the total ULOHS and TLOP accidents, where no heat extraction has been (unrealistically) hypothesized. Adopting very conservative assumptions, we have extrapolated the trend of the average salt temperature beyond the end of our simulations. Thus, we have been able to estimate that the grace time before the salt reaches a temperature dangerous for the reactor structural integrity is around 550 s in case of total ULOHS (more than one minute longer than what was estimated in previous studies) and almost 480 s in case of TLOP. This information is useful to guide the design of the freeze-plug valves and the draining system.
- We have found that the salt natural circulation in the primary circuit is very limited and this constitutes the major concerning aspect of the current design. At the end of the ULOFF transient, the salt flow rate is less than 10% of the nominal value and decreases even further in a TLOP accident when temperature gradients are progressively smeared out. The flow tends to relaminarize in the core cavity, with the appearance of secondary vortices that could lead to localized hot spots. These conditions have proven to be very challenging from a numerical point of view, because the low turbulence levels emphasize temperature gradients, demanding higher spatial resolution to avoid the onset of numerical instabilities. Based on these findings, we recommend an optimization of the design of the outer-core region and of the heat exchanger to reduce as much as possible the pressure losses in the primary circuit. A stronger natural circulation would lower the power requirements for the primary pumps during nominal operations and would enhance heat removal during loss of flow accidents.

In conclusion, the newly developed multi-physics code has proven capable of accurately simulating the physics phenomena characterizing a liquid salt fast reactor. It constitutes a valuable addition to the set of multi-physics codes dedicated to this reactor technology available in literature, as it is the first based on a full-transport neutronics model and on high-order finite element space discretization. Even if the MSFR design is still at a preliminary stage of development, and despite the

uncertainties in the salt composition and thermal properties, the results obtained have proven the general safety of the reactor and provide useful indications for future design optimization activities.

The work described in this thesis constitutes a solid basis for follow-up developments and studies. In the remainder of the chapter, we provide some suggestions.

6.2 Recommendations and perspectives

Future research can essentially follow two directions (not mutually exclusive): (i) improve and optimize the numerical schemes described in this work; and (ii) extend the models adopted, to take into account physics phenomena that have not been considered in this work.

6.2.1 Improvements and optimizations

The RANS manufactured solution test in Section 2.7.1 has shown that the convergence rate of the velocity error could be degraded by the slower convergence of the eddy viscosity. This is due to the lower polynomial order with which scalar quantities are discretized to avoid numerical instabilities, as previously mentioned. To prevent this, methods to reduce the divergence and continuity errors of the velocity field should be investigated. They could involve the addition of extra penalty terms in the momentum or pressure Poisson equations (Fehn et al., 2018) or an extra post-projection step on the convective field to ensure the incompressibility constraint is satisfied exactly (Cockburn et al., 2008; Rhebergen et al., 2013).

A very interesting improvement would be the implementation of positivity preserving schemes for the DG-FEM discretization in both the CFD and the neutronics solvers (Van der Vegt et al., 2019). This would avoid the appearance of negative neutron fluxes and might allow for the solution of the turbulence equations in their standard form instead of the logarithmic that contains extra non-linear terms.

On top of this, the neutronics code should be parallelized and an investigation on the possibility to improve the performance of the preconditioner for the pressure Poisson equation is recommended. These are currently the two most CPU time consuming portions of our computational scheme. Faster solvers would allow to analyze non-symmetric transients where the entire reactor (or at least a quarter of it) must be taken into account. Uncertainty and sensitivity analysis studies would certainly benefit from it as well. At the same time, it would open the door to the implementation of more tight coupling schemes within the CFD solver and between both codes, based for example on Jacobian-Free Newton-Krylov or quasi-Newton methods to better resolve the non-linearities of the problem.

6.2.2 Extension of the current models

More accurate safety assessments of the MSFR should be carried out once more precise information on the fuel salt composition and its physical properties will

become available, together with a more detailed characterization of the outer-core components (pump, heat exchanger, pipes, etc.) and external circuits. In this perspective, a significant improvement could already be constituted by the adoption of a better model for the intermediate loop and the Energy Conversion System (ECS). In this work, we have considered the average temperature of the intermediate salt and the total heat transfer coefficient in the heat exchanger as known boundary conditions, but in reality these parameters evolve according to the dynamics of the entire power plant. To better model this, without a significant impact on the total computational cost, one could couple our multi-physics tool with a reduced order model or a 1D model for the intermediate loop and ECS as the one presented by Tripodo et al. (2019).

In this work, only the $k-\epsilon$ model has been used. One could study the sensitivity of the results to turbulence models by implementing more advanced ones. For example, the SST $k-\omega$ model (Schoenawa and Hartmann, 2014) could be implemented, exploiting a wall-distance solver already available in our code (Bakker, 2018).

Finally, the capabilities of our tool could be expanded by adding models for physics phenomena that have not been considered in this work. For example, the balance equation (3.8) for the decay-heat fission products could be straightforwardly generalized to model the transport of any nuclide. Together with a proper manipulation of the macroscopic cross sections in each cell, it would allow simulating reactivity insertion accidents due to the injection or extraction of fissile material (Wan et al., 2020).

Radiative heat transfer has not been included in the energy equation. However, especially during some accident scenarios (e.g., ULOHS, TLOP), the salt might reach very high temperatures, and taking into account this extra heat transfer mechanism could lead to more accurate estimations of the grace time before the salt reaches the critical temperature of 1200 °C. The salt optical properties are not well known yet, but some experimental studies suggest it should be treated as a semi-transparent medium (Williams, 1988). A possible modeling approach is described in Rubiolo et al. (2017). Our tool is particularly suitable for the implementation of the radiative transfer equation (Chandrasekhar, 1960), given the availability of a discrete ordinates solver.

In some occasions, as during loss of flow accidents or particularly severe overcooling transients, the salt temperature in the heat exchanger might reach the freezing point, and the blockage induced by the solidified salt might affect significantly the flow and the heat removal capabilities. In other situations, the draining of the fuel salt might be initiated by the melting of a freeze-plug. To be able to simulate these scenarios, a phase change model should be implemented. Apparent heat capacity or source-terms models (Voller et al., 1990) seem particularly suitable as they require only limited modification to the single-phase enthalpy equation (3.1a).

BIBLIOGRAPHY

- M. Allibert et al. Molten salt fast reactors. In I. L. Piro (ed.), *Handbook of Generation IV Nuclear Reactors*, 157–188. Woodhead Publishing, 2016.
- M. Altahhan et al. 3D Coupled Transient simulation of a fast liquid fuel molten salt reactor primary loop using GeN-Foam. In *18th International Topical Meeting on Nuclear Reactor Thermal Hydraulics, NURETH 2019*, 4899–4911. Portland, OR, USA, 2019.
- D. N. Arnold et al. Unified Analysis of Discontinuous Galerkin Methods for Elliptic Problems. *SIAM Journal on Numerical Analysis*, **39**, 1749, 2002.
- M. Aufiero. Serpent-OpenFOAM coupling for criticality accidents modelling – Definition of a benchmark for MSRs multiphysics modelling. In *Serpent and Multiphysics meeting*. Grenoble, France, 2015.
- M. Aufiero and P. Rubiolo. Testing and Verification of Multiphysics Tools for Fast-Spectrum MSRs: The CNRS Benchmark. . In *Transactions of the 2018 ANS Annual Meeting*. Philadelphia, PA, USA, 2018.
- M. Aufiero, P. Rubiolo and M. Fratoni. Monte Carlo/CFD coupling for accurate modeling of the delayed neutron precursors and compressibility effects in molten salt reactors. In *Transactions of the American Nuclear Society*, volume 116, 1183–1186. San Francisco, California, 2017.
- M. Aufiero et al. Calculating the effective delayed neutron fraction in the Molten Salt Fast Reactor: Analytical, deterministic and Monte Carlo approaches. *Annals of Nuclear Energy*, **65**, 78, 2014a.
- M. Aufiero et al. Development of an OpenFOAM model for the Molten Salt Fast Reactor transient analysis. *Chemical Engineering Science*, **111**, 390, 2014b.

- J. C. Bakker. *Wall-Distance Calculation for Turbulence Modelling*. Master's thesis, Delft University of Technology, 2018.
- S. Balay et al. PETSc Users Manual. Technical Report ANL-95/11 - Revision 3.10, Argonne National Laboratory, 2018.
- F. Bassi et al. Discontinuous Galerkin solution of the Reynolds-averaged Navier-Stokes and $k - \omega$ turbulence model equations. *Computers & Fluids*, **34**, 507, 2005.
- F. Bassi et al. An artificial compressibility flux for the discontinuous Galerkin solution of the incompressible Navier-Stokes equations. *Journal of Computational Physics*, **218**, 794, 2006.
- F. Bassi et al. An implicit high-order discontinuous Galerkin method for steady and unsteady incompressible flows. *Computers & Fluids*, **36**, 1529, 2007.
- F. Bassi et al. A high-order Discontinuous Galerkin solver for the incompressible RANS and $k - \omega$ turbulence model equations. *Computers & Fluids*, **98**, 54, 2014.
- S. Beils et al. Application of the lines of defence method to the molten salt fast reactor in the framework of the SAMOFAR project. *EPJ Nuclear Sciences & Technologies*, **5**, 18, 2019.
- G. I. Bell and S. Glasstone. *Nuclear Reactor Theory*. Van Nostrand Reinhold Company, New York, USA, 1970.
- O. Beneš et al. Physico-Chemical properties of the MSFR fuel salt — Deliverable D3.2. Technical report, EVOL Project, 2013.
- E. S. Bettis et al. The Aircraft Reactor Experiment—Design and Construction. *Nuclear Science and Engineering*, **2**, 804, 1957a.
- E. S. Bettis et al. The Aircraft Reactor Experiment—Operation. *Nuclear Science and Engineering*, **2**, 841, 1957b.
- J. A. Blanco, P. Rubiolo and E. Dumonteil. Neutronic modeling strategies for a liquid fuel transient calculation. In *Physics of Reactors Conference 2020 (PHYSOR 2020)*. Cambridge, UK, 2020.
- G. Bosch and W. Rodi. Simulation of vortex shedding past a square cylinder with different turbulence models. *International Journal for Numerical Methods in Fluids*, **28**, 601, 1998.
- O. Botella and R. Peyret. Benchmark spectral results on the lid-driven cavity flow. *Computers and Fluids*, **27**, 421, 1998.

-
- P. Bradshaw, B. E. Launder and J. L. Lumley. Collaborative Testing of Turbulence Models. *Journal of Fluids Engineering*, **118**, 243, 1996.
- B. W. Brook et al. Why nuclear energy is sustainable and has to be part of the energy mix. *Sustainable Materials and Technologies*, **1-2**, 8, 2014.
- M. Brovchenko et al. Design-Related Studies for the Preliminary Safety Assessment of the Molten Salt Fast Reactor. *Nuclear Science and Engineering*, **175**, 329, 2013.
- M. Brovchenko et al. Neutronic benchmark of the molten salt fast reactor in the frame of the EVOL and MARS collaborative projects. *EPJ Nuclear Sciences & Technologies*, **5**, 2019.
- A. Cammi et al. A multi-physics modelling approach to the dynamics of Molten Salt Reactors. *Annals of Nuclear Energy*, **38**, 1356, 2011.
- E. Capelli, O. Beneš and R. J. M. Konings. Thermodynamics of soluble fission products cesium and iodine in the Molten Salt Reactor. *Journal of Nuclear Materials*, **501**, 238, 2018.
- E. Cervi et al. Development of a multiphysics model for the study of fuel compressibility effects in the Molten Salt Fast Reactor. *Chemical Engineering Science*, **193**, 379, 2019a.
- E. Cervi et al. Development of an SP₃ neutron transport solver for the analysis of the Molten Salt Fast Reactor. *Nuclear Engineering and Design*, **346**, 209, 2019b.
- E. Cervi et al. Multiphysics analysis of the MSFR helium bubbling system: A comparison between neutron diffusion, SP₃ neutron transport and Monte Carlo approaches. *Annals of Nuclear Energy*, **132**, 227, 2019c.
- S. Chandrasekhar. *Radiative Transfer*. Dover Publications, New York, US, 1960.
- K. A. Cliffe, E. J. C. Hall and P. Houston. Adaptive discontinuous Galerkin methods for eigenvalue problems arising in incompressible fluid flows. *SIAM Journal on Scientific Computing*, **31**, 4607, 2010.
- B. Cockburn, G. Kanschat and D. Schötzau. A locally conservative LDG method for the incompressible Navier-Stokes equations. *Mathematics of Computation*, **74**, 1067, 2004.
- B. Cockburn, G. Kanschat and D. Schötzau. An Equal-Order DG Method for the Incompressible Navier-Stokes Equations. *Journal of Scientific Computing*, **40**, 188, 2008.
- B. Cockburn, G. Kanschat and D. Schötzau. The local discontinuous Galerkin method for the Oseen equations. *Mathematics of Computation*, **73**, 569, 2003.

- B. Cockburn and C.-W. Shu. Runge-Kutta Discontinuous Galerkin Methods for Convection-Dominated Problems. *Journal of Scientific Computing*, **16**, 173, 2001.
- A. Crivellini and F. Bassi. An implicit matrix-free Discontinuous Galerkin solver for viscous and turbulent aerodynamic simulations. *Computers & Fluids*, **50**, 81, 2011.
- A. Crivellini, V. D'Alessandro and F. Bassi. A Spalart-Allmaras turbulence model implementation in a discontinuous Galerkin solver for incompressible flows. *Journal of Computational Physics*, **241**, 388, 2013a.
- A. Crivellini, V. D'Alessandro and F. Bassi. High-order discontinuous Galerkin solutions of three-dimensional incompressible RANS equations. *Computers & Fluids*, **81**, 122, 2013b.
- R. G. G. De Oliveira and K. Mikityuk. Analytical solutions to a coupled fluid dynamics and neutron transport problem with application to GeN-Foam verification. *Annals of Nuclear Energy*, **121**, 446, 2018.
- S. Delpech et al. Reactor physic and reprocessing scheme for innovative molten salt reactor system. *Journal of Fluorine Chemistry*, **130**, 11, 2009.
- C. Demaziere. *Modelling of Nuclear Reactor Multi-physics*. Academic Press, 2019.
- D. A. Di Pietro and A. Ern. *Mathematical Aspects of Discontinuous Galerkin Methods*. Springer Berlin Heidelberg, 2012.
- A. Di Ronco, A. Cammi and S. Lorenzi. Preliminary analysis and design of the heat exchangers for the Molten Salt Fast Reactor. *Nuclear Engineering and Technology*, **52**, 51, 2019.
- T. J. Dolan. *Molten Salt Reactors and Thorium Energy*. Series in Energy. Woodhead Publishing, Elsevier Ltd., Cambridge, MA, United States, 2017.
- M. Drosson and K. Hillewaert. On the stability of the symmetric interior penalty method for the Spalart-Allmaras turbulence model. *Journal of Computational and Applied Mathematics*, **246**, 122, 2013.
- M. Drosson, K. Hillewaert and J.-A. Essers. Stability and Boundary Resolution Analysis of the Discontinuous Galerkin Method Applied to the Reynolds-Averaged Navier-Stokes Equations Using the Spalart-Allmaras Model. *SIAM Journal on Scientific Computing*, **35**, B666, 2013.
- J. J. Duderstadt and L. J. Hamilton. *Nuclear Reactor Analysis*. John Wiley & Sons, Inc., 1976.

- S. Dulla, P. Ravetto and M. M. Rostagno. Neutron kinetics of fluid-fuel systems by the quasi-static method. *Annals of Nuclear Energy*, **31**, 1709, 2004.
- G. Durán-Klie, D. Rodrigues and S. Delpech. Dynamic Reference Electrode development for redox potential measurements in fluoride molten salt at high temperature. *Electrochimica Acta*, **195**, 19, 2016.
- P. A. Durbin. Limiters and wall treatments in applied turbulence modeling. *Fluid Dynamics Research*, **41**, 012203, 2009.
- C. R. Ethier and D. A. Steinman. Exact fully 3D Navier-Stokes solutions for benchmarking. *International Journal for Numerical Methods in Fluids*, **19**, 369, 1994.
- EVOL. Evaluation and viability of liquid fuel fast reactor system, 2010–2013.
- N. Fehn, W. A. Wall and M. Kronbichler. On the stability of projection methods for the incompressible Navier–Stokes equations based on high-order discontinuous Galerkin discretizations. *Journal of Computational Physics*, **351**, 392, 2017.
- N. Fehn, W. A. Wall and M. Kronbichler. Robust and efficient discontinuous Galerkin methods for under-resolved turbulent incompressible flows. *Journal of Computational Physics*, **372**, 667, 2018.
- E. Ferrer and R. H. J. Willden. A high order Discontinuous Galerkin Finite Element solver for the incompressible Navier-Stokes equations. *Computers & Fluids*, **46**, 224, 2011.
- C. Fiorina et al. Analysis of the MSFR core neutronics adopting different neutron transport models. In *International Conference on Nuclear Engineering, Proceedings, ICONE*. Anaheim, CA, USA, 2012.
- C. Fiorina et al. Investigation of the MSFR core physics and fuel cycle characteristics. *Progress in Nuclear Energy*, **68**, 153, 2013.
- C. Fiorina et al. Modelling and analysis of the MSFR transient behaviour. *Annals of Nuclear Energy*, **64**, 485, 2014.
- C. Fiorina et al. GeN-Foam: A novel OpenFOAM[®] based multi-physics solver for 2D/3D transient analysis of nuclear reactors. *Nuclear Engineering and Design*, **294**, 24, 2015.
- Generation IV International Forum. A Technology Roadmap for Generation IV Nuclear Energy Systems. Technical Report GIF-002-00, U.S. DOE Nuclear Energy Research Advisory Committee and the Generation IV International Forum, 2002.

- Generation IV International Forum. GIF R&D Outlook for Generation IV Nuclear Energy Systems: 2018 Update. Technical report, Generation IV International Forum, 2018.
- D. Gérardin. *Développement de méthodes et d'outils numériques pour l'étude de la sûreté du réacteur à sels fondus MSFR*. Ph.D. thesis, Grenoble Alpes University, France, 2018.
- D. Gérardin et al. Design evolutions of Molten Salt Fast Reactor. In *International Conference on Fast Reactors and Related Fuel Cycles: Next Generation Nuclear Systemes for Sustainable Development (FR17)*. Yekaterinburg, Russia, 2017.
- D. Gérardin et al. A methodology for the identification of the postulated initiating events of the Molten Salt Fast Reactor. *Nuclear Engineering and Technology*, **51**, 1024, 2019.
- B. Geurts. *Elements of direct and large-eddy simulation*. R. T. Edwards, Philadelphia, PA, 2004.
- C. Geuzaine and J. Remacle. Gmsh: A 3D finite element mesh generator with built-in pre- and post-processing facilities. *International Journal for Numerical Methods in Engineering*, **79**, 1309, 2009.
- U. Ghia, K. N. Ghia and C. T. Shin. High-Re solutions for incompressible flow using the Navier-Stokes equations and a multigrid method. *Journal of Computational Physics*, **48**, 387, 1982.
- A. Ghidoni et al. p-multigrid Discontinuous Galerkin method for compressible turbulent flows. In *51st AIAA Aerospace Sciences Meeting including the New Horizons Forum and Aerospace Exposition*. American Institute of Aeronautics and Astronautics, 2013.
- V. Girault, B. Rivière and M. F. Wheeler. A splitting method using discontinuous Galerkin for the transient incompressible Navier-Stokes equations. *ESAIM: Mathematical Modelling and Numerical Analysis*, **39**, 1115, 2005.
- G. H. Golub and C. F. Van Loan. *Matrix Computations*. The Johns Hopkins University Press, 4 edition, 2013.
- J. L. Guermond, P. Mineev and J. Shen. An overview of projection methods for incompressible flows. *Computer Methods in Applied Mechanics and Engineering*, **195**, 6011, 2006.
- X. Han, P. Sagaut and D. Lucor. On sensitivity of RANS simulations to uncertain turbulent inflow conditions. *Computers & Fluids*, **61**, 2, 2012.

- R. Hargraves and R. Moir. Liquid fluoride thorium reactors. *American Scientist*, **98**, 304, 2010.
- R. Hartmann, J. Held and T. Leicht. Adjoint-based error estimation and adaptive mesh refinement for the RANS and $k - \omega$ turbulence model equations. *Journal of Computational Physics*, **230**, 4268, 2011.
- P. N. Haubenreich and J. R. Engel. Experience with the Molten-Salt Reactor Experiment. *Nuclear Applications and Technology*, **8**, 118, 1970.
- A. Hennink, M. Tiberga and D. Lathouwers. A Pressure-based Solver for Low-Mach Number Flow using a Discontinuous Galerkin Method. *Journal of Computational Physics*, 2020. Submitted for publication.
- D. Heuer et al. Towards the thorium fuel cycle with molten salt fast reactors. *Annals of Nuclear Energy*, **64**, 421, 2014.
- K. Hillewaert. *Development of the discontinuous Galerkin method for high-resolution, large scale CFD and acoustics in industrial geometries*. Ph.D. thesis, Université Catholique de Louvain, 2013.
- D. E. Holcomb et al. Fluoride salt-cooled high-temperature reactor development roadmap. In *International Congress on Advances in Nuclear Power Plants, ICAPP 2014*, 345–352, 2014.
- T. Hu et al. Coupled neutronics and thermal-hydraulics simulation of molten salt reactors based on OpenMC/TANSY. *Annals of Nuclear Energy*, **109**, 260, 2017.
- L. Ignat, D. Pelletier and F. Ilinca. Adaptive computations of turbulent forced convection. *Numerical Heat Transfer, Part A: Applications*, **34**, 847, 1998.
- V. Ignatiev and A. Surenkov. Voltammetric measurements on the [U(IV)]/[U(III)] couple and embrittlement of high nickel alloys in fuel LiF-BeF₂-UF₄ salt with tellurium addition in application to molten salt reactor. *Corrosion Science*, **160**, 108164, 2019.
- V. Ignatiev et al. Molten salt actinide recycler and transforming system without and with Th-U support: Fuel cycle flexibility and key material properties. *Annals of Nuclear Energy*, **64**, 408, 2014.
- V. V. Ignatiev et al. Molten-salt reactors: new possibilities, problems and solutions. *Atomic Energy*, **112**, 157, 2012.
- F. Ilinca, J.-F. Héту and D. Pelletier. A unified finite element algorithm for two-equation models of turbulence. *Computers & Fluids*, **27**, 291, 1998.
- International Energy Agency. *Nuclear Power in a Clean Energy System*. OECD Publishing, Paris, 2019a.

- International Energy Agency. *World Energy Outlook 2019*. OECD Publishing, Paris, 2019b.
- IPCC. *Climate Change 2013: The Physical Science Basis. Contribution of Working Group I to the Fifth Assessment Report of the Intergovernmental Panel on Climate Change*. Cambridge University Press, Cambridge, United Kingdom and New York, NY, USA, 2013.
- G. Kalitzin et al. Near-wall behavior of RANS turbulence models and implications for wall functions. *Journal of Computational Physics*, **204**, 265, 2005.
- G. Karypis and V. Kumar. A Fast and High Quality Multilevel Scheme for Partitioning Irregular Graphs. *SIAM Journal on Scientific Computing*, **20**, 359, 1998.
- J. Kim, S. J. Kline and J. P. Johnston. Investigation of a reattaching turbulent shear layer: Flow over a backward-facing step. *Journal of Fluids Engineering, Transactions of the ASME*, **102**, 302, 1980.
- B. Klein, F. Kummer and M. Oberlack. A SIMPLE based discontinuous Galerkin solver for steady incompressible flows. *Journal of Computational Physics*, **237**, 235, 2013.
- B. Klein et al. A high-order discontinuous Galerkin solver for low Mach number flows. *International Journal for Numerical Methods in Fluids*, **81**, 489, 2015a.
- B. Klein et al. An extension of the SIMPLE based discontinuous Galerkin solver to unsteady incompressible flows. *International Journal for Numerical Methods in Fluids*, **77**, 571, 2015b.
- A. Koning et al. The JEFF-3.1 nuclear data library. Technical Report JEFF report 21, NEA-OECD, 2006.
- J. Kópházi and D. Lathouwers. Three-dimensional transport calculation of multiple alpha modes in subcritical systems. *Annals of Nuclear Energy*, **50**, 167, 2012.
- J. Kópházi, D. Lathouwers and J. L. Kloosterman. Development of a three-dimensional time-dependent calculation scheme for molten salt reactors and validation of the measurement data of the molten salt reactor experiment. *Nuclear Science and Engineering*, **163**, 118, 2009.
- B. Krank, M. Kronbichler and W. A. Wall. Wall modeling via function enrichment within a high-order DG method for RANS simulations of incompressible flow. *International Journal for Numerical Methods in Fluids*, **86**, 107, 2017a.
- B. Krank et al. A high-order semi-explicit discontinuous Galerkin solver for 3D incompressible flow with application to DNS and LES of turbulent channel flow. *Journal of Computational Physics*, **348**, 634, 2017b.

-
- J. Křepel et al. DYN1D-MSR dynamics code for molten salt reactors. *Annals of Nuclear Energy*, **32**, 1799, 2005.
- J. Křepel et al. DYN3D-MSR spatial dynamics code for molten salt reactors. *Annals of Nuclear Energy*, **34**, 449, 2007.
- P. Kundu and I. Cohen. *Fluid Mechanics*. Academic Press, 4 edition, 2007.
- D. Kuzmin, O. Mierka and S. Turek. On the implementation of the $k - \epsilon$ turbulence model in incompressible flow solvers based on a finite element discretisation. *International Journal of Computing Science and Mathematics*, **1**, 193, 2007.
- B. Landmann et al. A parallel, high-order discontinuous Galerkin code for laminar and turbulent flows. *Computers & Fluids*, **37**, 427, 2008.
- G. Lapenta, F. Mattioda and P. Ravetto. Point kinetic model for fluid fuel systems. *Annals of Nuclear Energy*, **28**, 1759, 2001.
- D. Lathouwers. Goal-oriented spatial adaptivity for the S_N equations on unstructured triangular meshes. *Annals of Nuclear Energy*, **38**, 1373, 2011a.
- D. Lathouwers. Spatially adaptive eigenvalue estimation for the S_N equations on unstructured triangular meshes. *Annals of Nuclear Energy*, **38**, 1867, 2011b.
- B. E. Launder and D. B. Spalding. The numerical computation of turbulent flows. *Computer Methods in Applied Mechanics and Engineering*, **3**, 269, 1974.
- A. Laureau. *Développement de modèles neutroniques pour le couplage thermo-hydraulique du MSFR et le calcul de paramètres cinétiques effectifs*. Ph.D. thesis, Grenoble Alpes University, France, 2015.
- A. Laureau et al. Transient coupled calculations of the Molten Salt Fast Reactor using the Transient Fission Matrix approach. *Nuclear Engineering and Design*, **316**, 112, 2017.
- S. Laville and J. Watts. Across the globe, millions join biggest climate protest ever. *The Guardian*, 2019.
- D. LeBlanc. Molten salt reactors: A new beginning for an old idea. *Nuclear Engineering and Design*, **240**, 1644, 2010.
- D. LeBlanc and C. Rodenburg. Integral molten salt reactor. In T. J. Dolan (ed.), *Molten Salt Reactors and Thorium Energy*, 541–556. Woodhead Publishing, 2017.
- D. Lecarpentier and V. Carpentier. A Neutronic Program for Critical and Nonequilibrium Study of Mobile Fuel Reactors: The Cinsf1D Code. *Nuclear Science and Engineering*, **143**, 33, 2003.

- J. Leppänen, M. Pusa and E. Fridman. Overview of methodology for spatial homogenization in the Serpent 2 Monte Carlo code. *Annals of Nuclear Energy*, **96**, 126, 2016.
- J. Leppänen et al. The Serpent Monte Carlo code: Status, development and applications in 2013. *Annals of Nuclear Energy*, **82**, 142, 2015.
- E. E. Lewis and W. F. Miller. *Computational Methods of Neutron Transport*. John Wiley & Sons, Inc., 1993.
- R. Li et al. Transient analyses for a molten salt fast reactor with optimized core geometry. *Nuclear Engineering and Design*, **292**, 164, 2015.
- E. Van der Linden. *Coupled neutronics and computational fluid dynamics for the molten salt fast reactor*. Master's thesis, Delft University of Technology, 2012.
- A. Lindsay et al. Introduction to Moltres: An application for simulation of Molten Salt Reactors. *Annals of Nuclear Energy*, **114**, 530, 2018.
- L. Luzzi, V. Di Marcello and A. Cammi. *Multi-physics Approach to the Modelling and Analysis of Molten Salt Reactors*. Physics research and technology. Nova Science Publishers, 2012.
- D. A. Lyn et al. A laser-Doppler velocimetry study of ensemble-averaged characteristics of the turbulent near wake of a square cylinder. *Journal of Fluid Mechanics*, **304**, 285, 1995.
- H. G. MacPherson. The Molten Salt Reactor Adventure. *Nuclear Science and Engineering*, **90**, 374, 1985.
- A. Markandya and P. Wilkinson. Electricity generation and health. *The Lancet*, **370**, 979, 2007.
- L. Martel et al. Insight into the Crystalline Structure of ThF₄ with the Combined Use of Neutron Diffraction, ¹⁹F Magic-Angle Spinning-NMR, and Density Functional Theory Calculations. *Inorganic Chemistry*, **57**, 15350, 2018.
- F. C. Massa et al. High-order Linearly Implicit Two-step Peer Methods for the Discontinuous Galerkin Solution of the Incompressible RANS Equations. In *Proceedings of the VII European Congress on Computational Methods in Applied Sciences and Engineering (ECCOMAS Congress 2016)*. Athens, Greece, 2016.
- M. Massone et al. Dimensioning of the emergency draining tank for a molten salt reactor through analytical modeling. *Annals of Nuclear Energy*, **138**, 107121, 2020.
- L. Mathieu et al. The thorium molten salt reactor: Moving on from the MSBR. *Progress in Nuclear Energy*, **48**, 664, 2006.

- L. Mathieu et al. Possible Configurations for the Thorium Molten Salt Reactor and Advantages of the Fast Nonmoderated Version. *Nuclear Science and Engineering*, **161**, 78, 2009.
- E. Merle et al. Preliminary design assessment of the molten salt fast reactor. In *European Nuclear Conference ENC2012*, 2012.
- E. Muller, D. Pelletier and A. Garon. Adaptive Meshing and Time-Integrators for monolithic Finite Element Solution of the URANS equations. In *2018 AIAA Aerospace Sciences Meeting*. American Institute of Aeronautics and Astronautics, 2018.
- K. Nagy et al. Steady-state and dynamic behavior of a moderated molten salt reactor. *Annals of Nuclear Energy*, **64**, 365, 2014.
- N. Nguyen, P.-O. Persson and J. Peraire. RANS Solutions Using High Order Discontinuous Galerkin Methods. In *45th AIAA Aerospace Sciences Meeting and Exhibit*. American Institute of Aeronautics and Astronautics, 2007.
- C. Nicolino et al. Coupled dynamics in the physics of molten salt reactors. *Annals of Nuclear Energy*, **35**, 314, 2008.
- G. Noventa et al. A high-order Discontinuous Galerkin solver for unsteady incompressible turbulent flows. *Computers & Fluids*, **139**, 248, 2016.
- A. Nuttin et al. Potential of thorium molten salt reactors detailed calculations and concept evolution with a view to large scale energy production. *Progress in Nuclear Energy*, **46**, 77, 2005.
- OpenFOAM. *User Guide*, 2013.
- S. V. Patankar. *Numerical Heat Transfer and Fluid Flow*. McGraw-Hill, Inc., 1980.
- A. Pautz and A. Birkhofer. DORT-TD: A Transient Neutron Transport Code with Fully Implicit Time Integration. *Nuclear Science and Engineering*, **145**, 299, 2003.
- S. D. Pautz. Verification of Transport Codes by the Method of Manufactured Solutions: The ATTILA Experience. Technical Report LA-UR-01-1487, Los Alamos National Laboratory, Los Alamos, USA, 2001.
- Z. Perkó. *Sensitivity and Uncertainty Analysis of Coupled Reactor Physics Problems*. Ph.D. thesis, Delft University of Technology, 2015.
- M. Piatkowski, S. Müthing and P. Bastian. A stable and high-order accurate discontinuous Galerkin based splitting method for the incompressible Navier-Stokes equations. *Journal of Computational Physics*, **356**, 220, 2018.

- A. Pini, A. Cammi and L. Luzzi. Analytical and numerical investigation of the heat exchange effect on the dynamic behaviour of natural circulation with internally heated fluids. *Chemical Engineering Science*, **145**, 108, 2016a.
- A. Pini et al. An Experimental Facility to Investigate the Natural Circulation Dynamics in Presence of Distributed Heat Sources. *Energy Procedia*, **101**, 10, 2016b.
- S. B. Pope. *Turbulent Flows*. Cambridge University Press, 2000.
- S. Qiu et al. Coupled neutronics/thermal-hydraulics and safety characteristics of liquid-fueled Molten Salt Reactors. *Kerntechnik*, **81**, 149, 2016.
- J. C. Ragusa and V. S. Mahadevan. Consistent and accurate schemes for coupled neutronics thermal-hydraulics reactor analysis. *Nuclear Engineering and Design*, **239**, 566, 2009.
- W. H. Reed and T. R. Hill. Triangular mesh methods for the neutron transport equation. Technical Report LA-UR-73-479, Los Alamos Scientific Laboratory, 1973.
- S. Rhebergen, B. Cockburn and J. J. W. van der Vegt. A space-time discontinuous Galerkin method for the incompressible Navier-Stokes equations. *Journal of Computational Physics*, **233**, 339, 2013.
- R. C. Robertson. MSRE Design and Operations Report — Part I — Description of Reactor Design. Technical Report ORNL-TM-728, Oak Ridge National Laboratory, 1965.
- R. C. Robertson. Conceptual Design Study of a Single-fluid Molten-salt Breeder Reactor. Technical Report ORNL-4541, Oak Ridge National Laboratory, 1971.
- W. Rodi. Comparison of LES and RANS calculations of the flow around bluff bodies. *Journal of Wind Engineering and Industrial Aerodynamics*, **69-71**, 55, 1997.
- W. Rodi et al. Status of Large Eddy Simulation: Results of a Workshop. *Journal of Fluids Engineering*, **119**, 248, 1997.
- D. Rodrigues, G. Durán-Klie and S. Delpech. Pyrochemical reprocessing of molten salt fast reactor fuel: focus on the reductive extraction step. *Nukleonika*, **60**, 907, 2015.
- H. Rouch et al. Preliminary thermal-hydraulic core design of the Molten Salt Fast Reactor (MSFR). *Annals of Nuclear Energy*, **64**, 449, 2014.

- P. Rubiolo et al. High temperature thermal hydraulics modeling of a molten salt: application to a molten salt fast reactor (MSFR). *ESAIM Proceedings and Surveys*, **58**, 98, 2017.
- A. Santamarina et al. The JEFF-3.1.1 Nuclear Data Library. JEFF Report 22, NEA-OECD, 2009.
- S. Schoenawa and R. Hartmann. Discontinuous Galerkin discretization of the Reynolds-averaged Navier-Stokes equations with the shear-stress transport model. *Journal of Computational Physics*, **262**, 194, 2014.
- J. Serp et al. The molten salt reactor (MSR) in generation IV: Overview and perspectives. *Progress in Nuclear Energy*, **77**, 308, 2014.
- K. Shahbazi, P. F. Fischer and C. R. Ethier. A high-order discontinuous Galerkin method for the unsteady incompressible Navier-Stokes equations. *Journal of Computational Physics*, **222**, 391, 2007.
- T.-H. Shih, J. Zhu and J. L. Lumley. A new Reynolds stress algebraic equation model. *Computer Methods in Applied Mechanics and Engineering*, **125**, 287, 1995.
- B. K. Sovacool et al. Balancing safety with sustainability: assessing the risk of accidents for modern low-carbon energy systems. *Journal of Cleaner Production*, **112**, 3952, 2016.
- A. I. Surenkov et al. Corrosion Resistance and Mechanical Stability of Nickel Alloys in Molten-Salt Nuclear Reactors. *Atomic Energy*, **124**, 43, 2018.
- S. Thangam and C. G. Speziale. Turbulent flow past a backward-facing step - A critical evaluation of two-equation models. *AIAA Journal*, **30**, 1314, 1992.
- M. Tiberger, D. Lathouwers and J. L. Kloosterman. A discontinuous Galerkin FEM multi-physics solver for the molten salt fast reactor. In *International Conference on Mathematics and Computational Methods Applied to Nuclear Science and Engineering, M & C 2019*, 1818–1827. Portland, OR, USA, 2019a.
- M. Tiberger et al. Preliminary investigation on the melting behavior of a freeze-valve for the Molten Salt Fast Reactor. *Annals of Nuclear Energy*, **132**, 544, 2019b.
- M. Tiberger et al. Results from a multi-physics numerical benchmark for codes dedicated to molten salt fast reactors. *Annals of Nuclear Energy*, **142**, 107428, 2020a.
- M. Tiberger et al. Results of the CNRS benchmark. Zenodo, 2020b.
- A. Tosolin et al. Isobaric Heat Capacity of Solid and Liquid Thorium Tetrafluoride. *Journal of Chemical & Engineering Data*, **64**, 3945, 2019a.

- A. Tosolin et al. Vaporization behaviour of a PuF₃-containing fuel mixture for the Molten Salt Fast Reactor. *Journal of Nuclear Materials*, **527**, 151780, 2019b.
- F. X. Trias, A. Gorobets and A. Oliva. Turbulent flow around a square cylinder at Reynolds number 22,000: A DNS study. *Computers & Fluids*, **123**, 87, 2015.
- C. Tripodo et al. Development of a control-oriented power plant simulator for the molten salt fast reactor. *EPJ Nuclear Sciences and Technologies*, **5**, 13, 2019.
- UNFCCC. Paris agreement. Technical report, United Nations, 2015.
- United Nations. World Population Prospects 2019 — Volume II — Demographic Profiles. Technical report, United Nations, Department of Economic and Social Affairs, Population Division, 2019.
- J. J. W. Van der Vegt and J. J. Sudirham. A space-time discontinuous Galerkin method for the time-dependent Oseen equations. *Applied Numerical Mathematics*, **58**, 1892, 2008.
- J. J. W. Van der Vegt, Y. Xia and Y. Xu. Positivity Preserving Limiters for Time-Implicit Higher Order Accurate Discontinuous Galerkin Discretizations. *SIAM Journal on Scientific Computing*, **41**, A2037, 2019.
- J. Van Kan. A second-order accurate pressure correction scheme for viscous incompressible flow. *SIAM Journal on Scientific and Statistical Computing*, **7**, 870, 1986.
- K. Van Maele and B. Merci. Application of two buoyancy-modified $k - \epsilon$ turbulence models to different types of buoyant plumes. *Fire Safety Journal*, **41**, 122, 2006.
- J. Vergnes and D. Lecarpentier. The AMSTER concept (actinides molten salt transmuter). *Nuclear Engineering and Design*, **216**, 43, 2002.
- P. R. Voke. Flow Past a Square Cylinder: Test Case LES2. In *Direct and Large-Eddy Simulation II*, 355–373. Springer Netherlands, 1997.
- V. R. Voller, C. R. Swaminathan and B. G. Thomas. Fixed grid techniques for phase change problems: A review. *International Journal for Numerical Methods in Engineering*, **30**, 875, 1990.
- A. E. Waltar, D. R. Todd and P. V. Tsvetkov. *Fast Spectrum Reactors*. Springer, 2012.
- C. Wan, T. Hu and L. Cao. Multi-physics numerical analysis of the fuel-addition transients in the liquid-fuel molten salt reactor. *Annals of Nuclear Energy*, **144**, 107514, 2020.

- S. Wang, A. Rineiski and W. Maschek. Molten salt related extensions of the SIMMER-III code and its application for a burner reactor. *Nuclear Engineering and Design*, **236**, 1580, 2006.
- S. Wang et al. A passive decay heat removal system for emergency draining tanks of molten salt reactors. *Nuclear Engineering and Design*, **341**, 423, 2019.
- Y. Wang and J. C. Ragusa. Diffusion synthetic acceleration for high-order discontinuous finite element S_N transport schemes and application to locally refined unstructured meshes. *Nuclear Science and Engineering*, **166**, 145, 2010.
- T. A. Wareing et al. Discontinuous Finite Element S_N Methods on Three-Dimensional Unstructured Grids. *Nuclear Science and Engineering*, **138**, 256, 2001.
- J. S. Warsa, T. A. Wareing and J. E. Morel. Krylov iterative methods and the degraded effectiveness of diffusion synthetic acceleration for multidimensional S_N calculations in problems with material discontinuities. *Nuclear Science and Engineering*, **147**, 218, 2004.
- P. T. Williams. Thermal radiative transport through LiF for temperatures near the melting point. Technical Report K/CSD/TM-77, Oak Ridge National Laboratory, 1988.
- R. Yoshioka. Nuclear Energy Based on Thorium Molten Salt. In *Molten Salts Chemistry*, 471–496. Elsevier, 2013.
- M. Zanetti et al. Extension of the FAST code system for the modelling and simulation of MSR dynamics. In *Proceedings of ICAPP 2015*. Nice, France, 2015.
- D. Zhang et al. Review of conceptual design and fundamental research of molten salt reactors in China. *International Journal of Energy Research*, **42**, 1834, 2018.
- M. Zijlema. *Computational modeling of turbulent flow in general domains*. Ph.D. thesis, Delft University of Technology, 1996.

MULTI-PHYSICS NUMERICAL BENCHMARK: OBSERVABLES FIELDS

This appendix reports plots of some observables in the entire domain relative to some steps of the multi-physics cavity benchmark described in Chapter 4. It is meant to complete Section 4.5. Each figure compares the results obtained by each code and shows an observable in three steady-state situations: fixed-velocity problem (indicated with “V”); buoyancy-only problem (indicated with “B”); and fully-coupled problem (indicated with “C”). Even if just qualitative, the agreement among partners for all cases and observables is excellent.

A.1 Velocity

Figure A.1 shows the velocity magnitude field with flow streamlines obtained by each code in three different benchmark steps: Step 0.1 (V); Step 1.3 (B); and Step 1.4 with $P = 1 \text{ GW}$ and $U_{lid} = 0.5 \text{ m s}^{-1}$ (C).

A.2 Temperature

Figure A.2 shows the temperature field obtained by each code in three different benchmark steps: Step 0.3 (V); Step 1.3 (B); and Step 1.4 with $P = 1 \text{ GW}$ and $U_{lid} = 0.5 \text{ m s}^{-1}$ (C).

A.3 Delayed neutron precursors

Figures A.3 and A.4 report the distributions of two delayed neutron precursors families (long and short lived, respectively) obtained by each code in three different benchmark steps: Step 1.1 (V); Step 1.3 (B); and Step 1.4 with $P = 1 \text{ GW}$ and $U_{lid} = 0.5 \text{ m s}^{-1}$ (C).

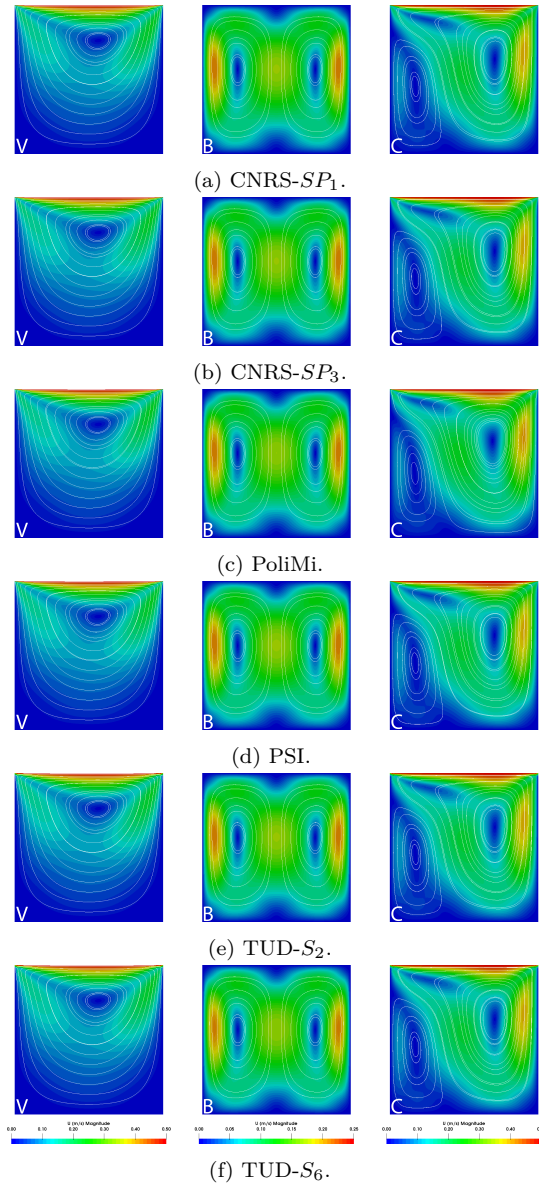


Fig. A.1. Velocity magnitude field and flow streamlines obtained by each code in three different benchmark steps. From left to right: Step 0.1 (V); Step 1.3 (B); and Step 1.4 with $P = 1 \text{ GW}$ and $U_{lid} = 0.5 \text{ m s}^{-1}$ (C). The streamlines were generated sampling 15 seeds along line BB' for case (V), 15 seeds along AA' for case (B), and 20 seeds along BB' for case (C). Please note that the color bar scale for each step is different, and, for clarity, it has been reported only once per column.

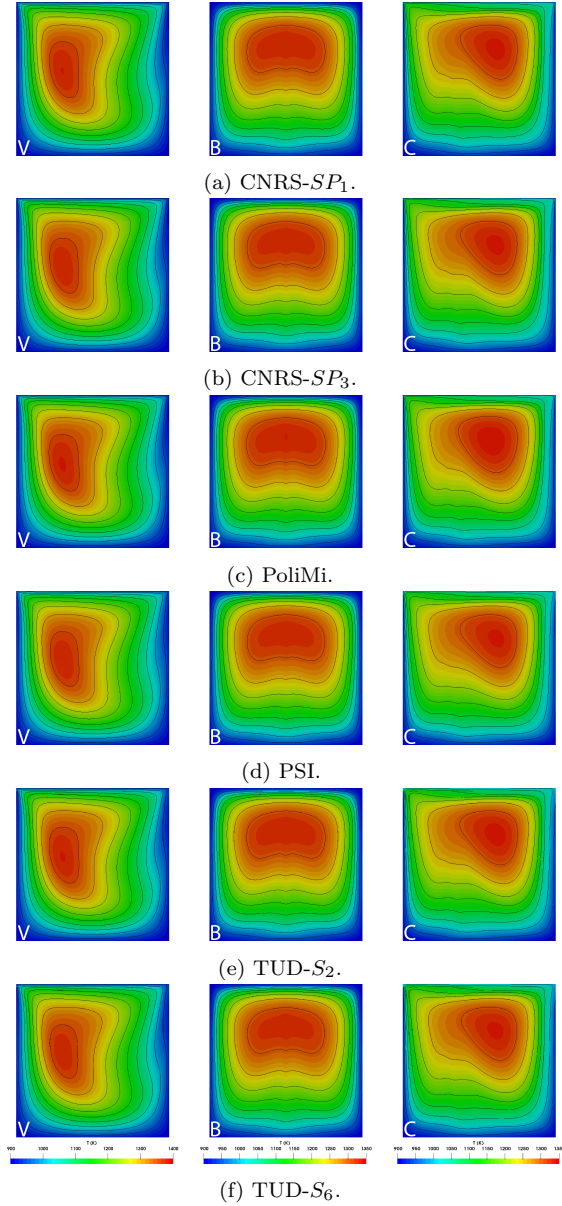


Fig. A.2. Temperature field with isolines obtained by each code in three different benchmark steps. From left to right: Step 0.3 (V); Step 1.3 (B); and Step 1.4 with $P = 1 \text{ GW}$ and $U_{lid} = 0.5 \text{ m s}^{-1}$ (C). 50 K was selected as isoline interval in all figures. Please note that the color bar scale for each step is different, and, for clarity, it has been reported only once per column.

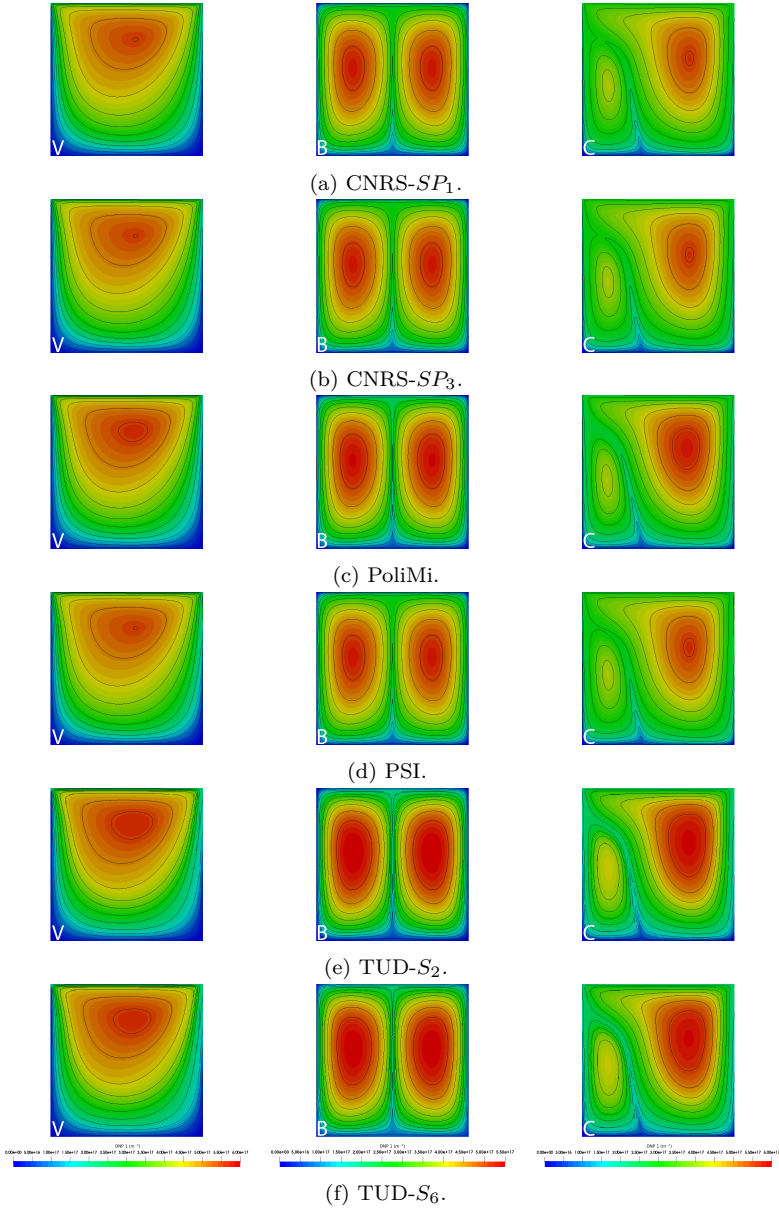


Fig. A.3. Distribution of the first family of delayed neutron precursors ($T_{1/2} = 55.6$ s) with isolines obtained by each code in three different benchmark steps. From left to right: Step 1.1 (V); Step 1.3 (B); and Step 1.4 with $P = 1$ GW and $U_{lid} = 0.5$ m s $^{-1}$ (C). 5.0×10^{16} m $^{-3}$ was selected as isoline interval in all figures. Please note that the color bar scale for each step is different, and, for clarity, it has been reported only once per column.

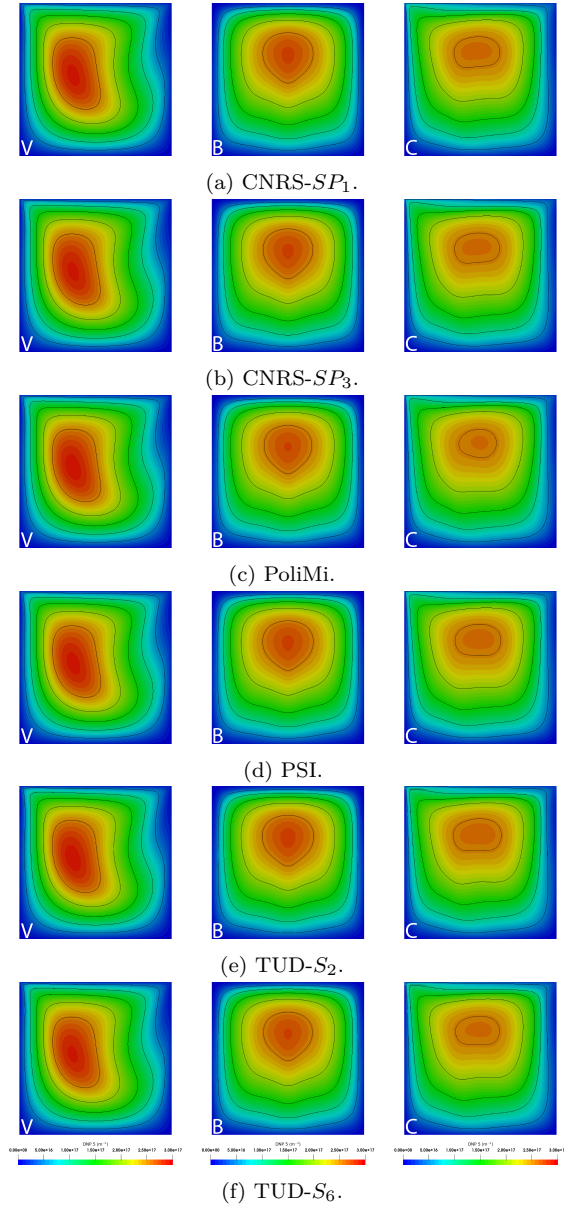


Fig. A.4. Distribution of the fifth family of delayed neutron precursors ($T_{1/2} = 2.37$ s) with isolines obtained by each code in three different benchmark steps. From left to right: Step 1.1 (V); Step 1.3 (B); and Step 1.4 with $P = 1$ GW and $U_{lid} = 0.5$ m s $^{-1}$ (C). 5.0×10^{16} m $^{-3}$ was selected as isoline interval in all figures. Please note that the color bar scale for each step is different, and, for clarity, it has been reported only once per column.

Acknowledgments

First of all, I want to thank my promoters Prof. Jan Leen Kloosterman and Dr. Danny Lathouwers for giving me the opportunity to pursue a PhD at the RPNM faculty. This experience contributed immensely to my professional and personal growth. In particular, a huge thanks goes to Danny, for his endless support and guidance throughout these years. In troublesome times, he remained optimistic and encouraged me; the few times I was satisfied of my results, he pushed me to stay focused on the problems yet to be solved to reach the bigger goal. Without his expertise and the countless stimulating discussions with him, I would not have been able to succeed. Thank you also for the help in the development of the multi-physics tool, especially in the first phase.

The work described in this thesis was performed in the framework of the Euratom SAMOFAR project. I am very grateful to all the colleagues I had the honor to meet, work, and especially have fun with in occasion of the project meetings. In particular, thanks to Stefano (or Stefàno?) for his constant availability and willingness to help (despite his busy agenda) with whatever concerned the simulations of the CNRS benchmark and the MSFR. It was a real pleasure to work with you.

Many thanks to all my colleagues at the RPNM group and the RID, without whom these years would have been way more lonely and boring. Thanks to Matteo, Denis, and Valentina, the “old generation” who helped me becoming familiar with the new environment and immediately made me feel part of a group organizing dinners and other fun activities. A big thank to Aldo: the `DGFloWS` code is the result of our combined efforts and countless fruitful discussions. Thanks to him, I never stopped improving my programming skills.

Fulvio, Fahad, Laura, Elisa, Enrica, Guilhem, Sara, Jaén, we spent so much time together that it is impossible for me to write down all the reasons why I have to thank you. We have been office and/or house mates, we have had endless fun during our dinner-nights, playing beach volley, tennis, going bouldering, having drinks at 't Koepeltje (Koos, you are the greatest barman!)...If my time in Delft was great, it is especially because of you.

Un grazie immenso ai miei genitori, Alessandro e Daniela, e a mia nonna Marisa, per il supporto costante ed incondizionato e per non avermi mai fatto sentire

Acknowledgments

la distanza (anche grazie a vagonate di cibo portate dall'Italia). Se le difficoltà incontrate nel mio percorso di studi mi sono sembrate grandi, è solo perché avete reso facile tutto il resto.

Finally, my dearest, Allegra. Thank you for your infinite patience and for constantly believing in me way more than I do. Look at where we are, look at where we started...Thank you for always being by my side.

List of publications

Journal Papers

- F. Alsayyari, M. Tiberga, Z. Perko, J.L. Kloosterman, and D. Lathouwers. Analysis of the Molten Salt Fast Reactor using Reduced-Order Models. Submitted for publication.
- M. Tiberga, A. Hennink, J.L. Kloosterman, and D. Lathouwers. A high-order discontinuous Galerkin solver for the incompressible RANS equations coupled to the $k - \epsilon$ turbulence model. Submitted for publication.
- A. Hennink, M. Tiberga, and D. Lathouwers. A Pressure-based Solver for Low-Mach Number Flow using a Discontinuous Galerkin Method. Submitted for publication.
- F. Alsayyari, Z. Perko, M. Tiberga, J.L. Kloosterman, and D. Lathouwers. A fully adaptive nonintrusive reduced order modeling approach for parametrized time-dependent problems. Accepted for publication in *Computer Methods in Applied Mechanics and Engineering*.
- M. Tiberga, D. Lathouwers, and J.L. Kloosterman. A multi-physics solver for liquid-fueled fast systems based on the discontinuous Galerkin FEM discretization, *Progress in Nuclear Energy*, **127**, 103427, 2020. doi:10.1016/j.pnucene.2020.103427
- M. Tiberga, R.G.G. de Oliveira, E. Cervi, J.A. Blanco, S. Lorenzi, M. Aufiero, D. Lathouwers, and P. Rubiolo. Results from a multi-physics numerical benchmark for codes dedicated to molten salt fast reactors. *Annals of Nuclear Energy*, **142**, 107428, 2020. doi:10.1016/j.anucene.2020.107428
- F. Alsayyari, M. Tiberga, Z. Perko, D. Lathouwers, and J.L. Kloosterman. A nonintrusive adaptive reduced order modeling approach for a molten salt reactor system. *Annals of Nuclear Energy*, **141**, 107321, 2020. doi:10.1016/j.anucene.2020.107321

- M. Tiberga, D. Shafer, D. Lathouwers, M. Rohde, and J.L. Kloosterman. Preliminary investigation on the melting behavior of a freeze-valve for the Molten Salt Fast Reactor. *Annals of Nuclear Energy*, **132**, pp. 544–554, 2019. doi:10.1016/j.anucene.2019.06.039

Conference Papers

- M. Santanoceto, M. Tiberga, Z. Perkó, S. Dulla, and D. Lathouwers. Uncertainty quantification in steady state simulations of a molten salt system using Polynomial Chaos Expansion analysis. *Physics of Reactors 2020 (PHYSOR 2020)*, Cambridge, UK, March 29–April 2, 2020.
- M. Tiberga, D. Lathouwers, and J.L. Kloosterman. A discontinuous Galerkin FEM multi-physics solver for the Molten Salt Fast Reactor. *International Conference on Mathematics and Computational Methods applied to Nuclear Science and Engineering (M&C 2019)*, Portland, OR, USA, August 25–29, 2019.
- M. Tiberga, D. Shafer, D. Lathouwers, and J.L. Kloosterman. Preliminary assessment of the freeze-plug melting behavior in the Molten Salt Fast Reactor. *Fourth International Conference on Physics and Technology of Reactors and Applications (PHYTRA4)*, Marrakech, Morocco, September 17–19, 2018.

About the author

Marco Tiberga was born in Asti (Italy) on October 26, 1991. He grew up in the city of the sparkling wine, where he finished his high school studies at Liceo Scientifico F. Vercelli in 2010.

In the autumn of the same year, he enrolled in the Energy Engineering Bachelor program at Politecnico di Torino. After three years, during which he grew enthusiast of nuclear science and technology, he graduated cum laude on October 7, 2013 with the thesis “Design of an intermediate heat exchanger for a sodium cooled fast reactor”. He continued his studies at Politecnico di Torino, enrolling in the Energy and Nuclear Engineering Master program. He carried out his thesis entitled “The use of the Spectral Element Methods for neutron transport calculations” in the DENERG Department at Politecnico, and on October 15, 2015 he obtained his MSc degree cum laude.

After two weeks, he left Turin and Italy to become a PhD candidate in multi-physics simulations of molten salt reactors in the Faculty of Applied Sciences at Delft University of Technology. This thesis is the result of the years spent working in the Reactor Physics and Nuclear Materials research group.

